FOSSIL ENERGY

DOE/MC/22042-10
(DE88001227)

RESERVOIR CHARACTERIZATION FOR THE CO_2 ENHANCED OIL RECOVERY PROCESS

FY 1987 Annual Report

By
Franklin M. Orr, Jr.
Abraham Sageev Grader

April 1988

Performed Under Contract No. AC21-85MC22042

Stanford University
Stanford, California

Bartlesville Project Office
U. S. DEPARTMENT OF ENERGY
Bartlesville, Oklahoma

DISCLAIMER

Printed in the United States of America. Available from:
National Technical Information Service
U.S. Department of Commerce
5285 Port Royal Road
Springfield, VA 22161

NTIS price codes
Paper copy: **A12**
Microfiche copy: **A01**

DOE/MC/22042-10
Distribution Category UC-122

RESERVOIR CHARACTERIZATION FOR THE CO_2 ENHANCED OIL RECOVERY PROCESS

FY 1987 Annual Report

By
Franklin M. Orr, Jr.
Abraham Sageev Grader

April 1988

Work Performed Under Contract No. AC21-85MC22042

Prepared for
U.S. Department of Energy
Assistant Secretary for Fossil Energy

Royal J. Watts, Project Manager
Morgantown Energy Technology Center
P.O. Box 880
Morgantown, WV 26505

Prepared by
Stanford University
Department of Petroleum Engineering
Stanford, California 94305

Table of Contents

List of Tables

List of Figures

Acknowledgements

The research program described here was supported by the U. S. Department of Energy under Contract DE-AC21-85MC-22042 and by the Stanford University Miscible Flooding Industrial Affiliates: Amoco, ARCO, Chevron, Conoco, Japan National Oil Company, Mobil, Shell, Standard Oil, Tenneco and Texaco. Support for laboratory equipment was also provided by the Mobil Foundation. We gratefully acknowledge all those sources of support.

Our colleagues in Petroleum Engineering, K. Aziz, W.E. Brigham, R.N. Horne and H.J. Ramey, and, of course, their students, contributed materially to the research effort described here. We also benefited from many discussions with A.M. Nur, A. Journel and their research groups in the Geophysics and Applied Earth Sciences Departments at Stanford. The problems considered here are sufficiently complex that that sort of collaboration is an essential part of progress. Finally, we thank our colleagues in the companies that support this work for their interest, for taking time to listen to and talk to our students and for many thoughtful comments and suggestions.

This report would never have been completed without J.C. Mankinen's careful attention. With assistance from R.J. Benelli, T.A. Ramey, T. Sumida and A. Jones she organized contributions from a group of unruly students and professors into the finished product presented here, and hence deserves our special thanks.

Abstract

This report summarizes progress in a research effort to quantify the effects of nonuniform flow on displacement performance in CO_2 floods. Results are reported in three areas:

(1) Effect of phase behavior in one-dimensional flow.

(2) Interaction of viscous instability and flow in heterogeneous porous media.

(3) Detection and representation of heterogeneity.

In the first area, the development of a new experimental apparatus for simultaneous measurement of phase compositions, viscosities, and densities is described. Also reported are results of calculations by the method of characteristics of the effects of the presence of dissolved methane on the development of miscibility. Those calculations show that measured minimum miscibility pressures are insensitive to the presence of methane, because it partitions so effectively into the CO_2-rich phase that all the methane has been displaced before the CO_2 arrives. The method of characteristics for analysis of the flow of CO_2-steam-heavy oil mixtures with varying temperatures and the flow of ternary mixtures in a two-layer porous medium with viscous crossflow is described. Also reported are results of an investigation of the interaction of phase behavior with dispersive mixing. Those calculations show that the sensitivity of the performance of a displacement to changes in the level of dispersion depends on the size and shape of the two-phase region for ternary systems.

In the second area, partly-scaled experiments to study the effects of viscous instability in the presence of permeability variation are described. In addition, results of detailed simulations of the growth of viscous fingers in both homogeneous and heterogeneous porous media are described. Those calculations indicate that when local permeability in a heterogeneous permeability field is correlated over a significant fraction of the flow length, the pattern of finger growth is dominated by the permeability variation.

In the third area, use of a combination of pressure transient and well-to-well tracer tests to detect the presence of reservoir heterogeneities is discussed. Also presented is a technique for calculation of the transient pressure response to large scale heterogeneities and an analysis of the pressure response of one- and two-dimensional composite reservoirs. Finally, results of calculations of the effects heterogeneity and capillary and viscous crossflow are reported. They show that for mild permeability variations, crossflow can mitigate effects of heterogeneity sufficiently that representation of the flow in terms of pseudorelative permeability functions is reasonable.

1. Introduction

Extensive laboratory testing and a considerable body of field experience indicate that CO_2 flood processes can displace oil effectively at both scales. The oil recovered at either scale results from a complex interplay of interacting and competing transport mechanisms: phase behavior, variations in fluid properties with phase compositions, diffusion and dispersion, viscous instability, density and capillary driven crossflow and, of course, reservoir heterogeneity. The scale dependence of process performance results from the fact that the length scales on which the various mechanisms have the largest impact change in different ways as the scale of the displacement changes. Quantification of that scale dependence is the central issue of current research on methods for more accurate prediction of CO_2 flood performance at field scale.

Unfortunately, fully detailed field-scale simulation of the combined effects of phase behavior and nonuniform flow caused by viscous instability, heterogeneity or both, is not possible using simulation techniques and computers currently available. Indeed, for the foreseeable future simulations will be conducted with grid blocks that are large compared to some of the scales of variation of rock properties and fluid compositions. Thus, large-scale simulation representations will rely on averages of process mechanisms operating at smaller scales. The objective of the research described in this report is to improve quantitative descriptions of the interplay of process mechanisms and scales, so that averaged representations can be developed that reflect those mechanisms with reasonable accuracy.

Because the overall problem is too complex to be attacked directly, we consider here a sequence of simpler problems that illustrate behavior in relevant limiting cases. In chapter 2 we describe experimental equipment developed to study the phase behavior and fluid properties of mixtures that occur during miscible displacements. Also reported in chapter 2 are formulations and results of several calculations that examine interactions of phase behavior and flow in one- and two-dimensional systems. Chapter 3 reports preliminary results of flow visualization experiments to examine the interaction of viscous fingering with variations in permeability. Also described are more extensive results of calculations of the long term growth of viscous fingers in both homogeneous and heterogeneous flow systems.

In chapter 4 we examine the question of detection of reservoir heterogeneities by pressure transient and well-to-well tracer tests. In addition, we report results of calculations that illustrate the importance of crossflow in flow in heterogeneous porous media and consider the implications of crossflow for representation of the effects of heterogeneity by averaged (pseudo-) relative permeability and fractional flow functions.

The results reported suggest that improved descriptions of process performance in nonuniform flow systems can be developed, though much work remains to be done. The research effort described here is a step toward that goal.

2. Phase Behavior and Flow

High local displacement efficiency in a CO_2 or other miscible process depends on the transfer of components between phases. If the transfer is efficient, and the effects of dispersion and nonuniform flow negligible, local displacement efficiency may approach 100 percent. Thus, in nearly one-dimensional displacements, such as occur in a slim tube, for example, phase behavior dominates the displacement process. Thus phase behavior and accompanying fluid property data are an important part of any description of miscible flood processes. In Section 2.1 we describe the design and testing of a new apparatus for phase behavior and fluid property measurements. In Section 2.2 we consider the combined effects of phase behavior and flow in one dimension. In that analysis the effect of methane (C_1) dissolved in an oil is studied by treating the CO_2-oil system as a four component mixture rather than as a ternary system. In Section 2.3 we apply a similar mathematical technique to study the behavior of steam-water-CO_2-oil displacements in which the temperature also varies. That analysis is an investigation of the combined effects of phase behavior and viscosity reduction of a heavy oil by heating and dissolved CO_2.

In actual CO_2 floods, the effect of phase behavior on composition path is modified by the nonuniform flow that inevitably results from reservoir heterogeneity and viscous instability. In Section 2.4 we describe an analysis by the method of characteristics of flow of two-phase, ternary mixtures in a two-layer system with crossflow. Because it includes effects of crossflow and nonuniform flow that problem is a simplified model for the effects of phase behavior and heterogeneity or viscous instability. In Section 2.5 we return to the effects of dispersion on composition path and show that the magnitude of the interaction of dispersion and phase behavior depends on the size and shape of the two-phase region. Those results may explain why slim tube displacements using nitrogen appear to show length effects not observed in similar displacements with CO_2.

2.1 Supercritical Extraction, Phase Behavior and Fluid Properties

Gersem Andrade and Aaron Stessman

Miscible displacement processes may use carbon dioxide (CO_2), nitrogen (N_2) or methane (CH_4) as the injected fluid. For all three fluids, efficient displacement results when the injected fluid is dense enough to extract hydrocarbons from the reservoir fluid. Slim tube displacement experiments indicate that pressures required for high recovery are much higher for N_2 and CH_4 than for CO_2. That behavior results from the low critical temperatures of N_2 (126°K) and CH_4 (191°K). Typical reservoir temperatures are farther above the critical temperatures of N_2 and CH_4 than of CO_2, and hence higher pressures are required to produce comparable molar densities. While it is known that high density is required for relatively efficient extraction, it is not clear whether N_2, CH_4, and CO_2 extract the same amounts or types of hydrocarbons when the injected fluid has similar molar density. To examine the relationship between the extraction for the three fluid systems, an apparatus for phase composition measurements was designed and assembled. The apparatus is designed to perform fluid property measurements in addition to phase composition measurements, and is described in the next section.

2.1.1 Apparatus

The apparatus is based on a PVT cell mounted in a temperature-controlled oven as shown in the schematic of Fig. 2.1.1.

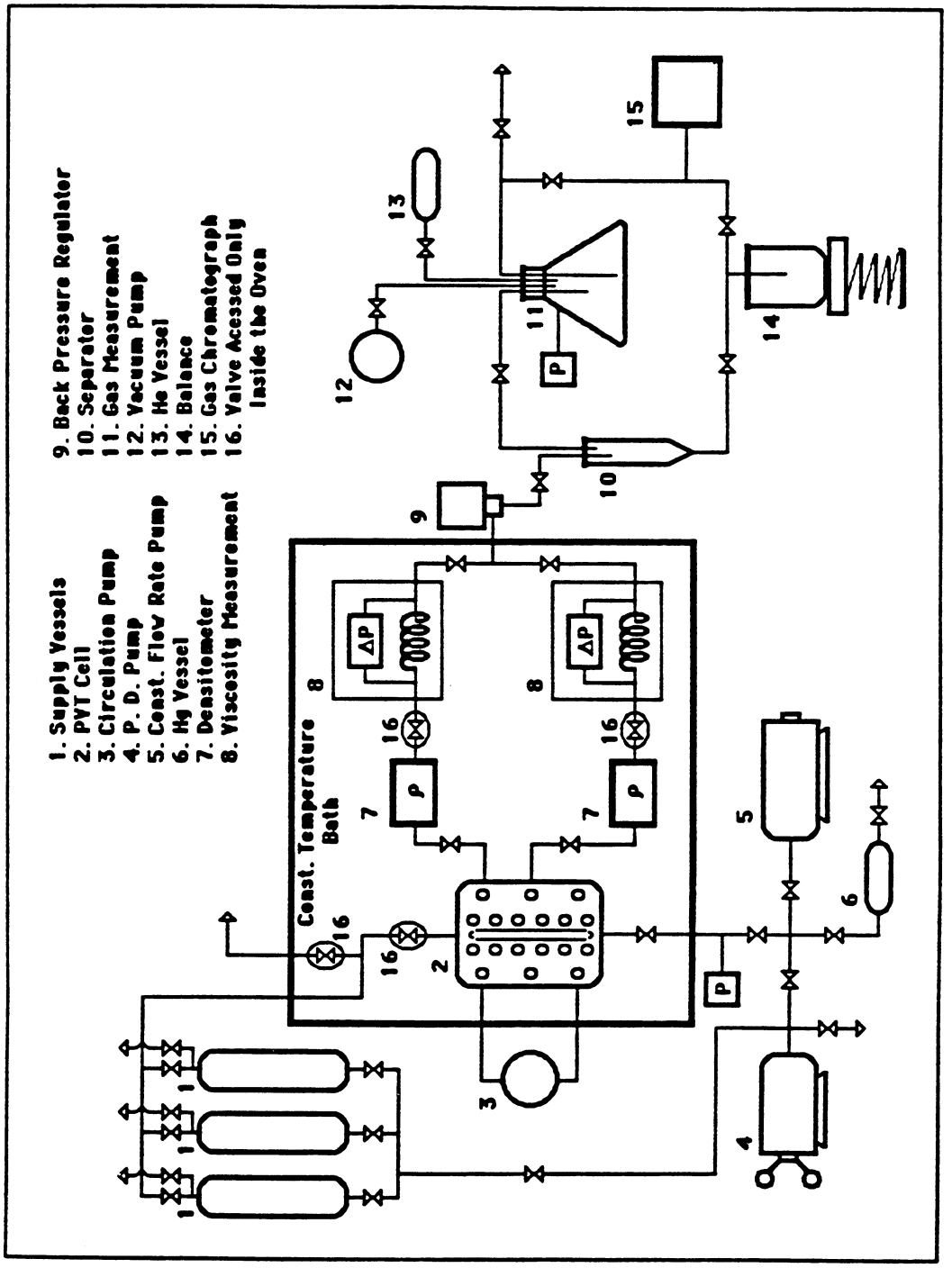

Fig. 2.1.1. Schematic diagram of the PVT apparatus.

The positive displacement pump shown in Fig. 2.1.1 (HIP, model 62-6-10) and the constant flow rate pump (Petrophysical Services, model M106-178) can be used to charge the PVT cell (Ruska, model 2329) with a mixture of known composition using fluids from the supply vessels (Temco, model CR-50). The pressure of the mixture is set by injecting or removing mercury from the PVT cell using the constant flow rate pump, and is measured by a quartz transducer (Paroscientific Digiquartz, model 1006K). The cell temperature is set by the controllers in the oven and is measured by a platinum resistance thermometer (Stolab, model PL-403). Once the cell is charged and the desired pressure and temperature conditions are achieved, the mixture can be brought to thermodynamic equilibrium by means of a circulation pump (Eldex, model B-100-1). After equilibrium is reached, the phases present are allowed to separate, and the volumes of the phases can be measured by a digital height meter (Sony, model H-2060).

To measure phase compositions and properties, the phases are then displaced, one at a time, at a known flow rate by the constant flow rate pump through one of the flow paths to the back pressure regulator (Temco, model BPR-5-9). Each path includes a densitometer (Mettler/Paar, DMA-512), for density measurement, and a capillary tube (high pressure tubing, 0.006 in ID) for viscosity measurement. The viscosity is determined from the value of the flow rate set by the pump and the pressure difference across the capillary tube, measured with a pressure difference transducer (Sensotec, model HL-Z/5549-01).

Once the sample is displaced through the densitometer and capillary tube, it is blown down to close to atmospheric pressure at the back pressure regulator. At low pressure and room temperature, the phase being analyzed is allowed to separate into a vapor phase and a liquid phase. The amount of liquid phase is determined by weight, and its composition is measured by simulated distillation in a gas chromatograph (Hewlett-Packard, model 5880). The low pressure vapor flows to an evacuated container of known volume. Measurement of the pressure in the container and the room temperature allows calculation of the total number of moles of gas using the ideal gas law. The gas in the container is then displaced by helium to the gas chromatograph where its composition is determined. From the amounts and compositions of liquid and vapor, the phase composition can be calculated. Thus the apparatus allows measurement of equilibrium phase compositions for all phases present in the PVT cell as well as their fluid properties. Furthermore, physical samples are obtained so that a more sophisticated compositional analysis can be performed if desired.

2.1.2 Calibration Runs

The accuracy of the results obtained with the apparatus described above depends on the accuracy which volumes and flow rates are estimated. Volumes and flow rates are estimated by the amounts of mercury displaced from the pumps to the system, and also by the measurement of the position of fluid interfaces seen through the windows of the cell. The flow rates must be known for the measurement of viscosity, and they are also related to the amount of mercury displaced from the pumps with time.

As different conditions of pressure and temperature may occur in the pumps and in the cell and in the capillary tubes, the volumes of mercury that are read directly from the pumps are not necessarily equal to the volume injected or withdrawn from the cell or capillary tubes. Thus, the response of the internal volumes of the pumps and cell when subjected to different pressures and temperatures, as well as the relationship between the volume in the cell and the position of the fluid interface seen through the windows of the cell, were evaluated in the calibration runs described below.

(1) In order to determine the relationship between the volume read in the pumps and the volume actually delivered, the pumps (HIP and PSI) are filled with mercury and then some amounts of mercury (about 10 cc) are pumped and weighed. Pressures and temperatures were recorded and the volume actually delivered was estimated using the densities of mercury at the temperature of the pump and at room temperature. The procedure

was repeated at different conditions of pressure and temperature and it was observed that the HIP pump delivers 0.36097 cc per revolution with a relative error no greater than 0.6%, and the PSI pump delivers 1.00788 cc per each cubic centimeter read with a relative error no greater than 0.03%. It was decided then to use the PSI pump as the volume reference for measurements with the apparatus.

(2) The compressibility of the pumps was estimated by compressing mercury in the pumps with the outlet valves closed and reading the volume required to raise the pressure to values desired (0 to 8000 psi with 1000 psi steps).

(3) The volume in the cell and the corresponding height read in the height meter were calibrated using the set up shown in Fig. 2.1.2. A high pressure nitrogen bottle was used to set pressures in the system, and the temperature was set by the controllers in the oven. The cell was completely filled with mercury and some amount of mercury was withdrawn (10 cc) with the PSI pump. The valve at the bottom of the cell was then closed and the height of the interface mercury-decane was read. The volume of mercury actually withdrawn from the cell was determined by using the densities of mercury in the pump and in the cell. The pressure was then increased stepwise (2000 psi steps) and new measurements were made. The temperature was also increased stepwise and the measurements repeated to access the volumetric behavior of the internal chamber of the cell and the volume factor for the height meter at different pressure and temperatures.

(4) The densitometers and capillary tubes are currently being calibrated by charging the cell with a fluid of known density and viscosity behavior at different conditions (decane and methane) and displacing the fluid through each one of the sampling branches shown in Fig. 2.1.1 at a known flow rate. The pressure difference across the capillary tube is measured, and new conditions of pressure and temperature are established for further measurements.

Addition of a microcomputer to the system is now underway. It will be used to automate acquisition of phase volume, temperature and pressure data, so that consistency of volumetric measurements can be checked while experiments are in progress.

2.2 Composition Paths in Four-Component Systems

Wesley W. Monroe

Understanding of the role of phase behavior in the development of miscibility in CO_2 floods, vaporizing gas drives and condensing gas drives is usually derived from analysis of composition paths represented on ternary or pseudo-ternary phase diagrams (Slobod and Koch 1953, Hutchinson and Braun 1961, Defrenne et al. 1961). Consideration of four-component systems has been limited to the qualitative discussions of Defrenne et al. (1961), Rathmell et al. (1971) and Stalkup (1983). Mathematical analysis of such flows has also been based on ternary representations of the phase behavior of mixtures of the injected and in-place fluids. For example, Welge et al. (1961) calculated composition paths for enriched gas drives and included the effects of volume change as components transferred between phases. Helfferich (1981) generalized the analysis of Welge et al. to systems containing an arbitrary number of components, but restricted consideration to those in which effects of volume change on mixing are negligible. Examples presented by Helfferich dealt with ternary systems only, however. Applications of similar theory to ternary systems of interest in surfactant floods have been presented by Larson (1979) and Hirasaki(1981). Dumore et al. (1984) extended the analysis of Welge et al. and Helfferich to describe condensing and vaporizing gas drives for ternary systems in which volume change on mixing is important.

All of those mathematical descriptions are for the limiting case of one-dimensional flow in which the effects of dispersion are negligible. In such cases, it can be shown (Welge et al.

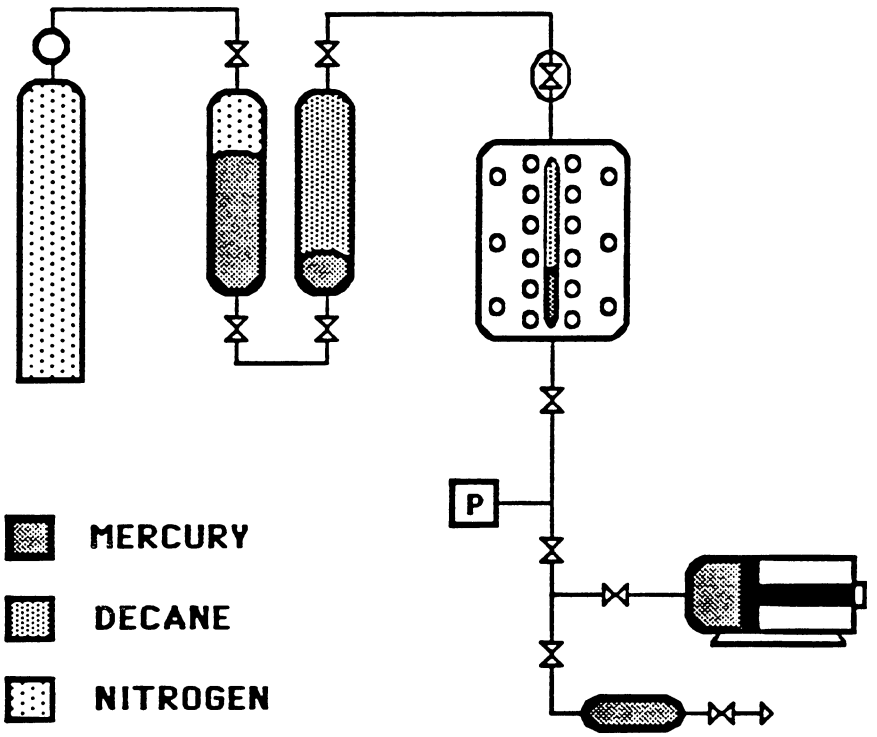

Fig. 2.1.2. Set up used for volumetric calibration of the PVT cell.

1961, Helfferich 1981, Larsen 1979, Hirasaki 1981, Dumore et al. 1984) that compositions of fluids that form during a displacement of oil by CO_2 do not pass through the two-phase region unless the oil composition lies within the region of tie-line extensions on a ternary diagram. Thus, the critical tie line, the tie line that is tangent to the binodal curve at the plait point, marks the boundary between oil compositions that develop miscibility and those that do not. According to the one-dimensional theory, the minimum miscibility pressure (MMP) is the pressure at which the oil composition lies on the critical tie line, so that additional pressure increases shrink the two-phase region enough to move the oil composition outside of the region of tie-line extensions. That theory applies equally well to systems containing an arbitrary number of components. In such systems, it is a surface in n_c dimensions that divides original oil compositions that develop miscibility from those that do not (Defrenne et al. 1961).

Experimental determination of the MMP is rarely based on analysis of phase diagrams, however. Instead it is usually obtained from measurements of the fraction of oil recovered in a slim tube displacement at a given pressure (Orr et al. 1982). Several criteria have been proposed by which the MMP can be determined from displacement data. Most require that the recovery be nearly 100 percent (typically greater than 90 percent) and that recovery increase only slightly in displacements at pressures greater than the MMP (Orr et al. 1982, Yellig and Metcalfe 1980, Holm and Josendal 1982). Numerous correlations have also been offered that account for the effects of variations in temperature and oil composition on MMP. Several of the correlations currently available (Yellig and Metcalfe 1980, Holm and Josendal 1982, Orr and Silva 1985) do not account for the effect of the amount of light hydrocarbons, such as methane (C_1), present in the oil. Yellig and Metcalfe (1980) found, for example, that addition of C_1 to an oil did not change MMP's appreciably. Neglect of the presence of light hydrocarbons is based on the assumption that such components volatilize and are transported ahead of the displacement front and hence, do not affect the development of miscibility (Holm and Josendal 1982). Thus, the correlations include the provision that when there is enough of the light components present to raise the bubble point pressure (BPP) of the oil above the MMP predicted for the dead oil, then the BPP is taken to be the MMP.

That provision is inconsistent with the analytical description of the development of miscibility. The composition of an oil at its BPP must be at the end of a tie line. Hence, such a composition must lie within the region of tie line extensions if the oil composition is plotted on a pseudoternary diagram. Thus, the definition of the MMP based on analysis of one-dimensional flow of a ternary systems is in conflict with a portion of the experimental evidence on the behavior of the MMP as the amount of gas dissolved in the oil increases.

To resolve the inconsistency we investigate the flow of a model four component CO_2-hydrocarbon system, CO_2, C_1, butane $(C)_4$, and decane (C_{10}), for which the Peng-Robinson equation of state (PREOS, Peng and Robinson 1976) reproduces observed behavior with reasonable accuracy (Larsen 1984, Monroe et al. 1987). We describe the extension of the calculations of Dumore et al. (1984) to four component systems, and then we use the PREOS representation of the phase behavior to construct composition paths for the CO_2-C_1-C_4-C_{10} system. The solutions obtained show that it is indeed possible to have high displacement efficiency even when the original oil composition does not lie outside the region of tie-line extensions.

2.2.1 Mathematical Model

Given the PREOS representation of the phase behavior, composition paths can be calculated. The formulation of the flow equations follows that of Dumore et al. (1984). Purely convective flow of a multicomponent, multiphase system through a one-dimensional, homogeneous porous medium is governed by the following mass balance equation

$$\frac{\partial}{\partial t} \sum_{j=1}^{n_p} x_{ij} \rho_j S_j + \frac{\partial}{\partial x} \frac{v}{\phi} \sum_{j=1}^{n_p} x_{ij} \rho_j f_j = 0 \qquad i = 1, n_c \tag{2.2.1}$$

where v is the total velocity, and f_j is the fractional flow of phase j, given by

$$f_j = \frac{k_j / \mu_j}{\sum_{j=1}^{n_p} k_j / \mu_j} \tag{2.2.2}$$

In the derivation of Eqs. (2.2.1) and (2.2.2), effects of dispersion and capillary pressure have been neglected. Substitution of the definitions

$$G_i = \sum_{j=1}^{n_p} x_{ij} \rho_j S_j \qquad F_i = \frac{v}{\phi} \sum_{j=1}^{n_p} x_{ij} \rho_j f_j \,. \tag{2.2.3}$$

into Eq. (2.2.1) gives

$$\frac{\partial G_i}{\partial t} + \frac{\partial F_i}{\partial x} = 0 \qquad i = 1, n_c. \tag{2.2.4}$$

Here G_i and F_i represent the overall component concentration and the overall flux of component i. Because phases present at any point are assumed to be in chemical equilibrium, the phase compositions and properties can be obtained by performing a flash calculation given the overall composition, C_i. Thus, G_i and F_i are functions of the overall compositions and F_i also depends on the total velocity, v. If the dependent variables C_i and v are represented as functions of a dummy variable $\eta = \eta(x,t)$, Eq. (2.2.4) can be written

$$\frac{dG_i}{d\eta} \frac{\partial \eta}{\partial t} + \frac{dF_i}{d\eta} \frac{\partial \eta}{\partial x} = 0 \qquad i = 1, n_c, \tag{2.2.5}$$

where

$$\frac{dG_i}{d\eta} = \sum_{k=1}^{n_c - 1} \frac{\partial G_i}{\partial C_k} \frac{dC_k}{d\eta} \qquad i = 1, n_c \tag{2.2.6}$$

and

$$\frac{dF_i}{d\eta} = \frac{\partial F_i}{\partial v} \frac{dv}{d\eta} + \sum_{k=1}^{n_c - 1} \frac{\partial F_i}{\partial C_k} \frac{dC_k}{d\eta} \qquad i = 1, n_c \tag{2.2.7}$$

Because η is a function of x and t

$$d\eta = \frac{\partial \eta}{\partial x} dx + \frac{\partial \eta}{\partial t} dt \tag{2.2.8}$$

We now seek solutions along characteristic curves, for which $d\eta = 0$. Rearrangement of Eq. (2.2.8) with substitution of any one of Eqs. (2.2.5) gives

$$\frac{dx}{dt} = -\frac{\dfrac{\partial \eta}{\partial t}}{\dfrac{\partial \eta}{\partial x}} = \frac{\dfrac{dF_i}{d\eta}}{\dfrac{dG_i}{d\eta}} \qquad i = 1, n_c \tag{2.2.9}$$

There is one equation of the form of Eq. (2.2.9) for each of the n_c components. The solution sought is one for which the velocities, $\frac{dx}{dt} = \lambda$, are the same for all components. If so, Eq. (2.2.9) can be rewritten in matrix form using Eqs. (2.2.6) and (2.2.7) as

$$\left[\overline{\overline{F}} - \lambda \, \overline{\overline{G}}\right] \overline{C} = 0 \tag{2.2.10}$$

where the entries in the ith row of $\overline{\overline{F}}$ are $\frac{\partial F_i}{\partial C_k}$ for k=1, n_c–1 and $\frac{\partial F_i}{\partial v}$, the entries in $\overline{\overline{G}}$, $\frac{\partial G_i}{\partial C_k}$ for

k=1, n_c–1 and 0 (because G_i is independent of v), and the vector $\overline{C}$ contains $\frac{dC_i}{d\eta}$ for i=1,n_c–1 and $\frac{dv}{d\eta}$.

Eq. (2.2.10) is an eigenvalue problem for which solutions exist for eigenvalues given by

$$\det\left[\overline{\overline{F}} - \lambda\overline{\overline{G}}\right] = 0 \tag{2.2.11}$$

For a system containing n_c components, there are n_c–1 eigenvalues that represent velocity of an overall composition along a composition (path) direction given by the associated eigenvector, $\overline{C}$. The eigenvectors represent composition variations that satisfy the restriction that individual concentrations, C_i, all move at the same velocity, referred to by Helfferich as coherence (Helfferich 1981). Integration along the eigenvector directions yields a set of composition "paths" that satisfy the coherence condition. Thus, there are three paths through any composition point in a four-component system. The last eigenvalue is infinite. It reflects the fact that changes in overall velocity propagate instantaneously.

Solutions to problems of the form of Eq. (2.2.4) may or may not vary continuously. If the solution varies continuously, Eq. (2.2.4) is the appropriate form of the material balance equation. At jump discontinuities, however, an overall mass balance across the shock and yields an expression for its velocity (Welge et al. 1961, Helfferich 1981, Larsen 1979, Hirasaki 1981, Dumore et al. 1984).

$$\Lambda_i = \frac{F_i^{II} - F_i^{I}}{G_i^{II} - G_i^{I}} \tag{2.2.12}$$

where the superscripts I and II refer to opposite sides of the shock. It can be shown that a two-phase region can be entered only via a shock from a composition in the single phase region to a composition in the two-phase region. Such a shock occurs along the extension of a tie line (Welge et al. 1961, Helfferich 1981, Larsen 1979, Hirasaki 1981, Dumore et al. 1984). Two types of jump discontinuities are observed in solutions for specific initial and injection compositions. The first occurs when the shock in or out of the two-phase region is the limit of a continuous variation along a tie line, which can occur because tie lines are themselves paths (Helfferich 1981, Hirasaki 1981, Dumore et al. 1984). In such cases, the shock velocity is given by (Dumore et al. 1984)

$$\Lambda_i = \frac{F_i^{II} - F_i^{I}}{G_i^{II} - G_i^{I}} = \frac{v}{\phi}\frac{df}{dS} \tag{2.2.13}$$

because the shock velocity is equal to the velocity of the composition on the two-phase side of the shock, the eigenvalue associated with the eigenvector that points along the tie line. As several investigators have shown, that velocity is $\lambda = \frac{v}{\phi}\frac{df}{dS}$ (Welge et al. 1961, Helfferich 1981, Hirasaki 1981, Dumore et al. 1984). We refer to such shocks as "tangent" shocks because their velocities can be found from a graphical construction analogous to the familiar Welge tangent construction for Buckley-Leverett solutions. The second type of shock is found when the jump discontinuity occurs between two known compositions. In that case, the velocity is given directly by Eq. (2.2.12). Such shocks will be called "nontangent" shocks in the discussion that follows.

2.2.2 Quaternary Grid Topology

Construction of a solution for a particular set of initial and injection conditions is completed by integrating along "paths," the directions given by the eigenvectors through a

particular composition point (Helfferich 1981). For example, paths through an arbitrarily chosen point can be found by solving Eq. (2.2.10) for the three composition eigenvectors. Then a small step is taken along one of the eigenvector directions and the procedure repeated. Similar integration for each of the three eigenvectors through each composition point in the quaternary diagram yields a mesh of composition paths that fills the diagram. Because paths represent composition variations that satisfy the coherence condition, the solution for specific initial and injection conditions follows a set of paths that connect the initial composition to the injection composition. Of the many potential paths available, only one will also satisfy the constraint that the composition velocity must increase monotonically from the inlet to the outlet, a statement that fast-moving compositions must lie downstream of slow-moving ones.

Fig. 2.2.1 shows selected composition paths for the CO_2-C_1-C_4-C_{10} system. Those paths were calculated using the following expressions for oil and gas phase relative permeabilities

$$k_{ro} = k_{rom}\left[\frac{1 - S_g - S_{or}}{1 - S_{or}}\right]^{n_o} \tag{2.2.14}$$

$$k_{rg} = k_{rgm}\, S_g^{\,n_g} \tag{2.2.15}$$

with $k_{rgm} = k_{rom} = 0.8$, $n_g = n_o = 3$ and $S_{or} = 0.05$. Phase viscosities were calculated using the Lohrenz-Bray-Clark (1964) correlation, and phase compositions and densities were obtained from a flash calculation using the PREOS. The three distinct paths through each point in the quaternary phase diagram are illustrated for a tie line in the CO_2-C_4-C_{10} face. Fig. 2.2.2 is a plot of the variation in eigenvalues with changes in gas saturation along a typical tie line. As in the ternary cases described by Dumore et al. (1984) and Monroe (1986), tie lines are paths, and the eigenvalue associated with the tie line is proportional to $\frac{df}{dS}$. As Fig. 2.2.2 indicates, composition variations along the tie-line path are slower (have smaller eigenvalues) than other paths at the ends of the tie line, are fastest in the middle of the tie line, and have intermediate velocities in between. Thus, a particular path may be a fast, slow or intermediate path at different positions along it.

As Fig. 2.2.1 shows, in addition to the tie-line path, there are also two nontie-line paths associated with a given composition. As Fig. 2.2.9 illustrates, we use the designation "horizontal" to refer to the nontie-line paths in the C_1-C_4-C_{10} and the CO_2-C_4-C_{10} faces, and "vertical" to refer to those paths that extend from the C_1-C_4-C_{10} face to the CO_2-C_4-C_{10} face. Fig. 2.2.2 and 10 show that there are four points along each tie line where the nontie-line paths are tangent to the tie-line path. The tangent points are singular points of intersection of tie-line and nontie-line paths where two of the eigenvalues are equal. Two of the singular points are at the intersection of the tie line and the horizontal nontie-line paths, and the other two singular points are at the intersection of the tie line and the vertical nontie-line path. Two of the singular points, one horizontal and one vertical path intersection point, are on either side of the equivelocity surface, the locus of points at which the liquid and vapor phase velocities are equal. The equivelocity and saturated phase surfaces are also paths that can be traversed either vertically or horizontally. In the example that follows, we use the description of path geometry shown in Fig. 2.2.1 and plots like Fig. 2.2.2 of velocity (eigenvalue) variations along tie lines to select solution composition paths for given constant initial and injection compositions.

2.2.3 Sample Solution Path

Data for the first example solution are given in Table 2.2.1. At time zero, pure CO_2 is injected into a porous medium containing a single-phase oil of constant composition. The injection velocity is 1.0 m/d. The solution path is plotted on a quaternary diagram in Fig. 2.2.3, and the composition, saturation and velocity data are given in Table 2.2.2.

Table 2.2.1
Initial and Injection Composition for Displacements of Live and Dead Oils at 160° F (71° C) and 1600 psia (11.0 MPa).

	Composition (mole fraction)				Molar
	CO_2	Methane	Butane	Decane	Density (g-mol/cc)
Injection Gas (mole fraction)	1.00	0.00	0.00	0.00	6.62×10^{-3}
Live Oil (mole fraction)	0.00	0.20	0.34	0.46	6.86×10^{-3}
Dead Oil (mole fraction)	0.00	0.00	0.42	0.58	5.99×10^{-3}

Table 2.2.2
Composition Path, Saturation and Velocity Results for a Quaternary Displacement at 160° F (71° C) and 1600 psia (11.0 MPa).

Comment	Composition (mole fraction)				Total Velocity	Gas Saturation	Wave Velocity
	CO_2	C_1	C_4	C_{10}	u (m/d)	S	λ(m/d)
Injection Composition	1.0	0.0	0.0	0.0	1.0	1.0	
Slow Shock	0.9566	0.0000	0.0000	0.0434	0.9480	0.910	0.2693
Zone of Constant State	0.9566	0.0000	0.0000	0.0434	0.9480	0.910	0.8765
Self Sharpening Wave	0.8483	0.0000	0.0978	0.0540	0.9481	0.642	0.8675
Continuous Variation	0.8450	0.0000	0.0990	0.0560	0.9482	0.618	0.9723
	0.8413	0.0006	0.1002	0.0578	0.9485	0.596	0.9725
	0.7025	0.0679	0.1269	0.1028	0.9586	0.446	0.9740
	0.5019	0.1819	0.1597	0.1565	0.9751	0.380	0.9787
	0.3001	0.3059	0.1892	0.2048	0.9897	0.340	0.9850
	0.1025	0.4319	0.2162	0.2494	1.0021	0.309	0.9916
	0.0000	0.4981	0.2299	0.2721	1.0077	0.294	0.9949
Zone of Constant State	0.0000	0.4981	0.2299	0.2721	1.0077	0.294	1.1009
Fast Shock	0.0000	0.4981	0.2299	0.2721	1.0077	0.000	1.1009
Initial Oil Composition	0.0000	0.2000	0.3394	0.4606	0.9489	0.0000	

Table 2.2.3
Variations of Saturations and Shock Velocities for Oil Containing Increasing Amounts of C_4 at 160° F (71° C) and 1600 psia (11.0 MPa).

	Oil Composition (mole fraction)			Slow Shock		Methane Bank		
				Velocity	Saturation	Trailing Vel.	Leading Vel.	Saturation
	C_1	C_4	C_{10}	ν (m/d)	S	ν_t (m/d)	ν_l (m/d)	S
System 1	0.10	0.21	0.69	0.147	0.797	1.024	1.147	0.301
System 2	0.10	0.38	0.52	0.277	0.919	1.007	1.061	0.298
System 3	0.10	0.45	0.45	0.503	0.965	1.004	1.047	0.290
System 4	0.10	0.50	0.40	0.828	0.983	1.003	1.047	0.289

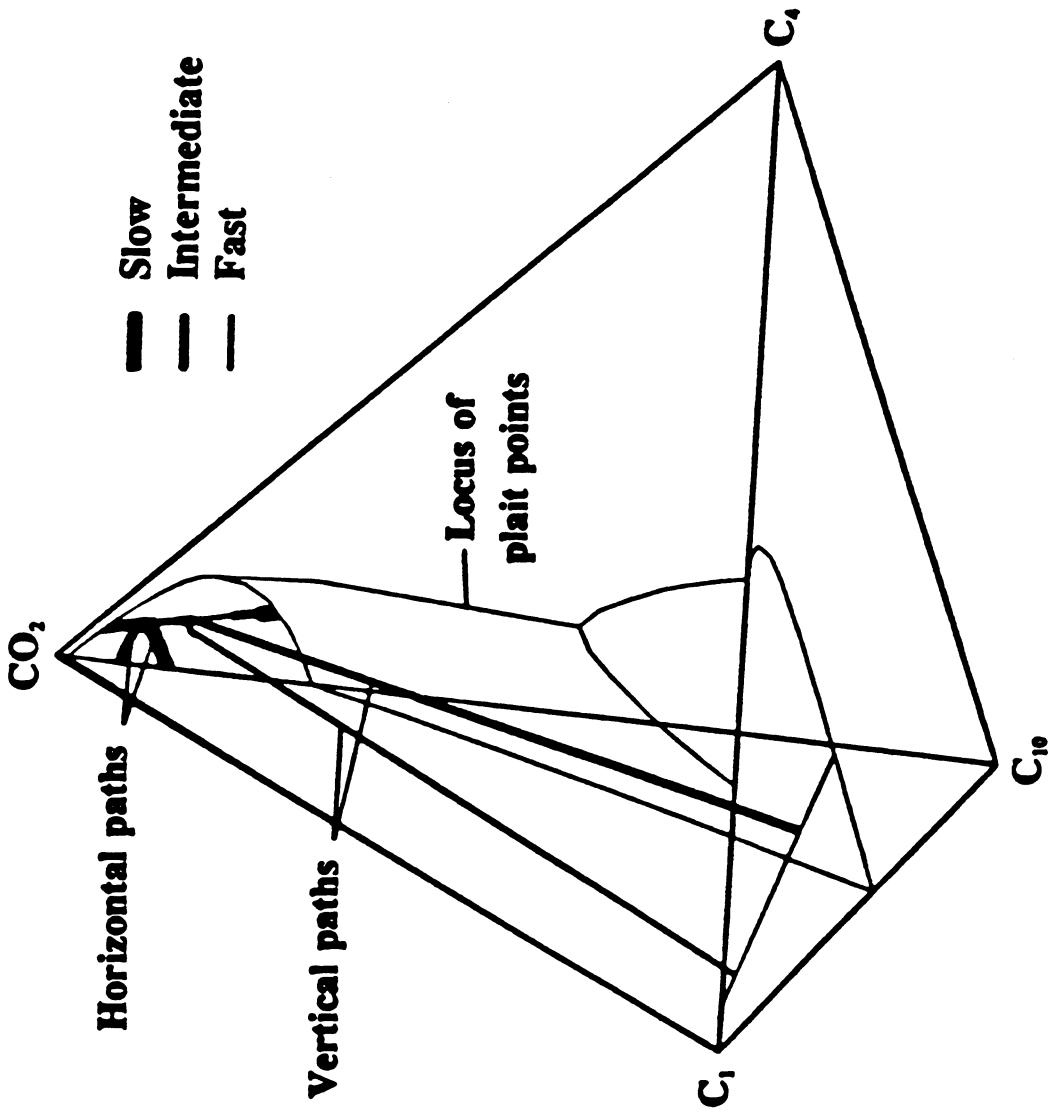

Fig. 2.2.1. Typical composition paths for a CO_2-C_1-C_4-C_{10} system.

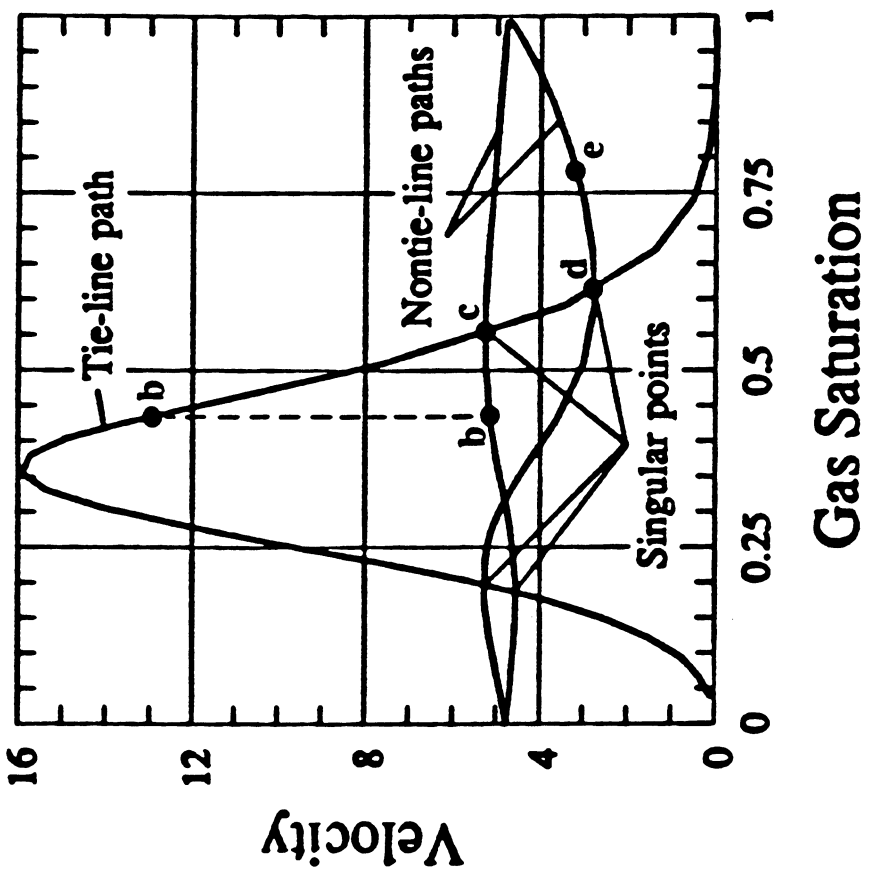

Fig. 2.2.2. Variation of composition velocities (eigenvalues) along a tie line.

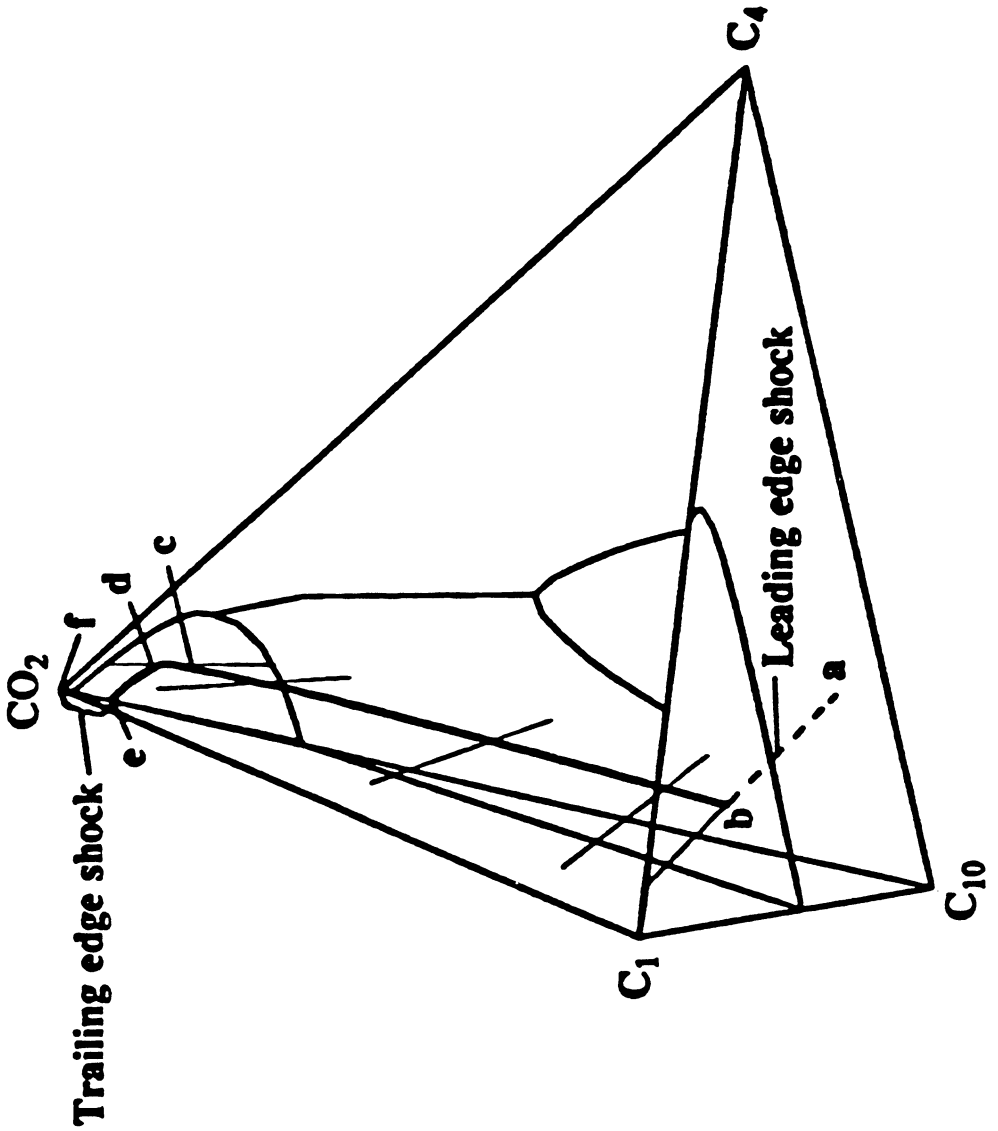

Fig. 2.2.3. Composition path for displacement of a CO_2-C_1-C_4 mixture by CO_2 at 160° F (71° C) and 1600 psia (11.0 MPa).

In the following discussion, the calculated composition path is traced from the initial oil composition to the injection gas composition. The composition variation that is the solution must lie exclusively on paths, and velocities must decrease from the initial oil composition to the injection gas composition. While the solution path may switch from one path to another, the only allowable switch is from a faster path to a slower one (Helfferich 1981, Dumore et al. 1984). Finally, if there is a leading or fast shock, the composition jump must cross the equivelocity surface, because composition jumps that do not cross that surface have velocities, given by Eq. (2.2.12), that are less than the average interstitial velocity and hence cannot be leading shocks.

The path enters the two phase region via a shock to a fast path along a tie line from the initial oil composition, point **a**, to point **b**. Across the shock there is a step in C_1 concentration with no CO_2 present. At point **b** the path switches immediately from a fast path to an intermediate path. The step change from the initial composition to the two-phase region is not a limit of a continuous variation. Therefore, it is a nontangent shock, and the velocity of the shock can be calculated from the material balance Eq. (2.2.12). Because there are two velocities associated with the same overall composition at point **b**, a fluid bank is formed. The leading edge moves with the fast, tie-line path velocity, and the trailing edge moves with the slower intermediate velocity of the vertical path. Fig. 2.2.2 illustrates the velocity change at point **b**. (For brevity, all the velocity changes are illustrated qualitatively on a diagram for one tie line; in reality the eigenvalues change slightly from tie line to tie line (Monroe 1986), though all have the qualitative form shown in Fig. 2.2.2). The constant phase saturations and compositions within the bank are illustrated in the profiles shown in Figs. 2.2.4 and 2.2.5. Along the vertical, intermediate velocity path between points **b** and **c**, the concentration of CO_2 is increasing, while the concentration of the other three components is decreasing. Point **c** is the singular point where the vertical path is tangent to a tie line in the CO_2-C_4-C_{18} face and where two of the eigenvalues are equal (see Fig. 2.2.2). From point **c** to **d** there is a continuous variation along a tie line. Thus saturations vary, while the phase compositions and the total velocity remain constant. At point **d** the solution switches at a second singular point from the tie-line path to path that is tangent to the tie line at that point. Between points **d** and **e** the wave velocities increase, and hence, a self-sharpening wave is formed. Point **e** is on the tie line that extends through the injection gas composition. Finally, there is a jump from **e** to **f**, the injection gas composition. The velocity of that nontangent shock is also calculated using Eq. (2.2.12). The velocity calculated is greater than the composition velocity of point **e** on the injection tie line. Therefore, the jump is not the limit of a continuous variation, and a trailing bank is formed.

The path just described satisfies all of the rules for path construction. A demonstration that the path selected is the only one that satisfies the velocity constraint is given by Monroe (1986). While the qualitative features of the solution can be seen from Figs. 2.2.2-2.2.5, the solution cannot be obtained explicitly. Because of the formation of the two fluid banks at the leading and trailing edge of the transition zone, the shocks to and from the two-phase region are non-tangent shocks. The key to finding the solution path for the quaternary system is the determination of the "crossover" tie line, the tie line that contains points **c** and **d** in Fig. 2.2.3. This tie line is uniquely identified because it is the only one that is tangent to both the vertical and horizontal nontie-line paths that also intersect the initial and injection tie lines. The tie line shown in the CO_2-C_4-C_{10} face of Fig. 2.2.1 is one such tie line. Each tie line in the CO_2-C_4-C_{10} face, for example, is a crossover tie line for an associated tie line in the C_1-C_4-C_{10} face. In fact, any tie line within the quaternary diagram is a crossover tie line for a set of initial and injection tie lines that intersect the horizontal and vertical paths that are tangent to the crossover tie line.

To construct a solution for given initial and injection compositions for a path that contains two fluid banks, a trial and error solution was required. To identify the crossover tie line, an initial guess was made of the landing composition (point **e** in Figs. 2.2.2-2.2.5) within the two phase region on the injection tie line. Then the intermediate path was followed to the crossover tie line and down the vertical path to the C_1-C_4-C_{10} face. If the resulting tie line in

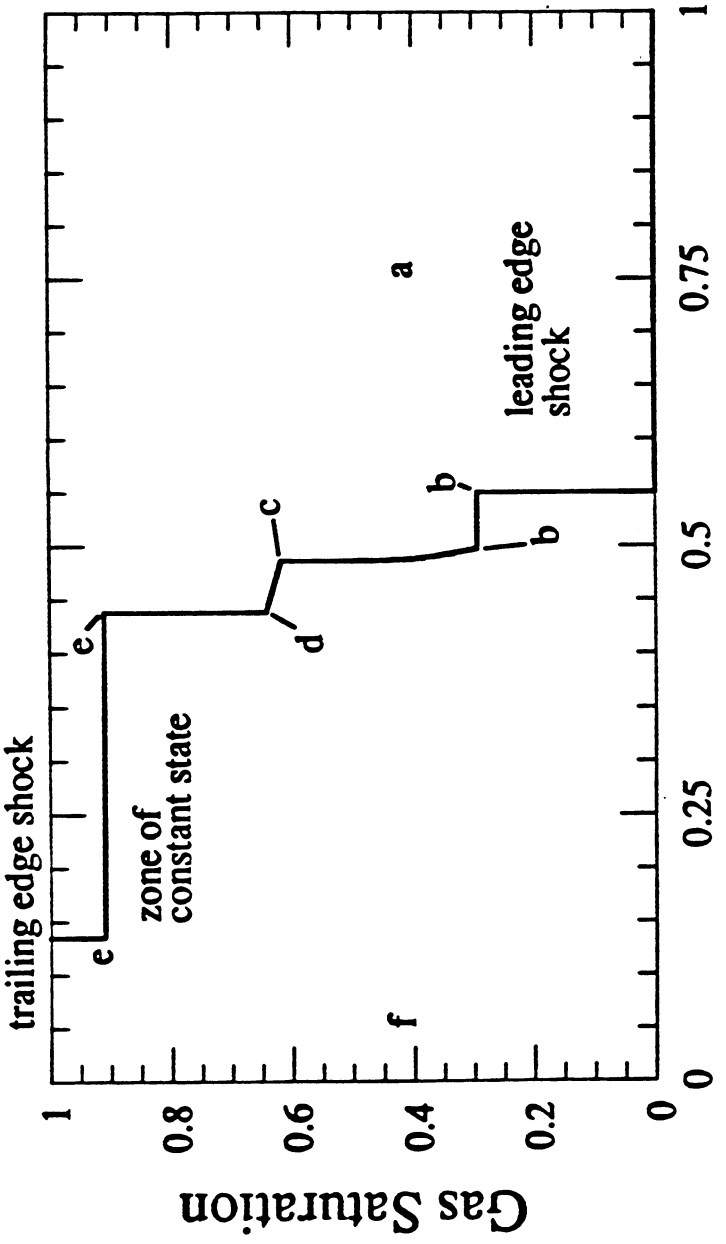

Fig. 2.2.4. Saturation profile for displacement of a CO_2-C_1-C_4 mixture by CO_2 at 160° F (71° C) and 1600 psia (11.0 MPa).

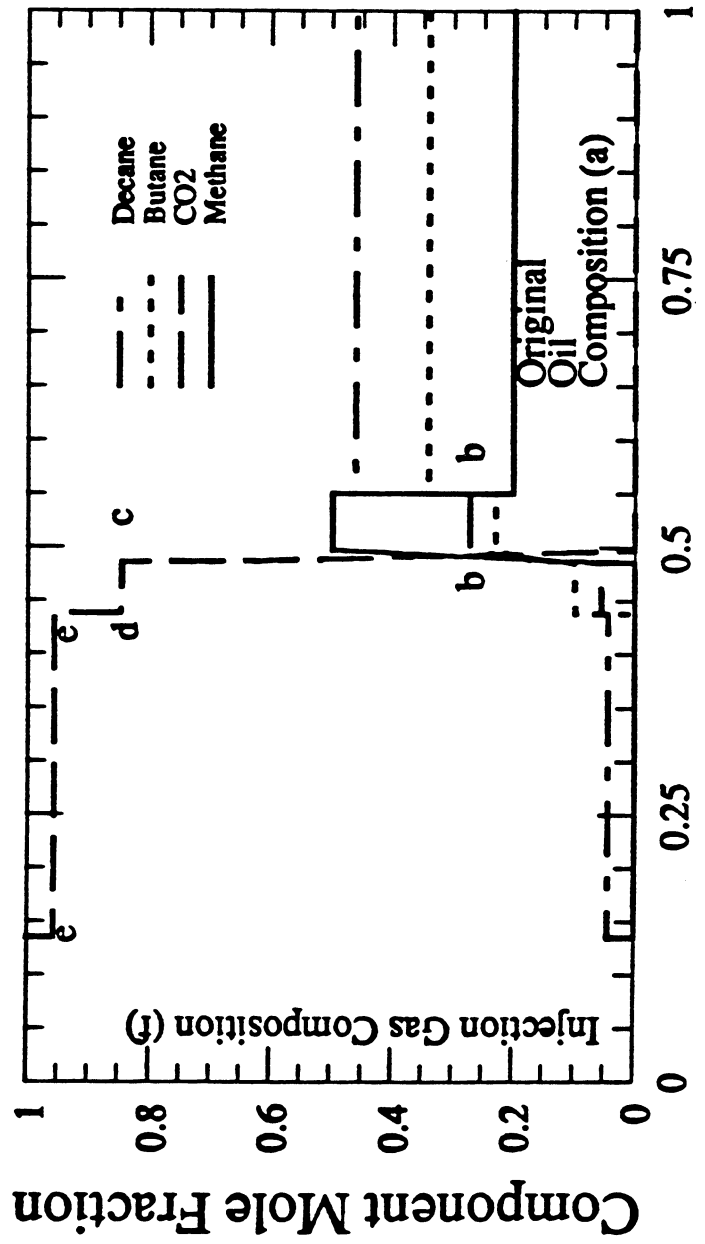

Fig. 2.2.5. Composition profile for displacement of a CO_2-C_1-C_4 mixture by CO_2 at 160° F (71° C) and 1600 psia (11.0 MPa).

the C_1-C_4-C_{10} face passed through the original oil composition, the correct crossover tie line was identified. If not, the injection landing point composition was adjusted until the path passed through the appropriate tie line through the initial composition.

2.2.4 Analysis

To determine the effect of dissolved C_1 on composition path, displacements were examined for live and dead oils with compositions shown in Table 2.2.1. Pure CO_2 was injected in both displacements, and the dead oil differed from the live oil only in that the C_1 was removed. Fig. 2.2.9 shows composition paths for the two displacements. The live oil path shows a shock in the C_1-C_4-C_{10} base, followed by a vertical path to the CO_2-C_4-C_{10} face. In the dead oil displacement, the leading shock lies in the CO_2-C_4-C_{10} face. While the two displacements traverse slightly different tie lines in the CO_2-C_4-C_{10} face, those tie lines lie so close together that they are difficult to distinguish in Fig. 2.2.6. Thus the portions of the composition paths for the two displacements that lie in the CO_2-C_4-C_{10} face differ only slightly, as Fig. 2.2.6. Therefore, if the displacement of the dead oil traverses a tie line that is close to the plait point in the CO_2-C_4-C_{10} face, the crossover tie line for a corresponding live oil will also be close to the plait point.

The primary difference between the saturation profiles shown in Fig. 2.2.7 are the position of the leading edge shock and the volume of the gas saturated zone behind the displacement front. Fig. 2.2.4 shows that C_1 is the primary constituent of the leading bank in the live oil displacement, and Fig. 2.2.7 shows that the bulk of the volume difference is also in that region. Behind the leading bank the C_1 composition quickly drops to zero. Thus, all of the C_1 moves in a bank ahead of the CO_2 front. The increased volume of the leading bank in the live oil displacement is the result of smaller volume change on mixing that results when CO_2 dissolves in the live oil, and C_1 vaporizes, replacing some of the lost CO_2 volume in the vapor phase. In the dead oil displacement, CO_2 also dissolves in the oil phase, losing volume as it does so, but smaller amounts of the oil components volatilize and replace the shrinkage of the vapor volume. Thus the leading edge advances more slowly in the dead oil displacement.

Behind the C_1 bank the saturation profiles are nearly identical. Where the composition path varies along the tie line between points **c** and **d** in Fig. 2.2.7, the C_4 travels in a bank. The C_4 partitions more strongly into the vapor phase than does C_{10}, and hence it travels at the front of the transition zone, as expected. C_{10} is the last component to be extracted completely at the trailing solubilization shock.

Fig. 2.2.8 reports C_1, C_4 and C_{10} recovery for the live and dead oil displacements. Before breakthrough of the leading shock, fractional recovery of each component is the same. After that point, the recovery curves show changes in slope that correspond to the arrival at the outlet of the trailing edge of the C_1 bank in the live oil case, the self-sharpening wave, and the trailing edge shock. Nearly all of the C_1 is recovered at CO_2 breakthrough, and all of the C_4 is recovered after the self-sharpening wave breaks through. Comparison of the results of the two displacements confirms that breakthrough of the leading edge shock occurs earlier in the four-component case, but that recovery is nearly the same at later times. That behavior results because there is very little difference in the saturation and composition profiles behind the self-sharpening wave.

Reasons for the observed behavior are made clearer by considering how composition paths change as miscibility develops. Table 2.2.3 shows calculated displacement data and results for four one-dimensional displacements of oils with increasing C_4 concentration. Addition of C_4 moves the overall composition of the oil toward the CO_2-C_1-C_4 face, and thus simulates the development of miscibility by moving the oil composition toward the boundary of the region of tie line extension. Composition paths for the four oils are shown in Fig. 2.2.9. As the oil is enriched with C_4 from system 1 to 4 the velocity of the leading shock decreases, and the velocity of the trailing shock increases (see Table 2.2.3). In addition, the portion of the

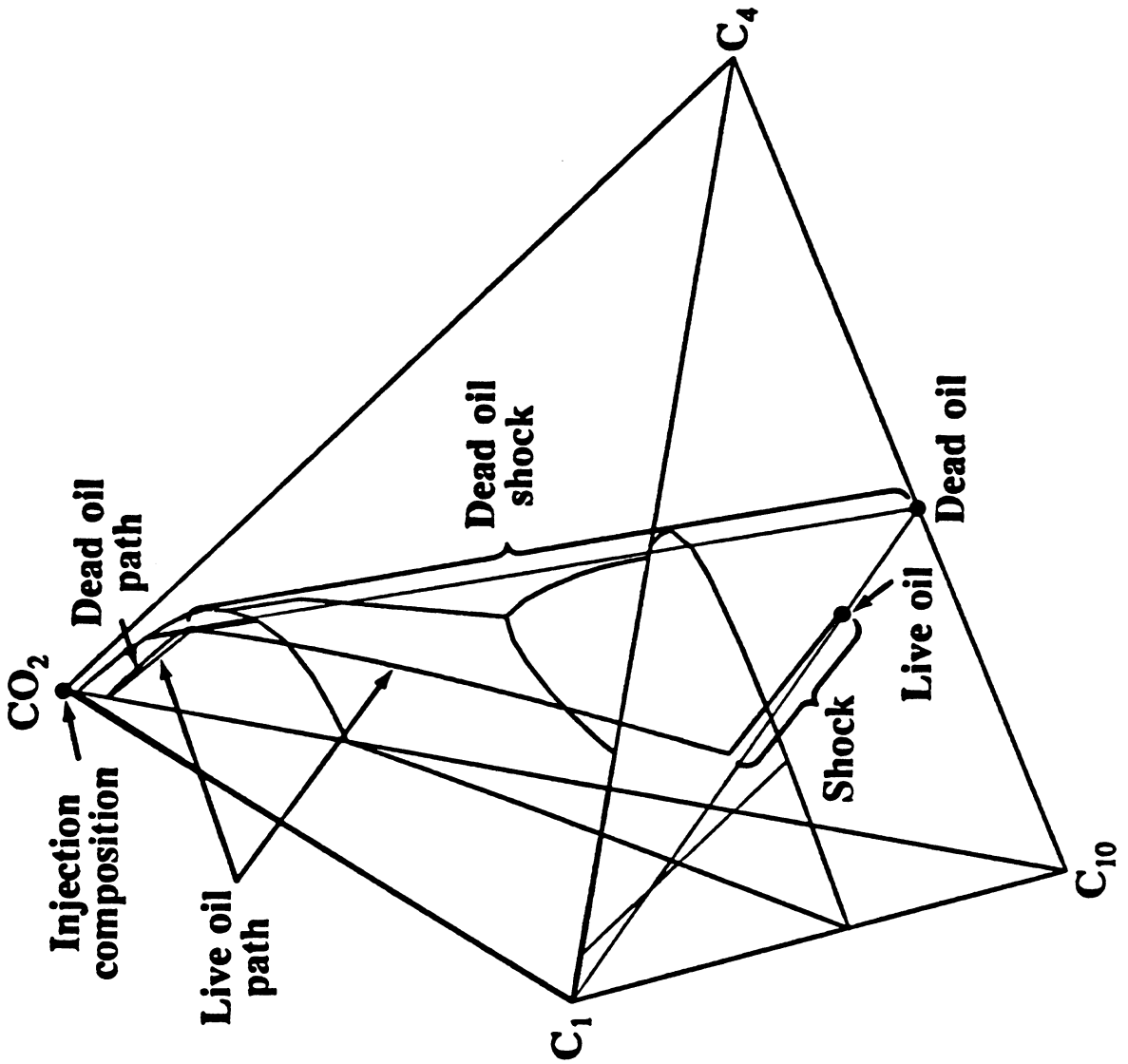

Fig. 2.2.6. Comparison of composition paths for live and dead oil displacements.

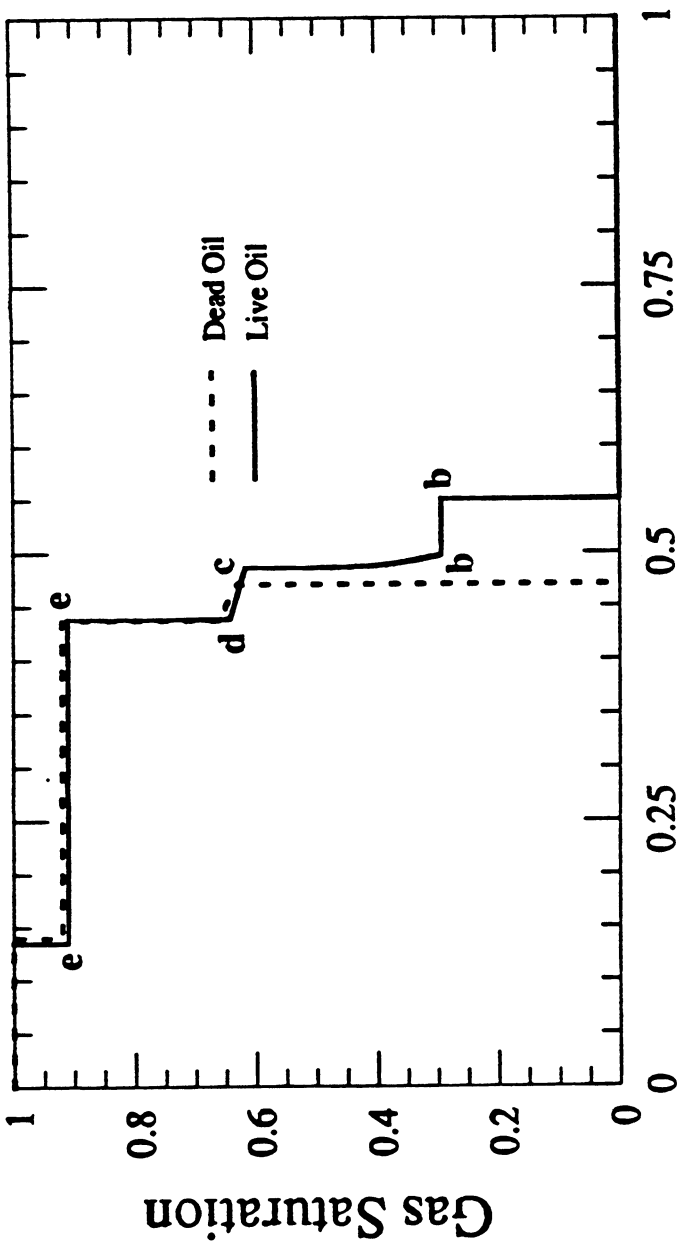

Fig. 2.2.7. Comparison of saturation profiles for live and dead oil displacements.

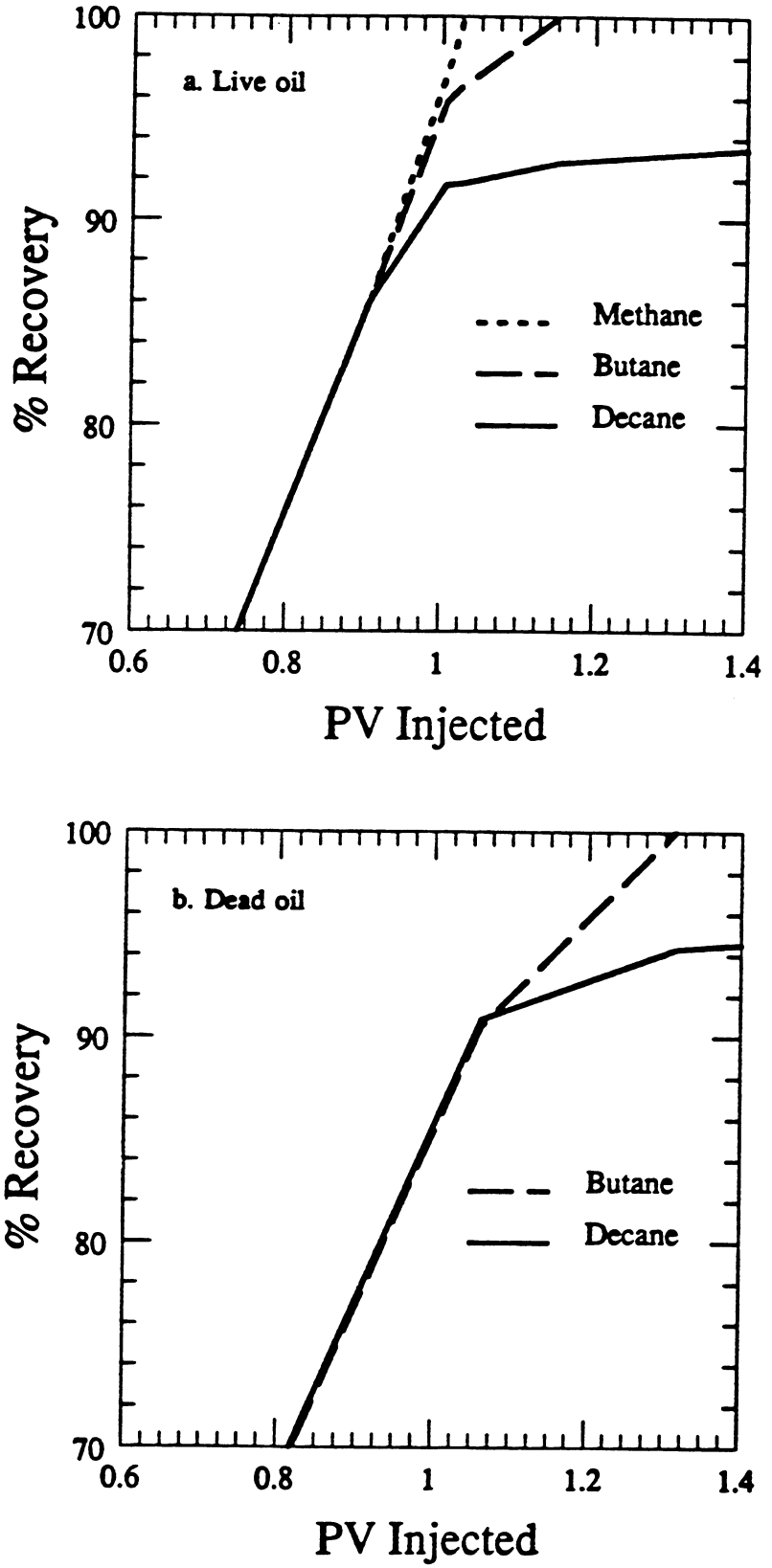

Fig. 2.2.8. Component recovery in live and dead oil displacements at 160° F (71° C) and 1600 psia (11.0 MPa).

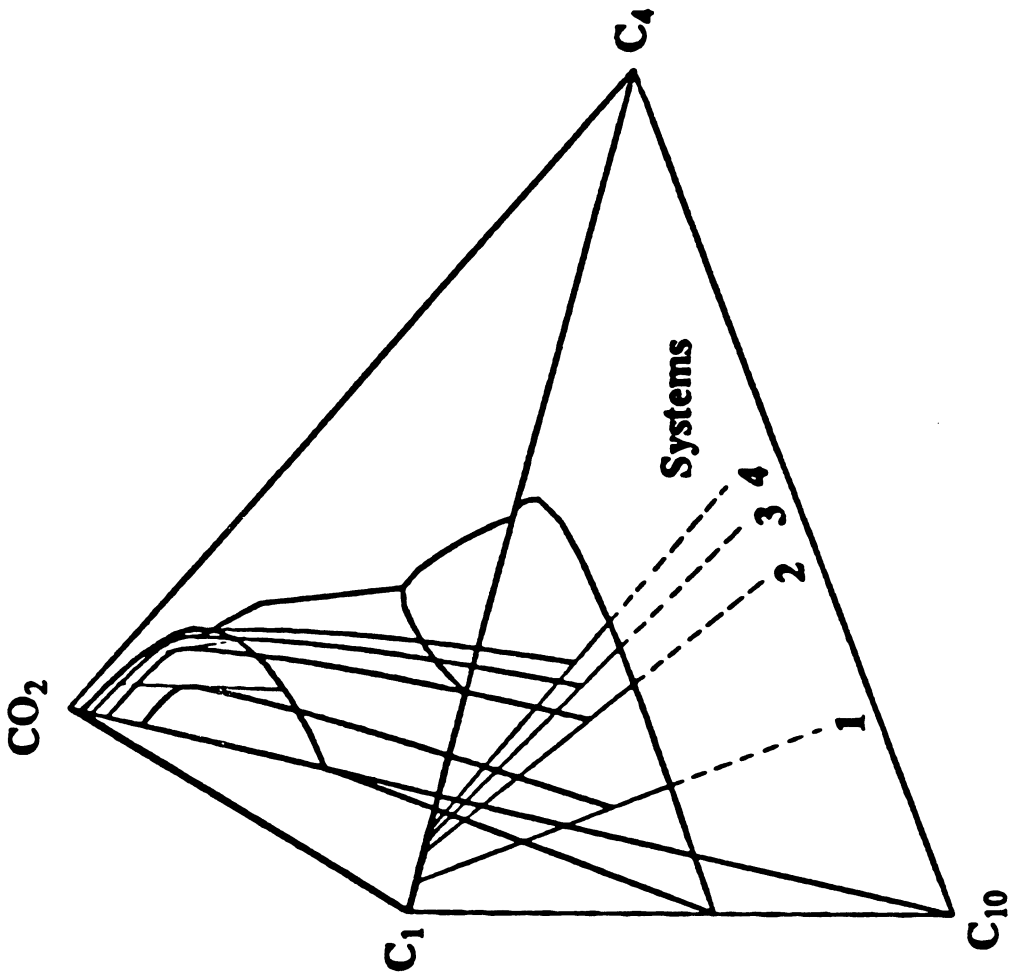

Fig. 2.2.9. Composition paths for displacement of live oils containing varying amounts of C_4 at 160° F (71° C) and 1600 psia (11.0 MPa).

path that lies in the CO_2-C_4-C_{10} face approaches the dew point locus on that face. Thus, in system 4, most of the hydrocarbons have been solubilized into the transition zone, and the system is nearly miscible. Because there is no plait point in the C_1-C_4-C_{10} face at 1600 psia, no oil composition at that pressure can develop miscibility completely. At some higher pressure (above the C_1-C_4 critical pressure), complete development of miscibility is possible for oils rich enough in C_4. When enough C_4 has been added that the original oil lies on the surface of critical tie lines, the composition path begins with a jump from the initial composition to the plait point in the C_1-C_4-C_{10} face, follows the locus of the plait points to the CO_2-C_4-C_{10} face and then follows the dew point locus.

It is interesting to note what happens to the C_1 bank as the system approaches miscibility. Table 2.2.3 shows that the velocity difference between the leading and trailing edges of the C_1 bank decreases with increasing C_4 concentration in the initial oil. Thus, though the size of the C_1 bank does decrease it does not disappear. In fact, because the two-phase region spans the ternary diagram from the C_1-C_{10} to the C_1-C_{10} binary edge, the analytical solution predicts that it is not possible for displacement of an oil containing C_1 to develop miscibility at that pressure. Recovery efficiency improves as the amount of C_4 is increased, however. Recovery at breakthrough ranged from 81.2% for system 1 to 93.0% and 94.7% for systems 3 and 4. The displacement of systems 3 and 4 would clearly be judged to be miscible by the criteria of Holm and Josendal (1982) or Yellig and Metcalfe (1980).

The explanation for the improvement in recovery is based on the observation that the crossover tie lines for the four oils approach the plait point in the CO_2-C_4-C_{10} face as the amount of C_4 is increased from system 1 to 4. For the oils of systems 3 and 4, the crossover tie lines are very near the plait point on the CO_2-C_4-C_{10} face, even though the composition paths fall well into the two-phase region in the C_1-C_4-C_{10} face. The final portion of the composition path passes so close to the plait point and the dew point portion of the binodal curve that recovery is very high, despite the fact that the displacement passes through the two-phase region.

The effect of the amount of C_1 present originally in the oil can be understood by observing the solution path for a series of oils with increasing C_1 concentration that lie along the same tie-line extension in the C_1-C_4-C_{10} face (Monroe 1986). In such cases, only the velocity of the leading edge shock changes, because the values of F_i^I and G_i^I in Eq. (2.2.12) change. All of the C_1 still moves at the leading edge of the transition zone, and the addition of C_1 has no effect on the remaining composition path. In fact, even if the initial oil composition were inside the two phase region, it would be possible for the oil to be displaced efficiently. As long as the trailing portion of the displacement path passes close to the plait point and the binodal curve, high recovery will be observed. Hence, use of the BPP as the MMP for systems that have BPP's that are above the predicted MMP may be overly conservative. Instead, it is apparently possible, for one-dimensional displacements, at least, to have a nearly miscible displacement for an oil that is below its bubble point pressure.

Finally the effect of addition of CO_2 to the original oil can also be seen from the composition path shown in Fig. 2.2.10. The vertical path intersects a sequence of tie lines in the interior of the quaternary diagram. Thus, the crossover tie line in the CO_2-C_4-C_{10} face is associated with a ruled surface made up of tie lines that all intersect the vertical path that is tangent to the crossover tie line. Any initial oil composition that lies on an extension of a tie line in that surface follows exactly the same composition path in the CO_2-C_4-C_{10} face. Hence, the only effect of changing oil composition within that surface of tie line extensions is to change the velocity and composition at the leading shock. As in the case of "oils" with no CO_2 present initially, it is location of the crossover tie line that has the largest effect on recovery efficiency.

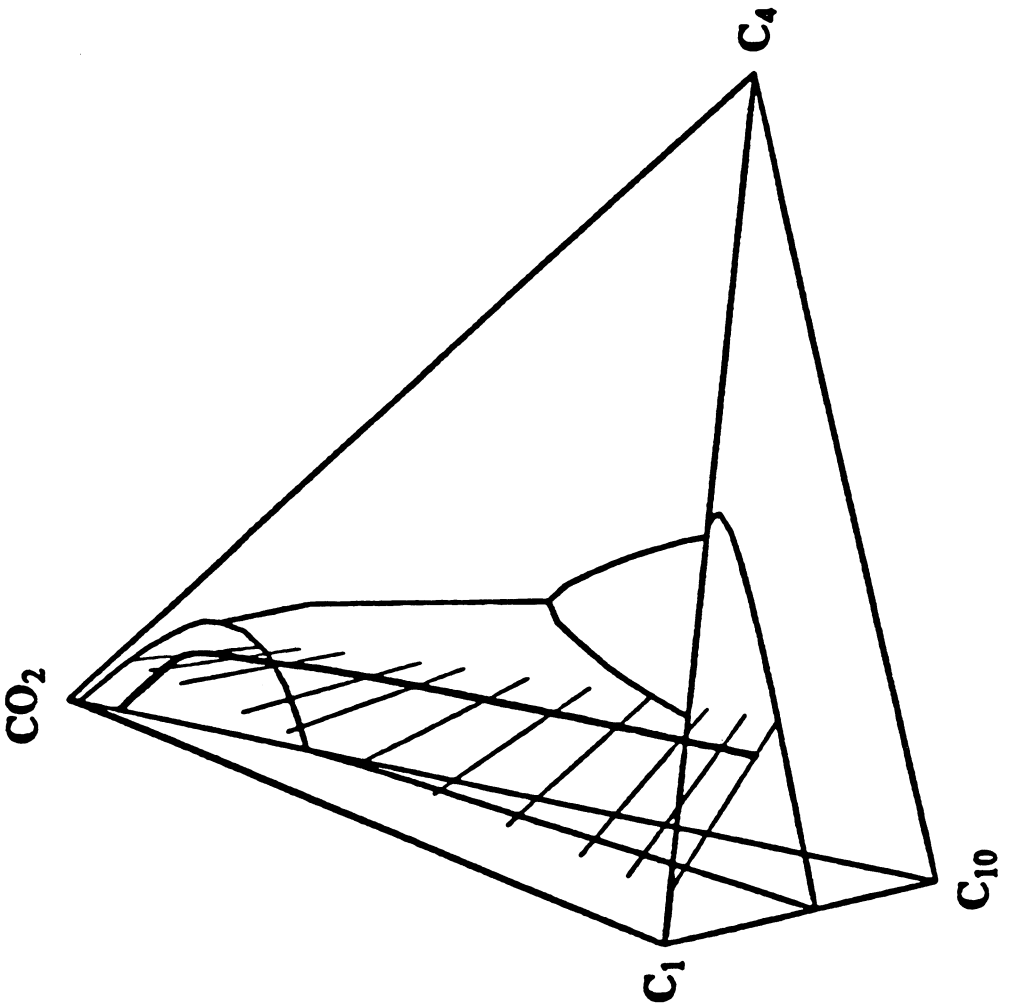

Fig. 2.2.10. Surface of tie lines associated with a vertical path.

2.2.5 Comparison with Experimental Displacements

Metcalfe and Yarborough (1979) reported results of displacement experiments for CO_2-C_4-C_{10} and CO_2-C_1-C_4-C_{10} mixtures. The displacements were performed in an 8 ft. x 2 in. (2.4 m x 5. cm) Berea sandstone core. Compositions of the mixtures displaced are shown in Fig. 2.2.11. Displacements were performed at 1500, 1700 and 1900 psia (10.3, 11.7 and 13.1 MPa). As Fig. 2.2.11 and similar plots at higher pressures given by Larsen (1984) indicate, the live oil displaced was within the region of tie line extensions on the C_1-C_4-C_{10} face at all three pressures. The displacement at 1500 psia recovered 80% of the hydrocarbons and was judged to be immiscible. The displacement of the corresponding dead oil at 1500 psia recovered 81% and was also taken to be immiscible. Thus, the experimental observation is consistent with the calculated composition paths shown in Figs. 2.2.6 and 2.2.7, which show that after passage of the C_1 bank, displacement performance is nearly the same for both the live and dead oils.

The displacements at 1700 and 1900 psia recovered 90 and 97% of the hydrocarbons and were interpreted to be multiple-contact and first-contact miscible, respectively. Displacements of the dead oil at the same pressures recovered 90 and 99% of the hydrocarbons. Analysis of composition paths suggests, however, that at 1500 and 1700 psia, the displacements passed through the two-phase region, but the crossover tie line at 1700 psia was close enough to the plait point that recovery was high anyway. At 1900 psia, a pressure above the critical pressure of the CO_2-C_{10} binary, the displacement developed miscibility because the injection fluid was outside the region of tie line extensions. Methane banks were detected experimentally at 1500 and 1700 psia, but no C_1 bank was observed at 1900 psia. That result is also consistent with the composition path calculations, which indicate that the length of the of the C_1 bank should decrease as the pressure increases. Because the displacement at 1500 psia was immiscible, enough liquid phase was left behind the displacement front that the C_1 bank was relatively large, as is required by a simple material balance on C_1. At 1700 psia, the amount of liquid left behind the CO_2 front was much smaller because the dead oil was multiple-contact miscible. Hence, the C_1 bank was much smaller.

Fig. 2.2.12 compares calculated normalized effluent C_1 concentrations with measure values at 1500 psia. Also shown in Fig. 2.2.12 is an effluent C_1 concentration calculated with a one-dimensional finite difference simulator. While the dispersion coefficient was set to zero in that calculation, numerical dispersion from the two-point upstream weighting scheme used caused the C_1 bank to be dispersed slightly. Both calculated C_1 banks arrived later than the measured peak. It is possible that part of the disagreement is due to the presence of viscous instability or gravity segregation (or both) in the corefloods, which would cause early breakthrough of injected CO_2 and faster movement of leading banks. If so, the experimental displacements were not strictly one-dimensional, and thus some disagreement with the analytical solution is to be expected. In any case, the calculated solutions reproduce the qualitative features of the measured effluent compositions. Successive banks rich in C_1 and C_4 were observed, the C_1 bank arrived later, and the length of the bank decreased as displacement pressure increased. The displacement performed at 1700 psia showed clearly that high recovery is possible in a displacement that exhibits a leading C_1 bank. The calculations reported here indicate that at that pressure, the displacement must have passed through the two-phase region, as the observation of a C_1 bank confirms. Thus, experiments and theory indicate that high recovery can be obtained even though the composition path passes through the two-phase region and hence does not meet the strict definition of multiple-contact miscibility.

2.2.6 Discussion

The composition paths described here explain qualitatively why dissolved gas has minimal effect on displacement efficiency, though crude oils are much more complex mixtures than the simple hydrocarbon systems considered here. Because experimentalists routinely use

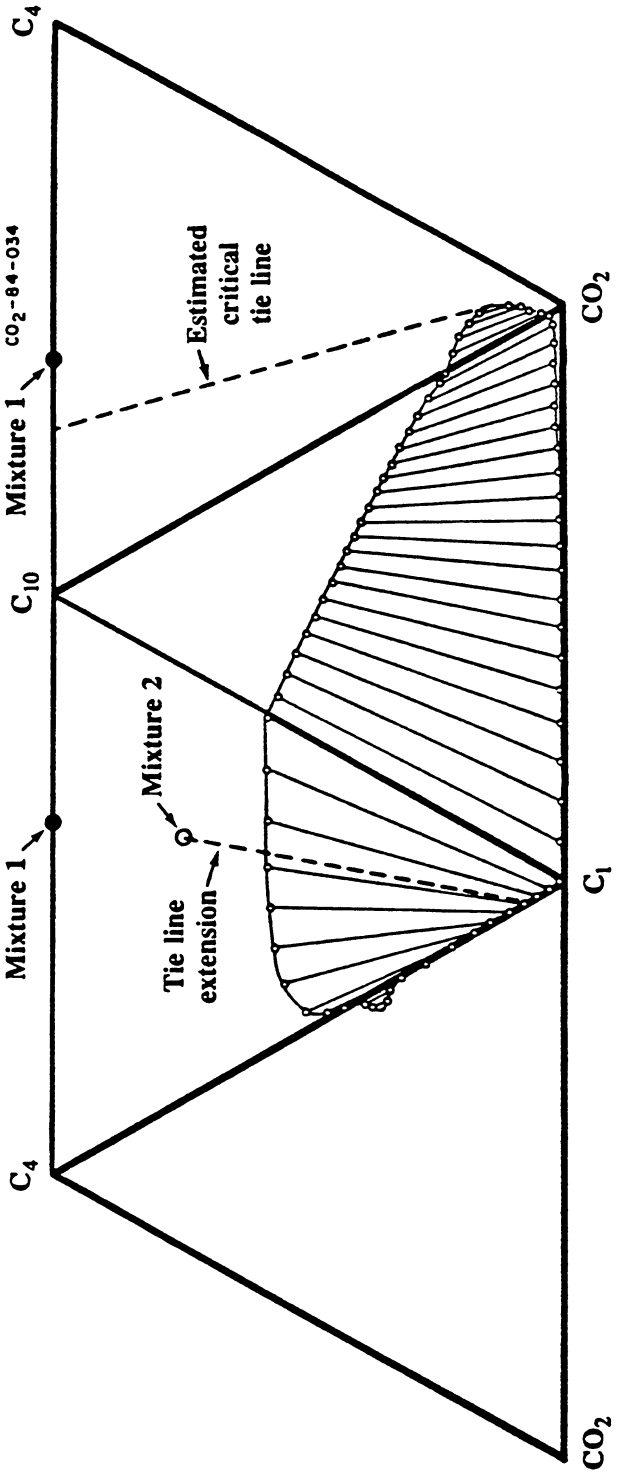

Fig. 2.2.11. Calculated ternary faces of a quaternary phase diagram for CO_2-C_1-C_4-C_{10} mixtures at 160° F (71° C) and 1750 psia (12070 kPa).

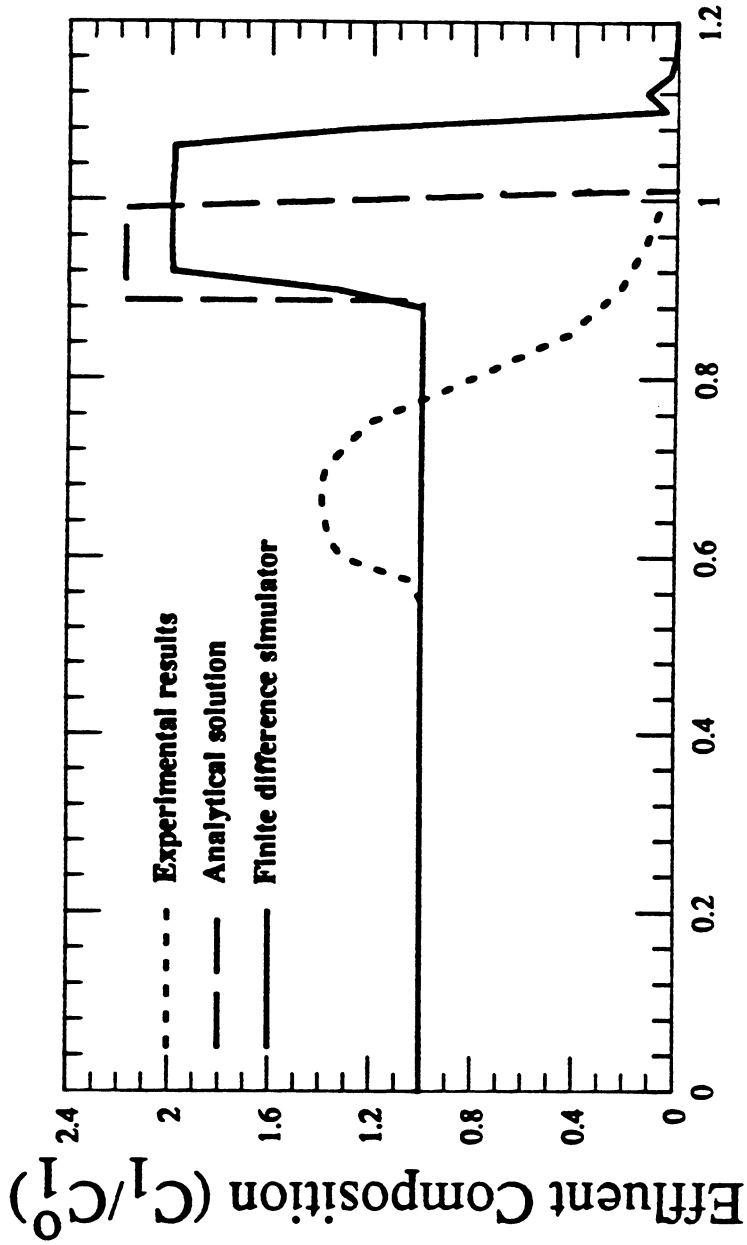

Fig. 2.2.12. Comparison of calculated and measured normalized effluent C_1 concentrations in displacement of a live oil by CO_2 at 160° F (71° C) and 1500 psia (10.3 MPa).

displacement efficiency as a criterion for "miscibility," the calculated composition paths also explain why the MMP is insensitive to the addition of dissolved gas to an oil. The calculate paths confirm the qualitative argument of Holm and Josendal (1982) that C_1 partitions strongly into the more mobile vapor phase and hence CO_2 following behind can displace efficiently the remaining dead oil.

The results presented show that the distinction between miscible and immiscible displacements is not sharp. High local displacement efficiency, which is most important, can occur even when the displacement takes place entirely within the two-phase region. Use of the term "miscible" to describe such displacements is unfortunate because it places the emphasis on the number of phases present rather than on displacement efficiency. Instead, evaluation of appropriate displacement pressures should focus on oil recovery rather than on indications of two-phase flow. According to the composition path calculations, the existence of a C_1 bank is evidence for two-phase flow, but the same calculations, as well as Metcalfe and Yarborough's experiments, indicate that if the definition of the MMP is based on recovery, a criterion for the MMP based on the absence of a C_1 bank is probably too restrictive.

Additional experimental work is needed to confirm the prediction that high efficiency displacement can occur at a pressure below the BPP. Verification of the theory will require that the experimental displacement be nearly one-dimensional. Separate questions of considerable importance for field-scale CO_2 floods are:

(1) What is the optimum displacement pressure when the flow is not one-dimensional, and

(2) Is that pressure substantially different from the one-dimensional MMP?

Answers to those questions will depend not only on the phase behavior of the CO_2-crude oil mixtures, but also on the length scales of the zones of fast and slow flow, whether due to viscous instability or reservoir heterogeneity, and on rates of mixing between those zones caused by dispersion, viscous and capillary crossflow and gravity segregation. Thus, the one-dimensional analysis given here is only a first step toward more complete understanding of the role of phase behavior in field-scale flows.

2.2.7 Conclusions

Analysis of composition paths for dispersion-free, one-dimensional displacement of C_1-C_4-C_{10} mixtures by CO_2 leads to the following conclusions:

(1) Addition of dissolved C_1 to a dead oil causes formation of a leading C_1 bank unless the live oil lies outside the region of tie line extensions in the quaternary diagram. If the pressure is high enough that the dead oil develops miscibility, however, the C_1 bank will appear at the outlet for a short time only.

(2) Oil recovery is controlled by the location of the crossover tie line. If that tie line lies close to the plait point on the CO_2-C_4-C_{10} ternary diagram, oil recovery will be high, even though the composition path passes through the two-phase region. If the oil that remains after all C_1 is removed develops miscibility, the crossover tie line will be very close to the plait point.

(3) Oils that share the same crossover tie line show the same recovery performance after CO_2 breakthrough. Breakthrough times of leading C_1 banks depend on amounts of C_1 and CO_2 present in the original oil, however.

(4) The presence of a C_1 bank should not be used as a single criterion for evaluating potential displacement pressures. Oil recovery is a more reliable indicator of performance for one-dimensional flows.

(5) Displacement of live oil at a pressure below its BPP will be efficient as long as the flow is one-dimensional, and the dead oil develops miscibility when the C_1 is removed.

2.3 Analytical Model of CO_2-Steam-Heavy Oil Displacements

Jeffrey Wingard

In thermal recovery processes, steam is injected to heat the oil, reduce its viscosity and improve recovery. If CO_2 is injected along with the steam or if CO_2 is created in situ by combustion with injected oxygen, then the transfer of CO_2, water and oil between phases affects the flow process because dissolved CO_2 can reduce the viscosity of a heavy oil. In this section we consider the flow of a three component system, CO_2, water and oil that can form up to three phases. In addition, we consider the effects of the temperature variations that occur when injected fluid is hotter than fluid originally in place.

2.3.1 Mathematical Model

Model Description

The model uses the method of characteristics to solve a simplified flow of an arbitrary number of components that partition into an arbitrary number of phases. The model is similar to that developed by Helfferich (1981) and Dumore et al. (1984) and described here in Section 2.2, with the addition that the system has a temperature variation along the direction of flow. The major assumptions of the model are:

1. The flow is one-dimensional
2. All mass and energy transport is by convection.
3 There is instantaneous chemical and thermal equilibrium.

Neglecting dispersion, a material balance on the i^{th} component gives,

$$\frac{\partial}{\partial t}\sum_{j=1}^{n_p}\phi\, x_{ij}\,\rho_j\, S_j + \sum_{j=1}^{n_p}\nabla\cdot\rho_j\, x_{ij}\,\vec{v}_j = 0 \qquad i=1,\, n_c. \tag{2.3.1}$$

The energy balance can be written in a similar form if all the transport is by convection. This gives,

$$\frac{\partial}{\partial t}\sum_{j=1}^{n_p}\phi\, H_j\,\rho_j\, S_j + (\,1-\phi\,)\,\rho_m\, H_m + \sum_{j=1}^{n_p}\nabla\cdot\rho_j\, H_j\,\vec{v}_j = 0 \tag{2.3.2}$$

where

- n_p is the number of phases,
- n_c is the number of components,
- x_{ij} is the mole fraction of component **i** in phase **j**
- ρ_j is the molar density (kg-mole/m^3) of phase **j**
- $\vec{v}_j$ is the phase velocity vector (m/day),
- S_j is the saturation of phase **j**
- ϕ is the porosity, and
- H_j is the enthalpy (J/kg-mole) of phase **j**

Following the derivation in Section 2.2, equations 2.3.1 and 2.3.2 can be simplified to,

$$\frac{\partial G_i}{\partial t} + \frac{\partial F_i}{\partial x} = 0 \qquad i = 1,\, n_c \tag{2.3.3}$$

and

$$\frac{\partial \Gamma}{\partial t} + \frac{\partial \Theta}{\partial x} = 0 \qquad i = 1,\, n_c \tag{2.4.4}$$

where the following definitions have been applied.

$$G_i \equiv \sum_{j=1}^{n_p} x_{ij}\,\rho_j\,S_j\,, \tag{2.4.5}$$

$$\Gamma \equiv \sum_{j=1}^{n_p} H_j\,\rho_j\,S_j + \left[\frac{1-\phi}{\phi}\right]\rho_m\,H_m \tag{2.4.6}$$

$$F_i \equiv \frac{\nu}{\phi}\sum_{j=1}^{n_p} x_{ij}\,\rho_j\,f_j\,, \tag{2.4.7}$$

and,

$$\Theta \equiv \frac{\nu}{\phi}\sum_{j=1}^{n_p} H_i\,\rho_j\,f_j\,. \tag{2.4.8}$$

The composition and temperature solution sought is one for which sets of compositions move at the same velocity. Helfferich (1981) calls this constraint "coherence". It means that certain sets of composition and temperature move together through the flow system; these special composition vectors are the solution to the problem. This constraint leads to the formulation of the eigenvalue problem.

$$\begin{bmatrix} \frac{dF_1}{dC_1} & \frac{dF_1}{dC_2} & \cdots & \frac{dF_1}{dC_{nc-1}} & \frac{dF_1}{dT} & \frac{dF_1}{dv} \\ \frac{dF_2}{dC_1} & \frac{dF_2}{dC_2} & \cdots & \frac{dF_2}{dC_{nc-1}} & \frac{dF_2}{dT} & \frac{dF_2}{dv} \\ \vdots & \vdots & \cdots & \vdots & \vdots & \vdots \\ \frac{dF_{nc}}{dC_1} & \frac{dF_{nc}}{dC_2} & \cdots & \frac{dF_{nc}}{dC_{nc-1}} & \frac{dF_{nc}}{dT} & \frac{dF_{nc}}{dv} \\ \frac{d\Theta}{dC_1} & \frac{d\Theta}{dC_2} & \cdots & \frac{d\Theta}{dC_{nc-1}} & \frac{d\Theta}{dT} & \frac{d\Theta}{dv} \end{bmatrix} \begin{bmatrix} \frac{dC_1}{d\eta} \\ \frac{dC_2}{d\eta} \\ \vdots \\ \frac{dT}{d\eta} \\ \frac{dv}{d\eta} \end{bmatrix} =$$

$$\lambda \begin{bmatrix} \frac{dG_1}{dC_1} & \frac{dG_1}{dC_2} & \cdots & \frac{dG_1}{dC_{nc-1}} & \frac{dG_1}{dT} & 0 \\ \frac{dG_2}{dC_1} & \frac{dG_2}{dC_2} & \cdots & \frac{dG_2}{dC_{nc-1}} & \frac{dG_2}{dT} & 0 \\ \vdots & \vdots & \cdots & \vdots & \vdots & \vdots \\ \frac{dG_{nc}}{dC_1} & \frac{dG_{nc}}{dC_2} & \cdots & \frac{dG_{nc}}{dC_{nc-1}} & \frac{dG_{nc}}{dT} & 0 \\ \frac{d\Gamma}{dC_1} & \frac{d\Gamma}{dC_2} & \cdots & \frac{d\Gamma}{dC_{nc-1}} & \frac{d\Gamma}{dT} & 0 \end{bmatrix} \begin{bmatrix} \frac{dC_1}{d\eta} \\ \frac{dC_2}{d\eta} \\ \vdots \\ \frac{dT}{d\eta} \\ \frac{dv}{dx} \end{bmatrix} \tag{2.3.9}$$

where η is the dummy variable of the characteristic solution.

Eq. 2.3.9 is a general eigenvalue problem for which a solution exists if and only if $\det\left[\mathbf{F} - \boldsymbol{\lambda}\,\mathbf{G}\right] = 0$. For a three component system **F** and **G** are 4 x 4 matrices. The eigenvalues correspond to n_c characteristic rates, or composition velocities and the last eigenvalue is infinite. In both cases, the eigenvectors correspond to characteristic directions in the hodograph space.

Analytical Derivatives

The construction of the eigenvalue matrix , Eq. 2.3.9, requires that derivatives in the form of $\partial G/\partial C$ and $\partial F/\partial C$ be calculated. These derivatives are usually approximated by finite difference calculations, the most common being a simple forward difference. This technique is usually very accurate where the conditions do not change much with composition. Near phase boundaries conditions can change drastically with the addition of even minute amounts of a component. Under these conditions the simple finite difference scheme can fail to give accurate results.

The derivatives required for the eigenvalue problem are represented by eight different forms. These derivatives are, $\partial G/\partial C$, $\partial F/\partial C$, $\partial G/\partial T$, $\partial F/\partial T$, $\partial \Gamma/\partial C$, $\partial \Theta/\partial C$, $\partial \Gamma/\partial T$, and $\partial \Theta/\partial T$. Equations for each of these derivatives will be developed from the most simple to the more complex.

G-Derivatives

Taking the $\partial G/\partial C$ derivative and expanding using the definition of G gives,

$$\frac{\partial G_i}{\partial C_j} = \sum_k^{n_p} \rho_k S_k \frac{\partial x_{ik}}{\partial C_j} + x_{ik} S_k \frac{\partial \rho_k}{\partial C_j} + x_{ik} \rho_k \frac{\partial S_k}{\partial C_j} \tag{2.3.10}$$

The saturation term can be defined as the volume fraction, $S_k = V_k/V_T$. Substituting this definition into Eq. 2.3.10 and expanding the volume quotient gives,

$$\frac{\partial G_i}{\partial C_j} = \sum_k^{n_p} \rho_k S_k \frac{\partial x_{ik}}{\partial C_j} + x_{ik} S_k \frac{\partial \rho_k}{\partial C_j} + \frac{x_{ik}\rho_k}{V_T}\left[\frac{\partial V_k}{\partial C_j} - S_k \frac{\partial V_T}{\partial C_j}\right] \tag{2.3.11}$$

The density term can also be expanded to variables that are given by the equation of state, remembering that $\rho = P/ZRT$ the final representation of the G-Derivative is,

$$\frac{\partial G_i}{\partial C_j} = \sum_k^{n_p} \rho_k S_k \frac{\partial x_{ik}}{\partial C_j} - x_{ik} S_k \frac{P}{R\, Z_k^2\, T} \frac{\partial Z_k}{\partial C_j} + \frac{x_{ik}\rho_k}{V_T}\left[\frac{\partial V_k}{\partial C_j} - S_k \frac{\partial V_T}{\partial C_j}\right] \tag{2.3.12}$$

The derivative with respect to temperature is calculated in the same manner, and all the terms are similar with C_j being replaced with T. The only change is in the density derivative. Because the equation for density contains a temperature term, the results are slightly different. The final equation is,

$$\frac{\partial G_i}{\partial T} = \sum_k^{n_p} \rho_k S_k \frac{\partial x_{ik}}{\partial T} - x_{ik} S_k \frac{P}{RZ_k T}\left[\frac{1}{Z_k}\frac{\partial Z_k}{\partial T} + \frac{1}{T}\right] + \frac{x_{ik}\rho_k}{V_T}\left[\frac{\partial V_k}{\partial T} - S_k \frac{\partial V_T}{\partial T}\right] \tag{2.3.13}$$

Analytic representation of these derivatives is possible when an equation of state is used. Nuttaki, *et. al.*, present method for calculating the compressibility derivatives analytically using three different equations of state. These methods can be used to provide analytic representations for the derivatives in Eqs. 2.3.12 and 2.3.13.

Γ–Derivatives

The derivatives for the enthalpy analog to the saturation terms, Γ, follow the same development as the G-Derivatives, in this case, the concentration or mole fraction term x_{ik} is replaces with the enthalpy of the phase, H_k. The derivatives are,

$$\frac{\partial \Gamma_i}{\partial C_j} = \sum_k^{n_p} \rho_k S_k \frac{\partial H_k}{\partial C_j} - H_k S_k \frac{P}{R\, Z_k^2\, T} \frac{\partial Z_k}{\partial C_j} + \frac{H_k \rho_k}{V_T}\left[\frac{\partial V_k}{\partial C_j} - S_k \frac{\partial V_T}{\partial C_j}\right] \tag{2.3.14}$$

and the temperature derivatives is,

$$\frac{\partial \Gamma_i}{\partial T} = \sum_k^{n_p} \rho_k S_k \frac{\partial H_k}{\partial T} - H_k S_k \frac{P}{R Z_k T}\left[\frac{1}{Z_k}\frac{\partial Z_k}{\partial T} + \frac{1}{T}\right] + \frac{H_k \rho_k}{V_T}\left[\frac{\partial V_k}{\partial T} - S_k \frac{\partial V_T}{\partial T}\right] \tag{2.3.15}$$

The G and Γ derivatives are straight forward because all the terms involved are calculated directly from the equation of state. The F and Θ derivatives deal with flux terms and must take into account models that deal with the flowing properties of the fluids that are described by relatively complex models.

F-Derivatives

The first two terms in the derivation of the F-Derivatives are similar to the development of the G and Γ equations. The term that gives the trouble is the fractional flow term. Looking at the fractional flow term it is similar to the saturation terms in the G-Derivatives because the fractional flow is also the mobility fraction,

$$f_k = \frac{M_k}{M_T} = \frac{(kr_k/\mu_k)}{\sum_k^{n_p} (kr_k/\mu_k)} \tag{2.3.16}$$

Using this definition, the fractional flow derivative can be written as,

$$\frac{\partial f_k}{\partial C_j} = \frac{1}{M_T}\left[\frac{\partial M_k}{\partial C_j} - f_k \frac{\partial M_T}{\partial C_j}\right] \tag{2.3.17}$$

Using the definition of M_k allows us to calculate the derivatives,

$$\frac{\partial M_k}{\partial C_j} = \frac{\partial}{\partial C_j}\left[\frac{kr_k}{\mu_k}\right] = \frac{1}{\mu_k}\left[\frac{\partial kr_k}{\partial C_j} - M_k \frac{\partial \mu_k}{\partial C_j}\right] \tag{2.3.18}$$

now substitution of this definition into Eq. 2.3.16 gives,

$$\frac{\partial f_k}{\partial C_j} = \frac{1}{M_T}\left\{\frac{1}{\mu_k}\left[\frac{\partial kr_k}{\partial C_j} - M_k \frac{\partial \mu_k}{\partial C_j}\right] - f_k \sum_l^{n_p} \frac{1}{\mu_l}\left[\frac{\partial kr_l}{\partial C_j} - M_l \frac{\partial \mu_l}{\partial C_j}\right]\right\} \tag{2.3.19}$$

The derivatives of kr_k and μ_k are dependent on the type of flow model that is used to calculate these quantities. Depending on the complexity of the relative permeability and viscosity model, these derivatives may be possible to calculate analytically. The viscosity model is the most difficult to represent accurately with a few simple equations. The compositional and temperature dependence of viscosity is complex and does not lend itself to simple interpretation.

Θ–Derivatives

The enthalpy analog to the flux derivatives follow the same development as the F-Derivatives, but have an added term that is not present in the mass fluxes. The term $\partial\mu_k/\partial T$ is *very* important in calculating the viscosity changes. The mass analog, $\partial\mu_k/\partial C_j$, drops out due to

the assumption that the pure component viscosity *does not* depend on the concentration of other components in the mixture, but only on the temperature and pressure. Again, this term depends strongly on the models used for the viscosities and relative permeabilities.

Temperature Shock Calculations

When the composition paths indicate a jump or shock condition, a material balance across the discontinuity is done to get the conditions on either side of the shock. When there is a temperature shock a similar calculation is done using the enthalpy balance on either side of the shock. The enthalpy balance over the volume covered by a moving shock contains an accumulation term and a flux term. The accumulation term sums the enthalpy content for each of the phases and the enthalpy stored in the matrix, this is written as,

$$\sum_{j}^{n_p} \rho_j^- S_j^- H_j^- + \left[\frac{1-\phi}{\phi}\right] \rho_m^- h_m^- - \sum_{j}^{m_p} \rho_j^+ S_j^+ H_j^+ \left[\frac{1-\phi}{\phi}\right] \rho_m^+ H_m^+ \qquad (2.3.20)$$

The flux terms are written,

$$\sum_{j}^{n_p} \rho_j^- f_j^- H_j^- - \sum_{j}^{n_p} \rho_j^+ f_j^+ H_j^+ \qquad (2.3.21)$$

where:

ρ_j =	molar density of phase j (kg-mol/m^3)
ρ_m =	density of matrix (kg/m^3)
S_j =	saturation of phase j
f_j =	fractional flow of phase j
H_j =	enthalpy of phase j (kJ/kg-mol)
H_m =	enthalpy of matrix kJ/kg
v =	total velocity (m/sec)
ϕ =	porosity
Superscript + =	conditions ahead of the shock
Superscript - =	conditions behind the shock

equating Eqs. 2.3.20 and 2.3.21 represents the enthalpy analog to the material balance across a shock.

The transition from the single phase region to the two phase region must occur via a shock. This is because the velocities as given by the eigenvalues are discontinuous at the binodal curve. The material balance tells us that this shock must lie along the tie-line extension that passes through the single phase composition. Applying the same procedure on the enthalpy balance will indicate how the temperature changes from the single phase to the two phase region.

Assume that the leading shock is being considered, this means that ahead of the shock (+) there is a single phase, and behind (-) there are two phases. For simplicity call these two phases oil and gas. The enthalpy balance across the shock is

$$\rho_o^- S_o^- H_o^- + \rho_g^- S_g^- H_g^- + \left[\frac{1-\phi}{\phi}\right] \rho_m^- H_m^- - \rho^+ H^+ - \left[\frac{1-\phi}{\phi}\right] \rho_m^+ H_m^+$$

$$= \frac{v^-}{\phi} (\rho_o^- f_o^- H_o^- + \rho_g^- f_g^- H_g^-) - \frac{v^+}{\phi} \rho^+ H^+ \qquad (2.3.22)$$

Solution of Eq. 2.3.22 for $\rho^+ H^+$,

$$\rho^+ H^+ = \frac{1}{(1 - v^+/\phi)} \left[\left[S_o^- - \frac{v^-}{\phi} f_o^- \right] \rho_o^- H_o^- + \left[S_g^- - \frac{v^-}{\phi} f_g^- \right] \rho_g^- H_g^- + \left[\frac{1 - \phi}{\phi} \right] \rho_m (H_m^- - H_m^+) \right] \tag{2.3.23}$$

The final term in Eq. 2.3.23 represents the contribution of the matrix. As the porosity goes to one or the heat capacity of the matrix goes to zero, the enthalpy balance looks similar to the component balances.

When the the matrix term is significant the fluid enthalpy is not a linear combination of the enthalpies on the other side of the shock.

2.3.2 Programming

The *Pathfinder* program now calculates shock velocities and jump conditions along a composition path using a set of end conditions. The velocities are calculated by doing a material balance over one of the components and calculating the shock velocity.

For a simple composition path the calculation proceeds from the injection conditions to the initial conditions. At the injection end both the composition and the injection velocity are specified. A point in the two phase region is chosen that is on a tie-line that extends through the injection conditions. The trailing shock is the point along the tie-line path that has the *minimum* velocity as calculated by,

$$\Lambda_{trail} = \frac{1}{\phi} \left[\frac{v^{inj} F_i^{inj} - v^{II} F_i^{II}}{G_i^{inj} - G_i^{II}} \right]_{\min} \tag{2.3.24}$$

The point where this minimum occurs is the landing point of the trailing shock.

Once in the two phase region, there is variation of the total velocity. Along the tie-line path this velocity change is zero. The compositions of the phases do not change, hence the densities, and the total velocity are constant. When the composition path moves along the non tie-line path, the velocity change is given by the last component in the eigenvector.

The number of jumps or shocks depend on the composition paths, most of the step changes encountered in the two phase region are the result of a self-sharpening wave, where the velocities along a path decrease as towards the initial conditions.

The composition path exits the two phase region in a way similar to the entrance procedures. The composition path continues until the path intersects or is tangent to the tie-line that extends through the exit conditions. From this point three alternatives are possible:

1) The location of the fast shock is between the landing point and the initial conditions. In this case the composition path can move along the tie-line to the jump conditions without violating the velocity constraint.
2) The location of the landing point is between the fast shock and the initial conditions. This requires an immediate jump from the landing point to the initial conditions.
3) The landing point and the fast shock are the same. This case behaves like case #2, there is an immediate jump to the initial conditions.

2.3.3 Results

The solution for the two-phase, constant temperature, system has been completed. The results agree qualitatively with earlier expectations. The solution is essentially an injection of two slightly soluble gases into an oil phase. The gases are in competition. As the

concentration of a component in the vapor phase increases, that component is forced into the liquid phase. Since the oil is already saturated, some of the other gas is forced out of the liquid phase, back to the vapor.

Three components, water, n-C_{16}, and CO_2, were studied at a temperature of 900° R at a pressure of 250 psia to keep the water in the vapor phase.

The phase diagram shown in Fig. 2.3.1 shows a large two phase region with the tie-lines sweeping from the CO_2 to the water corners. According to the Schmidt-Wenzel equation, at least, the solubility of water in the oil is small if any CO_2 is present, but as the CO_2 concentration drops, the water begins to readily dissolve in the oil, reaching a maximum of approximately 18 mole percent with no CO_2 present.

For this sample solution, injection conditions were set at 20 mole percent steam and 80 mole percent CO_2 . This mixture was injected into 100 percent C_{16}. Table 2.3.1 gives the details of the proposed solution.

Figure 2.3.2 shows the proposed solution path and the eigenvalues along the path. The eigenvalues are plotted against CO_2 mole fraction to locate the corresponding position on the ternary diagram. The points marked A, B, and C are locations of shocks or significant breaks in the composition and saturation profiles. These profiles are shown in Fig. 2.3.3.

For the solution path to be valid, the composition velocities must *increase* as the path moves from injection to initial conditions. On the eigenvalue plot, the injection conditions correspond to the 80 mole percent condition at the right end of the path. As the path moves from the injection condition to the initial condition, the marked path is followed to the initial condition of no CO_2 present. This represents a valid solution, one that satisfied the velocity constraints as well as the continuity equation.

Points **A**, **B**, and **C** represent special conditions along the solution path. Point **A** is the location of the trailing shock. It has been illustrated that the only way to enter a two-phase region from single-phase conditions is by a shock along the tieline that extends through the single-phase composition (Dumore et al. 1984).

This point represents the composition with the *minimum* velocity along the entrance tie-line. Compositions with a greater CO_2 fraction move at a greater velocity and are swamped by the compositions that follow the shock.

From point **A** to **B**, the solution path shows a continuous variation along the injection tie-line. As the path moves from **A** to **B**, the phase compositions are constant, only the phase saturations change (see Fig. 2.3.2). The liquid saturation increases from 0.055 at the slow shock to 0.283 at point **B**.

Point **B** is a singular point where the path eigenvalues are equal. At this point, the solution path moves from the tie-line path to the non tie-line path.. This switch is required if the path is to intersect the initial tie-line extension eventually.

Examination of the eigenvalues shows that the switch from the tie-line path to the non tie-line path must take place at the first singular point. If the switch were to take place later, the path would follow the tie-line path up to the top of the peak (see Fig. 2.3.2) and begin to descend to the second switch. This decrease in velocity violates the constraint that velocities must increase moving downstream. In addition, any path jump from the tie-line to nontie-line path would also cause a decrease in velocity, so the tie-line path after the first singular point is ruled out.

The solution now follows the non tie-line path from point *B* to *C* where the CO_2 fraction goes to zero. During this period the C_{16} fraction rapidly increases to a maximum of 0.73 then decreases back to 0.65. This indicates the formation of a small oil bank as the water moves from the vapor phase into the liquid phase. It is important to note that at 900° R the water is much more soluble in the oil phase than is CO_2 (see the phase diagram, Fig. 2.3.1).

Table 2.3.1. Details of Sample Solution with CO_2-Steam Injection into Oil at 900° R and 250 psia.

Condition	Ref. Point	Composition			Liquid Saturation	Wave Velocity
		CO_2	$n - C_{16}$	Water		
Injection		0.800	0.000	0.200	0.000	
Slow Shock	A	0.569	0.275	0.356	0.055	0.092
Tie-Line	A	0.569	0.275	0.356	0.055	0.092
	B	0.245	0.660	0.095	0.283	0.859
Non Tie-Line	B	0.245	0.660	0.095	0.283	0.859
	C	0.000	0.650	0.350	0.641	1.170
Initial		0.000	1.000	0.000	1.000	

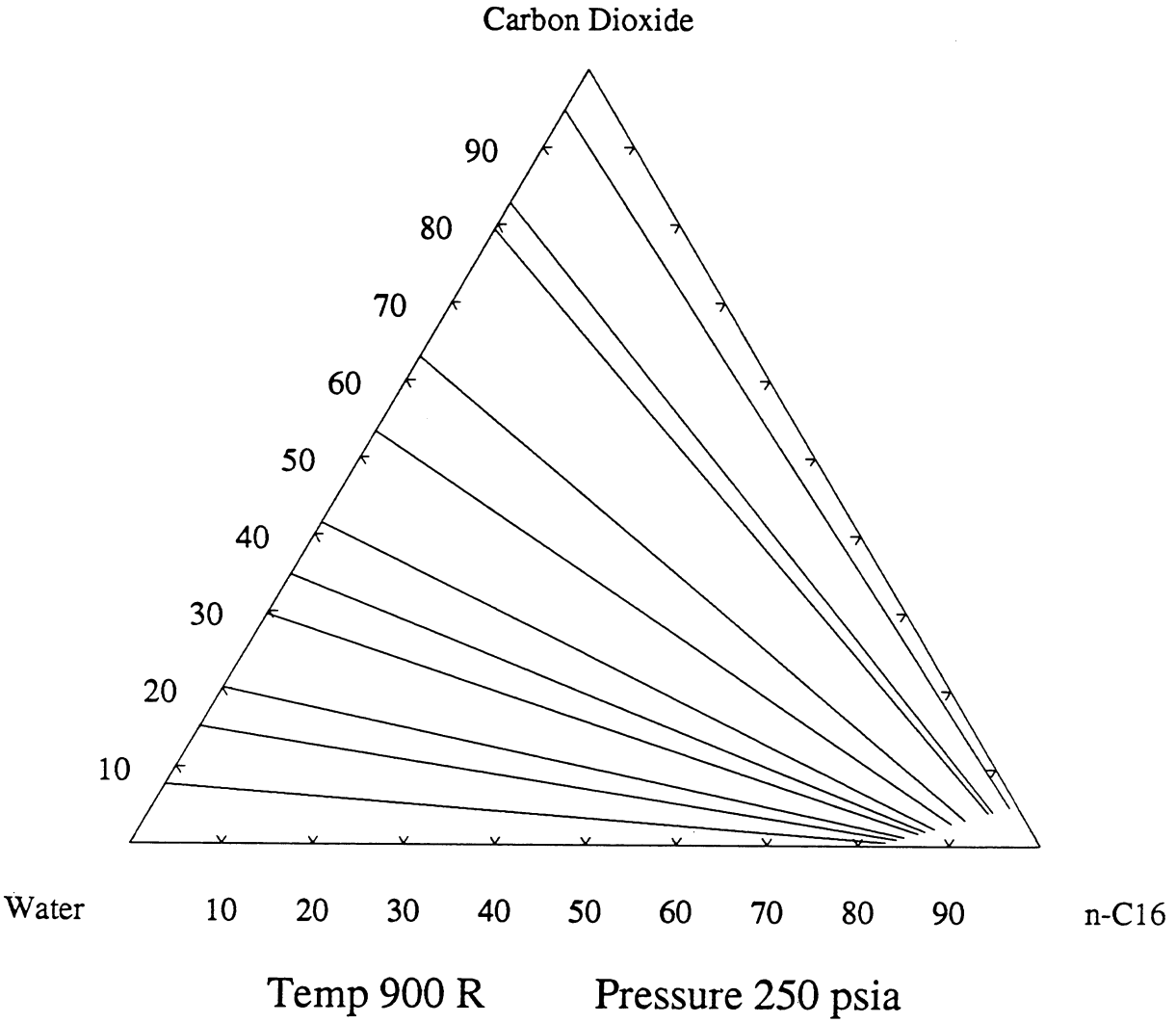

Fig. 2.3.1. Phase Diagram for CO_2 - Oil - Water system at 900 ° R and 250 psia using Schmidt-Wenzel Equation Of State

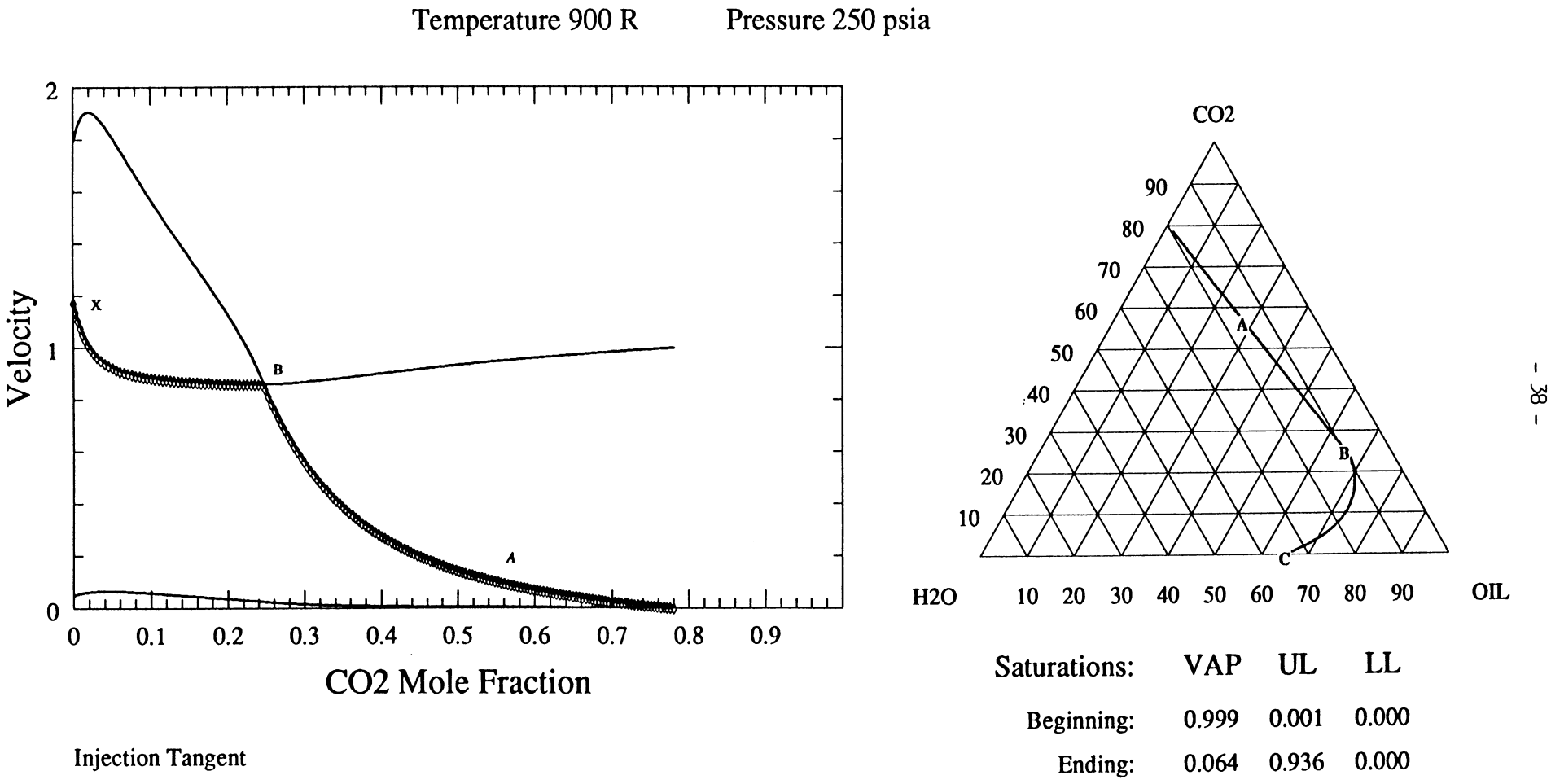

Fig. 2.3.2. Eigenvalue Plot and Composition Path for Sample Solution

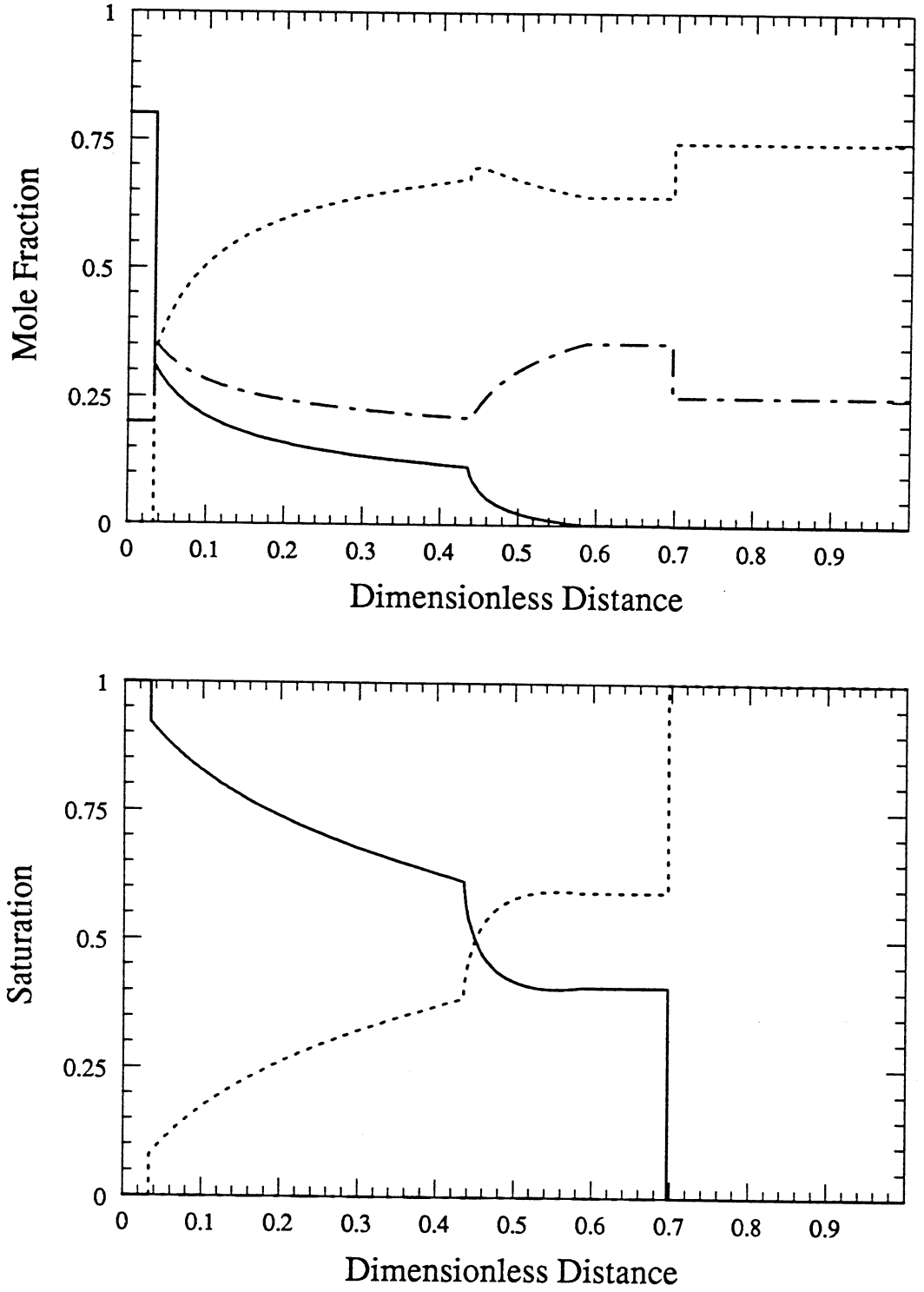

Fig. 2.3.3. Saturation and Composition Profiles after τ=0.5.

After the composition path intersects the exit tie line, one of the three cases mentioned in Section 2.2.3. applies. For this case, the second situation is the one that applies. The shock velocities for the exit tie line are calculated using an equations similar to Eq. 2.3.22 replacing the injections G and F with the G and F at the initial conditions. In this case, however, the maximum velocity is chosen as the location of the fast shock. The point on the exit tie line representing the fast shock is to the water side (or right side) of the landing point. This indicates that there is an immediate jump to the initial conditions from the landing point.

2.3.4 Future Work

The problem of temperature variation for a strictly two-phase system is currently under investigation. The grid of composition paths that change in temperature is calculated and the velocities along these paths examined. As in the constant temperature case, the solution procedure includes construction of a path that moves from an injection point to an initial condition at a different temperature and composition. While there are many potential paths, only one will also satisfy the velocity constraint.

After these paths are characterized, the next step will be to examine solutions that traverse the three-phase region. This will be done using the same three components at a lower temperature where the water forms an aqueous phase. Initially, isothermal paths will be used, then temperature variation added to these solutions.

Other areas of interest are:

- Formulation of solutions for cases where the oil is divided into a volatile and non-volatile fractions.
- Examination of the phase behavior more closely by breaking the oil into many components.
- Investigation of the solutions where lateral heat losses are included into the model. This treatment may parallel some work done with layered systems by treating the enthalpy as a component that has a flow term out of the system.
- Study of the influence of relative permeability models, especially in the three-phase region.

2.4 Interaction of Reservoir Heterogeneity and Phase Behavior

Kiran K. Pande

This project is aimed at describing the effect of phase behavior on flow in a linear, layered reservoir with viscous crossflow between the layers.

Helfferich (1981) calculated composition paths for multicomponent, multiphase displacement in one-dimensional porous media. That theory uses the method of characteristics to solve the governing differential material balance equations and construct a composition path grid for the system. In the case of a three-component system, the composition path grid is mapped on a ternary phase diagram. The composition route or solution path for a given set of initial and injection conditions is determined using the constraint of monotonically increasing velocities from the inlet to the downstream initial compositions. Dumore *et al.* (1984) extended Helfferich's analysis to include the effects of volume change on mixing. Extension of that representation to four component systems is described in Section 2.2.

These theories of multicomponent, multiphase displacement have been applied to study the effect of phase behavior on development of miscibility in displacement processes such as CO_2 flooding. The analytical models provide an important tool to understand displacement

mechanisms in multicomponent, multiphase flow processes. These analytical models are also useful for calibrating and checking numerical reservoir simulation models which model multicomponent, multiphase flow. Analyses presented to date, however, have dealt only with the effects of phase behavior in one-dimensional flow.

Immiscible displacement in a layered system with viscous crossflow has been modeled by Zapata and Lake (1981). This project extends their work by considering the effects of phase behavior as well. Thus, the combined effects of heterogeneity and phase behavior on process performance are studied for the case of displacement in a layered porous medium with viscous crossflow and component transfer between phases. The results of this study will be used to answer a number of questions. For displacements in a homogeneous reservoir, it can be shown (Helfferich (1981)) that a gas drive will develop miscibility as long as the original oil composition does not lie within the region of tie line extensions on a ternary diagram. An important question for the two layer problem considered here is whether the critical tie line, the tie line tangent to the binodal curve, still constitutes the boundary between oil compositions which will and will not develop miscibility. Simulations by Gardner and Ypma (1984) suggest that viscous crossflow causes composition paths to fall deeper into the two-phase region when flow is not uniform. An additional question of interest is whether further increases in pressure can alleviate adverse effects of nonuniform flow.

2.4.1 Theory

Material balance equations are derived based on the following assumptions:

1. All fluids are incompressible.
2. The reservoir is a linear, layered system with uniform properties within a layer.
3. Capillary pressure effects are negligible.
4. Gravitational effects are negligible.
5. Viscous fingering can be neglected.
6. The displacement process is isothermal.
7. Fractional flow functions are unique functions of composition.
8. Phases are in local equilibrium everywhere.
9. Partial molar volumes of components are constant, i.e., there is no change in total volume upon transfer of components between phases.

We consider the driving forces for viscous crossflow by examining the pressure distribution in a two layer linear reservoir with no vertical communication between layers (Zapata and Lake (1981)). Figs. 2.4.1a and 2.4.1b illustrate the driving forces for viscous crossflow for $M < 1$ and $M > 1$ respectively, based on piston-like displacement within each layer. For a layered system with vertical communication and maximum viscous crossflow resulting in vertical equilibrium, there will be no vertical pressure gradients. Figs. 2.4.1a and 2.4.1b show that there is a point in the displacement where the pressure in layer 1 is equal to the pressure in layer 2. Thus, there is no driving force for viscous crossflow at this point. Analysis of Figs. 2.4.1a and 2.4.1b suggests that the two-layer reservoir may be divided into two regions based on the direction of crossflow in each region. The two regions are connected by the no crossflow point. A unique pair of compositions exists at this point such that there is no driving force for viscous crossflow. Figs. 2.4.2a and 2.4.2b illustrate schematically the directions of crossflow for displacements with $M < 1$ and $M > 1$ respectively. Material balance equations can be derived for each region. The solutions to these equations can be linked at the no crossflow point. The material balance equations for each region are as follows:

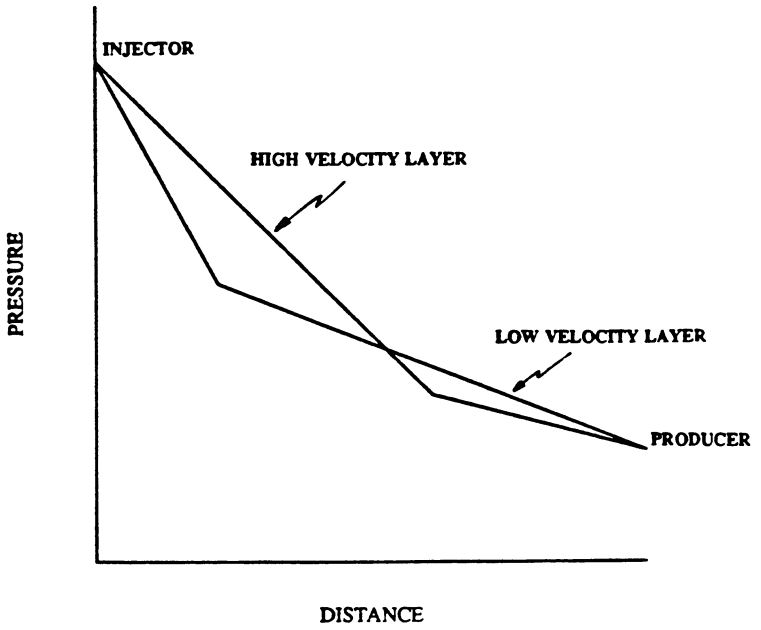

Fig. 2.4.1a. Driving forces for viscous crossflow - M < 1.

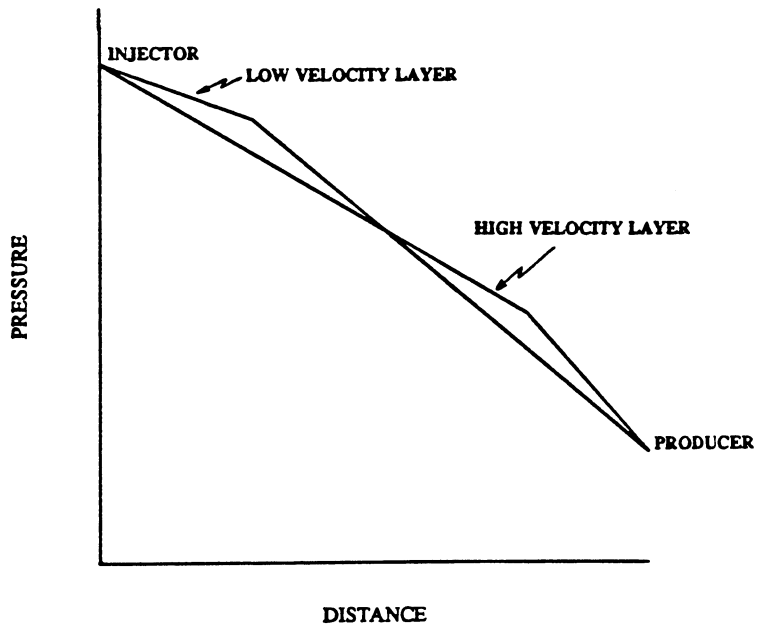

Fig. 2.4.1b. Driving forces for viscous crossflow - M > 1.

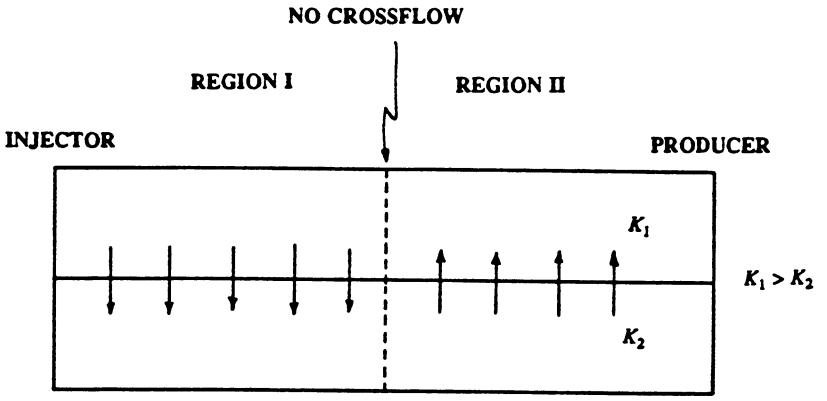

Fig. 2.4.2a. Illustration of directions of crossflow - M < 1.

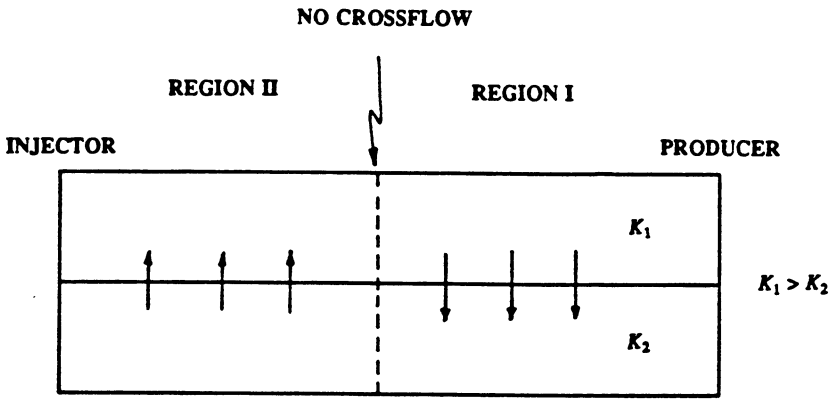

Fig. 2.4.2b. Illustration of directions of crossflow - M > 1.

Region I

Layer 1:

$$-q_{1D}\frac{\partial F_i^1}{\partial x_D} = R_{\phi h_1}\frac{\partial C_i^1}{\partial t_D}, \qquad i = 1, n_c \tag{2.4.1}$$

Layer 2:

$$-q_{2D}\frac{\partial F_i^2}{\partial x_D} + (F_i^1 - F_i^2)\frac{\partial q_{2D}}{\partial x_D} = R_{\phi h_2}\frac{\partial C_i^2}{\partial t_D}, \qquad i = 1, n_c \tag{2.4.2}$$

Region II

Layer 1:

$$-q_{1D}\frac{\partial F_i^1}{\partial x_D} + (F_i^2 - F_i^1)\frac{\partial q_{1D}}{\partial x_D} = R_{\phi h_1}\frac{\partial C_i^1}{\partial t_D}, \qquad i = 1, n_c \tag{2.4.3}$$

Layer 2:

$$-q_{2D}\frac{\partial F_i^2}{\partial x_D} = R_{\phi h_2}\frac{\partial C_i^2}{\partial t_D}, \qquad i = 1, n_c \tag{2.4.4}$$

where F_i^k and C_i^k are the overall fractional flows and concentrations in the kth layer, q_{kD} is the dimensionless flow rate in the kth layer and $R_{\phi h_k}$ is the dimensionless porosity-thickness product. The definitions of those variables are:

$$R_{\phi h_k} = \frac{\phi_k h_k}{\overline{\phi} H} \tag{2.4.5}$$

$$\overline{\phi} = \frac{\sum_{k=1}^{n_l} \phi_k h_k}{\sum_{k=1}^{n_l} h_k} \tag{2.4.6}$$

$$H = \sum_{k=1}^{n_l} h_k \tag{2.4.7}$$

$$F_i^k = \sum_{j=1}^{n_p} c_{ij}^k f_j^k, \qquad i = 1, n_c \tag{2.4.8}$$

$$C_i^k = \sum_{j=1}^{n_p} S_j^k c_{ij}^k , \qquad i = 1, n_c \tag{2.4.9}$$

$$q_{kD} = \frac{q_k}{Q_T} \tag{2.4.10}$$

$$q_k = W K_k h_k \lambda_{rt}^k \tag{2.4.11}$$

$$\lambda_{rt}^k = \text{total mobility in layer } k \tag{2.4.12}$$

$$\lambda_{rt}^k = \sum_{j=1}^{n_p} \lambda_{rj}^k = \sum_{j=1}^{n_p} \frac{k_{rj}^k}{\mu_j^k} \tag{2.4.13}$$

$$t_D = \frac{Q_T t}{\bar{\phi} H W L} \tag{2.4.14}$$

$$Q_T = \sum_{k=1}^{n_l} q_k \tag{2.4.15}$$

$$x_D = \frac{x}{L} \tag{2.4.16}$$

and W and L are the width and length.

Since C_i^k is only a function of x_D and t_D, we can write the total differential as follows

$$dC_i^k = \frac{\partial C_i^k}{\partial x_D} dx_D + \frac{\partial C_i^k}{\partial t_D} dt_D , \qquad i = 1, n_c \tag{2.4.17}$$

We can follow a fixed composition by setting $dC_i^k = 0$ in Eq. 2.4.17. The velocity of some constant composition, C_i^k, is given by

$$v_{ci}^k = - \frac{\dfrac{\partial C_i^k}{\partial t_D}}{\dfrac{\partial C_i^k}{\partial x_D}} , \qquad i = 1, n_c \tag{2.4.18}$$

We can substitute for $\partial C_i^k/\partial t_D$ in the expression for v_{ci}^k using the material balance equations (Eqs. 4.2.1 - 4.2.4). For region I

$$v_{ci}^1 = \frac{\dfrac{q_{1D}}{R_{\phi h_1}} \dfrac{\partial F_i^1}{\partial x_D}}{\dfrac{\partial C_i^1}{\partial x_D}}, \qquad i = 1, n_c \tag{2.4.19}$$

$$v_{ci}^2 = \frac{\dfrac{q_{2D}}{R_{\phi h_2}} \dfrac{\partial F_i^2}{\partial x_D} + \dfrac{(F_i^1 - F_i^2)}{R_{\phi h_2}} \dfrac{\partial q_{1D}}{\partial x_D}}{\dfrac{\partial C_i^2}{\partial x_D}}, \qquad i = 1, n_c \tag{2.4.20}$$

The method of characteristics, as discussed by Helfferich (1981), is used to solve the material balance equations. The coherence condition, which states that all components move at the same velocity, requires that

$$v_{ci}^1 = v_{ci}^2, \qquad i = 1, n_c \tag{2.4.21}$$

The material balance equations for Region I and Region II, coupled with the coherence condition, allows the problem to be formulated as an eigenvalue problem. In the formulation of the eigenvalue problem $v_{ci}^k = \lambda$. Then for Region I we have,

$$\lambda \frac{\partial C_i^1}{\partial x_D} = \frac{q_{1D}}{R_{\phi h_1}} \frac{\partial F_i^1}{\partial x_D}, \qquad i = 1, n_c \tag{2.4.22}$$

$$\lambda \frac{\partial C_i^2}{\partial x_D} = \frac{q_{2D}}{R_{\phi h_2}} \frac{\partial F_i^2}{\partial x_D} + \frac{(F_i^1 - F_i^2)}{R_{\phi h_2}} \frac{\partial q_{1D}}{\partial x_D}, \qquad i = 1, n_c \tag{2.4.23}$$

The derivatives $\partial F_i^1/\partial x_D$, $\partial F_i^2/\partial x_D$, and $\partial q_{1D}/\partial x_D$ can be expanded as follows since F_i^1, F_i^2, and q_{1D} are only functions of x_D and t_D:

$$\frac{\partial F_i^1}{\partial x_D} = \sum_{m=1}^{n_c - 1} \frac{\partial F_i^1}{\partial C_m^1} \frac{\partial C_m^1}{\partial x_D}, \qquad i = 1, n_c \tag{2.4.24}$$

$$\frac{\partial F_i^2}{\partial x_D} = \sum_{m=1}^{n_c - 1} \frac{\partial F_i^2}{\partial C_m^2} \frac{\partial C_m^2}{\partial x_D}, \qquad i = 1, n_c \tag{2.4.25}$$

$$\frac{\partial q_{1D}}{\partial x_D} = \sum_{m=1}^{n_c - 1} \left[\frac{\partial q_{1D}}{\partial C_m^1} \frac{\partial C_m^1}{\partial x_D} + \frac{\partial q_{1D}}{\partial C_m^2} \frac{\partial C_m^2}{\partial x_D} \right], \qquad i = 1, n_c \tag{2.4.26}$$

Substituting for the derivatives $\partial F_i^1/\partial x_D$, $\partial F_i^2/\partial x_D$, and $\partial q_{1D}/\partial x_D$ in the coherence equations for Region I (Eqs. 2.4.22 - 2.4.23) yields:

$$\lambda \frac{\partial C_i^1}{\partial x_D} = \frac{q_{1D}}{R_{\phi h_1}} \sum_{m=1}^{n_c-1} \frac{\partial F_i^1}{\partial C_m^1} \frac{\partial C_m^1}{\partial x_D}, \qquad i = 1, n_c \tag{2.4.27}$$

$$\lambda \frac{\partial C_i^2}{\partial x_D} = \frac{q_{2D}}{R_{\phi h_2}} \sum_{m=1}^{n_c-1} \frac{\partial F_i^2}{\partial C_m^2} \frac{\partial C_m^2}{\partial x_D} + \tag{2.4.28}$$

$$+ \frac{(F_i^1 - F_i^2)}{R_{\phi h_2}} \sum_{m=1}^{n_c-1} \left[\frac{\partial q_{1D}}{\partial C_m^1} \frac{\partial C_m^1}{\partial x_D} + \frac{\partial q_{1D}}{\partial C_m^2} \frac{\partial C_m^2}{\partial x_D} \right], \qquad i = 1, n_c$$

A similar analysis for Region II yields the following coherence equations:

$$\lambda \frac{\partial C_i^1}{\partial x_D} = \frac{q_{1D}}{R_{\phi h_1}} \sum_{m=1}^{n_c-1} \frac{\partial F_i^1}{\partial C_m^1} \frac{\partial C_m^1}{\partial x_D} + \tag{2.4.29}$$

$$+ \frac{(F_i^1 - F_i^2)}{R_{\phi h_1}} \sum_{m=1}^{n_c-1} \left[\frac{\partial q_{1D}}{\partial C_m^1} \frac{\partial C_m^1}{\partial x_D} + \frac{\partial q_{1D}}{\partial C_m^2} \frac{\partial C_m^2}{\partial x_D} \right], \qquad i = 1, n_c$$

$$\lambda \frac{\partial C_i^2}{\partial x_D} = \frac{q_{2D}}{R_{\phi h_2}} \sum_{m=1}^{n_c-1} \frac{\partial F_i^2}{\partial C_m^2} \frac{\partial C_m^2}{\partial x_D}, \qquad i = 1, n_c \tag{2.4.30}$$

The Region I solution and the Region II solution are coupled at the no crossflow point.

Ternary System

The system of equations in matrix form for a ternary system is as follows:

Region I

$$\begin{bmatrix} A_1 & B_1 & C_1 & D_1 \\ A_2 & B_2 & C_2 & D_2 \\ A_3 & B_3 & C_3 & D_3 \\ A_4 & B_4 & C_4 & D_4 \end{bmatrix} \begin{bmatrix} \frac{\partial C_1^1}{\partial x_D} \\ \frac{\partial C_2^1}{\partial x_D} \\ \frac{\partial C_1^2}{\partial x_D} \\ \frac{\partial C_2^2}{\partial x_D} \end{bmatrix} = \lambda \begin{bmatrix} \frac{\partial C_1^1}{\partial x_D} \\ \frac{\partial C_2^1}{\partial x_D} \\ \frac{\partial C_1^2}{\partial x_D} \\ \frac{\partial C_2^2}{\partial x_D} \end{bmatrix} \tag{2.4.31}$$

where,

$$A_1 = \frac{q_{1D}}{R_{\phi h_1}} \frac{\partial F_1^1}{\partial C_1^1} \tag{2.4.32}$$

$$A_2 = \frac{q_{1D}}{R_{\phi h_1}} \frac{\partial F_2^1}{\partial C_1^1} \tag{2.4.33}$$

$$A_3 = \frac{F_1^1 - F_1^2}{R_{\phi h_2}} \frac{\partial q_{1D}}{\partial C_1^1} \tag{2.4.34}$$

$$A_4 = \frac{F_2^1 - F_2^2}{R_{\phi h_2}} \frac{\partial q_{1D}}{\partial C_1^1} \tag{2.4.35}$$

$$B_1 = \frac{q_{1D}}{R_{\phi h_1}} \frac{\partial F_1^1}{\partial C_2^1} \tag{2.4.36}$$

$$B_2 = \frac{q_{1D}}{R_{\phi h_1}} \frac{\partial F_2^1}{\partial C_2^1} \tag{2.4.37}$$

$$B_3 = \frac{F_1^1 - F_1^2}{R_{\phi h_2}} \frac{\partial q_{1D}}{\partial C_2^1} \tag{2.4.38}$$

$$B_4 = \frac{F_2^1 - F_2^2}{R_{\phi h_2}} \frac{\partial q_{1D}}{\partial C_2^1} \tag{2.4.39}$$

$$C_1 = 0 \tag{2.4.40}$$

$$C_2 = 0 \tag{2.4.41}$$

$$C_3 = \frac{q_{2D}}{R_{\phi h_2}} \frac{\partial F_1^2}{\partial C_1^2} + \frac{F_1^1 - F_1^2}{R_{\phi h_2}} \frac{\partial q_{1D}}{\partial C_1^2} \tag{2.4.42}$$

$$C_4 = \frac{q_{2D}}{R_{\phi h_2}} \frac{\partial F_2^2}{\partial C_1^2} + \frac{F_2^1 - F_2^2}{R_{\phi h_2}} \frac{\partial q_{1D}}{\partial C_1^2} \tag{2.4.43}$$

$$D_1 = 0 \tag{2.4.44}$$

$$D_2 = 0 \tag{2.4.45}$$

$$D_3 = \frac{q_{2D}}{R_{\phi h_2}} \frac{\partial F_1^2}{\partial C_2^2} + \frac{F_1^1 - F_1^2}{R_{\phi h_2}} \frac{\partial q_{1D}}{\partial C_2^2} \tag{2.4.46}$$

$$D_4 = \frac{q_{2D}}{R_{\phi h_2}} \frac{\partial F_2^2}{\partial C_2^2} + \frac{F_2^1 - F_2^2}{R_{\phi h_2}} \frac{\partial q_{1D}}{\partial C_2^2} \tag{2.4.47}$$

Region II

$$\begin{bmatrix} A_1 & B_1 & C_1 & D_1 \\ A_2 & B_2 & C_2 & D_2 \\ A_3 & B_3 & C_3 & D_3 \\ A_4 & B_4 & C_4 & D_4 \end{bmatrix} \begin{bmatrix} \frac{\partial C_1^1}{\partial x_D} \\ \frac{\partial C_2^1}{\partial x_D} \\ \frac{\partial C_1^2}{\partial x_D} \\ \frac{\partial C_2^2}{\partial x_D} \end{bmatrix} = \lambda \begin{bmatrix} \frac{\partial C_1^1}{\partial x_D} \\ \frac{\partial C_2^1}{\partial x_D} \\ \frac{\partial C_1^2}{\partial x_D} \\ \frac{\partial C_2^2}{\partial x_D} \end{bmatrix} \tag{2.4.48}$$

where,

$$A_1 = \frac{q_{1D}}{R_{\phi h_1}} \frac{\partial F_1^1}{\partial C_1^1} + \frac{F_1^1 - F_1^2}{R_{\phi h_1}} \frac{\partial q_{1D}}{\partial C_1^1} \tag{2.4.49}$$

$$A_2 = \frac{q_{1D}}{R_{\phi h_1}} \frac{\partial F_2^1}{\partial C_1^1} + \frac{F_2^1 - F_2^2}{R_{\phi h_1}} \frac{\partial q_{1D}}{\partial C_1^1} \tag{2.4.50}$$

$$A_3 = 0 \tag{2.4.51}$$

$$A_4 = 0 \tag{2.4.52}$$

$$B_1 = \frac{q_{1D}}{R_{\phi h_1}} \frac{\partial F_1^1}{\partial C_2^1} + \frac{F_1^1 - F_1^2}{R_{\phi h_1}} \frac{\partial q_{1D}}{\partial C_2^1} \tag{2.4.53}$$

$$B_2 = \frac{q_{1D}}{R_{\phi h_1}} \frac{\partial F_2^1}{\partial C_2^1} + \frac{F_2^1 - F_2^2}{R_{\phi h_1}} \frac{\partial q_{1D}}{\partial C_2^1} \tag{2.4.54}$$

$$B_3 = 0 \tag{2.4.55}$$

$$B_4 = 0 \tag{2.4.56}$$

$$C_1 = \frac{F_1^1 - F_1^2}{R_{\phi h_1}} \frac{\partial q_{1D}}{\partial C_1^2} \tag{2.4.57}$$

$$C_2 = \frac{F_2^1 - F_2^2}{R_{\phi h_1}} \frac{\partial q_{1D}}{\partial C_1^2} \tag{2.4.58}$$

$$C_3 = \frac{q_{2D}}{R_{\phi h_2}} \frac{\partial F_1^2}{\partial C_1^2} \tag{2.4.59}$$

$$C_4 = \frac{q_{2D}}{R_{\phi h_2}} \frac{\partial F_2^2}{\partial C_1^2} \tag{2.4.60}$$

$$D_1 = \frac{F_1^1 - F_1^2}{R_{\phi h_1}} \frac{\partial q_{1D}}{\partial C_2^2} \tag{2.4.61}$$

$$D_2 = \frac{F_2^1 - F_2^2}{R_{\phi h_1}} \frac{\partial q_{1D}}{\partial C_2^2} \tag{2.4.62}$$

$$D_3 = \frac{q_{2D}}{R_{\phi h_2}} \frac{\partial F_1^2}{\partial C_2^2} \tag{2.4.63}$$

$$D_4 = \frac{q_{2D}}{R_{\phi h_2}} \frac{\partial F_2^2}{\partial C_2^2} \tag{2.4.64}$$

Eqs. 2.4.31 and 2.4.48 are general eigenvalue problems where solutions exist if and only if $\det [\overline{\overline{J}} - \lambda \overline{\overline{I}}] = 0$. As in analyses of three-component flows composition paths are found by solving the eigenvalue problem for eigenvalues (velocities of a given overall composition) and eigenvectors (composition directions that satisfy coherence). In this case, however, the composition paths will appear on separate ternary diagrams for each of the layers. The actual solution path is chosen, as before, subject to the constraint of monotonically increasing velocities from the inlet to the downstream initial compositions.

The Peng-Robinson equation of state is used to calculate phase compositions. Phase viscosities are calculated using the Lohrenz *et al.* (1964) version of the Jossi *et al.* (1962) correlations. All phase composition and viscosity calculations are performed using the phase behavior package developed by Nutakki *et al.* (1985). Phase densities are calculated as follows:

$$\rho_j^k = \frac{\sum_{i=1}^{n_c} x_{ij}^k}{\sum_{i=1}^{n_c} \frac{x_{ij}^k}{\rho_{ci}}}, \qquad j = 1, n_p \tag{2.4.65}$$

where ρ_{ci} is the molar density of component i at the reservoir temperature and pressure as calculated from the Peng-Robinson equation of state, and x_{ij}^k is the mole fraction of component i in phase j in layer k. Phase densities are calculated using Eq. 2.4.65 rather than using the phase densities predicted by the Peng-Robinson equation of state because of the assumption of no volume change on mixing.

Relative permeabilities of the fluid phases are calculated using the following expressions:

$$k_{rg} = k_{rg}^o \left[\frac{S_g}{1 - S_{wr} - S_{or}} \right]^{n_g} \tag{2.4.66}$$

$$k_{ro} = k_{ro}^o \left[\frac{1 - S_g - S_{or} - S_{wr}}{1 - S_{wr} - S_{or}} \right]^{n_o} \tag{2.4.67}$$

The following fractional flow expression is assumed:

$$f_j^k = \frac{\frac{k_{rj}^k}{\mu_j^k}}{\sum_{j=1}^{n_p} \frac{k_{rj}^k}{\mu_j^k}}, \qquad j = 1, n_p \tag{2.4.68}$$

The derivatives in Eqs. 2.4.18 and 2.4.35 are evaluated using finite difference approximations since analytical evaluation of these derivatives is difficult due to the complexity of the equation of state representation of phase compositions. In general a centered finite difference approximation is used to approximate the derivatives, for example:

$$\frac{\partial F_1^1}{\partial C_1^1} = \frac{F_1^1 (C_1^1 + \Delta C_1^1, C_2^1, C_1^2, C_2^2) - F_1^1 (C_1^1 - \Delta C_1^1, C_2^1, C_1^2, C_2^2)}{2 \Delta C_1^1} \tag{2.4.69}$$

Binary System

The system of equations in matrix form for a binary system is as follows:

Region I

$$\begin{bmatrix} A_1 & B_1 \\ A_2 & B_2 \end{bmatrix} \begin{bmatrix} \frac{\partial C_1^1}{\partial x_D} \\ \frac{\partial C_1^2}{\partial x_D} \end{bmatrix} = \lambda \begin{bmatrix} \frac{\partial C_1^1}{\partial x_D} \\ \frac{\partial C_1^2}{\partial x_D} \end{bmatrix} \tag{2.4.70}$$

where,

$$A_1 = \frac{q_{1D}}{R_{\phi h_1}} \frac{\partial F_1^1}{\partial C_1^1} \tag{2.4.71}$$

$$A_2 = \frac{F_1^1 - F_1^2}{R_{\phi h_2}} \frac{\partial q_{1D}}{\partial C_1^1} \tag{2.4.72}$$

$$B_1 = 0 \tag{2.4.73}$$

$$B_2 = \frac{q_{2D}}{R_{\phi h_2}} \frac{\partial F_1^2}{\partial C_1^2} + \frac{F_1^1 - F_1^2}{R_{\phi h_2}} \frac{\partial q_{1D}}{\partial C_1^2} \tag{2.4.74}$$

Region II

$$\begin{bmatrix} A_1 & B_1 \\ A_2 & B_2 \end{bmatrix} \begin{bmatrix} \frac{\partial C_1^1}{\partial x_D} \\ \frac{\partial C_1^2}{\partial x_D} \end{bmatrix} = \lambda \begin{bmatrix} \frac{\partial C_1^1}{\partial x_D} \\ \frac{\partial C_1^2}{\partial x_D} \end{bmatrix} \tag{2.4.75}$$

where,

$$A_1 = \frac{q_{1D}}{R_{\phi h_1}} \frac{\partial F_1^1}{\partial C_1^1} + \frac{F_1^1 - F_1^2}{R_{\phi h_1}} \frac{\partial q_{1D}}{\partial C_1^1} \tag{2.4.76}$$

$$A_2 = 0 \tag{2.4.77}$$

$$B_1 = \frac{F_1^1 - F_1^2}{R_{\phi h_1}} \frac{\partial q_{1D}}{\partial C_1^2} \tag{2.4.78}$$

$$B_2 = \frac{q_{2D}}{R_{\phi h_2}} \frac{\partial F_1^2}{\partial C_1^2} \tag{2.4.79}$$

Eqs. 2.4.70 and 2.4.75 are general eigenvalue problems where solutions exist if and only if $\det [\overline{\overline{J}} - \lambda \overline{\overline{I}}] = 0$. Composition paths are found by solving the eigenvalue problem for eigenvalues (velocities of a given composition) and eigenvectors (composition directions that satisfy coherence.

2.4.2 Results

Immiscible Binary System

The work of Zapata and Lake (1981) on immiscible displacement in a layered system with viscous crossflow is actually a simple special case of the binary system theory described above. If all components are immiscible, then $c_{ij}^k = 0$, for all $i \neq j$. Some features of the more complicated three-component system solution may be illustrated using this simple case of immiscible displacement. For the binary case the eigenvalues for Regions I and II are given by:

$$\lambda_1 = A_1 \tag{2.4.80}$$

$$\lambda_2 = B_2 \tag{2.4.81}$$

The results presented in this section are for an immiscible water-oil displacement process with the reservoir and fluid properties shown in Table 2.4.1. Relative permeabilities of the oil and water phases are calculated using the following expressions:

$$k_{rw} = k_{rw}^o \left[\frac{S_w - S_{wr}}{1 - S_{wr} - S_{or}} \right]^{n_w} \tag{2.4.82}$$

$$k_{ro} = k_{ro}^o \left[\frac{1 - S_w - S_{or}}{1 - S_{wr} - S_{or}} \right]^{n_o} \tag{2.4.83}$$

The derivatives in Eqs. 2.4.70 and 2.4.75 are evaluated analytically.

The composition path is shown in Fig. 2.4.3. The solution path passes through the initial and injection conditions. Note that the Region I and Region II solutions intersect at the no crossflow point. The variation in velocity along the solution path as a function of the saturation in layer 1 is shown in Fig. 2.4.4. A similar graph showing the variation in velocity along the solution path as a function of the saturation in layer 2 is presented in Fig. 2.4.5. Note that there is only one path which satisfies the constraint that the velocity must increase monotonically from the inlet to the downstream initial compositions. The saturation distributions in layers 1 and 2 at $t_D = 0.2$ are presented in Figs. 2.4.6 and 2.4.7 respectively. From Figs. 2.4.6 and 2.4.7 it is evident that there is a zone of constant state which corresponds to the no crossflow region which couples the Region I and Region II solutions together.

2.4.3 Summary and Future Work

The analysis of immiscible binary systems indicates that similar calculations are possible for systems with limited solubility of one component in another.

Currently composition paths are currently being computed for binary and ternary miscible systems of CO_2 and C_4, C_{10}. Those solutions are constructed by the same procedure as that described for the immiscible system. Eigenvalues and eigenvectors are calculated, and the solution composition path is identified by applying the velocity constraint. When available, the solutions to these problems will illustrate the interaction of crossflow with chromatographic effects that control composition paths in multiple contact miscible displacements.

Table 2.4.1. Reservoir and Fluid Properties

K_1/K_2	3.0
h_1/h_2	0.25
ϕ_1/ϕ_2	1.0
k_{rw}^o	1.0
k_{ro}^o	1.0
μ_w	1.0
μ_o	1.5
S_{or}	0.1
S_{wr}	0.1
n_w	1.0
n_o	1.0

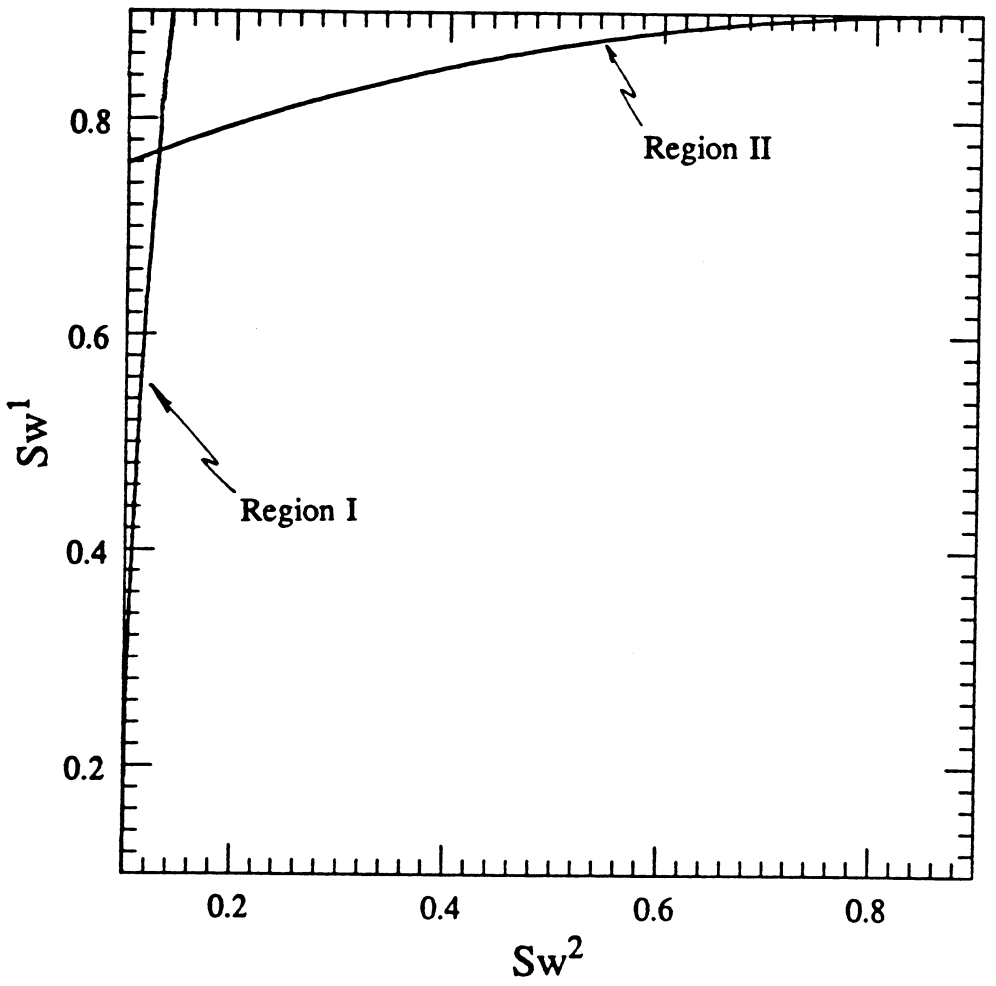

Fig. 2.4.3. Solution path for the example binary immiscible problem.

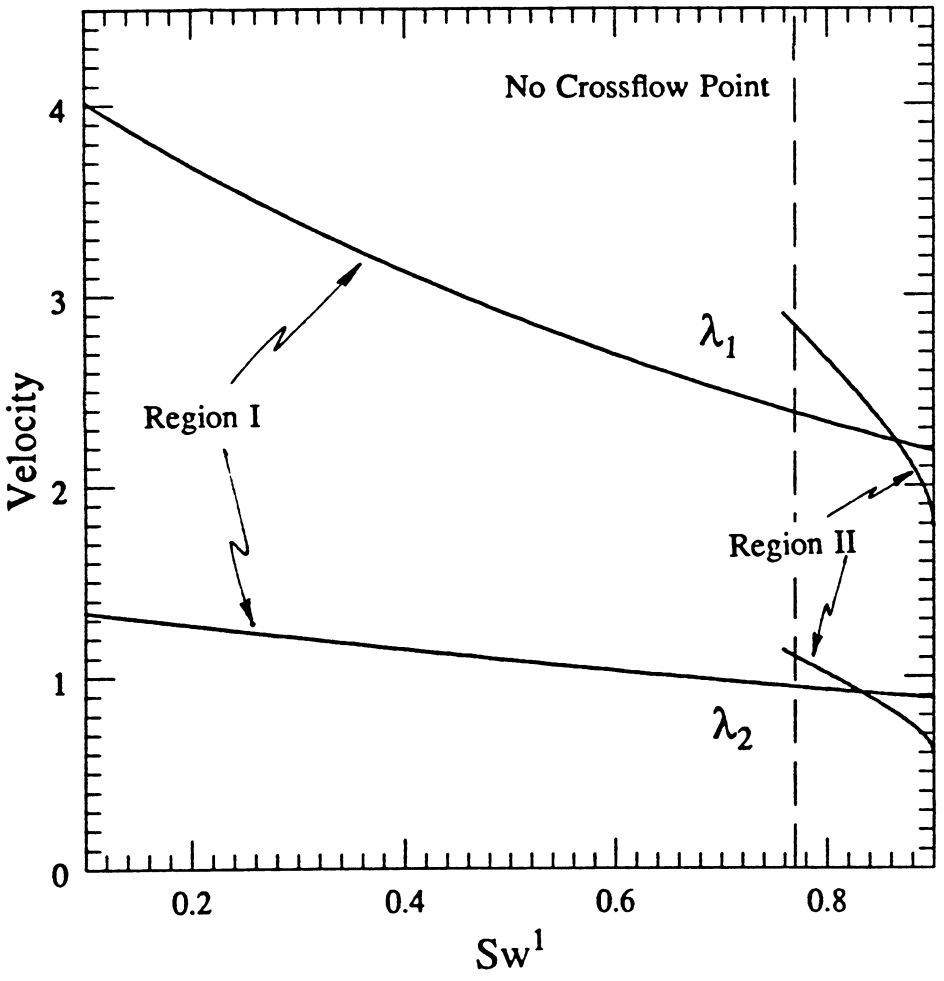

Fig. 2.4.4. Variation of eigenvalues along solution path as a function of Sw^1.

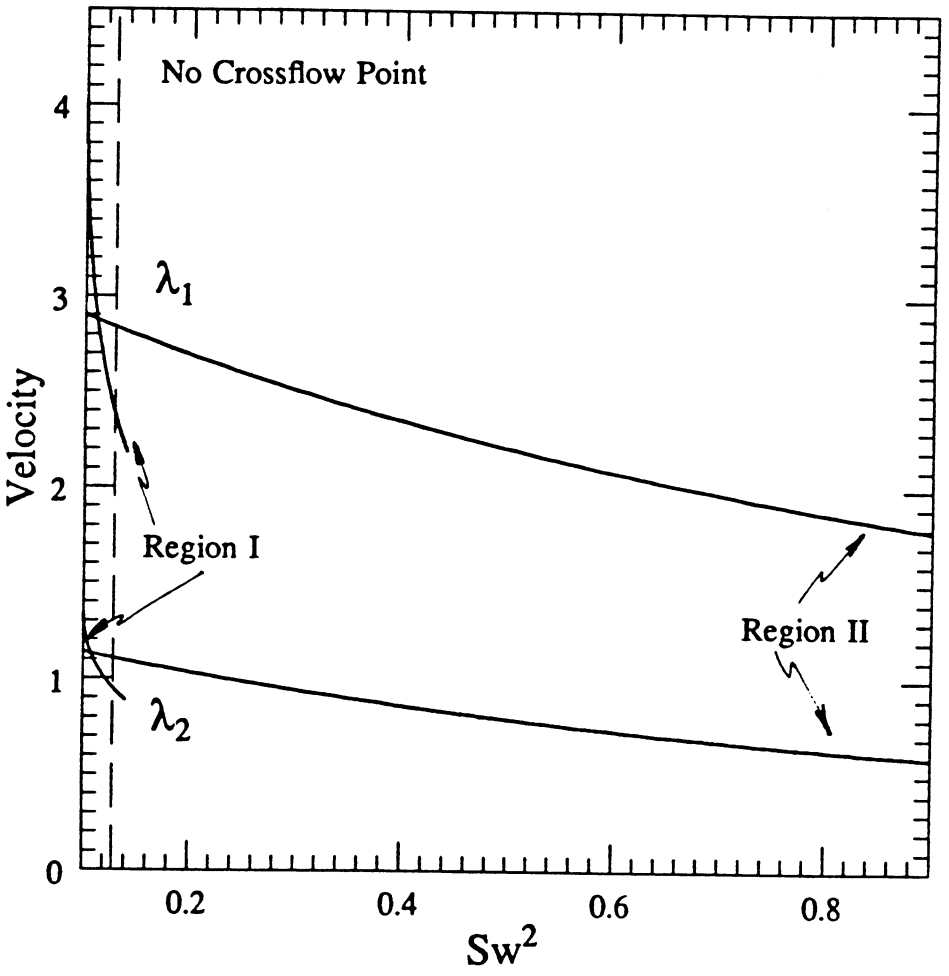

Fig. 2.4.5. Variation of eigenvalues along solution path as a function of Sw^2.

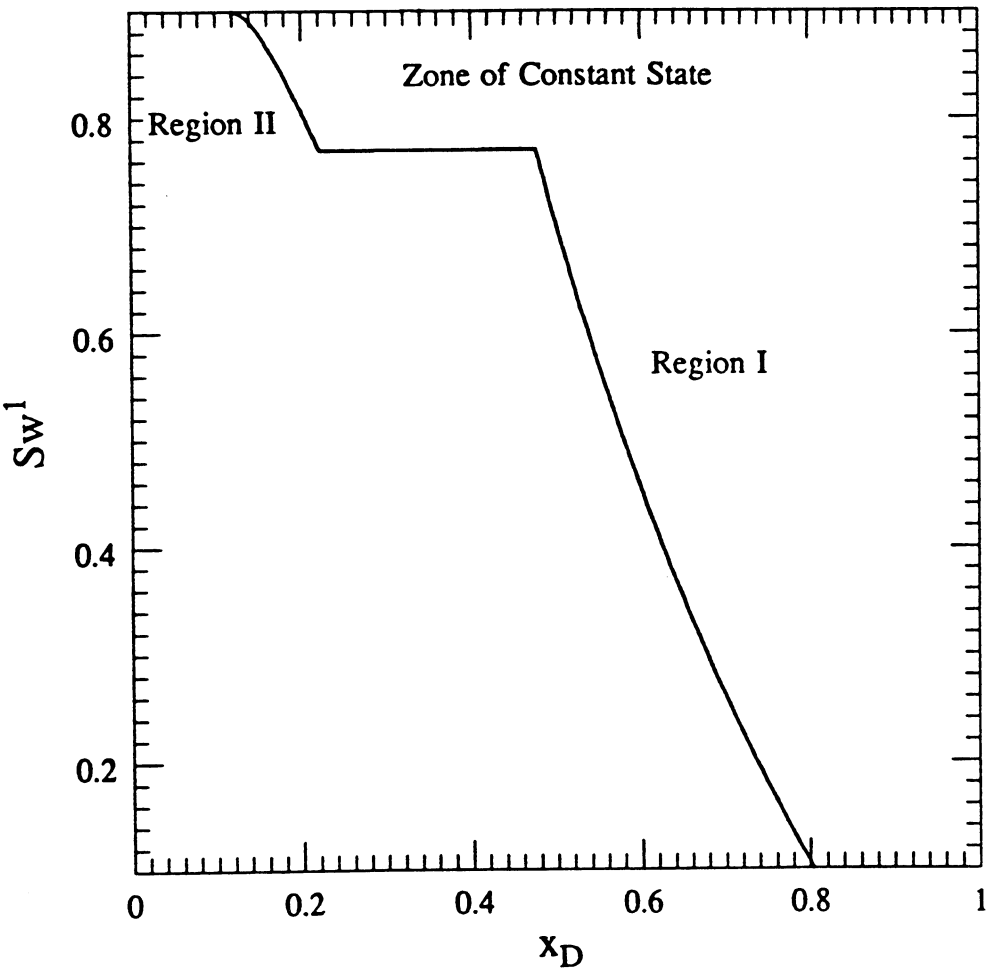

Fig. 2.4.6. Saturation distribution in layer 1 at $t_D = 0.2$.

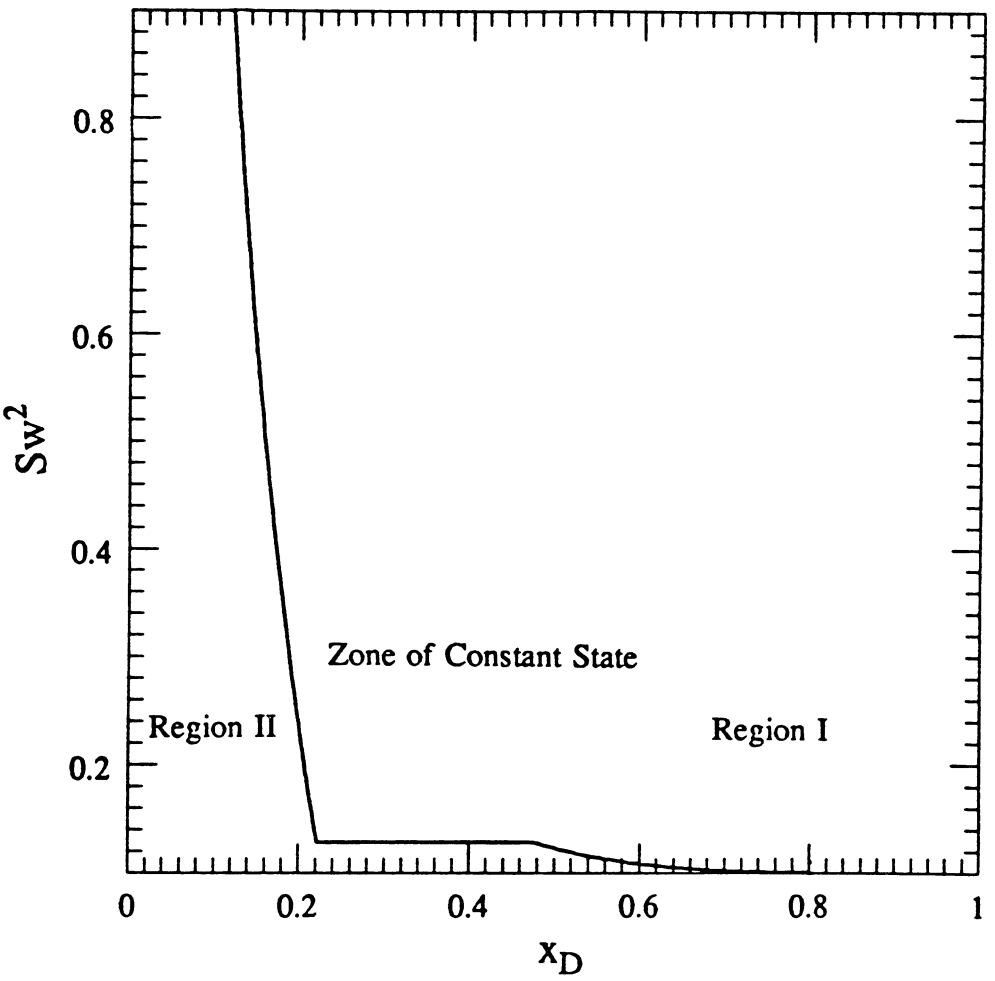

Fig. 2.4.7. Saturation distribution in layer 2 at $t_D = 0.2$.

2.5 Effect of Dispersion on Composition Paths in One-Dimensional Displacements

B. Walsh

In one dimensional flow in the absence of dispersion, composition paths on a ternary diagram will avoid the two-phase region if the original oil composition lies outside the region of tie line extensions (Hutchinson and Braun 1961, Helfferich 1981). When dispersion is present, however, as it is in any real flow, composition paths may enter the two-phase region even when the oil composition lies outside the region of tie line extensions (Gardner, et al. 1981, Orr et al. 1983). In this section, we examine the quantitative impact of dispersive mixing on composition paths for various ternary phase diagrams.

Fig. 2.5.1 is a typical pseudoternary diagram that represents solvent (CO_2), light hydrocarbons (say C_2-C_7), which we will refer to as LPG, and heavy hydrocarbons. It has been constructed using the following rules that are common to all the phase diagrams used in this discussion:

(1) The size and shape of the two phase regions are determined by the phase compositions of the solvent-heavies "binary", and the plait point composition. Normally we have used a solubility of 0.5% heavies in solvent as the upper binary composition.

(2) There is no three-phase region in this or in any of the diagrams that follow.

(3) The tie lines are fan-like from a common apex on the zero-LPG axis. In the phase diagram of Fig. 2.5.2 and in all the diagrams that follow it, only one tie line is shown. We refer to that tie line as the pivot line. The remaining tie lines are constructed in the following manner: tie lines to the left of the pivot line have a common focal point at the intersection of the zero-LPG axis and the pivot line; tie lines to the right of the pivot line have a common focal point at the intersection of the pivot line and the line tangent to the binodal curve at the plait point.

(4) The tangent to the plait point passes through 0.1 LPG on the zero-solvent axis.

If oil of composition, 0.2 LPG and 0.8 Heavies, is displaced by solvent in a one-dimensional slim tube in which there is no dispersion, the composition path can be calculated using the method of characteristics (Helfferich 1981). It is shown in Fig. 2.5.1 as the dashed line from 0.2 LPG to the binodal curve, and then as a line coincident with the dew point arm of the binodal curve to the zero LPG axis, and thence to the solvent apex.

Figs. 2.5.2 and 2.5.3 show the results for the same displacement process calculated by an explicit finite difference simulator. The simulator has been described previously (Orr 1980). It assumes no volume change on mixing. Fig. 2.5.2 shows the composition paths for grid blocks number 20, 100 and 200, calculated up to 1.2 PV (based on 200 grid blocks total). Fig. 2.5.3 shows the liquid saturation and mixture composition profiles at 0.4 PV. Also shown is the liquid saturation profile at 1.2 PV.

In its original form the simulator neglected both physical dispersion and the pressure drop across the displacement length. Thus, there is no length scale set in the simulator. Fig. 2.5.2 can therefore be taken to represent either composition paths at locations corresponding to 10%, 50% and 100% of the tube length, or the composition path at the end of the tube, where the tube length has been represented by either 20, 100, or 200 grid blocks.

When considered in the first way, the figure illustrates the effect of length on the vaporizing gas drive enrichment process (though since there is no length scale in the equations, the length corresponding to a single grid block could be in the order of mm or inches). When considered in the second way, the figure might illustrate the improved recovery of heavy hydrocarbons associated with either an increased number of equilibrium mass transfer stages, or a lower level of dispersion. In either case a length scale has been introduced into the problem.

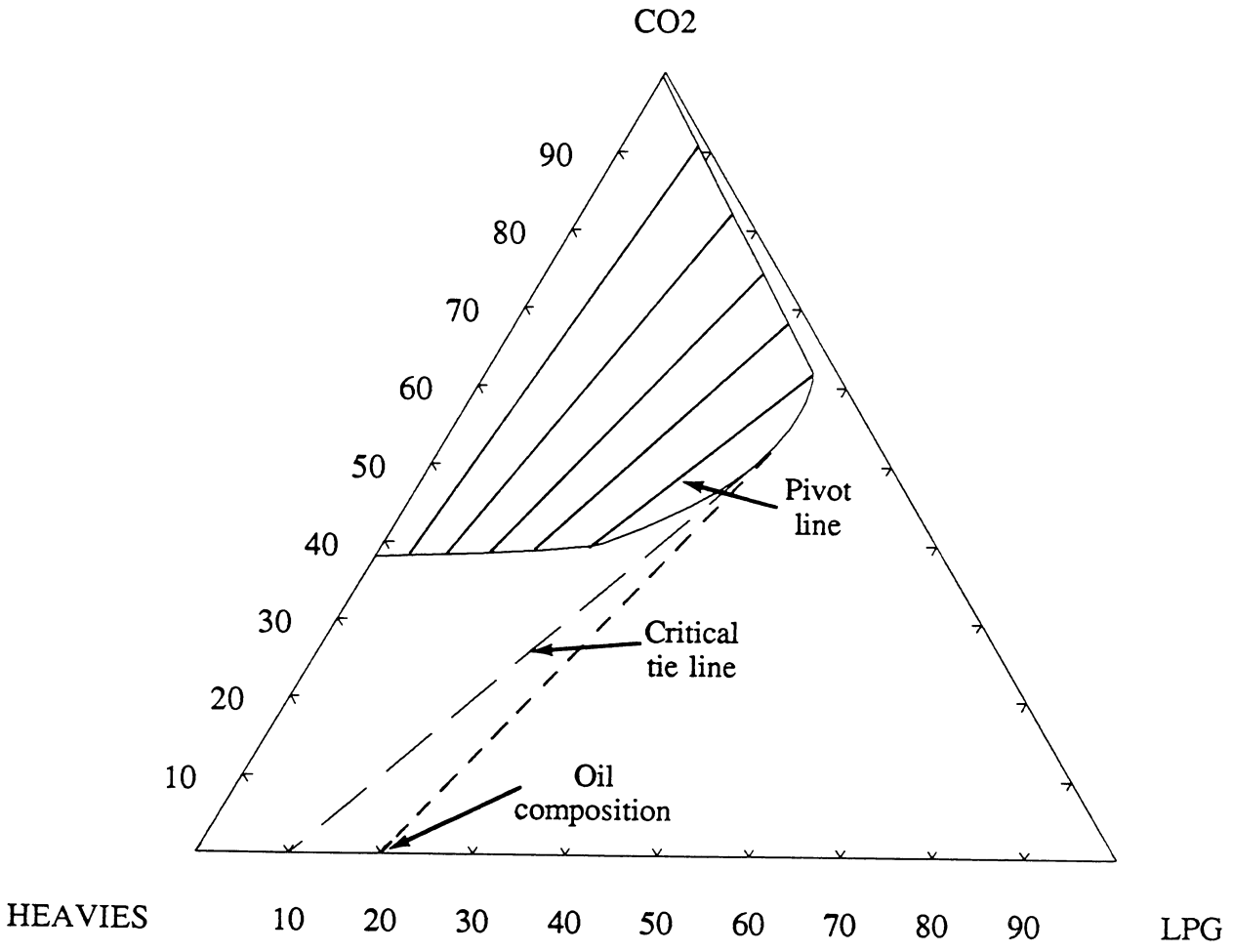

Fig. 2.5.1. Typical phase diagram used in composition path calculations.

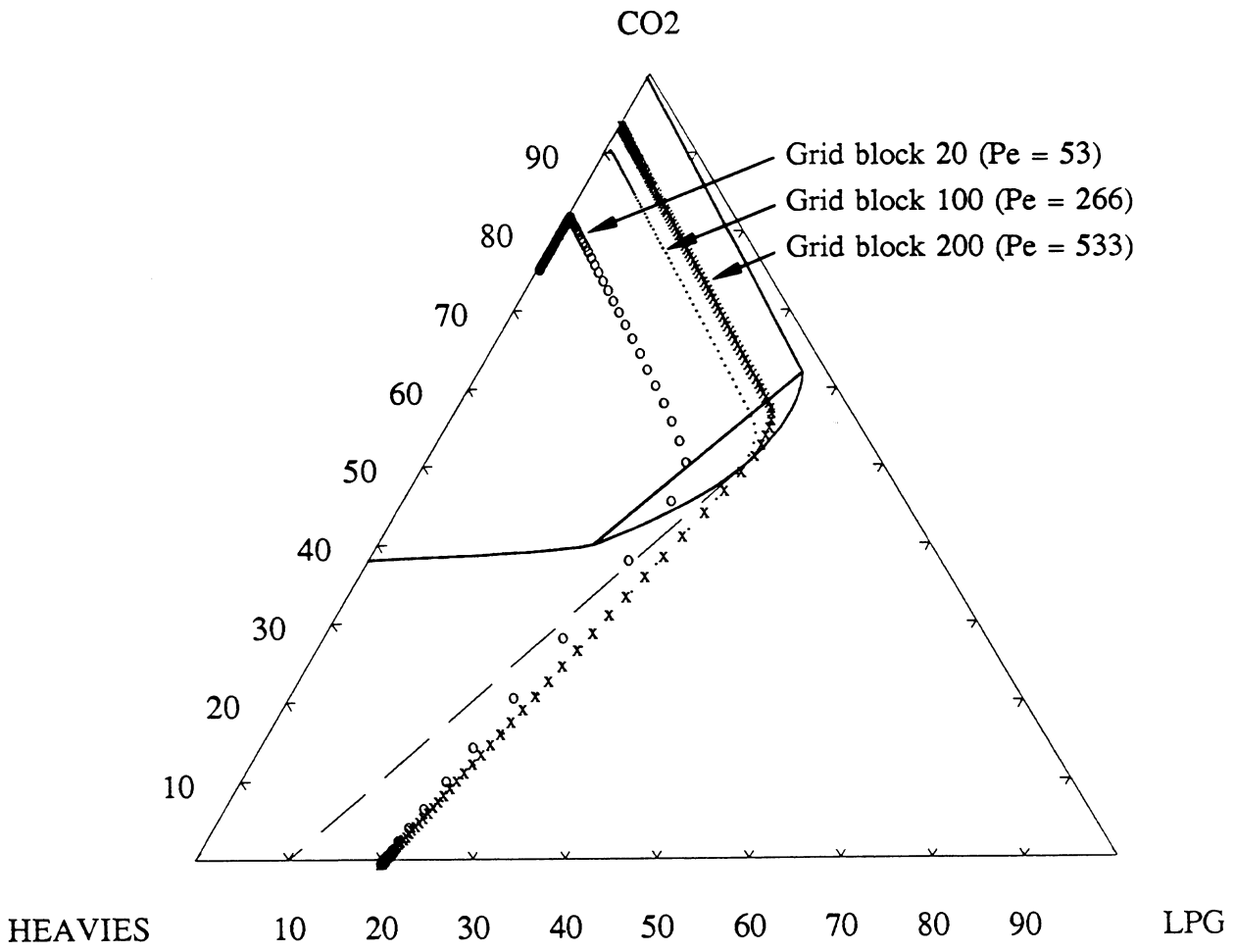

Fig. 2.5.2. Composition path calculated for varying levels of numerical dispersion.

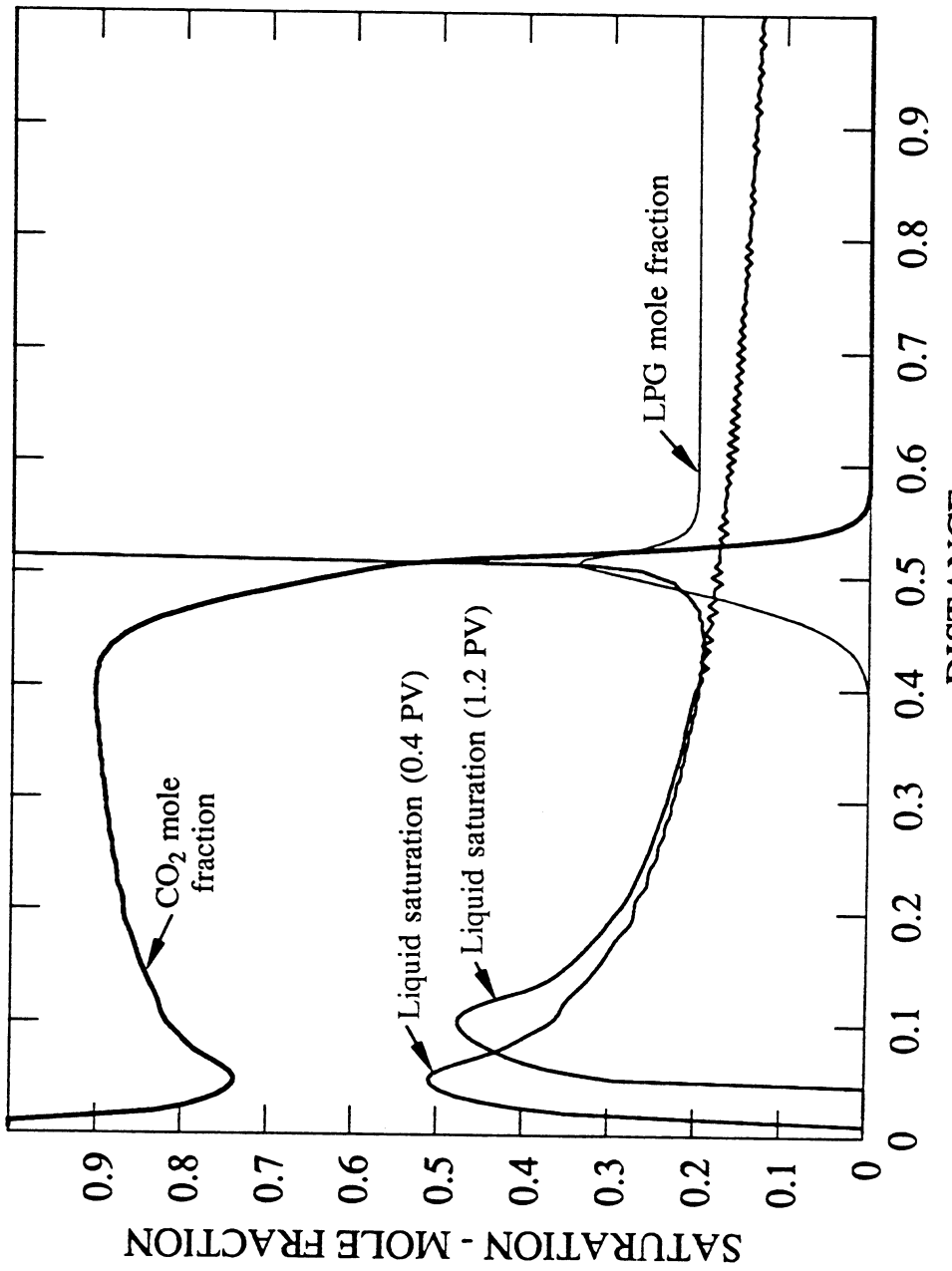

Fig. 2.5.3. Saturation and composition profiles at 0.4 PV injected for the phase diagram shown in Fig. 2.5.2.

As implied in the previous paragraph the composition paths shown in Fig. 2.5.2 are indicators of the ultimate recovery of heavies by the vaporizing gas drive process. "Higher" composition paths indicate higher recoveries.

Fig. 2.5.4 presents recovery curves for identical displacement processes, but with the tube length divided into 50, 200, and 1000 grid blocks. If numerical dispersion is equivalent to physical dispersion, these correspond to single phase Peclet numbers of 133, 533, and 2666. Clearly, recovery improves as the level of numerical dispersion decreases, as several investigators have pointed out.

Fig. 2.5.2 illustrates an interesting effect in the entrance length of the tube (i.e., the 20 grid block path). For this grid block, after all the LPG has been removed, the composition of heavies increases from 0.18 to about 0.25, and then gradually decreases by successive extraction with solvent. Fig. 2.5.3 shows this as a bank of heavies being gradually displaced through the tube. (Note how little this bank has moved between the two times.) The high liquid saturations in the entrance length of the tube are a consequence of the phase behavior of mixtures of the un-enriched solvent and original oil.

2.5.1 Representation of Physical Dispersion by Numerical Dispersion

It was assumed in the preceding section, and it is generally assumed, that numerical dispersion or truncation error can be used to represent actual physical dispersion using the relationships derived by Lantz (1971) for single phase flow

$$(N_{Pe})^{-1} = \frac{1}{2}(\Delta x_D - \Delta t_D) \tag{2.5.1}$$

In a recent paper Ypma (1985) reported on a comparison between simulations of nitrogen displacement of a light oil, using truncation error to represent dispersion in the first set of runs, and then including a finite difference representation of dispersion in the simulator and repeating the runs with very low levels of numerical dispersion. He observed that when actual physical dispersion was included, the simulator predicted higher recoveries.

Fig. 2.5.5 is taken from Ypma's paper. It indicates differences in calculated recoveries of about 5% at a dispersion number of 0.01. (Ypma uses "dispersion number, D_{num}" instead of inverse Peclet number.) That value would correspond to 40 grid blocks and $\Delta x_D/\Delta t_D = 0.2$, if based on numerical dispersion only. Fig. 2.5.6 recasts our results from Fig. 2.5.4 and from other simulations in the form used by Ypma, and also presents results of simulations in which physical dispersion was included in the model. We observe minor (of the order of 1%) differences between the two cases, but these differences do not widen as dispersion number increases, as Ypma had observed.

We then constructed a phase diagram that was similar in its general features to the one used by Ypma (Fig. 2.5.7) and repeated the comparison at total dispersion numbers of 0.0023 and 0.023. Recoveries obtained were higher than those reported by Ypma, but once again we obtained differences of only 1-1.5% between the cases at both levels of dispersion. It is our view therefore that the inclusion of explicit physical dispersion terms in the finite difference simulator does not add substantially to the accuracy of the solution.

2.5.2 Effect of Phase Diagrams on Composition Paths

We observed when describing the features of Fig. 2.5.2 that the location of the composition path is an indicator of the degree of dispersion that is being simulated. Figs. 2.5.8 and 2.5.9 show the extent to which composition paths are modified by either the composition of the oil being displaced, or the size of the two phase region. Fig. 2.5.10 shows the composition paths observed with an unusually shaped phase diagram. In this case the trend towards the dew point curve that is normally observed with decreasing levels of dispersion (increasing n), is extremely slow. Note that the composition paths here are for 100, 500 and 1000 grid blocks, instead of the 20, 100, 200 used previously.

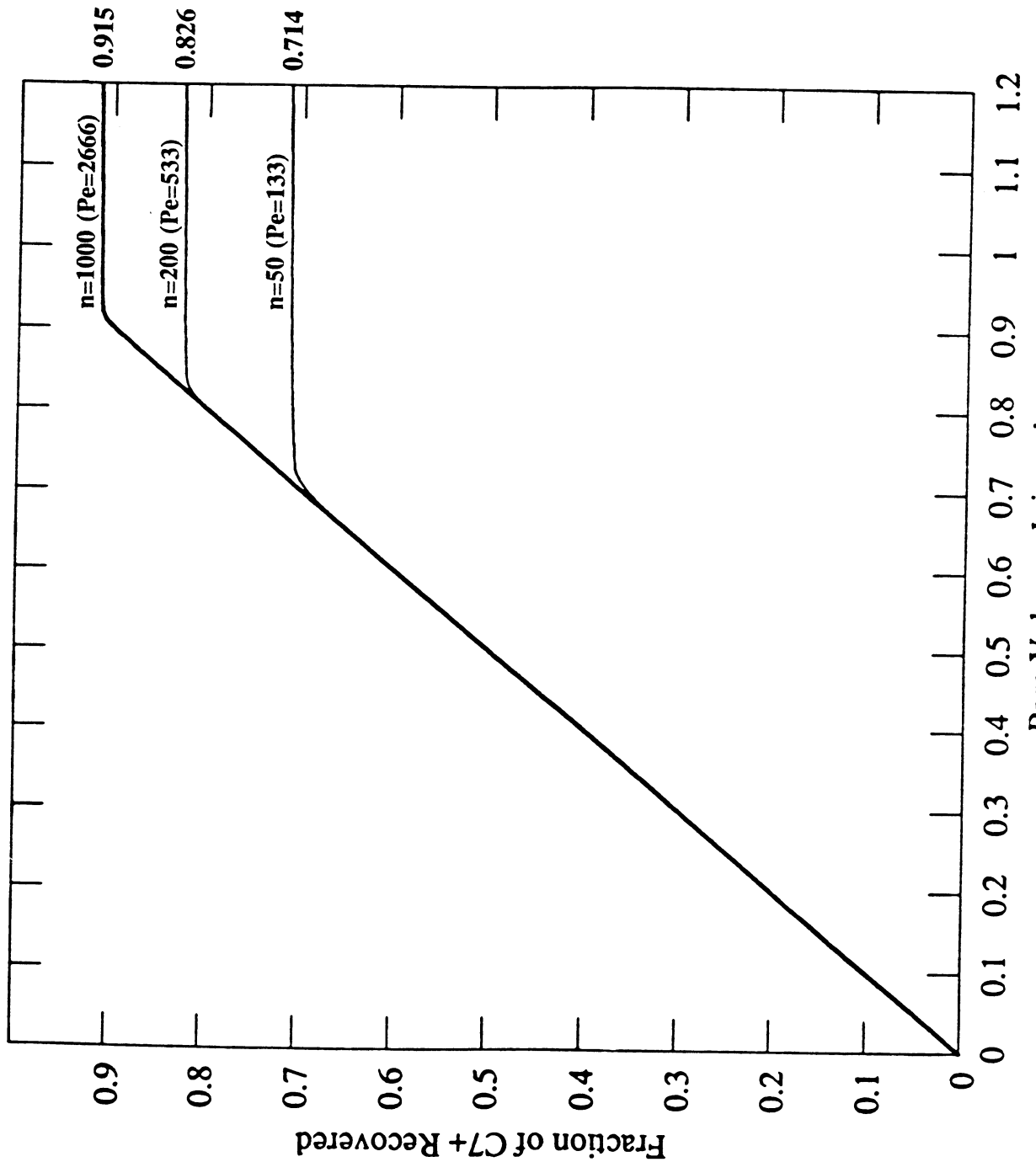

Fig. 2.5.4. Recovery of heavy hydrocarbons in displacements with varying levels of numerical dispersion.

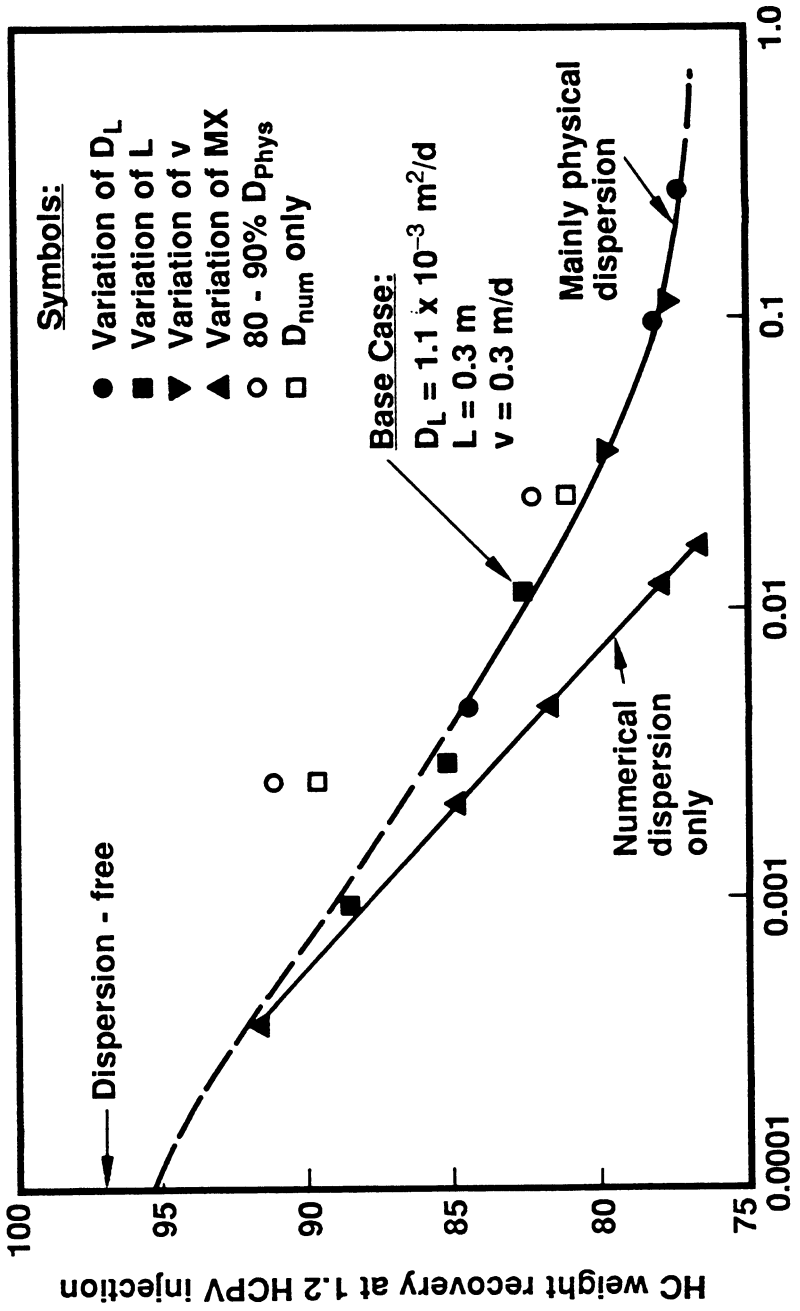

Fig. 2.5.5. Dependence of recovery on longitudinal dispersion level (after Ypma 1985).

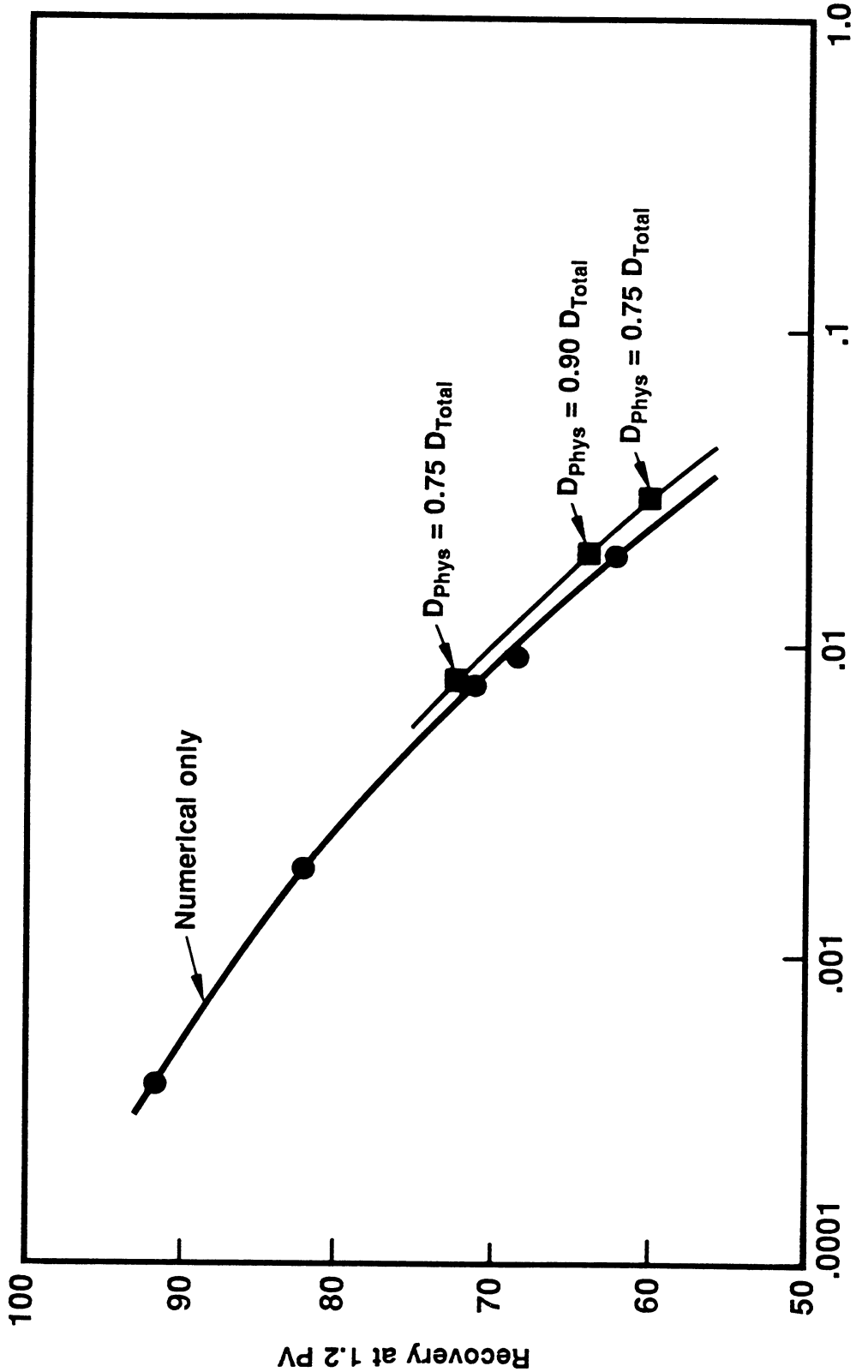

Fig. 2.5.6. Comparison of the effects on recovery of numerical dispersion with that of a finite difference representation of the dispersion term.

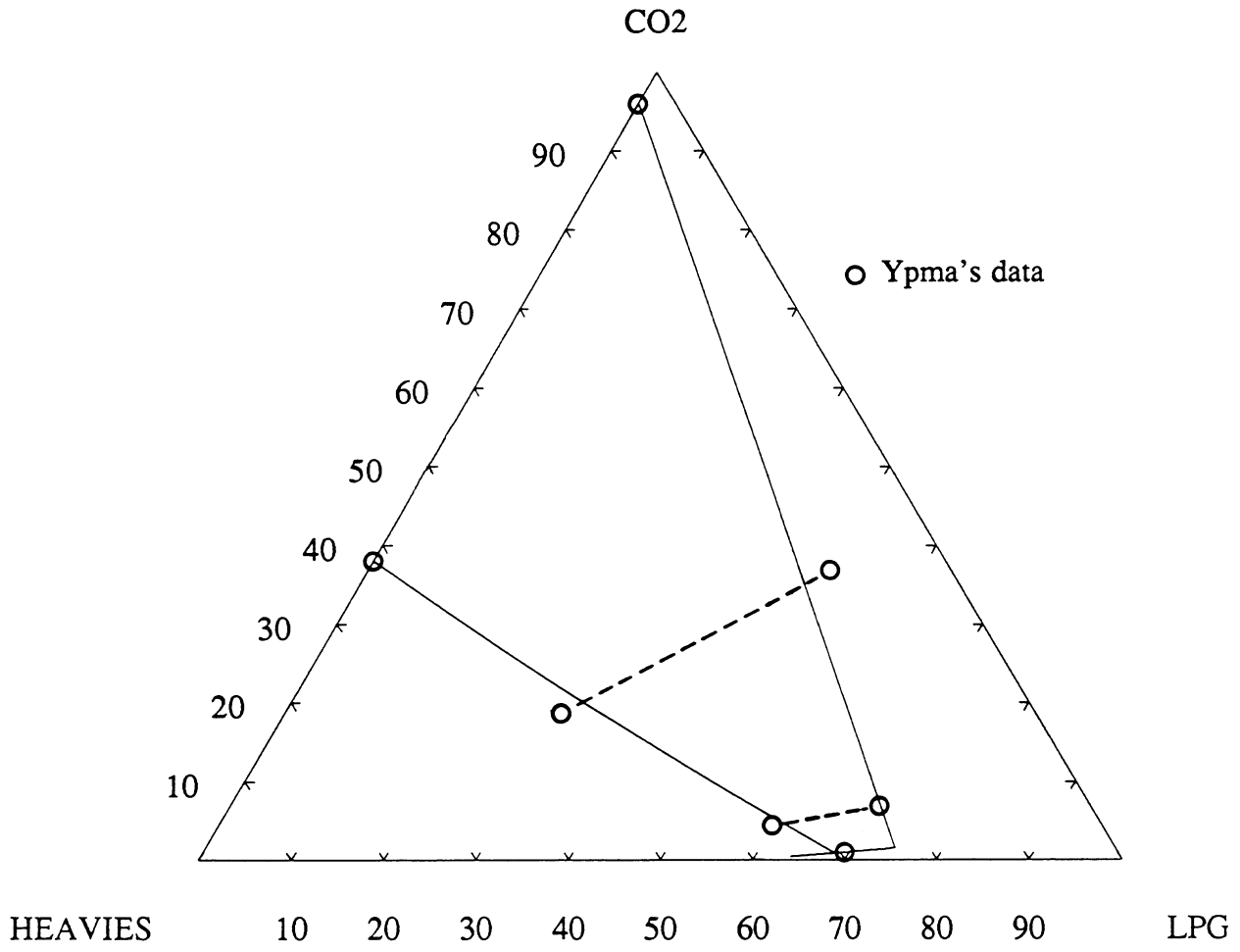

Fig. 2.5.7. Phase diagram based on Ypma's data (1985).

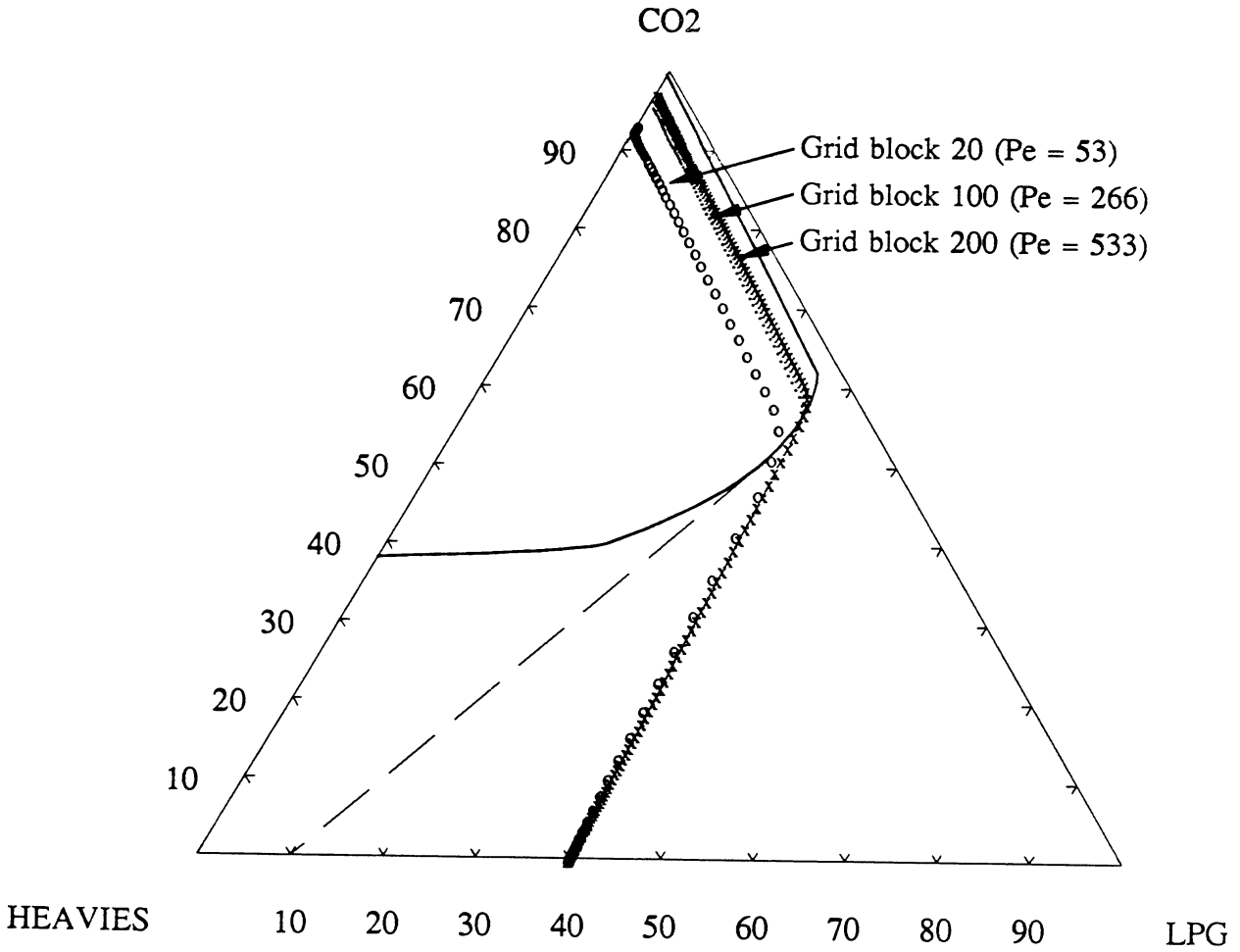

Fig. 2.5.8. Composition paths for a CO_2 - hydrocarbon system with a large two-phase region and varying levels of numerical dispersion.

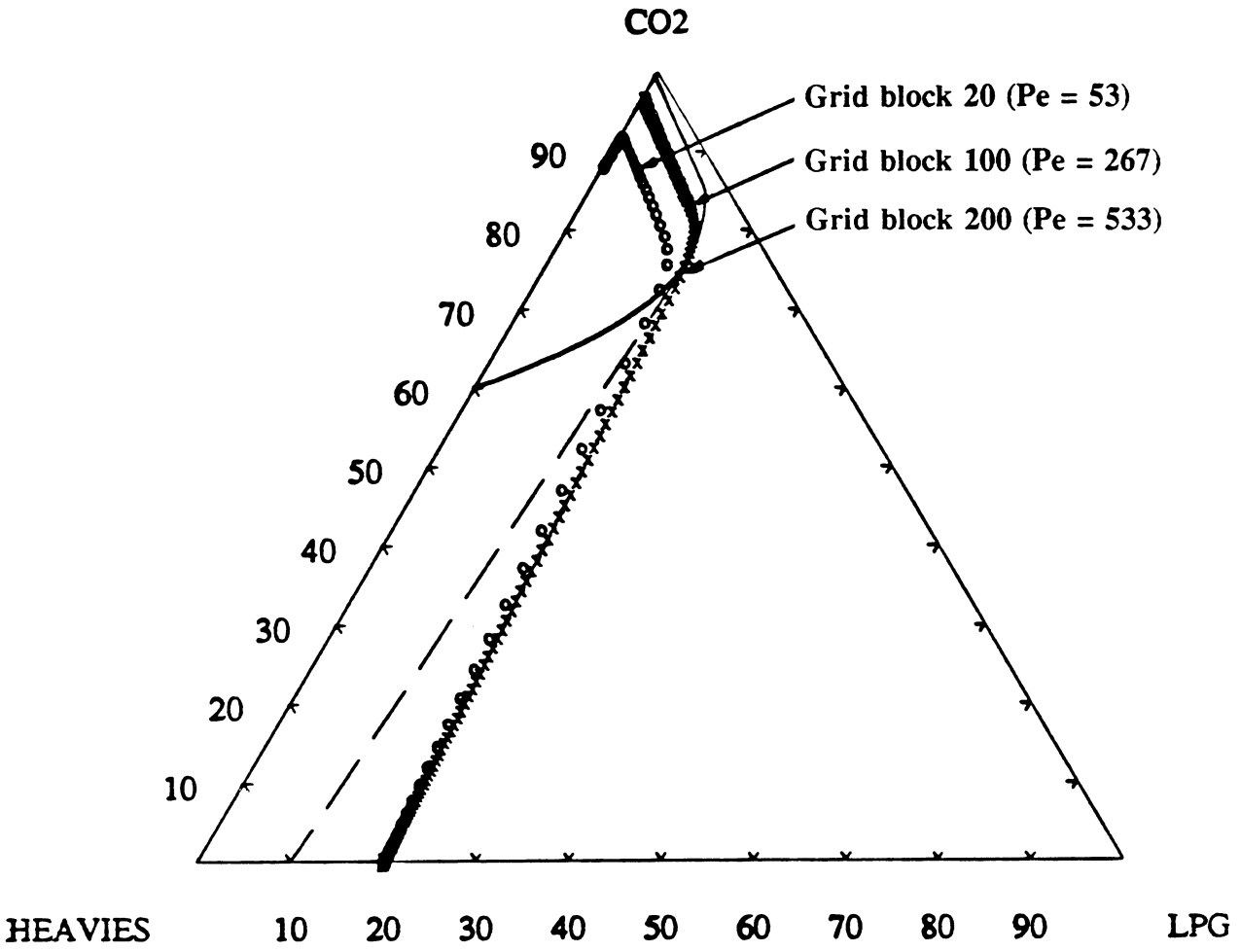

Fig. 2.5.9. Composition paths for a CO_2 - hydrocarbon system with a small two-phase region and varying levels of numerical dispersion.

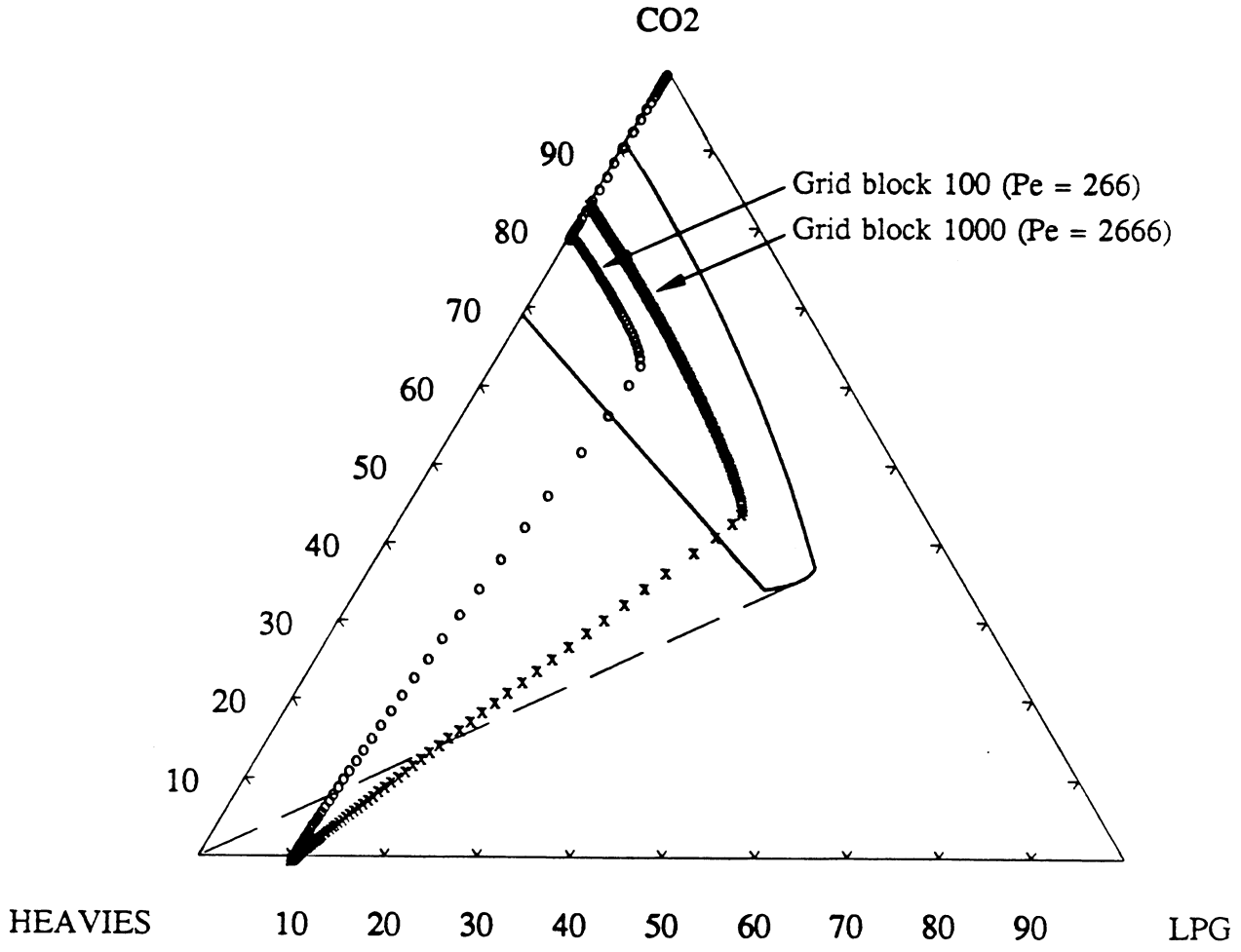

Fig. 2.5.10. Composition paths calculated for varying levels of dispersion for a phase diagram like that of Tirrawarra (Jap 1985).

The phase diagram shown in Fig. 2.5.10 is similar to that of a light crude oil from an Australian oil field, "Tirrawarra" in South Australia. Note that the oil composition is to the right of the critical tie line, so the method of characteristics would indicate a composition path tangent to the binodal curve near the plait point and then along the dew point line. The unusual composition paths observed prompted us to ask again whether we are adequately representing physical dispersion by truncation error in a case like this. When the runs were repeated with a finite difference representation for physical dispersion and much lower truncation errors, we got essentially identical paths for corresponding values of dispersion number. And Fig. 2.5.11 shows in a more familiar way the comparison between effective dispersion levels as reflected in the relative shapes and heights of the LPG slug when the simulator uses 200 grid blocks (D_{num} = .002) and 1000 grid blocks (D_{num} = .0004). That is, in this case, even though larger numbers of grid blocks do not cause the composition path to move close to the dew point curve, they still can be taken as a measure of the level of dispersion.

2.5.3 Geometrical Interpretation

In order to explain the observed effects we first recast the phase diagram (which is normally expressed in mole fractions) into volume fractions. We note that since we have already made the assumption of zero volume change on mixing, straight lines on the mole fraction diagram will map to straight lines on the volume fraction diagram, though parallelism will not necessarily be maintained.

The explicit finite difference simulator solves the following balance equation for component i in cell number k

$$C_{i,k}^{n+1} = C_{i,k}^{n} + \frac{\Delta t_D}{\Delta x_D}[F_{i,k-1}^{n} - F_{i,k}^{n}] \tag{2.5.2}$$

In what follows, we drop the subscript i to simplify the notation. Eq. 2.5.1 can be rewritten then as

$$C_k^{n+1} + \alpha F_k^n = C_k^n + \alpha F_{k-1}^n \tag{2.5.3}$$

where C_k^n is the volume fraction of component i in the kth grid block at time n, F_k^n is the volume fraction of component i in the flowing stream leaving the kth grid block at time n, $\alpha = \Delta t_D/\Delta x_D$ where Δt_D is expressed in pore volumes and Δx_D is the dimensionless grid block length.

Eq. 2.5.3 shows how C_k^{n+1} is determined by the compositions in the current grid block and in the upstream grid block at the previous time level. The equation can be represented geometrically when expressed in its second form. Fig. 2.5.12 illustrates the geometrical solution of the equation for the three possible cases that would be encountered along a composition path.

Case 1. The composition C_k is already in the 2-phase region. F_k is on the tie line since the flowing stream composition is a mixture of the two phases that are in equilibrium with C_k. F_{k-1} is on the tie line that contains C_{k-1}. M is determined by C_k and F_{k-1} by the lever rule. From the geometry, the trajectory C_k^n to C_k^{n+1} is parallel to the line joining F_k and F_{k-1}.

Case 2. C_{k-1} is in the two phase region, but C_k is still single phase. M is on the line joining F_{k-1} and C_k. Since C_k and F_k are coincident, C_k^{n+1} must be on the same line.

Case 3. Both C_{k-1} and C_k are single phase. The same construction applies as in Case 2.

Thus the composition path will follow a straight line from the initial oil composition to the two-phase region. Once in the two-phase region it will follow a path parallel to lines joining the flowing stream compositions leaving the previous and the current grid block. Since in most EOR processes the solvent-rich phase has gas-like viscosities, the flowing stream compositions quickly approach the dew point curve, and hence the composition paths are parallel to the dewpoint curve.

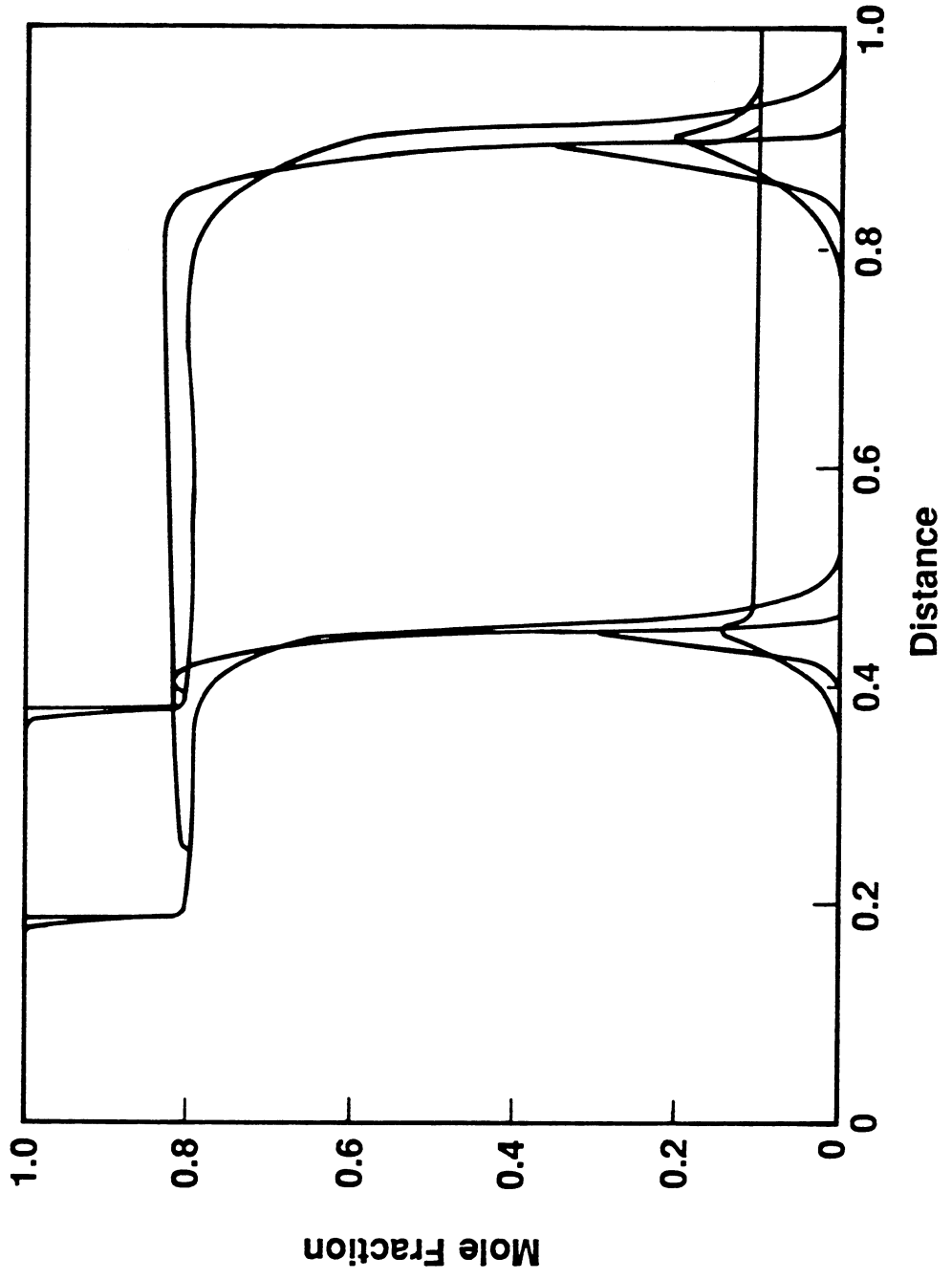

Fig. 2.5.11. Effect of numerical dispersion on composition profiles for the phase diagram shown in Fig. 2.5.10

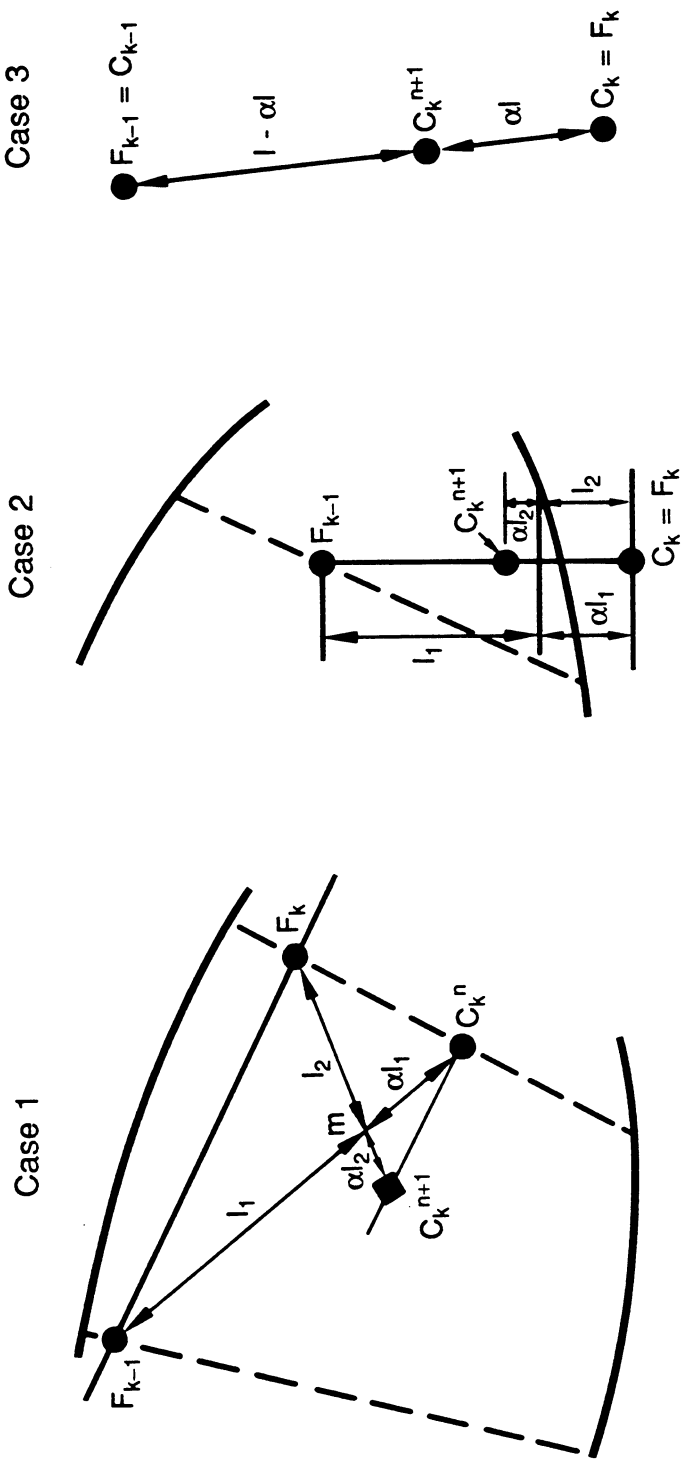

Fig. 2.5.12. Geometry of composition paths.

Also successive grid blocks enter the two-phase region to the right of the previous block, so long as the tie line at the point of entry has a lower slope than the entry path. That behavior is illustrated in Fig. 2.5.13. Suppose that the flowing stream composition of the (k-1)th grid block is as shown in Fig. 2.5.13a. The labels are for the n-2, n-1, and nth time step. (Note that in the case of an explicit finite difference simulator it is possible to solve the composition paths for all times for each grid block in turn, even though it is conventional to solve for all grid blocks at each time, and then to increment the time. It is this property that is the basis for the comment on the duality of interpretation of Fig. 2.5.2 made previously.) C_k^{n-2} is on the line joining F_{k-1}^{n-2} to the oil composition.

Fig. 2.5.13b illustrates the construction of the C_k path at successive times for $\Delta t_D/\Delta x_D$= 0.25. The composition does not enter the two-phase region until the nth time step. Here it is almost all liquid so we would expect a relatively small fractional flow of vapor, and hence F_k^n will have a value close to the izuid portion of the binodal curve. The trajectory C_k^n to C_k^{n+1} is parallel to the line joining F_{k-1}^n and F_k^n. Because *Fsubk*^{n} is the sum of the phase compositions weighted by the fractional flow, and because the fractional flow of the low viscosity vapor is relatively high, F_k^n will lie to the right of the C_k composition path for the tie line slopes shown, so the (k+1)th path will enter the two-phase diagram to the right of the kth path.

As implied in Fig. 2.5.13b, the starting points for the two phase trajectories will be determined by the fractional flow curve for the system and by the (random) entry saturation for each grid block. We would expect, and we observe, that within a few time steps after entry into the two-phase region, the final straight line composition path is established at about the same initial liquid saturation for all grid blocks.

Figs. 2.5.14 and 2.5.15 demonstrate the consequences of these geometrical rules for two arbitrary phase diagrams. Fig. 2.5.14 is similar to Fig. 2.5.2 and others we have used. The composition paths move to the right as the number of grid blocks is increased; they are approximately parallel to the dew point line; and successive paths are higher than previous ones. This is because, though each path is established on entry at a liquid saturation of about 40%, the shape of the binodal curve and the fact that the paths are parallel to the dew point line, causes relative liquid volumes to decrease with time.

Fig. 2.5.15 is similar to Fig. 2.5.10, but we have made it more extreme by making the dew point and bubble point curves parallel. Once again the paths in the two phase region are parallel to the dew point line; successive paths enter to the right of previous paths; all paths establish about the same liquid saturation on entry; in this case however the parallelism of the dew point and bubble point lines causes the paths to be essentially colinear. Whether that behavior is a consequence of numerical effects or simply reflects composition paths that would be obtained by the method of characteristics in the absence of dispersion requires further investigation.

Conclusions

Geometrical interpretation of calculated composition paths leads to the following conclusions:

(1) Successive composition paths enter the two phase region richer in LPG by virtue of the difference in slopes between the tie lines and the entry path.

(2) Within a few time steps, the final straight line composition path is established at a liquid saturation determined by the fractional flow curves for the system.

(3) The composition paths are then all approximately parallel to the dew point curve.

(4) We observe an upward trend with increasing numbers of grid blocks (and hence increased recovery) when we have a "conventional" phase diagram, i.e., when the bubble point and dew point curves converge uniformly towards the plait point.

(5) When the bubble point and dew point curves are parallel, or nearly parallel, recovery increases very slowly with increased numbers of grid blocks. Displacement performance for systems exhibiting such phase diagrams will be sensitive to the level of dispersion.

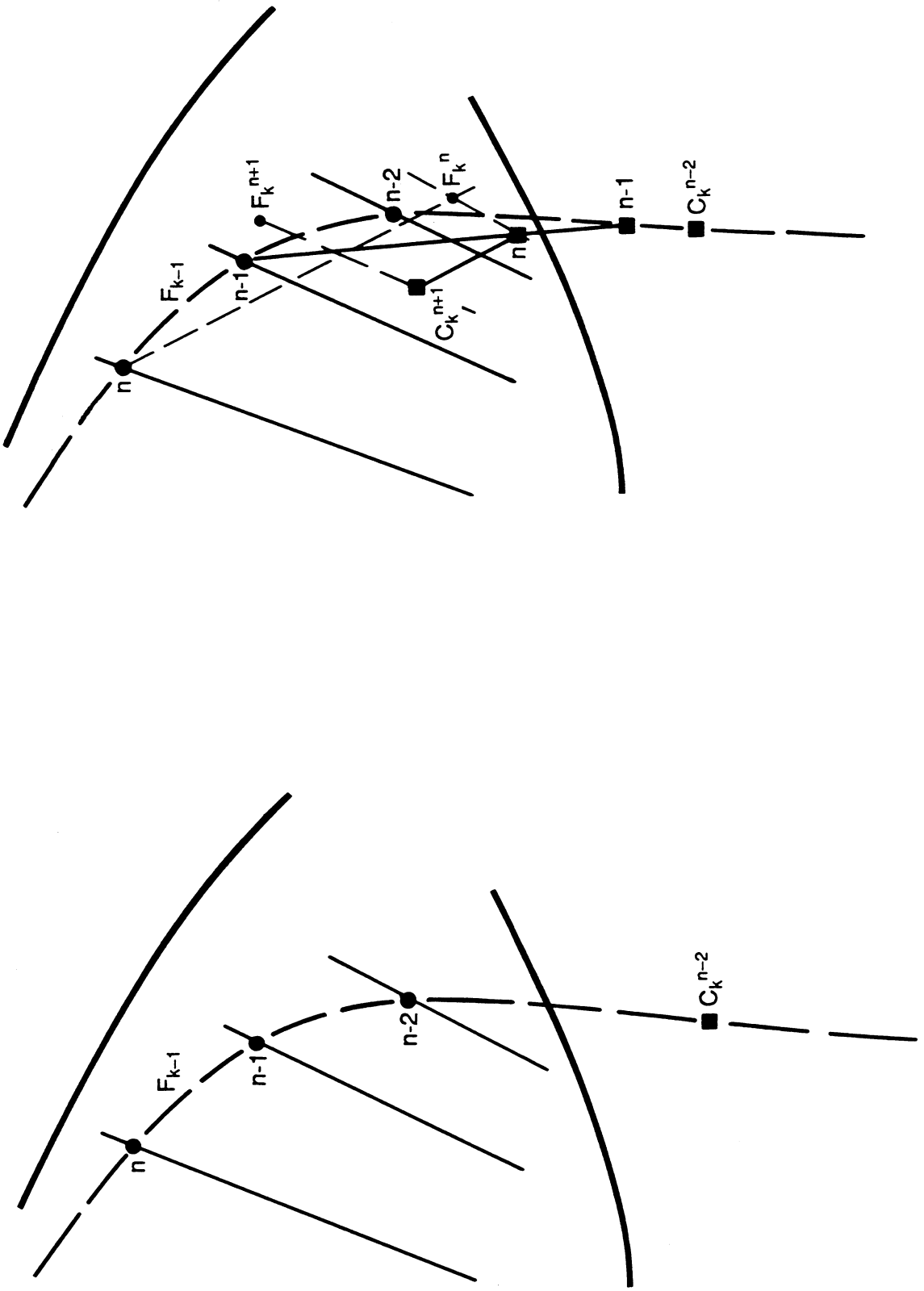

Fig. 2.5.13. Evaluation of composition paths in successive time steps.

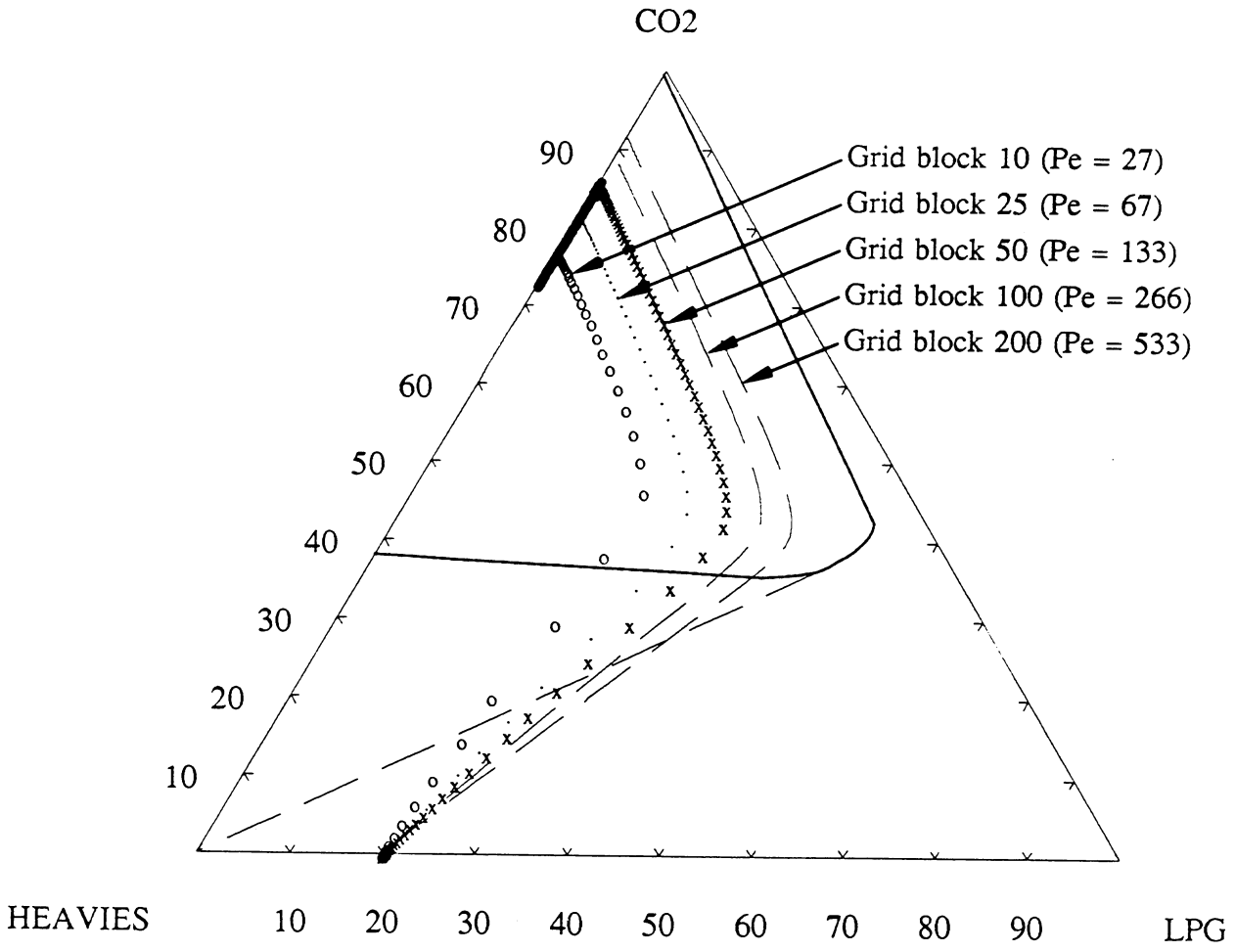

Fig. 2.5.14. Composition paths calculated for varying levels of numerical dispersion.

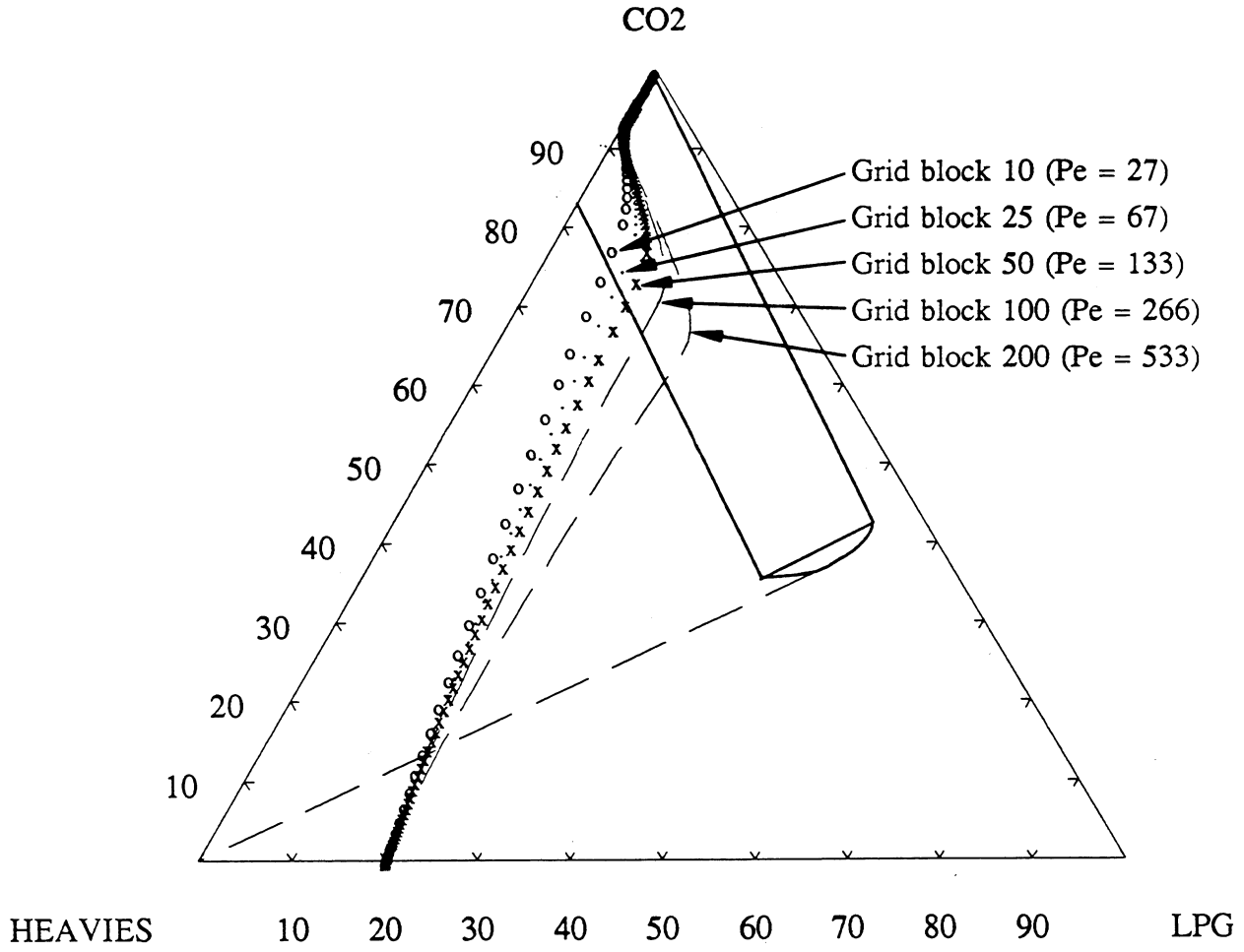

Fig. 2.5.15. Composition paths for varying levels of numerical dispersion for a binodal curve with parallel sides.

2.6 Summary

The results presented in this chapter delineate further the role of component partitioning as it influences displacement performance. Analysis of a model four-component system by the method of characteristics indicates why the addition of dissolved methane to a dead oil has small effect on measured minimum miscibility pressures, despite the fact that the displacement of the resulting mixture is no longer strictly "miscible" because the composition path of the displacement passes through the two-phase region. That analysis resolves a long-standing inconsistency between experimental observations and analysis of composition paths based on ternary representations of phase behavior.

Application of the mathematical approach used in the analysis of four-component systems is underway for two additional problems, flow of ternary mixtures with temperature variation, and flow of ternary mixtures in a two-layer system with viscous crossflow. When completed, both analyses will represent significant extensions of current theory for multiphase, multicomponent flow in one dimension. The first problem is a model for the design of improved thermal recovery processes, and the second is a prototype for study of the combined effects of phase behavior and crossflow during nonuniform flow caused by heterogeneity or viscous instability or both. We consider the interaction of viscous instability with unstable flow, but without the effects of phase behavior, in Chapter 3.

Finally, the impact of dispersive mixing on composition paths in ternary systems was described. Direct computations show that sensitivity of composition paths to dispersion is dependent on the size and shape of the two-phase region. That result suggests that careful control of numerical dispersion may be required for some systems, especially those involving displacement by N_2, if accurate composition path information is to be obtained.

3. Viscous Instability and Reservoir Heterogeneity

Miscible displacement processes, such as CO_2 flooding, rely on coupled phase behavior and flow to generate compositions that avoid the two-phase region. Because there are no capillary forces, which are usually responsible for oil entrapment, a miscible displacement can be potentially one hundred percent efficient. In practice, however, this high recovery potential is usually not realized because hydrodynamic instability leads to macroscopic fingering of the displacing fluid, resulting in a nonuniform displacement. This unfavorable behavior is further magnified by the heterogeneity of the porous media. The physical processes involved in this interaction are not fully understood. Consequently, currently available commercial reservoir simulators are unable to predict accurately the performance of miscible displacements.

Most miscible displacement processes are influenced to some extent by the frontal fingering phenomenon, caused by the usually unfavorable ratio of mobilities of the in-place oil and the displacing solvent. In addition, all oil reservoirs are heterogeneous on some length scale. Therefore if process simulation are to be accurate, some description of unstable flow in heterogeneous porous media must be included in the formulation of a reservoir simulator. Before this can be achieved, a better understanding of the length scales associated with the fingering phenomenon and the porous media heterogeneities will be required. These length scales control the extent of the mass transfer between the unswept oil and the displacing fluid. Mixing, in turn, is important because it influences the phase behavior of the CO_2-hydrocarbon mixtures, which controls microscopic displacement efficiency. If, for example, fingers that grow in field-scale flows are large and widely spaced, then compositional effects of mixing between oil and CO_2 will be confined to a small portion of the reservoir and hence will have minimal impact on displacement performance. For such cases, simulators need only represent the gross movements of fluids in the reservoir. If, on the other hand, fingers are small and closely spaced, mixing will be important and representations of the phase behavior of CO_2-hydrocarbon mixtures will have to be included in the simulations. Thus, resolution of these questions of scale is needed for design of improved reservoir simulation tools.

In this chapter, only fingers driven by viscous instabilities will be examined. The main purpose here is to quantify the transverse length scale, or wavelength, of viscous fingers that form in unstable displacements in heterogeneous porous media. In homogeneous porous media, the most unstable finger wavelength at initiation is controlled by dispersion. In subsequent growth, viscous forces cause spreading at the tip of the finger and pinching at the tail. Finger widths must be controlled by a competition between dispersion, which causes growth of a transition zone in viscosity that reduces the driving force for instability, and subsequent splitting of fingers at the tip. If the permeability distribution has large variance and exhibits correlation over a significant fraction of the flow length, then finger widths are likely to be determined by the spatial correlation in the permeability field. If the permeability field has large variance but is correlated only at small scale, permeability variations in the inlet region probably initiate fingers, but it is not clear how the permeability variation affects subsequent growth. Thus, the objective of the computations to be performed is to establish whether permeability variation dominates finger formation and growth and if so, what correlation length is required for a given permeability variance. In this chapter, results of calculations of the growth of fingers in both uniform and heterogeneous permeability fields are presented. Also, we describe the design and preliminary results of flow visualization experiments aimed at testing the accuracy of the calculations.

3.1 Numerical Simulation of the Growth of Viscous Fingers in Heterogeneous Porous Media

Udo Araktingi

Much of the theory of viscous instability has been based on the analysis of the onset of instability (Gardner and Ypma, 1984, Heller, 1966, Perrine, 1963, Peters *et al.*, 1984, Lee *et al.*, 1984, Tan and Homsy, 1986, Schowalter, 1965) in an attempt to predict growth rates and critical wavelengths. The essential steps involved in all of these studies may be summarized as follows. First, an unperturbed mathematical model is specified. Next, perturbations are introduced into the dependent variables of the mathematical model. The resulting equations are subtracted from the unperturbed model to derive the hydrodynamic equations for the perturbations. Then the perturbation equations are usually solved by decomposing the initial perturbations into separate Fourier components. This ensures that the stability analysis can proceed without concern about the exact nature of the initial perturbation because the theory of Fourier transforms ensures the perturbations can be synthesized from their Fourier components. Finally, the stability conclusions are drawn from the behavior of the solutions. If the perturbations grow with time, then the displacement is judged to be unstable and subject to fingering. If the perturbations diminish with time, then the displacement is judged to be stable and will be free of fingering. The resulting linear stability theory can be used to determine the conditions for the onset of instability, but cannot be used to predict the long term behavior of the unstable displacement.

An alternate approach, the use of conventional finite difference techniques (Peacemen and Rachford, 1962, Christie and Bond, 1986, Christie, 1987, Giordano *et al.*, 1985) was first undertaken using a large number of grid blocks to solve the convection-dispersion equation. However, the resulting poor resolution masked any potential viscous fingers, and the use of a permeability fluctuation was required to initiate the instabilities. Resulting effluent curves were found to be dependent on the permeability distribution used. Consequently, with the advent of faster computers and the development of more accurate numerical techniques, fine grid simulation of the growth of viscous fingers has been used. However, the match between computed and published experimental results has not been entirely satisfactory. On another level, empirical models (Koval, 1963, Todd and Longstaff, 1972, Dougherty, 1963, Fayers, 1984, Fayers and Newly, 1987, Odeh, 1987) have been suggested to give a basis for computation of miscible displacement. These models suffer from the fact that the principal parameters involved have little or no direct physical significance. These parameters can be fitted to simple one-dimensional laboratory experiments, for example, but translation of the same parameter values to a three-dimensional reservoir is uncertain at best.

Recently a novel computational approach (Hatziavramidis, 1987, Tan and Homsy, 1987), based on the method of weighted residuals, has been proposed. This method is still in the process of being validated through experimental data matching. Chebyshev polynomials and Fourier functions have both been used for the transform functions. The advantages of this method are improved accuracy and computational speed. Because the equations are solved exactly, numerical error at the grid points is eliminated. The use of fast Fourier transform (FFT) techniques allows for much finer grids resulting in better finger resolution while still remaining faster than finite difference schemes. There are also several drawbacks. First, periodic boundary conditions are required in order to avoid any Gibbs phenomenon in the solutions. Such behavior was exhibited in the one-dimensional results obtained using Chebyshev polynomials. The method is also awkward for long time simulations because of the need to extend the current domain. Since the use of FFT requires 2^N calculations where N is the number of grid points, this could result in a severe computational burden.

Another promising approach (Meiburg and Homsy, 1987, Tryggvason and Aref, 1983), currently only being applied to immiscible displacements in Hele Shaw cells is the vortex method. The vorticity field is discretized with the corresponding velocity field being constructed by using the Biot-Savart law. Since the flow is everywhere irrotational except at the interface between the

two phases, only the vortex sheet at the interface needs to be discretized. This allows for a highly accurate numerical technique. In the miscible case, the area to be discretized will now consist of part, or the whole mixing zone. Efforts to apply this method to unstable miscible displacements and determine its effectiveness are currently being undertaken by the same researchers.

Finally, a probabilistic approach (King and Scher, 1986, DeGregoria, 1985, King and Scher, 1985) based upon random-walk simulations of the solution of Laplace's equation has been investigated. In the limit of infinite mobility ratio, the method produces solutions to the problem of diffusion-limited aggregation (DLA). This method uses a finite difference solution of the material balance equations. Tracer particles carrying a concentration equivalent to one grid block are added to the domain at a rate of one per time step. To determine where this particle should go, a streamline and an injected fluid concentration are chosen randomly. The intersection of those two contours gives the location at which a tracer particle is added. When a streamline intersects a saturation contour at more than one place, the one with the highest flow velocity is chosen. Fingers are generated because low viscosity fluid replaces high viscosity fluid, streamlines become more closely spaced, increasing the probability that a streamline in that neighborhood will be selected in subsequent time steps. However, these models produce lower recoveries than observed in laboratory experiments due to the absence of any transverse dispersion (Orr and Sageev, 1986).

To investigate further the combined effects of instability and permeability variations, a new model was formulated. This scheme uses a finite difference solution of the material balance equations to determine the pressure field, given the distribution of permeability and the current distribution of fluid viscosities. Tracer particles that carry a finite concentration of injected fluid are then moved with velocities based on the pressure field. Effects of transverse and longitudinal dispersion are included by perturbing the position of the particles after the convection step by amounts selected from a normal distribution with a mean of zero and a variance that sets the relevant dispersion coefficient. In effect, we assume that local velocity variations at scales smaller than a grid block can be represented adequately by dispersion. Once the locations of all the tracer particles are determined, local viscosities can be evaluated and the process repeated for the next time step. This scheme has the advantage that it controls the effects of numerical dispersion, but it requires that many particles be tracked. In the next section, this computational scheme will be discussed in more detail. Also, it will be validated using analytical results and recoveries from displacement runs at different mobility ratios will be compared to experimental results. Next, a brief description of a method to generate heterogeneous permeability fields will be given. These permeability distributions will be used in the random-walk model to study the interaction between the viscous fingers and the porous media. Finally, an attempt to include dispersion into the original probabilistic model, formulated previously (Orr and Sageev, 1986), will be made.

3.1.1 Formulation of the Random-Walk Model

The assumptions made in developing this model were:

(1) First contact miscible, incompressible fluids with equal densities.

(2) Quarter power blending rule used to obtain viscosity of mixtures

(3) Darcy's law applies.

(4) Two-dimensional flow for current model.

(5) Harmonic weighting used to calculate the mobilities.

The random-walk technique is based on the concept that dispersion in porous media is a random process. This idea was explored in some detail by Prickett *et al.* (1981) for single-phase flows in which the fluid viscosity is everywhere the same. In this section, we summarize the approach they used for unit mobility flows, verify that our code reproduces their results, and then show that the technique can also be applied to flows with variable viscosity.

Prickett *et al.* argued that at the microscopic level, dispersion occurs because fluid elements that start at adjacent positions follow a distribution of flow paths with slightly different lengths and local flow velocities, as Fig. 3.1.1. illustrates. To represent that behavior, Prickett *et al.* modeled the motion of a collection of particles, each of which is taken to represent an increment of volume of the displacing fluid. Each particle is assumed to move in two ways during a time step. First, the particle is moved with the mean flow velocity in the direction of the streamline passing through the particle's current location. Then the particle position is perturbed by random amounts (governed by scaled probability distributions) to reflect the effects of transverse and longitudinal dispersion.

The problem examined here is a first contact miscible flood in which a displacing fluid is injected into a porous medium initially saturated with a resident fluid that is miscible in all proportions with the displacing fluid. The mathematical model for such a displacement, neglecting gravity effects and assuming incompressible fluids, is

$$\nabla \cdot (\vec{D} \cdot \nabla C) - \vec{v} \cdot \nabla C = \frac{\partial C}{\partial t} \pm Q \tag{3.1.1}$$

$$\vec{v} = -\frac{k}{\mu} \nabla p \tag{3.1.2}$$

$$\nabla \cdot \vec{v} = 0 \tag{3.1.3}$$

where $\vec{v}$ is the local velocity, C, the local composition, $\vec{D}$, the dispersion tensor, Q, the injection rate per unit volume, k, the permeability, μ the viscosity and p, the pressure.

In this method, the convection dispersion equation (Eq. 3.1.1) is not solved. Instead, the continuity equation (Eq. 3.1.3), in conjunction with Darcy's law (Eq. 3.1.2) is solved using a point finite difference scheme. As a result, velocity components are obtained at each grid point. The basis for the displacement calculations is that the distribution of the concentration of displacing fluid in a porous medium can be represented by the distribution of a finite number of discrete particles. Each of these particles is moved by Darcy flow and is assigned a volume that represents a fraction of the total volume of displacing fluid involved. In the limit, as the number of particles gets extremely large and approaches the molecular level, an exact solution to the actual situation is obtained. However, it will be shown that relatively few particles are needed to arrive at a solution accurate enough for the applications considered here.

The connection between the random-walk approach and the statistics of the particles was demonstrated by Prickett *et al.* They considered the motion of a unit slug of tracer in an infinite one-dimensional medium. In that case, the solution to Eq. 3.1.1 is (Bear, 1972)

$$C(x,t) = \frac{1}{(4\pi D_L t)^{1/2}} \exp\left[-\frac{(x - Vt)^2}{4D_L t}\right], \tag{3.1.4}$$

where V is the flow velocity, D_L is the longitudinal dispersion coefficient, and x and t are space and time. Fig. 3.1.2 shows the resulting concentrations of tracer plotted around the location of mean flow $x' = x - Vt$.

To see how the flow problem is connected to the statistics of particles, consider a normal probability distribution, which has the density function, $n(x)$,

$$n(x) = \frac{1}{\sqrt{2\pi}\sigma} \exp\left[-\frac{(x-u)^2}{2\sigma^2}\right] \tag{3.1.5}$$

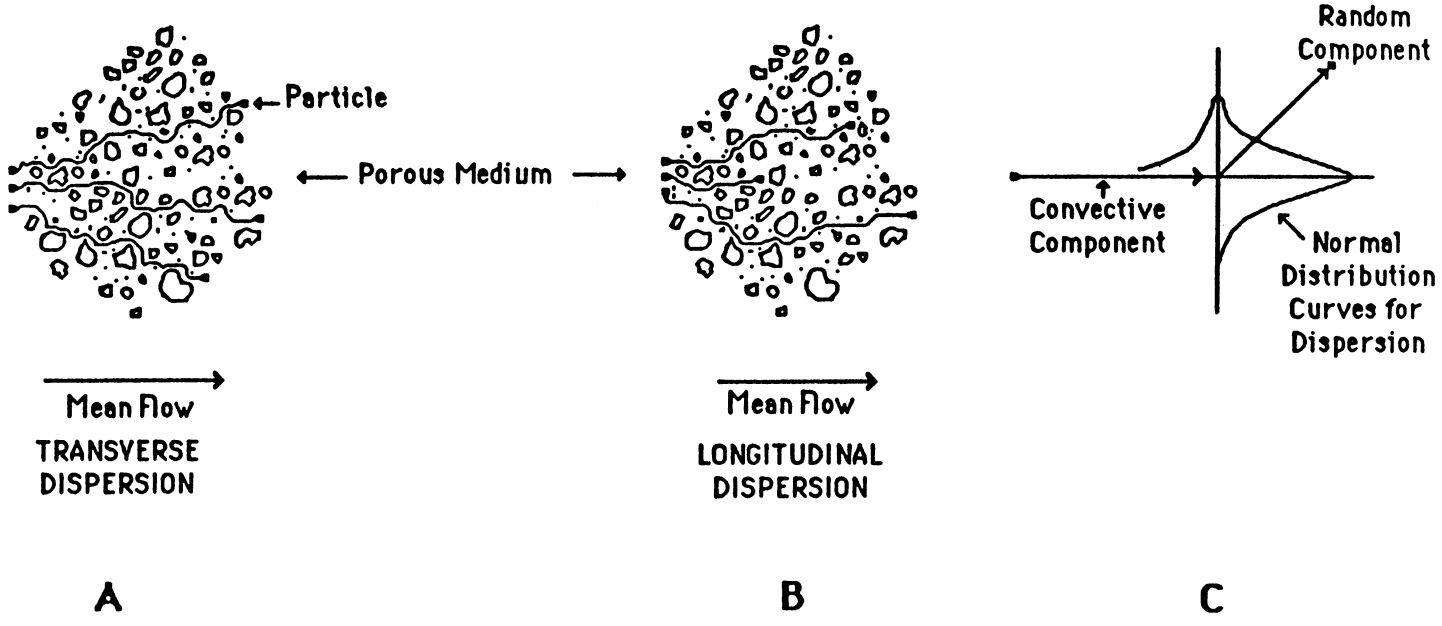

Fig. 3.1-1 Representation of dispersion as random perturbations to flow along a streamline (Prickett et al. 1981).

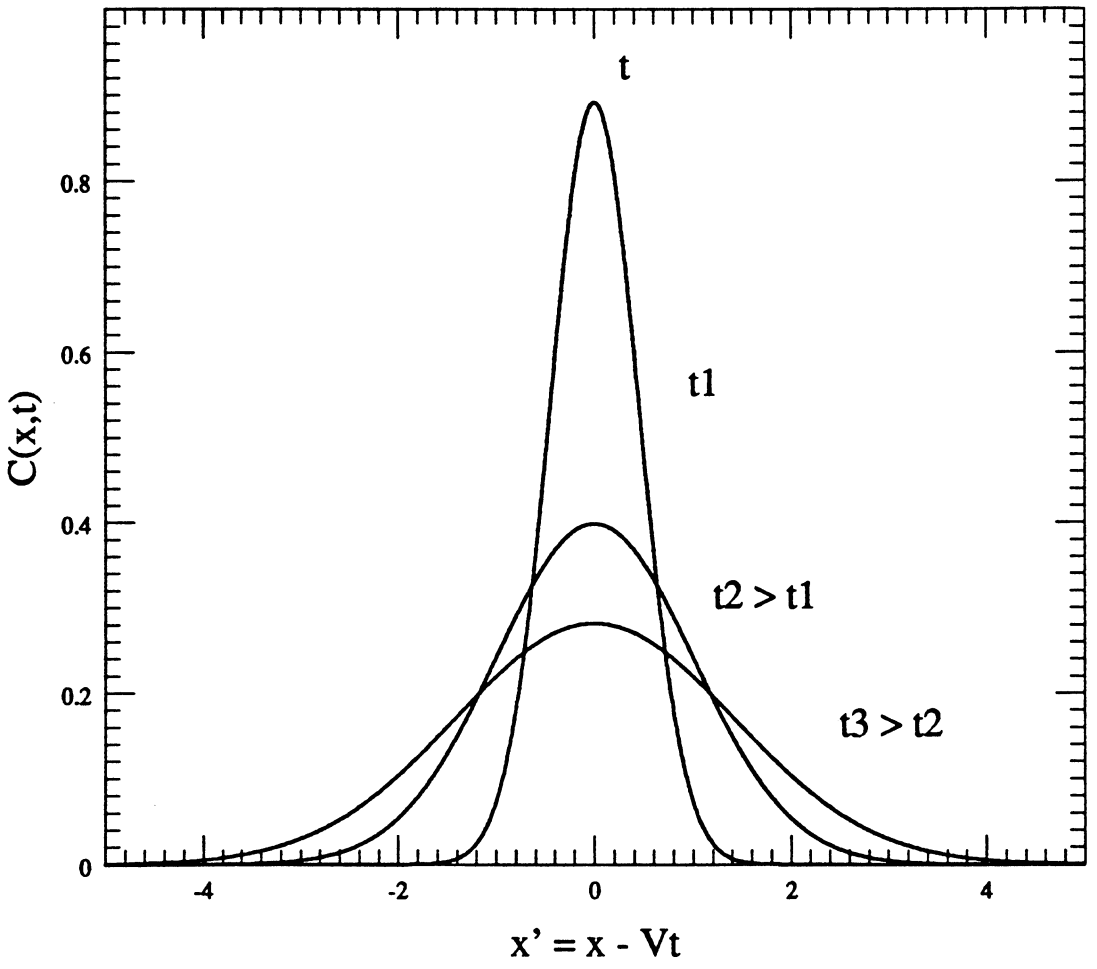

Fig. 3.1-2 Solution of the convection-dispersion equation (Bear 1972).

If we set

$$\sigma = \sqrt{2D_L t} \tag{3.1.6}$$

and

$$u = Vt, \tag{3.1.7}$$

then Eqs. 3.1.4 and 3.1.5 are equivalent, and

$$n(x) = C(x,t) \tag{3.1.8}$$

Therefore, the dispersion of particles can be represented as a random process.

Details of how the random-walk representation is implemented in a computational algorithm are given by Prickett *et al.* Our code follows closely their implementation for the portion of the code that deals with particle convection and dispersion.

3.1.2 Validation

Several tests were used to validate the random-walk model. First, it was compared to analytical solutions published by Prickett *et al.* Second, ideal miscible displacements similar to those used to measure longitudinal and transverse dispersion coefficients were simulated to determine if the input dispersivities were recovered in the calculated Peclet numbers. Finally, the experiments performed by Blackwell *et al.* (1959) for displacements in a linear two-dimensional model at various mobility ratios were simulated.

Analytical Solutions

Three different cases were simulated, all with unit mobility ratio and for a homogeneous porous medium.

Case -1- Longitudinal dispersion in uniform one dimensional flow with continuous injection at inlet.

The theoretical equation for this case is approximated well by:

$$C \,/\, C_o = \frac{1}{2}\, erfc\left[\frac{x - Vt}{2\sqrt{D_L t}}\right] \tag{3.1.11}$$

where $D_L = 4.5\ ft^2/day$, $V = 1\ ft/day$. The transverse dispersivity was set to zero. This calculation is identical to that described in Fig. 51 of Prickett *et al.* (the same random number generator and seed were used). Fig. 3.1.3 shows the results plotted for different times. The numerical solution does approximate the analytical one, and the results reproduce those of Prickett *et al.*, an indication that the implementation in our code is correct. The match can easily be improved by increasing the number of particles used (in the case shown it was 100 particles to represent unit solvent concentration in a grid block) and finer grid mesh (3x30 grid was used here). Note that $C/C_o > 1$ at the inlet. This is a statistical phenomenon, which could be eliminated by increasing the number of particles injected and the number of grid blocks. It occurs when the composition of a block is near 1.0 because occasionally random motions cause the number of particles to exceed that required to give a concentration of 1.0. In subsequent time steps, however, the concentration drops again due to the same random motions.

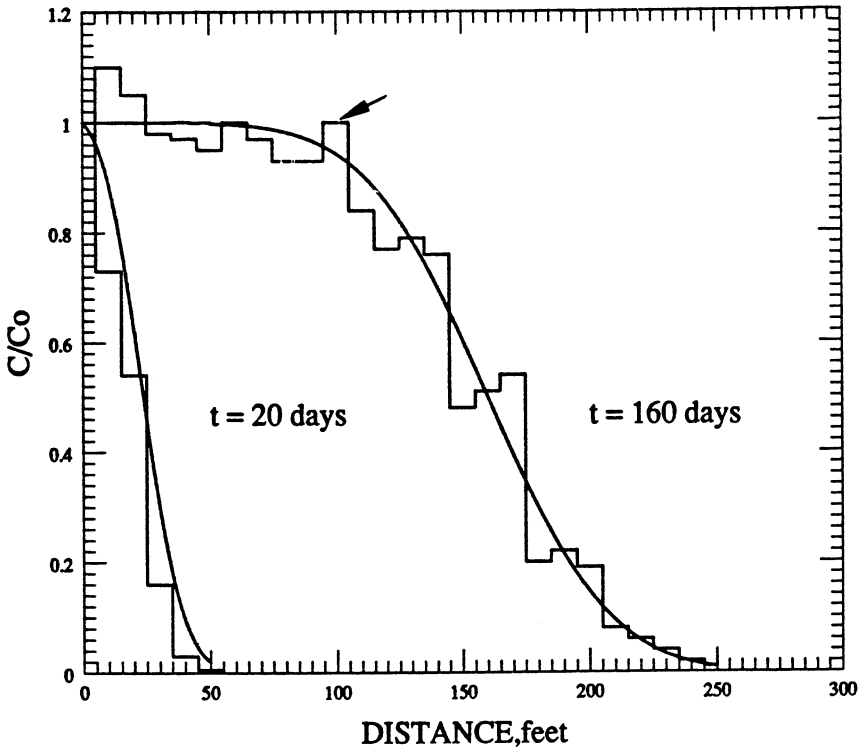

Fig. 3.1-3 Longitudinal dispersion in one-dimensional flow with continuous injection at inlet.

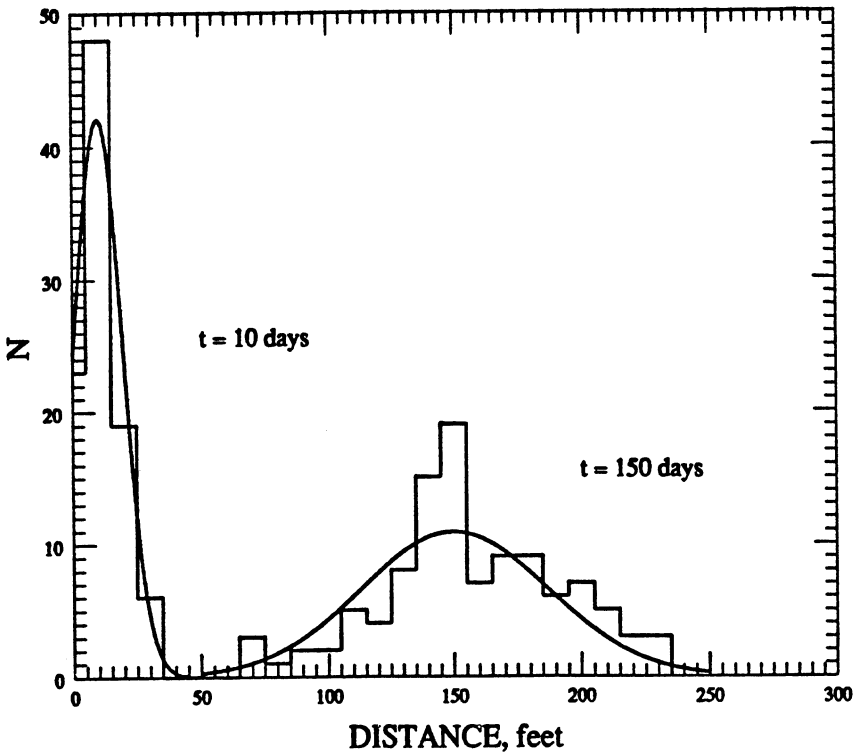

Fig. 3.1-4a Longitudinal dispersion in uniform one-dimensional flow with a slug of tracer injected at inlet (100 particles).

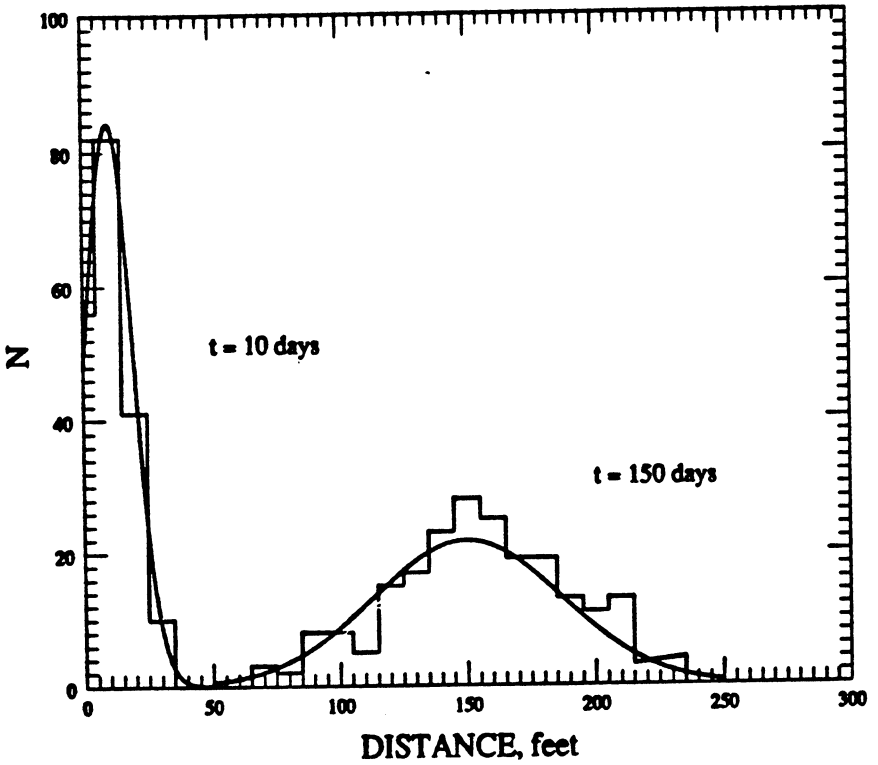

Fig. 3.1-4b Longitudinal dispersion in uniform one-dimensional flow with a slug of tracer injected at inlet (200 particles).

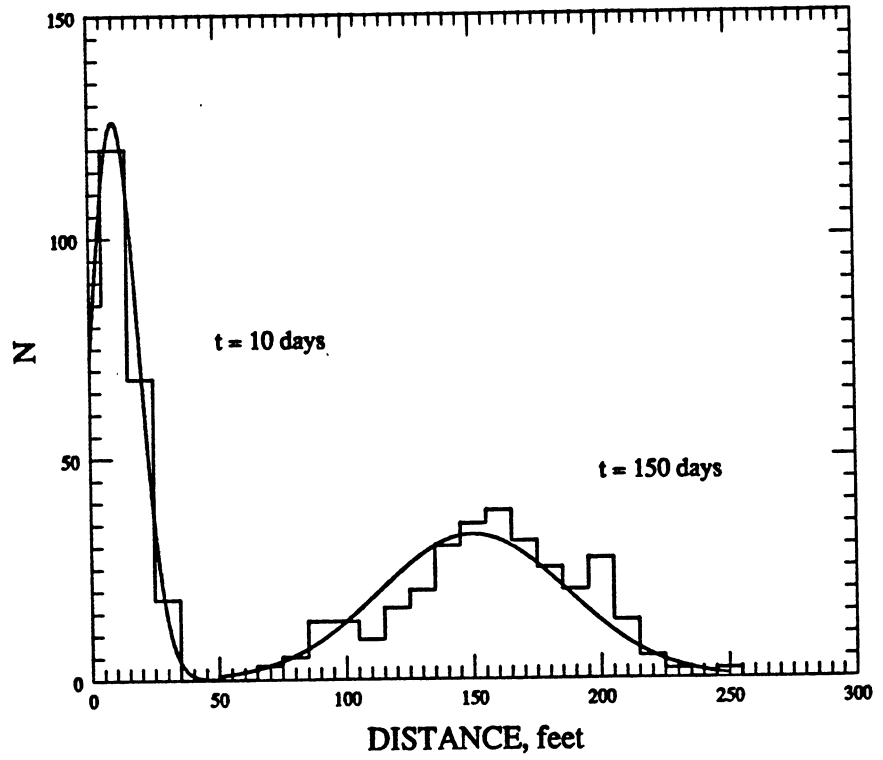

Fig. 3.1-4c Longitudinal dispersion in uniform one-dimensional flow with a slug of tracer injected at inlet (300 particles).

Case -2- Longitudinal dispersion in uniform one-dimensional flow with a slug of tracer injected at inlet.

The data for this problem are the same as the those used in the previous case, except that a slug is injected. This calculation duplicates that reported by Prickett *et al.* in their Fig. 53. Fig. 3.1.4 compares the results of this simulation with the theoretical results given by the following equation (Bear, 1972)

$$N = \frac{N_o\, dx}{\sqrt{4\pi D_L\, t}} \exp\left[- \frac{(x - Vt)^2}{4D_L\, t} \right] \tag{3.1.12}$$

where $N_o\, dx$ is the number of particles times the grid length over which particles are counted. The effects of injecting slugs of increasing number of particles are illustrated by comparing Figs. 3.1.4a, 3.1.4b and 3.1.4c. The agreement between the approximate solution and the analytical solution improves as the number of particles taken to represent unit concentration increases.

Case -3- Longitudinal and transverse dispersion in uniform one dimensional flow with a slug of tracer injected at the inlet.

Again, the data for this problem are the same as previously used except that the transverse dispersivity is no longer zero. These results reproduce those reported by Prickett *et al.* in their Fig. 58. Now $D_T = 1.125\ ft^2/day$. The theoretical solution for this case is given by Fried (1975).

$$N = \frac{N_o}{4\pi Vt\sqrt{d_L\, d_T}} \exp\left[- \frac{(x - Vt)^2}{4d_L\, Vt} - \frac{y^2}{4d_T\, Vt} \right] \tag{3.1.13}$$

where N_o is the number of particles times flow rate times time increment. Figs. 3.1.5a-3.1.5d show that the agreement between the analytical and numerical results is good.

Recovery of input dispersion values

In order to examine how the random-walk model mimics numerically the effects of dispersion, ideal miscible displacement simulations were performed. Approximate longitudinal Peclet numbers were obtained by fitting calculated effluent composition data to a straight line in arithmetic probability coordinates. The longitudinal dispersion coefficient was then calculated from the Peclet number as:

$$D_L = \frac{VL}{Pe} \tag{3.1.14}$$

where $V = 40\ ft/day$, $L_x = 6\ ft$, $L_y = 2\ ft$ and the input $D_L = 0.1457\ ft^2/day$. Fig. 3.1.6 shows the range of the calculated dispersion coefficients and its dependence on grid size and seed number for the random number generator.

Transverse Peclet numbers were measured by developing code that simulated the sand packed column arrangement (Perkins and Johnston, 1963) shown in Fig. 3.1.7. The transverse dispersion number was then obtained from the Peclet number in the same manner described above. The data used were also the same with $D_T = 0.0055\ ft^2/day$.

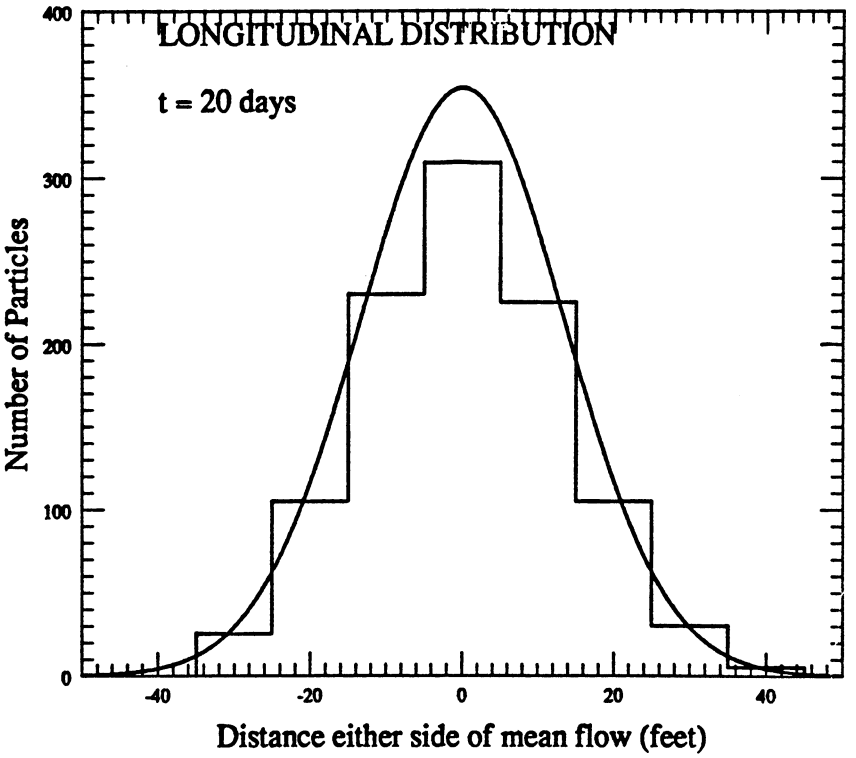

Fig. 3.1-5a Longitudinal distribution on both sides of the mean flow after 20 days.

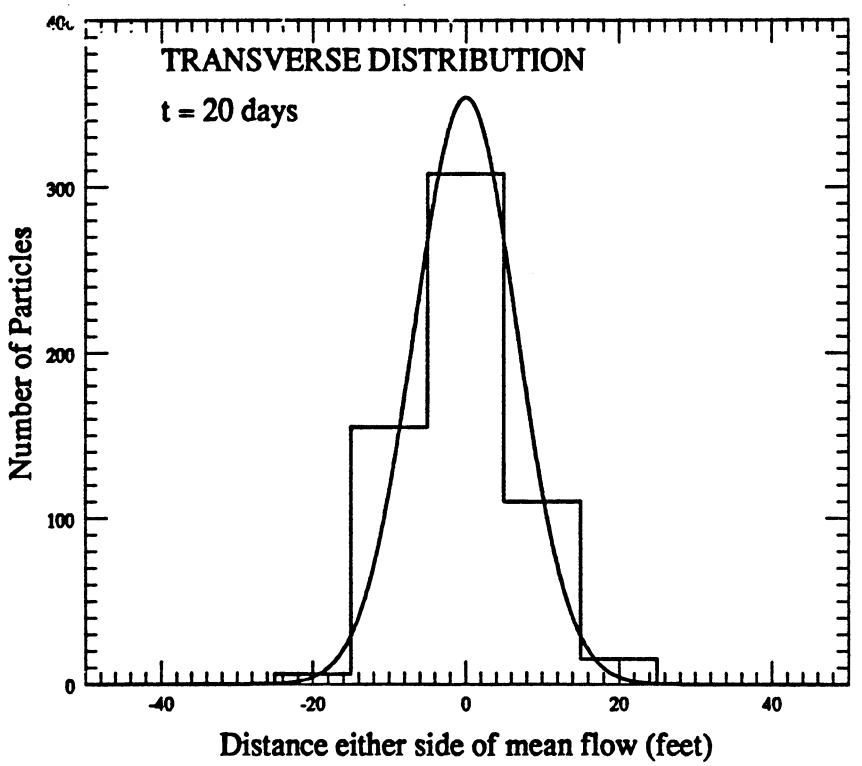

Fig. 3.1-5b Transverse distribution on both sides of the mean flow after 20 days.

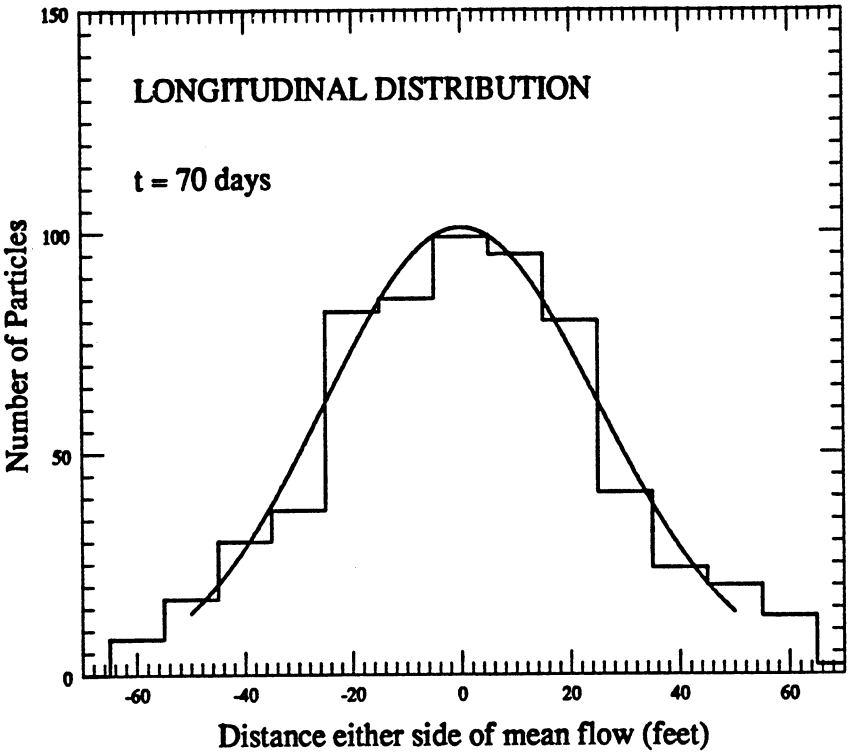

Fig. 3.1-5c Longitudinal distribution on both sides of the mean flow after 70 days.

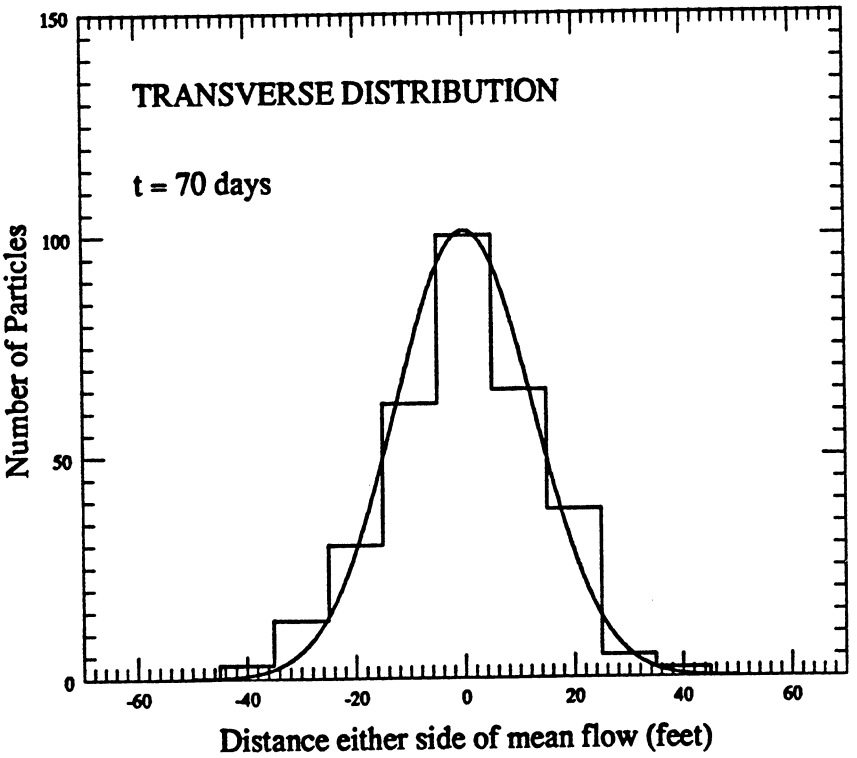

Fig. 3.1-5d Transverse distribution on both sides of the mean flow after 70 days.

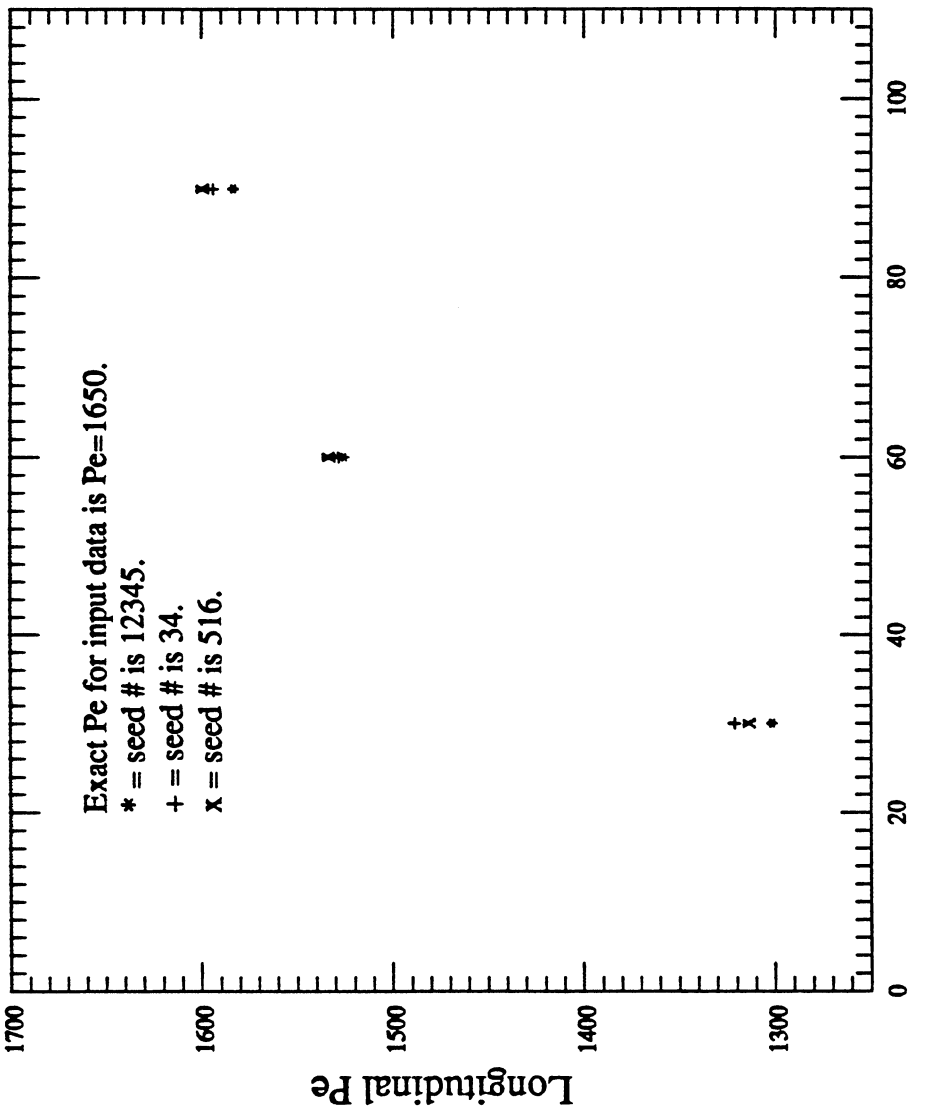

Fig. 3.1-6 Longitudinal Pe number as a function of grid size and seed number.

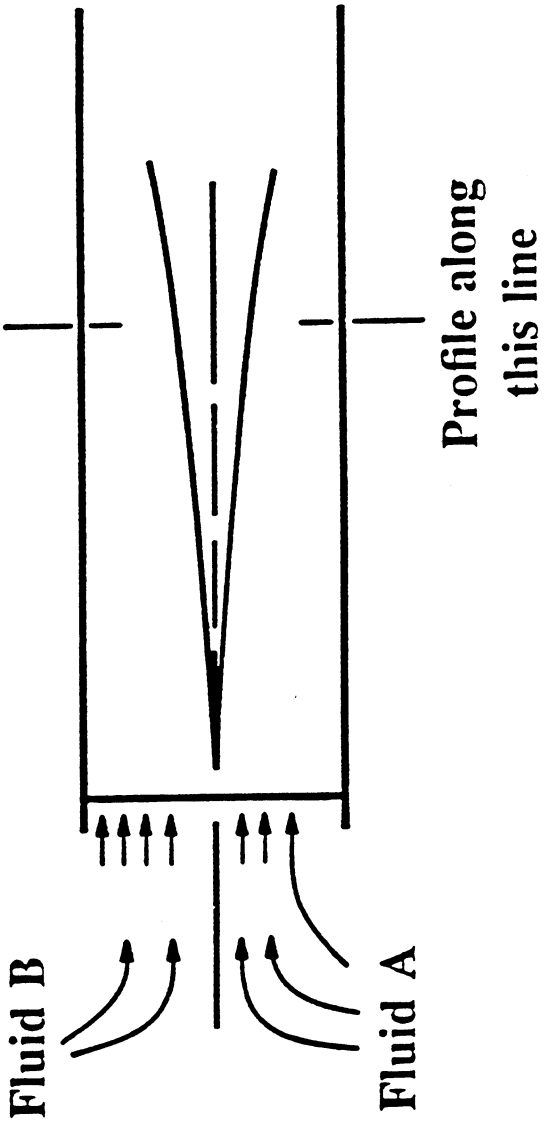

Fig. 3.1-7 Measurement of transverse dispersion coefficients.

For both cases, the magnitudes of values calculated increased with increasing mesh size and were nearly independent of the seed number used. The ranges varied from about ± 20% for a 30×20 grid to about ± 5% for a 90×20 grid in the longitudinal dispersion case. Figs. 3.1.6 and 3.1.8 indicate that the computational scheme used reproduces well the input values.

The examples shown here demonstrate that the code written to perform the particle-tracking calculations reproduces the unit mobility results reported by the originators of the method, and they confirm that the method gives accurate numerical solutions. Furthermore, they show that effects of numerical dispersion are small if reasonable grid resolution is used. Hence we are now ready to test whether the approach is suitable for flows in which the viscosity of the injected fluid differs from that of the fluid displaced.

Comparison with experimental results

Blackwell's experiments were carried out to investigate fingering in homogeneous sands. The results used were those obtained from a sandpack model with dimensions 3/8" x 24" x 72" at reported flow rates between $30 - 50\ ft/day$. The sandpack was tested to assess the homogeneity of the packing using equal density and viscosity fluids containing dyes. The results of the assessment also allowed calculation of the effective dispersion coefficient. The values of dispersion coefficients used in these simulations were calculated using previously derived formulae (Pozzi and Blackwell, 1963). At a flow rate of $40\ ft/day$ the calculated dispersion coefficients were

$$D_L = 0.1457\ ft^2/day$$
$$D_T = 0.0045\ ft^2/day$$

Fig. 3.1.9 shows the experimental data for four different mobility ratios ranging from 5 to 375, and the results obtained from the simulation runs. The agreement between calculated and experimental values of the oil recovery is very good. For the mobility ratio of 5, 86 and 150 a 60×60 grid was used. For the last mobility ratio case (M = 375) a finer grid (80×60) was needed in order to simulate the experimental results satisfactorily. Except for refinement of the grid, no adjustment of input parameters was made to achieve the agreement shown in Fig. 3.1.9.

It was found throughout this set of simulation runs that the transverse grid resolution was the dominant factor in obtaining a good match of the experimental results because it controlled the amount of crossflow between streamlines. Runs were made with even finer grid meshes (120×60) but the results were unchanged. The number of grids in the longitudinal direction did not greatly affect the outcome of the simulations. Additional numerical experiments showed that the choice of seed number for the random number generator did not significantly alter the results.

3.1.3 Model Performance Characteristics

A problem with the model is that concentrations greater than unity are possible. Such behavior is exhibited in Fig. 3.1.3, where concentrations of 1.1 occur. In the two-dimensional case, concentrations exceed values of two and even more are quite common. However, they occur only in the impermeable boundary grid blocks. This behavior can be explained as follows. Since each injected particle represents a volume of fluid, a grid block can only contain only so many particles before the concentration exceeds unity. Because dispersion process in the model is random, particles tend to drift into adjacent blocks. In the inner grid blocks, this behavior is averaged out over time and space and concentrations rarely exceed unity. And if so, only by a small fraction, usually smaller than a tenth. However, the same does not happen in the boundary blocks. First of all, these blocks are half the size of inner grid blocks. Secondly, since the boundaries are impermeable, the transverse velocities are very small meaning that particles drifting into these blocks will tend to remain there and accumulate over time. As a result, these outer boundary blocks are dropped when mapping concentration contours.

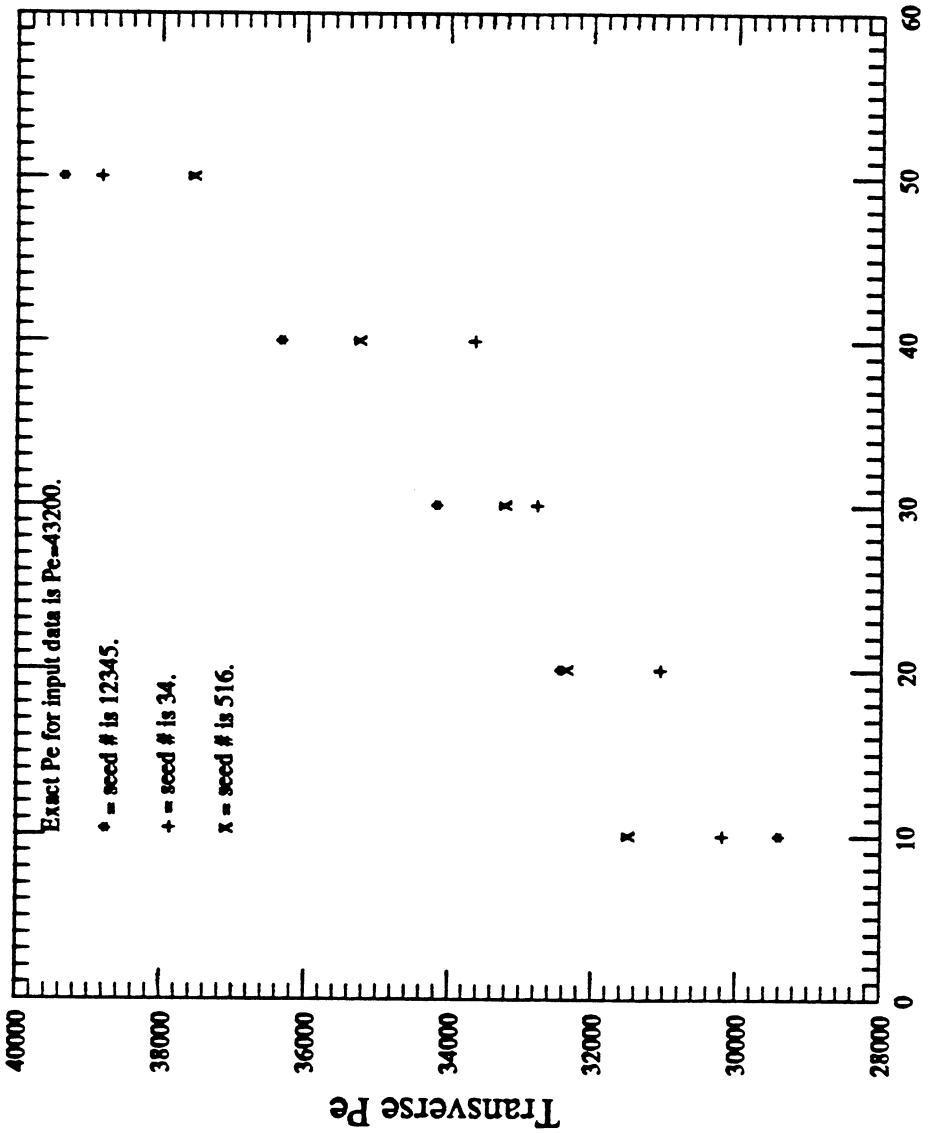

Fig. 3.1-8 Transverse Pe number as a function of grid size and seed number.

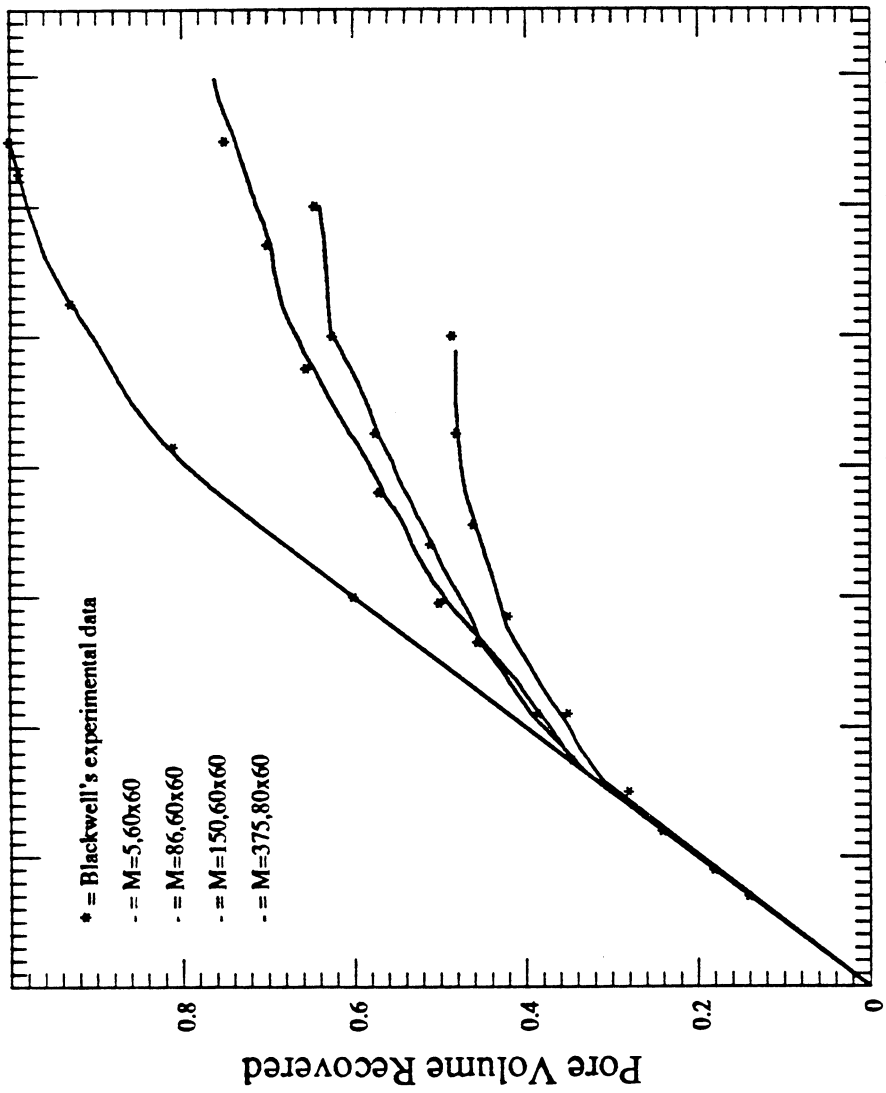

Fig. 3.1-9 Comparison of random-walk model results with Blackwell's experimental results.

The behavior described above is dependent on the number of particles use to fill a grid block. Twenty-five particles per grid block were used in the validation runs made to reproduce Blackwell's experimental data. Fig. 3.1.10 shows the recovery curve obtained using only ten particles per grid block. It can be seen that the experimental data is not reproduced as well as for the 25 particle case. Also some boundary blocks displayed concentrations greater than nine. These concentrations dropped to about three with 25 particles and dropped even further to 1.3 with 100 particles per grid block. It would obviously be ideal to run all cases using 100 or more particles per grid block. Unfortunately this is not feasible because the model's run time is directly proportional to the number of particles in the system. Run times on a Gould 9080 for several cases are shown in Table 3.1. Run time is also dependent on the mobility ratio because the number of iterations required by the matrix solver at each time step increase, with increasing mobility ratio.

When performing the validation runs, good resolution in the transverse direction was shown to be very important. An insufficient number of rows results in high velocities occurring at very few grid blocks. Breakthrough time is not affected by this, but after breakthrough recovery is always much higher than the experimental recovery. For runs with mobility ratios ranging between 5 and 150 a 60×60 grid size gave very satisfactory results, as shown in Fig. 3.1.9. However, for a mobility ratio of 375 a 80×60 grid size was needed to obtain the same level of accuracy as for the previous cases. To test the convergence, additional runs with a 120×60 grid size were made for different mobility ratios. The results were identical to the ones obtained for the smaller grid size.

This model can easily be used to represent linear, radial or five-spot patterns. All that needs to be done is to solve the diffusivity equation with the appropriate boundary conditions. This amounts to rewriting one subroutine in the model's code. Also any type of injection and production pattern can be modeled, meaning that particles can be introduced anywhere into the system by specifying the initial position of the particles.

3.1.4 Inclusion of Heterogeneities

In order to study the interaction between viscous fingering and heterogeneous porous media, a permeability field must be generated. To use existing methods (Journel and Huijbregts, 1978), it is assumed that permeability is a regionalized variable with second order stationarity meaning that the mean of the distribution is independent of location and that spatial correlation between two samples depends only on the distance separating them.

The Dykstra-Parsons coefficient (Dykstra and Parsons, 1950) defined below can be used to describe the permeability variation:

$$V_{dp} = \frac{k_{50} - k_{84.1}}{k_{50}} = 1 - e^{-\sigma_{lnk}} \tag{3.1.15}$$

To express spatial correlation, a correlation length scale λ is introduced. The degree of correlation between the permeabilities at two points decreases as the distance separating them increases. When that distance becomes greater than the correlation length scale, the permeabilities become uncorrelated. The correlation length is made dimensionless by normalizing it as follows:

$$\lambda_D = \frac{\lambda}{L} \tag{3.1.16}$$

The moving average method (Luster, 1984, Mishra, 1987) is used to generate a correlated permeability field. Using an average permeability of 100 md. with a small variance ($V_{dp} = 0.1$) and a correlation length of 3 feet, the permeability field shown in Fig. 3.1.11 was obtained. Figs. 3.1.12 through 3.1.15 show the progression of a displacement for a mobility ratio $M = 20$ through the permeability field. The contour line represents a concentration of 0.4. Approximately twelve

Table 3.1.1. Run Times for Simulation of Blackwell's Viscous Fingering Experiments

Grid Size	Mobility Ratio	Particles per block	PVI	CPU time(min)
60x60	86	25	1.5	1980
60x60	86	25	1.0	1360
60x60	86	100	1.0	4830
60x60	86	10	1.0	480
60x60	375	25	1.0	1740
60x60	5	25	1.0	720
120x60	86	25	1.0	3570
60x40	86	25	1.0	1140

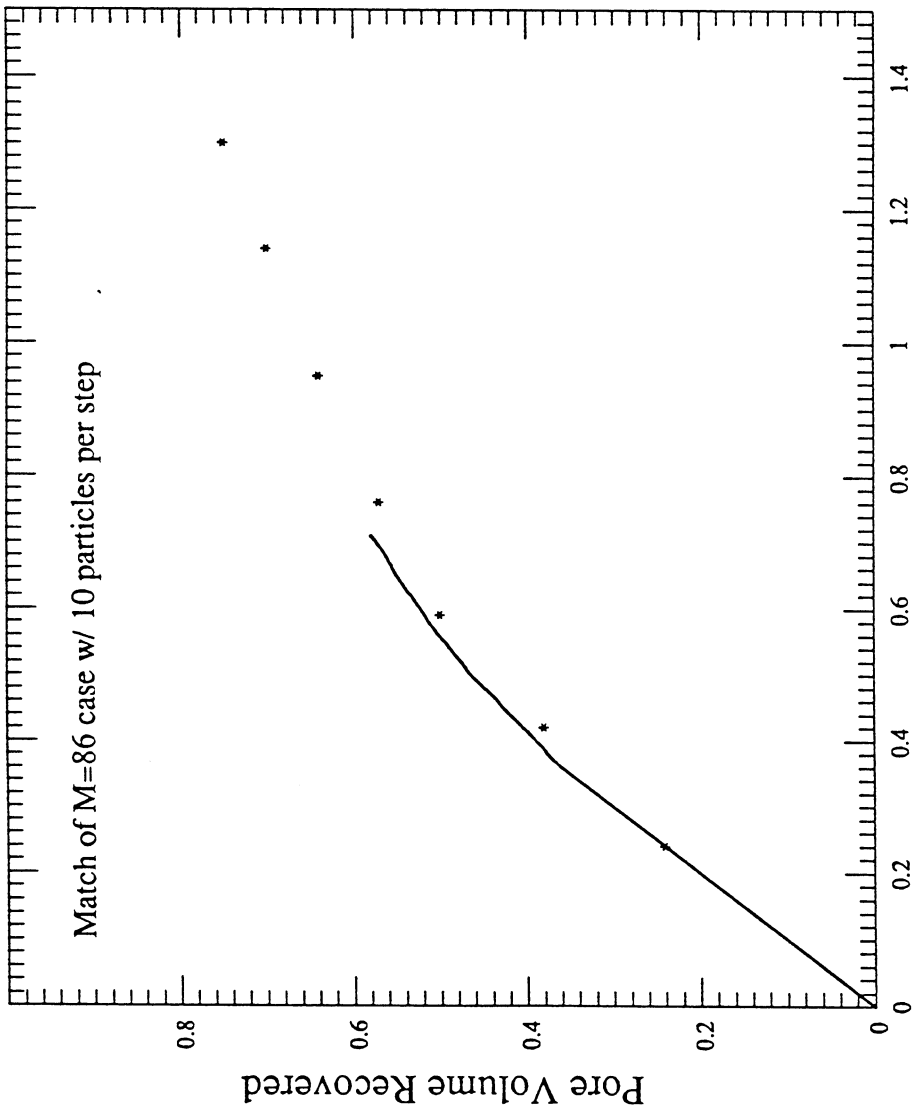

Fig. 3.1-10 Dependence of results on number of particles injected per grid block.

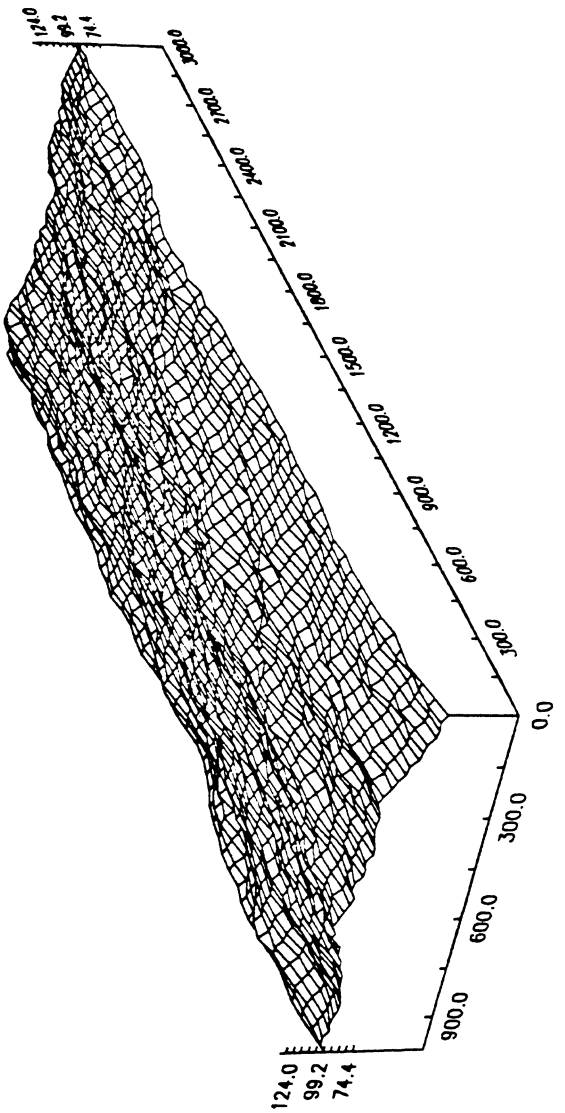

Fig. 3.1-11 Permeability field with k_{avg} = 100 md, V_{dp} = 0.1

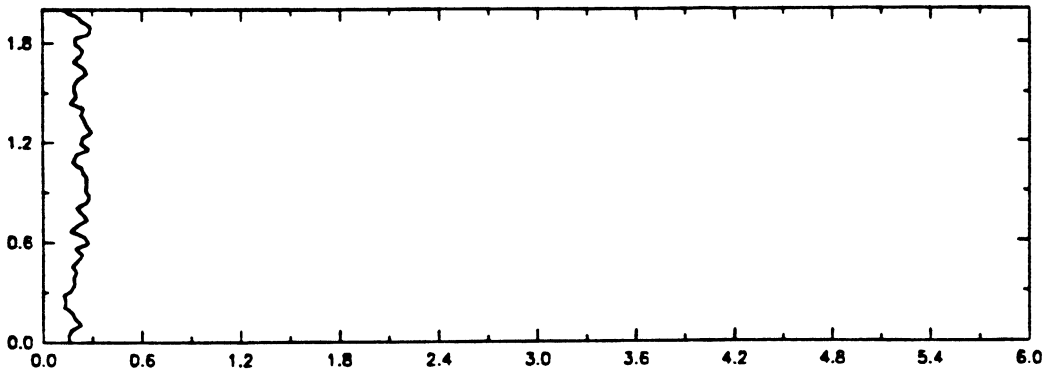

Fig. 3.1-12 Displacement for M = 20, PVI = 0.05 showing the 0.4 concentration contour line.

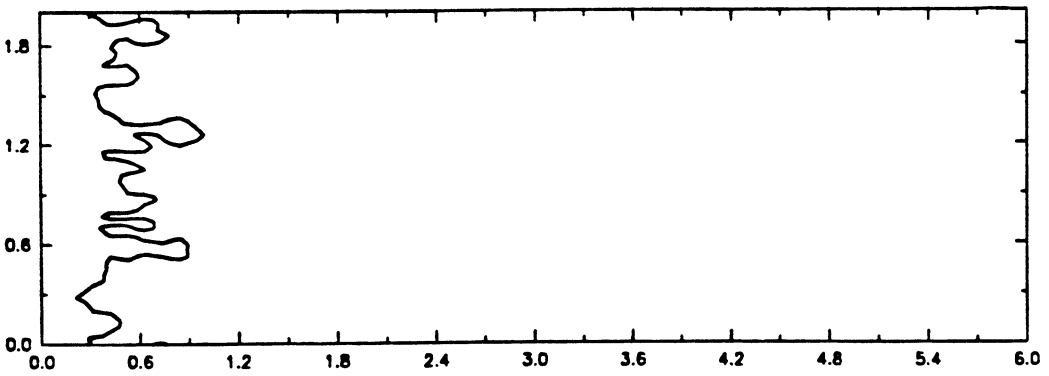

Fig. 3.1-13 Displacement for M = 20, PVI = 0.10 showing the 0.4 concentration contour line.

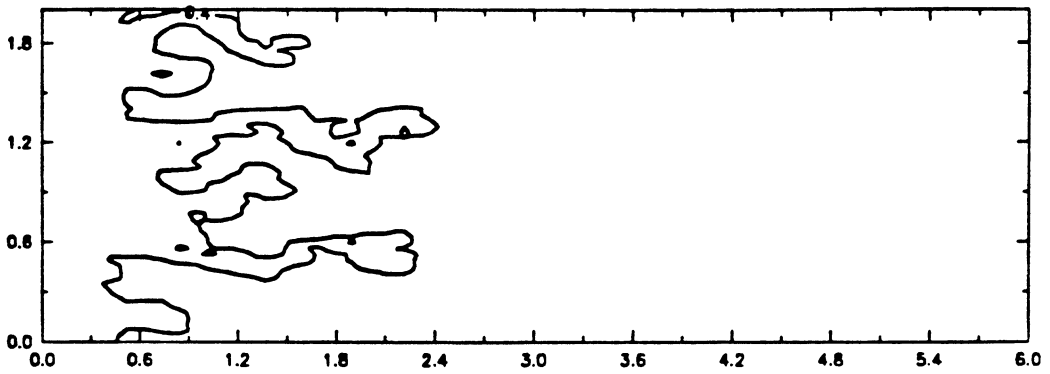

Fig. 3.1-14 Displacement for M = 20, PVI = 0.20 showing the 0.4 concentration contour line.

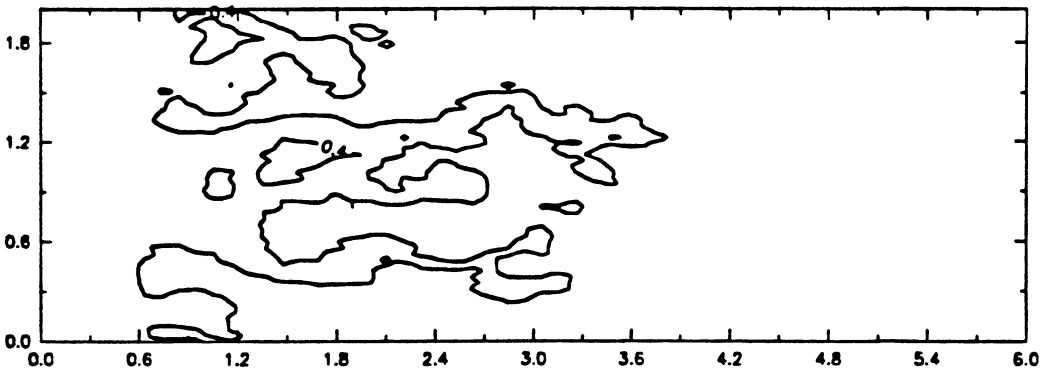

Fig. 3.1-15 Displacement for M = 20, PVI = 0.30 showing the 0.4 concentration contour line.

fingers formed initially, but only four fingers survive at 0.30 pore volumes injected. The variance of the permeability field was then increased (V_{dp} = 0.9) while keeping the remaining parameters identical. Results are shown in Figs. 3.1.16 through 3.1.20. Now only one finger dominates the displacement. The finger follows the high permeability streak and at breakthrough splits up due to several high permeability regions near the outlet.

An additional case was run for a completely homogeneous permeability field and is presented in Fig. 3.1.21 through 3.1.25 for comparison. As expected, this displacement approximates the behavior displayed in the smaller variance run discussed above, with the four fingers dominating. As injection is continued, the four fingers coalesced into one large finger.

3.1.5 Probabilistic Model

After considering the encouraging results obtained with the random-walk model, the probabilistic model was modified so that dispersion would be treated similarly to the dispersion step described in the previous section. After determining the intersection of the randomly chosen streamline and concentration contour, that location is perturbed by random amounts corresponding to longitudinal and transverse dispersion, as described for the random-walk scheme. The injected fluid concentration at that location is then incremented. This method generates fingers because low viscosity fluid replaces high viscosity fluid, streamlines become more closely spaced, and hence the

---

NOTE: This report was revised on July 20, 1995. The text of this portion of the report continues on p. 116.

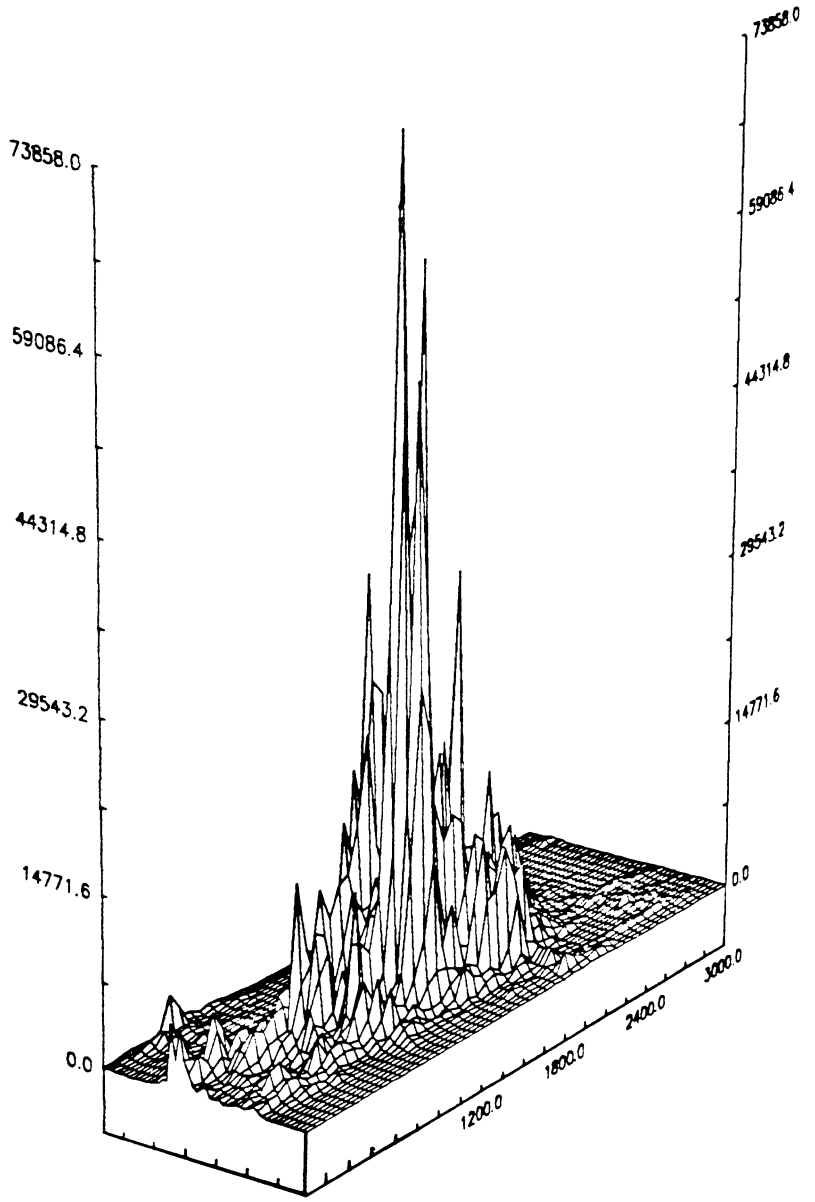

Fig. 3.1-16 Permeability field with k_{avg} = 100 md, V_{dp} = 0.9

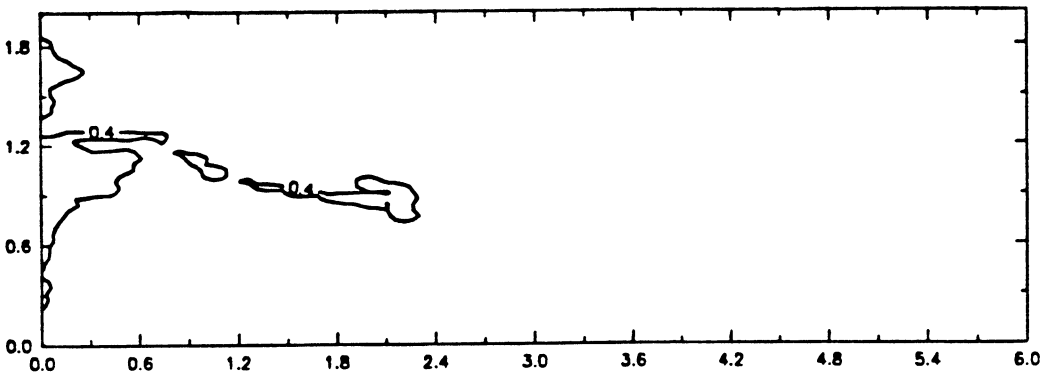

Fig. 3.1-17 Displacement for M = 20, PVI = 0.05 showing the 0.4 concentration contour line.

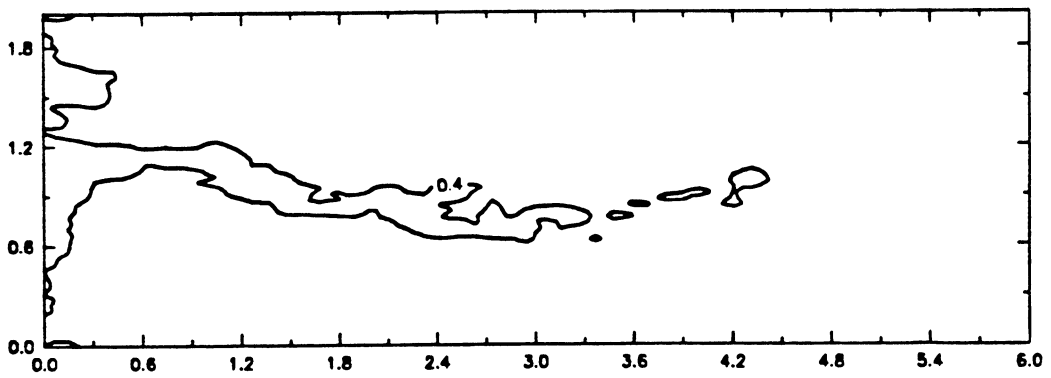

Fig. 3.1-18 Displacement for M = 20, PVI = 0.10 showing the 0.4 concentration contour line.

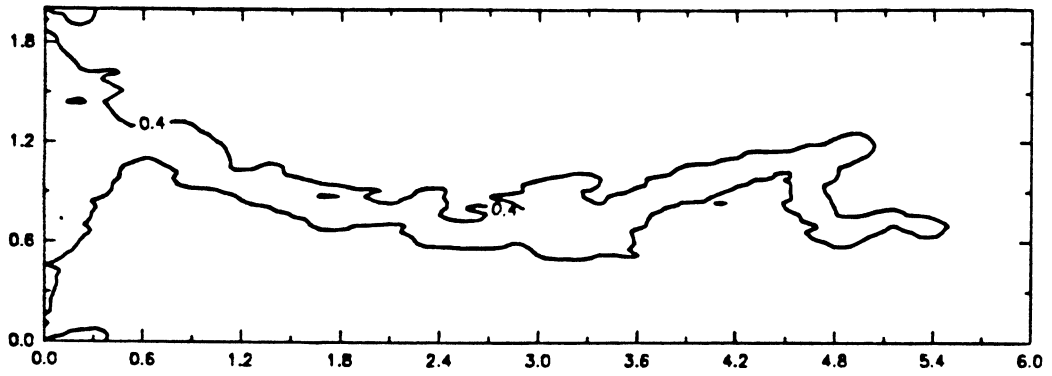

Fig. 3.1-19 Displacement for M = 20, PVI = 0.20 showing the 0.4 concentration contour line.

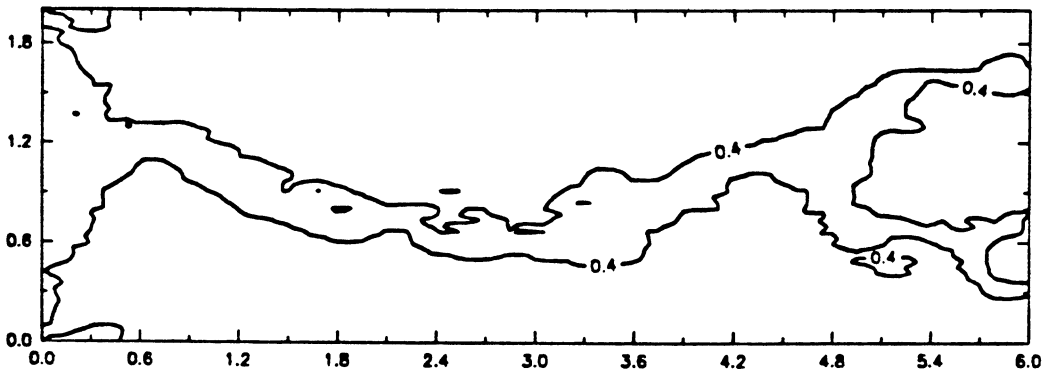

Fig. 3.1-20 Displacement for M = 20, PVI = 0.30 showing the 0.4 concentration contour line.

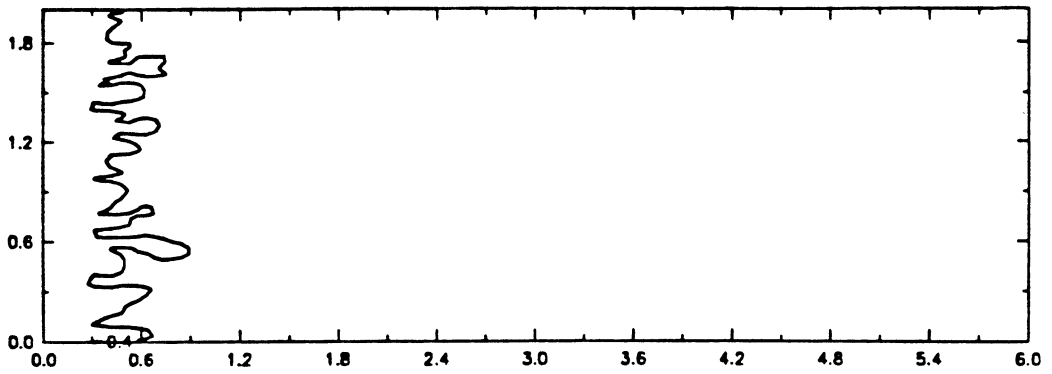

Fig. 3.1-21 Displacement for M = 20, PVI = 0.10 showing the 0.4 concentration contour line in a homogeneous permeability field.

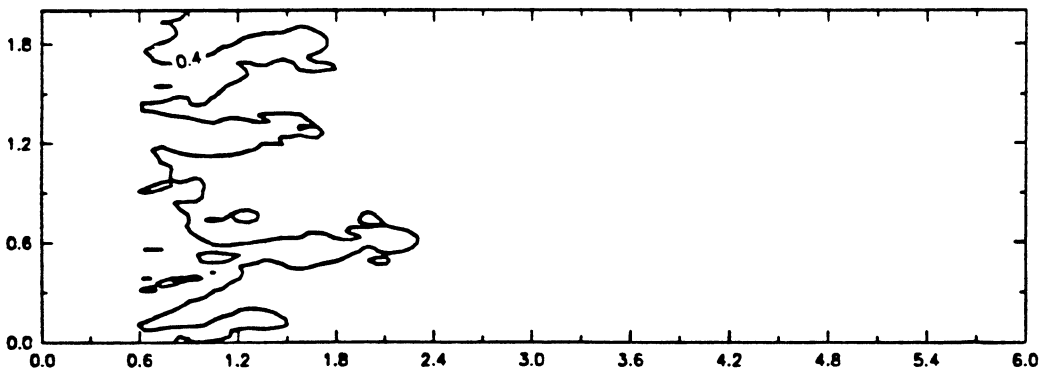

Fig. 3.1-22 Displacement for M = 20, PVI = 0.20 showing the 0.4 concentration contour line in a homogeneous permeability field.

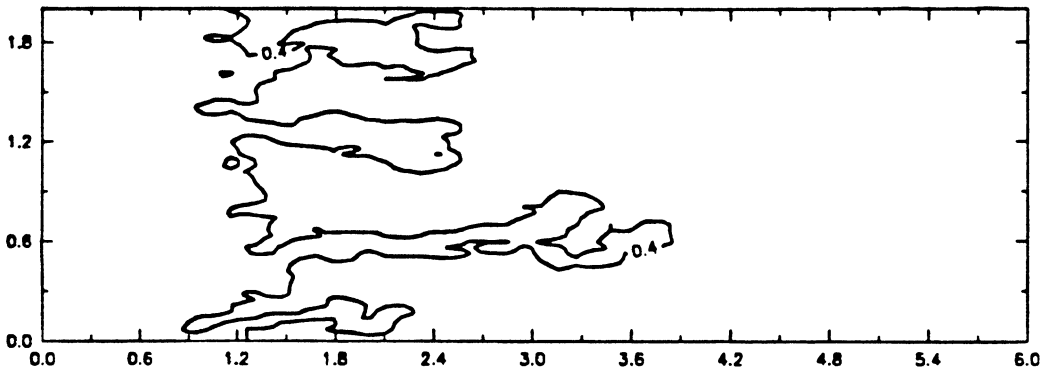

Fig. 3.1-23 Displacement for M = 20, PVI = 0.30 showing the 0.4 concentration contour line in a homogeneous permeability field.

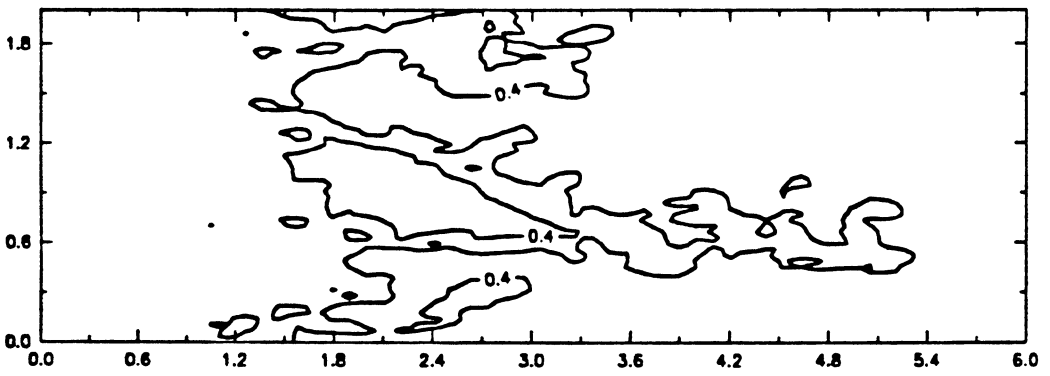

Fig. 3.1-24 Displacement for M = 20, PVI = 0.40 showing the 0.4 concentration contour line in a homogeneous permeability field.

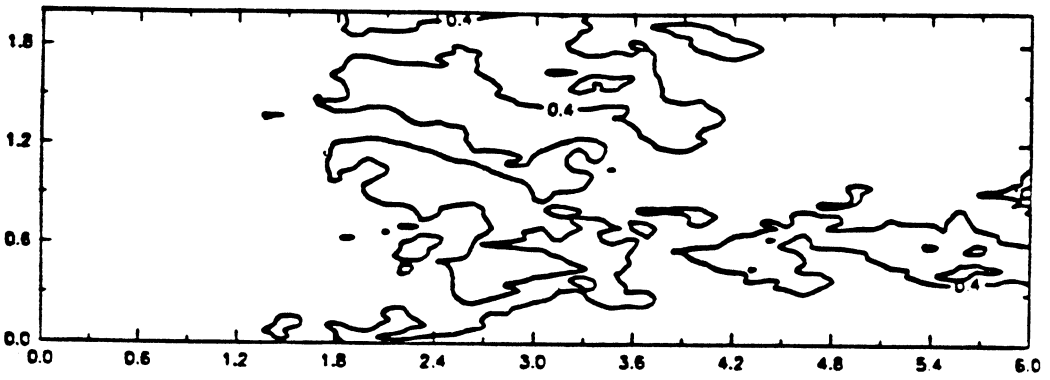

Fig. 3.1-25 Displacement for M = 20, PVI = 0.50 showing the 0.4 concentration contour line in a homogeneous permeability field.

NOTE: This report was revised on July 20, 1995. The text of this portion of the report continues on p. 116.

---

probability increases that a streamline in the neighborhood will be selected in subsequent time steps. Unfortunately, as shown in Fig. 3.1.29, recoveries obtained with the model do not agree well with experimental results. As the number of grid blocks is increased, breakthrough occurred earlier and the ensuing recovery was also lower, an indication that the viscous fingers developed were function of the grid block size. This failure to reproduce experimental results was to be expected since the input dispersivities were not recovered in unit mobility displacements as described previously. Thus, the inclusion of dispersion as an additional perturbation of the position of the streamline and saturation chosen for evolution by the probabilistic scheme is apparently not consistent with the convection-dispersion equation. For that reason, future computations will make use of the random-walk model only.

3.1.6 Summary and Future Work

In this section, we described a scheme to model the long term growth of viscous fingers in heterogeneous porous media. This model was validated against analytical and experimental results. The predictions of the model agree well enough with experimental results that additional investigation of the variation of transverse length scales of fingers with changes in the correlation structure of the permeability field appear warranted. In particular, the development of fingers over longer displacement lengths will be investigated to determine whether one finger always dominates eventually or whether a cascade of coalescence and tip-splitting leads to some average finger size. In addition, flows in permeability fields with a range of correlation lengths will be simulated to determine when finger growth is dominated by viscous effects and when permeability variation controls finger scales. That result is of considerable importance to the design of representations of viscous instability for reservoir simulators that use large grid blocks. If average fingers are small compared to grid block sizes, a very different approach will be required than will be appropriate if the size of the fingers are comparable to or larger than the grid block size.

3.2 Scaled Flow Visualization Experiments

David Brock

Experimental data with which the theoretical predictions of Section 3.1 can be tested are quite limited. Indeed, there are only minimal data for systems with permeability variation. In this section we describe experiments to test the interaction of heterogeneity with instability. The approach is a series of scaled flow visualization experiments in models with known, controlled permeability variations, using miscible fluids. Thus phase behavior effects are not included. Phase behavior of CO_2 - oil and other miscible systems are being examined separately in other parts of the project, and will be included in subsequent experiments. Because the experiments are scaled, the results will describe reservoir behavior more accurately than unscaled experiments.

Little work has been published on the combined effects of viscous instability and heterogeneity. Blackwell *et al.* (1957) described experiments using miscible fluids with unstable viscosity ratios in unconsolidated sands. It was determined that permeability heterogeneity decreased overall recovery in their experiments. Habermann (1960) studied the effect of mobility ratio on finger patterns in a quarter five spot geometry. Although the experiments were solely in uniform packs, the effects of heterogeneity were discussed qualitatively. Slobod and Thomas (1963) reported on finger shapes and effluent compositions as a function of rate. These experiments were done only in uniform sand packs. Giordano et al. (1985) reported experiments in which finger development in a Berea sandstone slab was studied. In that study, finger dimensions were measured by microwave attenuation. The flow experiments were performed in slabs for which extensive surface permeability measurements were obtained. The permeability variations present were mild, however.

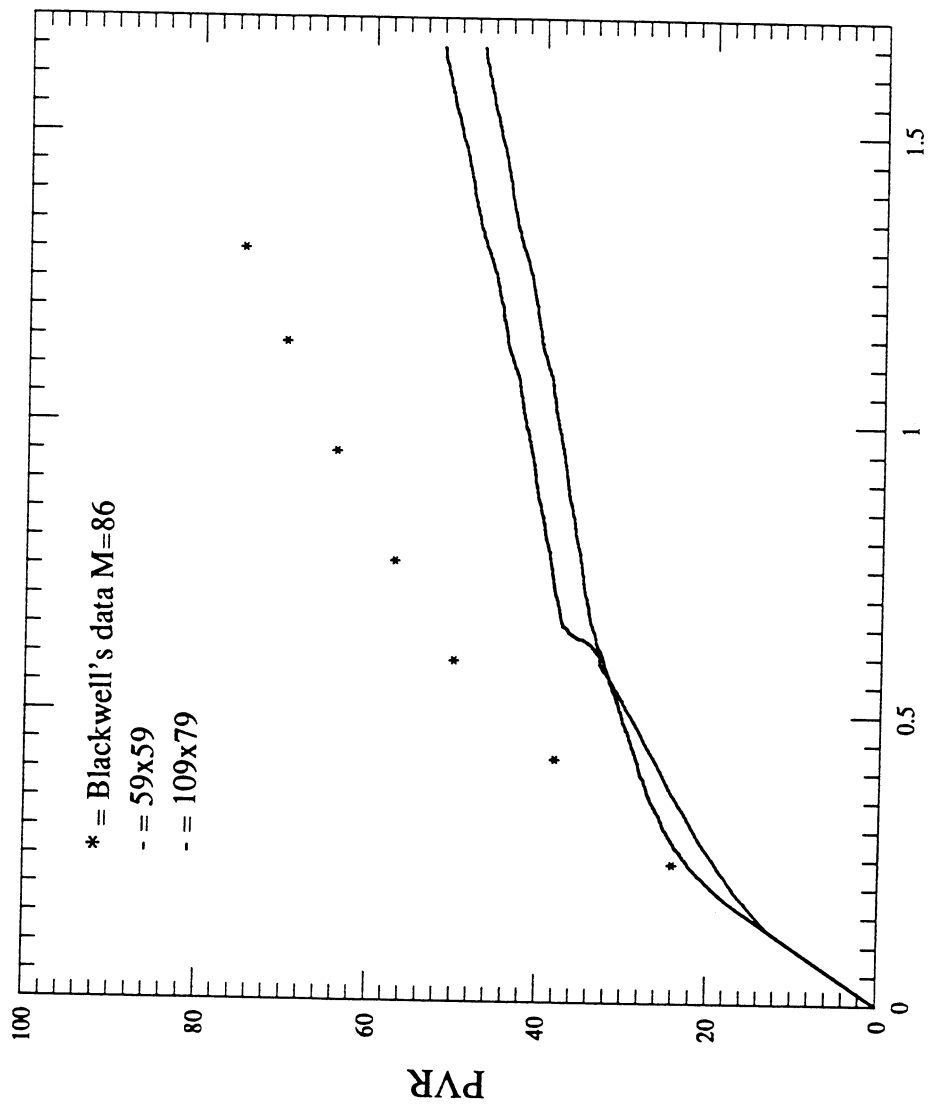

Fig.3.1.29. Comparison of modified King model results with Blackwell's experimental results.

If results of a flow experiment done at laboratory scales are to represent accurately the behavior of a petroleum reservoir, the experiment must be carefully scaled. One method of deriving the scaling criteria for a system is inspectional analysis (Geertsma *et al.*,1956). In inspectional analysis, the governing mathematical equations are made dimensionless, and the resulting dimensionless groups, for proper scaling, must be identical in reservoir and model. A miscible flood in a homogeneous one-dimensional system is simple enough to be scaled properly (Offeringa and van der Poel, 1954). The scaling criteria for more complicated displacements often cannot be fully satisfied under reasonable laboratory conditions (Pozzi and Blackwell, 1963). In such situations, certain scaling criteria of less importance to the physical phenomenon of interest can be relaxed. A basic inspectional analysis of the convection-dispersion equation and Darcy's Law shows that a linear reservoir 500 feet long by 100 feet thick, with permeability varying from 5 to 40 mD can be represented using a model measuring 1 foot by 2.4 inches, with permeabilities ranging from 2.4 to 19.2 D, which correspond to permeabilities that can be obtained using glass bead packs (Orr and Sageev 1986).

3.2.1 Experimental Description

The experimental apparatus is shown in Fig. 3.2.1. The displacing fluid is injected into the model at constant rate using a liquid chromatography pump. The pump can deliver at rates from 0.1 to 9.9 ml/min. After flowing through the bead pack, the effluent passes through a refractive index detector (so that effluent composition is recorded), and is collected for material balance confirmation. The flow in the model is recorded using a high-resolution video tape system. Video images are digitized to give the spatial distribution of compositions. Thus, composition information is available in time and space.

The model is made of glass beads within a glass casing. Permeability variations are created by varying the size of the beads. Bead sizes used range from 0.05 to 0.5 mm diameter, allowing a permeability range from 2.3 to 145 D, with little change in porosity. The casing is first epoxied, packed with beads, and sealed. The model is then heated in a 650^{o}C. oven which vaporizes the epoxy and sinters the glass surfaces and consolidates the bead pack. Model size varies, but a current representative model has an 8.5 by 5 inch, 1/4 inch thick flow matrix, set up with headers to facilitate linear flow. The model is placed on a light table with camera above for taping the experiments.

The base fluids used are refined hydrocarbon oils: light and medium mineral oils, and a series of isoparaffin oils . The mineral oils (Spectrum Chemical Manufacturing Corporation) have viscosities of 20 and 45 cp. The isoparaffin oils are Soltrol 10 through Soltrol 220 (Phillips Petroleum Company), a series of mixtures of C_7 to C_{17} isoparaffins. They range in viscosity from 0.5 to 3.7 cp. For flow visualization, the fluids are dyed. An alternate method is to match the refractive index (RI) of one fluid with that of the glass bead matrix, making the matrix less visible. The effluent composition is monitored using a refractometer calibrated for the fluids used in a given flow experiment. The effluent refractive index along with the pressure drop across the model are collected on a microcomputer-based data acquisition system now being assembled.

The refractive indices of the fluids are manipulated using high refractive index compounds miscible with the base oils. Refractive index of the fluids is varied for two reasons: to modify the refractive index contrast between the two fluids in an experiment (for better refractometer performance), and to match the refractive index of one of the fluids to that of the matrix (for flow visualization). The light mineral oil has a RI of 1.461, and the refractive indices of the Soltrols range from 1.389 to 1.433. Since the RI of glass is approximately 1.51, high refractive index compounds are mixed with the base oils to raise the refractive index to that of glass. Compounds used for manipulating the refractive indices are Styrene (RI=1.545), Toluene (RI=1.494), Benzyl Benzoate (RI=1.568), and Dibutylphthalate (RI=1.490). If the refractive index of the glass matrix is matched exactly with the refractive index of a fluid, the matrix will theoretically be invisible there. Unfortunately, the refractive index of each glass bead is slightly different. It is under investigation now

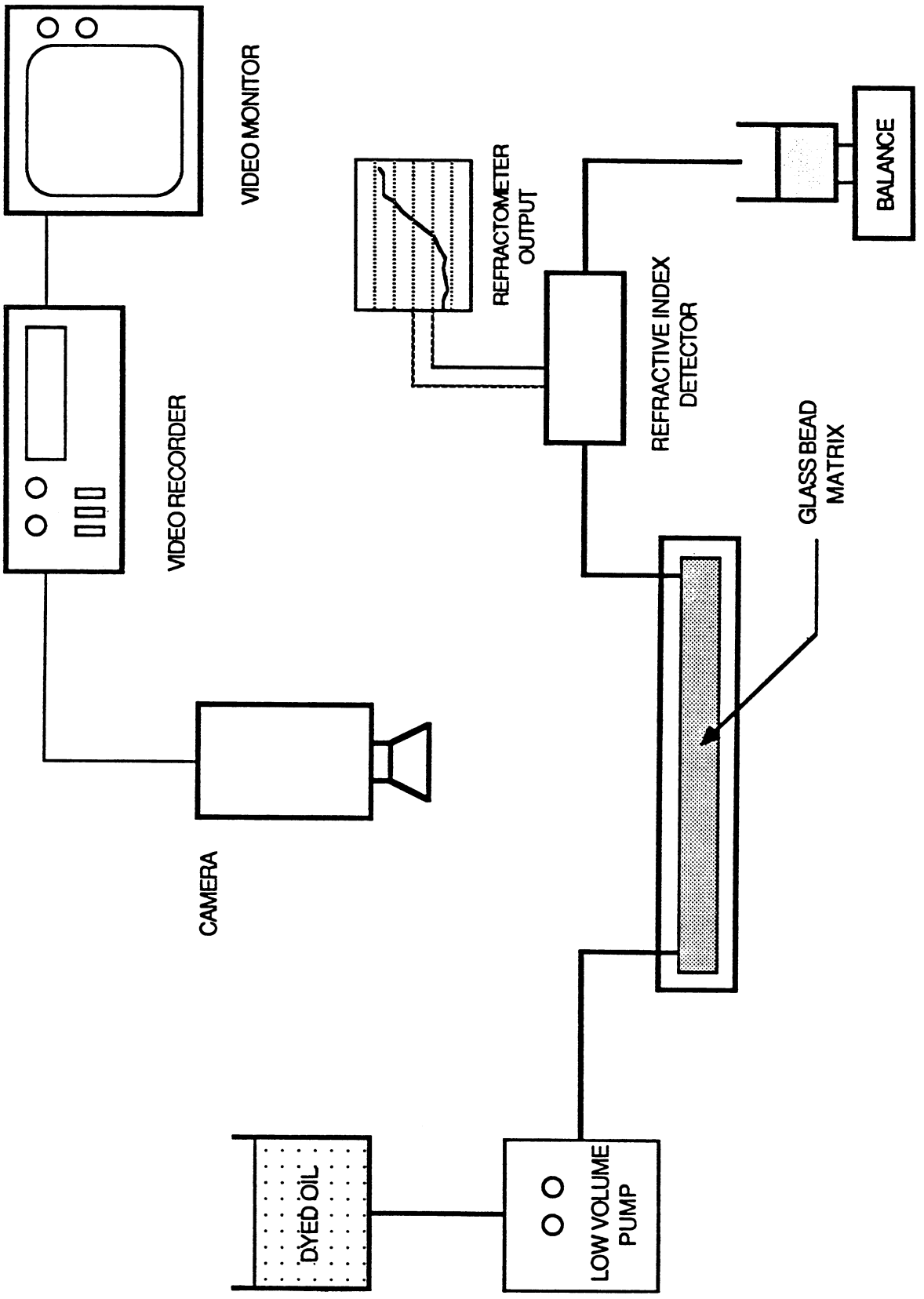

Fig. 3.2.1. Schematic diagram of the experimental apparatus.

whether this variation is small enough to allow the technique of matching fluid and glass refractive indices to be applied for flow visualization.

The runs are taped on a high resolution, 3/4" video tape system. The video tape carries a composite video signal. Single frames of the composite video signal are separated into the red, green, and blue components (RGB separation), and each signal is digitized using equipment available through the Department of Geophysics. Whether the red, green, or blue signal is of most use depends on the colors of dyes used. A frame is digitized into a 512 by 480 array of intensity values ranging from 0 to 255. The intensity data can be transformed into a map of compositions within the bead pack. Such quantitative data can be used for taking cross sectional composition averages, front tracking, finger shape characterization, and comparison with simulations. A contour plot of such digitized data is shown in Fig. 3.2.2. The flow was in a homogeneous medium, with fluids having an adverse viscosity ratio of 14. To verify this digitized image, the picture on the video monitor was frozen and the front traced by hand. The tracing was then digitized at approximately the same resolution. This image is also shown in Fig. 3.2.2. While the computer-digitized contours capture the overall finger structure, they also have some details that are not seen in the video image. These details are artifacts introduced by the digitization process. Work is being done to refine the technique so that digitization noise is reduced.

3.2.2 Summary and Future Work

An experimental apparatus has been developed in which flow visualization experiments can be performed in models with various heterogeneity configurations. The model design has been finalized and the flow apparatus completed. Automated data acquisition for the effluent composition and pressure drop is being set up. At present, control runs in the uniform pack are being done. These will be compared to published data as well as to the simulations described in Section 3.1. Also now underway is experimentation on refractive index matching as described above.

3.3 Summary

The simulation results presented in Section 3.1 offer encouragement that the influence of reservoir heterogeneity on the growth of viscous fingers can be explored computationally. Much remains to be done, however. Additional testing of simulation results against experimental evidence, such as that to be obtained in the displacements described in Section 3.2, is needed to verify that the simulations capture accurately the physical mechanisms that determine transverse finger scales during the sort of extended growth of fingers that would occur in reservoir-scale flows. If that can be established, then simulations can be conducted with confidence to investigate the transition from finger scales that are dominated by viscous effects to those determined by the permeability variation. Those calculations, in turn, are needed to guide development of average representations of the effects of fingering when it has scales smaller than grid blocks used in field-scale simulations. In addition, information about finger scales is needed for assessments of the impact of fingering, transverse mixing and phase behavior on local composition paths and hence displacement efficiency.

The development of adequately verified simulation tools is essential if finger development in large-scale systems is to be studied. The results presented here represent progress toward that goal.

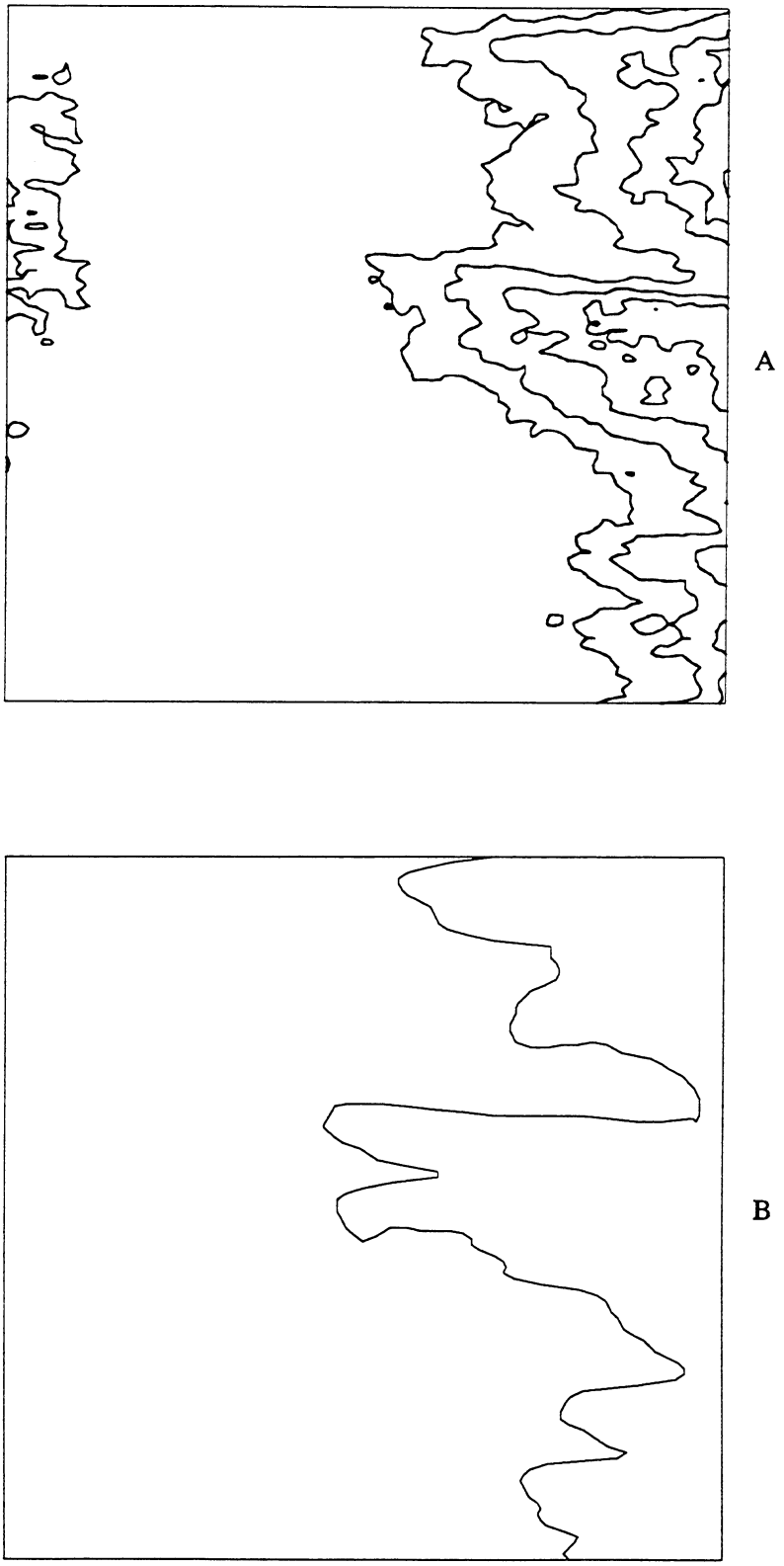

Fig. 3.2.2. Digitized images of an unstable displacement with viscosity ratio of 14; A: contours of the digitized image; B: front traced by hand from monitor.

4. Detection of Reservoir Heterogeneity

The computations of the growth of viscous fingers in heterogeneous porous media reported in Chapter 3 indicate that description of the permeability within a reservoir will be an important component of improved performance predictions. Information about the permeability distribution can be obtained in a variety of ways. Plugs taken from cores obtained from wells give direct information about the vertical distribution, though it is often true that sampling of core plugs is biased to leave out low permeability zones. When porosity and permeability can be correlated, permeability data can be inferred from log data, though there is inevitable averaging that occurs given the limits of resolution of the logging tools used. Core plugs and logs give detailed information in the vertical direction, but little information about variations in permeability in the areal direction. In this chapter we consider the use of pressure transient and tracer tests to obtain additional information about the presence of heterogeneities. In Section 4.1 we examine how correlation in the permeability field influences the performance of both pressure transient and well-to-well tracer tests. Based on the analysis, a test method that makes use of both tracer and pressure test results is proposed. In Section 4.2, the detection in impermeable regions by pressure testing is considered. That study shows that certain large regions that disturb the flow near a well can be detected. In Section 4.3, the effects of a partially communicating fault dividing regions of different flow properties are considered, and the problem of uniqueness of parameters determined is considered. Finally, scaling of the effects of heterogeneity when capillary and viscous crossflow are also important is examined in Section 4.4. Those calculations indicate that under some circumstances, effects of heterogeneity can be represented adequately through the use of pseudo- (or "averaged") relative permeability functions.

4.1 Analysis of Pressure and Tracer Test Data for Characterization of Areally Heterogeneous Reservoirs

S. Mishra

The performance of an enhanced oil recovery process depends primarily on the interaction of the injected fluid with the oil in situ, the heterogeneity of the reservoir rocks and the coupling between these two effects. While fluid mixing and phase behavior can be studied in the laboratory, the nature of variations in the properties of porous media (e.g. permeability, porosity) can only be unravelled through indirect means. Typically, some disturbance is imposed on the physical system, and the resultant response is analyzed to obtain a qualitative and/or quantitative description of the material properties of the system. Thus the detection of reservoir heterogeneities represents a classic inverse problem. Two kinds of well tests are commonly used for this purpose, well-to-well tracer testing and transient pressure testing.

Interwell tracer tests are used to track subsurface fluid movement and infer formation characteristics (Brigham and Abbaszadeh-Dehghani 1987). Such a test involves injecting a tracer slug, driven by a chase fluid, and monitoring the tracer concentration at an adjacent producer. Quantitative interpretation of tracer test data is based on solutions of the convection-dispersion equation

$$\frac{\partial C}{\partial t} = \nabla \cdot \left[D \nabla C - vC \right] \tag{4.1.1}$$

where C is the concentration of tracer and D is the dispersion coefficient.

Pressure transient tests are useful for estimating average formation properties and wellbore conditions, and detecting barriers for fluid flow (Ramey 1982). Such a test is carried out by

perturbing the flow rate at one well and monitoring the resultant pressure response at the same or adjacent wells. Analysis of pressure data is based on solutions of the pressure-diffusion equation

$$\nabla \cdot \left[k \nabla p \right] = \phi \mu c_t \frac{\partial p}{\partial t} \tag{4.1.2}$$

where k is the permeability, p the pressure, ϕ the porosity, μ the viscosity and c_t the total compressibility.

Most well test interpretation models compute an *effective* medium property (e.g. permeability, dispersivity) corresponding to a fictitious homogeneous system, whose behavior matches that of the real heterogeneous system. However, if distributed heterogeneities are to be detected qualitatively and/or quantitatively by well tests, some knowledge of the relationship between these effective parameters and system heterogeneities is required. An associated question of importance is the definition of conditions under which such effective medium approximations can be used for describing heterogeneous media. It is also useful to know the relation between tracer and pressure test responses for the same system, so that information from both tests can be integrated.

This study is concerned with the use of well tests for characterizing macroscopic variations in permeability at the interwell scale. The system of interest, shown schematically in Fig. 4.1.1, is one quarter of a single-layer five-spot within a repeated and balanced production-injection pattern in two-dimensional areal geometry. Our objective is to simulate both well-to-well tracer tests and transient pressure tests in order to examine (a) the sensitivity of well test responses to a heterogeneous permeability field, and (b) the quantification of in-situ permeability variation from the analysis of well test data.

We focus on pressure responses at the injection and production wells, as well as on apparent mixing (dispersion) at the interwell scale due to purely convective tracer flow. Previous studies of flow and transport through heterogeneous permeable media have been restricted to analysis of either the pressure test response (Warren and Price 1961), or the tracer test response (Warren and Skiba 1964, Heller 1971, Smith and Brown 1984, Arya et al. 1985). Similar work in the groundwater literature has been summarized recently (Gelhar 1986). In this section, and the companion work of Mishra and Ramey (1985), we assess the impact of heterogeneities on pressure and tracer test responses.

The methodology adopted in this study, which is similar to the Monte Carlo simulation procedure first presented by Warren and Price (1964), can be briefly described as follows. First, permeability values are assigned to each node of the grid shown in Fig. 4.1.1, such that the assumed statistics of permeability variation are honored. Then pressure history at the injection and production wells is simulated till the attainment of steady-state, and pressure-time data is analyzed. Finally, convective tracer flow is simulated (so that observed tracer dispersion is due to permeability variation only) and breakthrough tracer concentration data are analyzed. This procedure is then repeated for several arrangements of the permeability field for each set of statistical parameters.

4.1.1 Representation of Heterogeneous Media

Field evidence indicates that properties of porous media such as permeability and porosity vary from point to point in a random manner, and also exhibit spatial correlation. In the petroleum literature, variation of permeability has been analyzed statistically by many investigators (Law 1944, Jensen et al. 1985). However, measurements of spatial continuity have been undertaken only recently using geostatistical techniques (Da Costa e Silva 1985). An analysis of the spatial variability and structure of material properties from several groundwater aquifers is also available (Hoeksema and Kitanidis 1985).

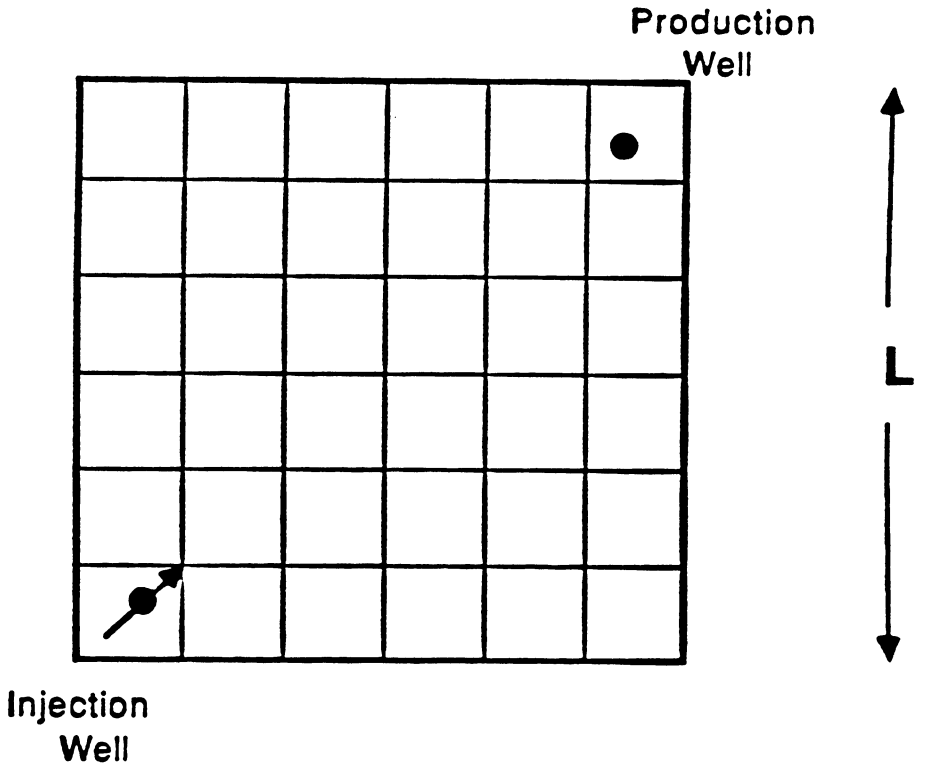

Fig. 4.1.1. System schematic, showing a quadrant from a repeated 5-spot.

Our discussion is restricted to heterogeneous media with variations in permeability only, since the effects of porosity variations on subsurface fluid flow and transport have been shown to be small (Journel and Huijbregts 1978). As it is difficult to describe heterogeneities (i.e. permeability variations) in complete deterministic detail, a stochastic approach is adopted. Permeability is assumed to be a random function with known mean, variance and spatial correlation structure. Furthermore statistical homogeneity is also assumed to be valid in the flow domain, which implies that (i) the mean is independent of location, and (ii) spatial correlation between two samples depends only on their separation (Journel and Huijbregts 1978).

Permeability is characterized by a log-normal frequency distribution, so that variability can be expressed by the Dykstra-Parsons coefficient, V_{DP} (Dykstra and Parsons 1950)

$$V_{DP} = \frac{k_{50} - k_{84.1}}{k_{50}} = 1 - \exp\left(-\sigma_{ln(k)}\right) \tag{4.1.3}$$

where k_{50} and $k_{84.1}$ are the 50^{th} and the 84.1^{th} percentile values from a log-permeability cumulative distribution function (cdf) and $\sigma^2_{ln(k)}$ is the variance. Fig. 4.1.2 shows a hypothetical log-permeability CDF.

Spatial continuity implies correlation between permeabilities of grid blocks that fall within a given area in a two-dimensional system, or a given volume in a three-dimensional system. This can be expressed quantitatively through the semi-variogram, which measures variability, and hence, inversely reflects spatial correlation. For a discrete grid in one dimension, the semi-variogram estimator is given by (Journel and Huijbregts 1978)

$$\gamma(l) = \frac{1}{2\,(n-l)} \sum_{i=1}^{(n-l)} \Big[\, z(i+l) - z(i) \,\Big]^2 \tag{4.1.4}$$

where γ is the semi-variance of z and z is the parameter of interest, in this case $z = ln(k)$, i the grid-block index, l the lag, the distance between block i and block $i + l$ expressed in grid-block lengths and $(n–l)$ the number of samples at lag l. Fig. 4.1.3 shows a hypothetical semi-variogram. Notice that variability increases (and correlation decreases) with increase in lag l. Variability reaches a maximum and equals the variance, $\sigma^2_{ln(k)}$, at some lag, a, beyond which parameter values will be uncorrelated. If Δx is the lag length (i.e. the grid block dimension), then the product $a\Delta x$ is defined to be the range, λ, of the semi-variogram. We shall use the term correlation length scale in preference to range. A dimensionless measure of correlation is then given by the correlation length, λ_D, obtained by normalizing λ with some characteristic flow length, L (see Fig. 4.1.1).

Generation of Autocorrelated Permeability Fields

Several methods are available for generating spatially correlated parameter fields when the mean, variance and correlation length scales are known (Luster 1985). We have used the moving average method, which is conceptually simple and produces an isotropic log-permeability field with a circular semi-variogram in two-dimensions. Briefly, this technique can be described as follows.

1. Extend the simulation grid in each dimension by λ, and generate a set of uniform random numbers, $r(u)$, ranging from zero to one, over the entire augmented grid.
2. Attribute to each node, s, in the simulation grid a value, $y(s)$, equal to the sum of all $r(u)$ located inside a circle of diameter, λ, and centered at s .
3. Standardize the resulting realization, $y(s)$, to a mean of zero and a variance of one, and then rescale so that the mean equals $\ln(\overline{k})$, and variance equals $\sigma^2_{ln(k)}$. This produces the normally distributed log-permeability field, $z(s)$.

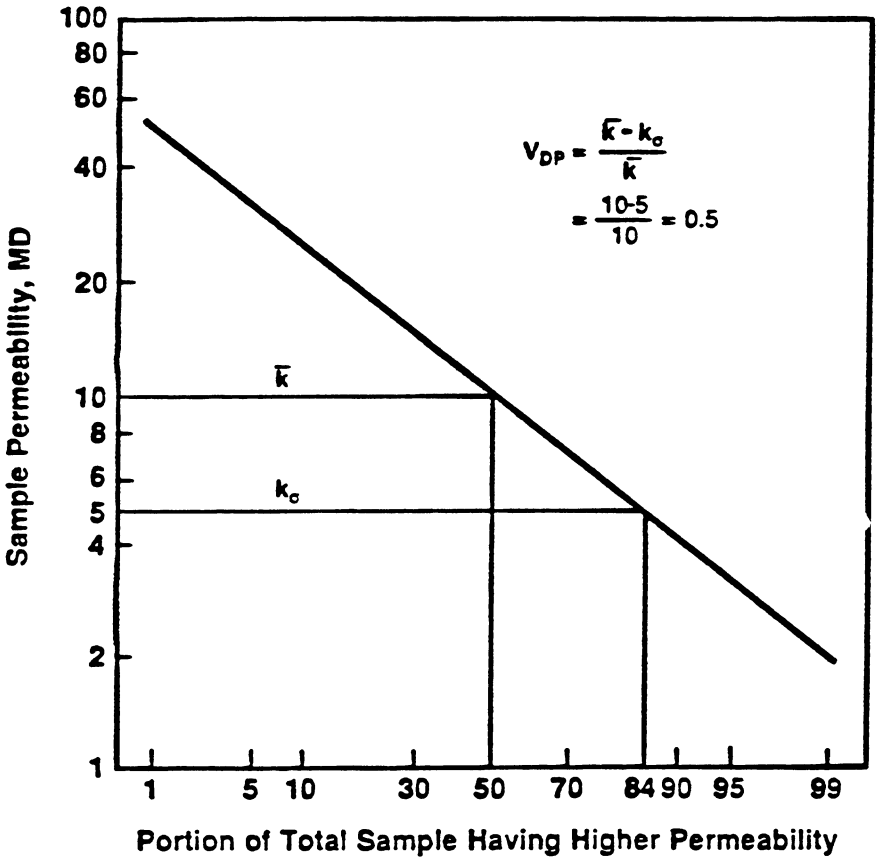

Fig. 4.1.2. Hypothetical log-normal CDF of permeability.

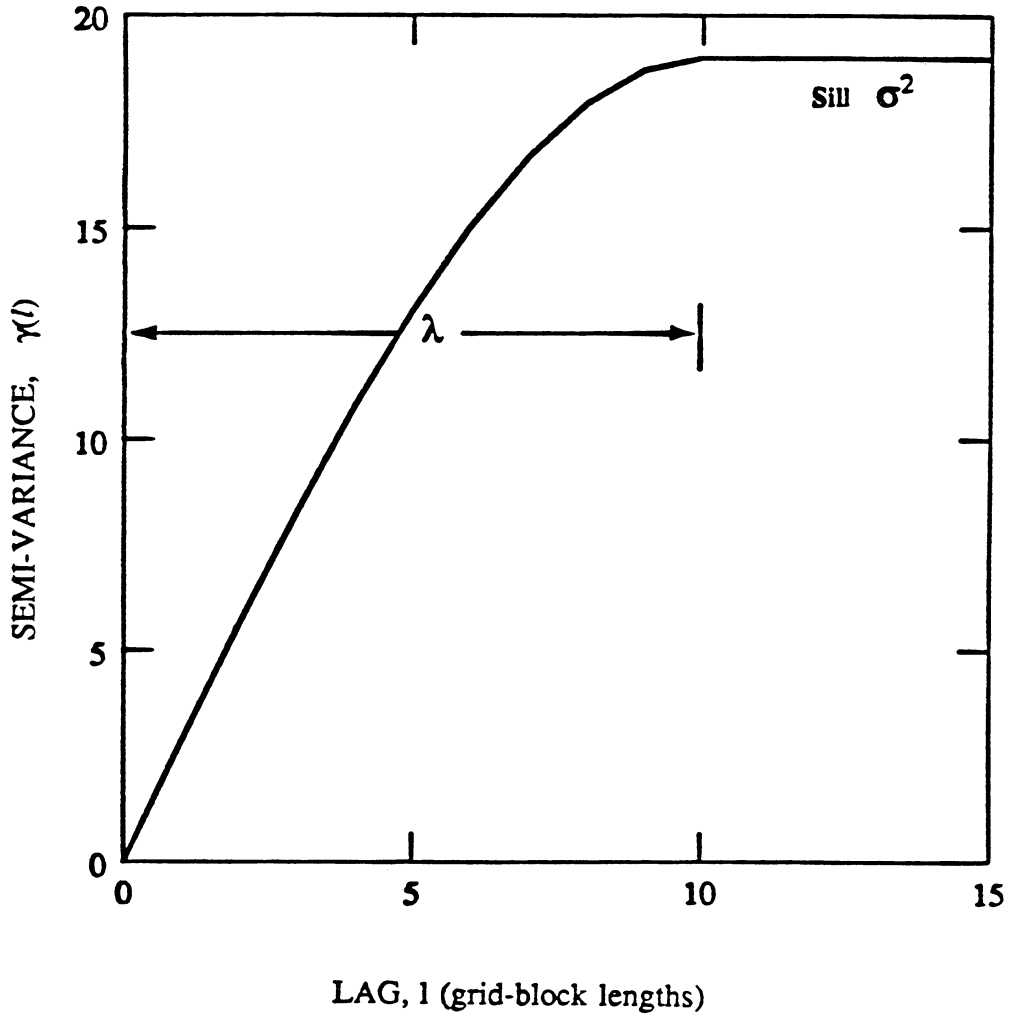

Fig. 4.1.3. Hypothetical semi-variogram.

4. Exponentiate these values of $z(s)$ to obtain permeability values over the required simulation grid.

Fig. 4.1.4a shows the perspective of a typical permeability data set (shown as the natural log of permeability, $ln(k)$) generated using this procedure, and Fig. 4.1.4b shows the corresponding semi-variogram, which is obtained by weighting equally the x- and y-directional semi-variograms calculated with Eq. 4.1.4. As seen from Fig. 4.1.4b, the moving average procedure reproduces reasonably the input variance ($\sigma^2_{ln(k)} = 0.48$) and correlation length ($\lambda_D = 6/15$). For each set of V_{DP} and λ_D, twenty permeability realizations were generated and used as input to the pressure and tracer test simulation codes. Other input parameters are given in Table 4.1.1.

4.1.2 Pressure Test Response

A common observation from well test analysis to date is that field pressure data can be matched with homogeneous system models, even when *a priori* information suggests that the system is heterogeneous. In effect then, pressure tests act like filters to smooth the effect of heterogeneous elements. However, effective medium properties (e.g. permeability) obtained from a homogeneous system match could still contain some information regarding the distribution of heterogeneities, particularly when the medium is sampled at different spatial locations. In what follows, we examine this identification problem in some detail.

Simulation of Pressure Behavior

Pressure behavior was modelled with a single phase simulator, which solves a finite difference analog of Eq. 4.1.2 in two space dimensions. The discretization procedure results in a system of equations implicit in pressure, which is solved directly using a banded-matrix solver. An automatic time-step selector was used to ensure logarithmic time incrementing suitable for conventional pressure analysis. Details of the simulation procedure are given by Mishra (1987).

Since we are considering a balanced injection-production pattern, the system will reach steady-state some time after the onset of injection and withdrawal. The transient pressure decline at the production well, and the transient pressure rise at the injection well, can be analyzed to estimate effective permeabilities around these wells. Assuming infinite-acting radial flow, we can relate permeability k_j to the slope m_j of the linear portion in a semi-log pressure-time graph

$$k_j = \frac{162.6\, q\mu}{m_j\, h} \tag{4.1.5}$$

where q is the flow rate, and h the thickness and the subscript j denotes injection (*inj*) or production (*prd*) as the case may be. The effective permeability calculated with Eq. 4.1.5 measures some average property in a finite zone of influence around the well block. We refer to this value as the injection (or production) well permeability. Note that the well permeability is not necessarily the permeability of the block containing the well.

The steady-state pressure drop between the wells, Δp_{ss}, can also be used to calculate a steady-state interwell permeability, k_{ss}. The appropriate interpretive equation, based on the injectivity equation for a repeated 5-spot, is given as

$$k_{ss} = \frac{282.4\, q\mu F}{h\, \Delta p_{ss}} \tag{4.1.6}$$

The geometric factor F is a function of the inter-well distance, d, and effective well radius, r_o, which was calculated by calibrating a steady-state simulation of a homogeneous system

Table 4.1.1. System Data for Modeling Pressure and Tracer Response

Area, A	20 acres
Grid size (NX * NY)	15 * 15
Thickness, h	10 ft
Porosity, ϕ	0.10
Median k, k_{50}	10 md
Injection rate, q_{inj}	106.3 bbl/day (0.50 pore volumes/year)
Production rate, q_{prd}	106.3 bbl/day (0.50 pore volumes/year)
Tracer Slug size, V_{TR}	0.10 pore volumes
V_{DP} $[\sigma^2_{ln(k)}]$	0.35(0.18), 0.50(0.48), 0.65(1.10)
λ_D	1/15, 6/15, 16/15

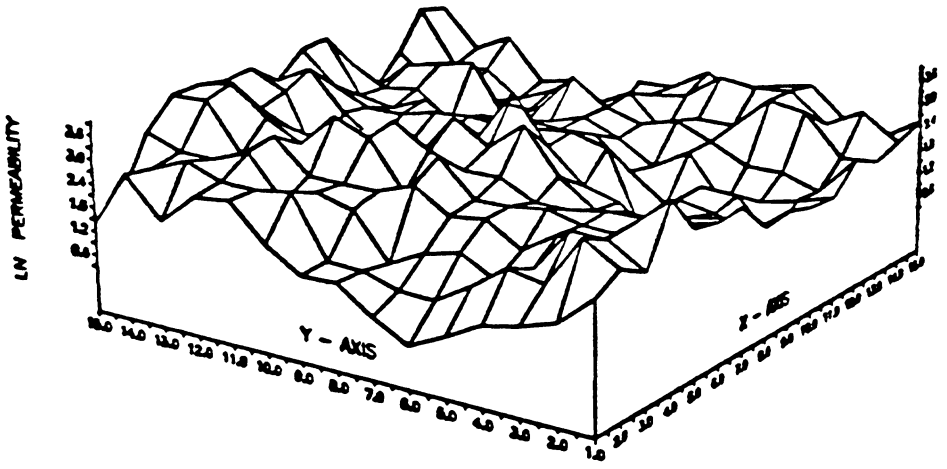

A

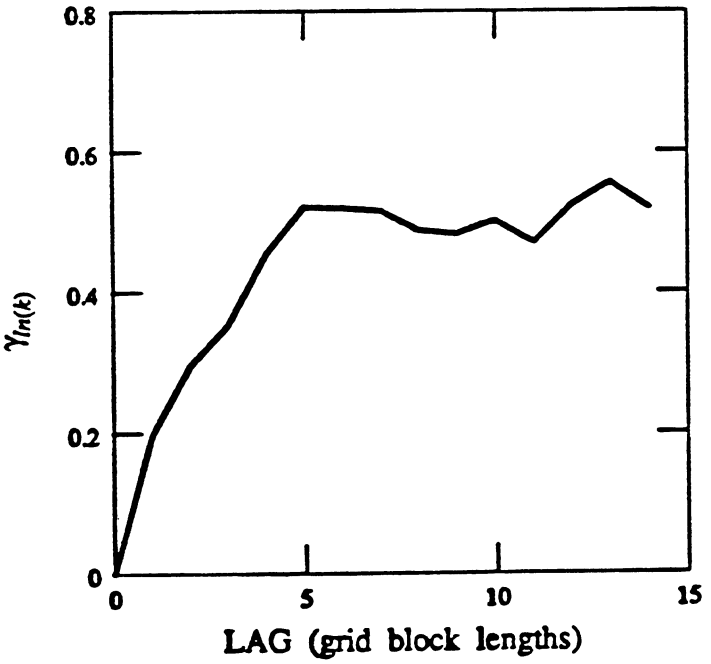

B

Fig. 4.1.4. Simulated permeability field with $V_{DP} = 0.50$ and $\lambda_D = 6/15$; A: perspective plot; B: experimental semi-variogram.

with known permeability. This value of r_o was checked with that computed using an analytical well model formula derived for the same geometry as Fig. 4.1.1 (Abou-Kassem and Aziz 1985), and was found to agree within 1%.

Analysis of Pressure Test Data

For each combination of V_{DP} and λ_D, pressure responses were simulated for the twenty different permeability realizations. Only a few sample pressure-time graphs are shown in Figs. 4.1.5-4.1.7. Notice that when permeability variation and spatial correlation are small, injection and production well responses are nearly symmetrical around the initial pressure level of 4000 psi, and the variability from one realization to another is small (i.e. Fig. 4.1.5). As the measures of heterogeneity V_{DP} and λ_D increase, however, there is greater asymmetry in production and injection well behavior, as well as greater variability in the response of different realizations (i.e. Figs. 4.1.6-4.1.7).

Use of Eq. 4.1.5 for computing transient permeabilities requires the development of a semi-log straight line on a pressure-time graph. Acceptable straight lines were found in all cases, and internal consistency checks were made to verify that appropriate dimensionless time bounds (as calculated from homogeneous system simulations) were satisfied. The slopes of these semi-log straight lines were then used to calculate effective injection and production well permeabilities. Steady-state permeabilities k_{ss} were calculated from Eq. 4.1.6, and with only a few exceptions, these values were found to lie between k_{inj} and k_{prd}. That behavior suggested that some weighted average of k_{inj} and k_{prd} could be used as an estimator of k_{ss}. The geometric mean was tested for this purpose and found to yield good results. Fig. 4.1.8 shows the agreement between k_{ss} values calculated from Eq. 4.1.6, and those predicted by the geometric mean approximation.

Also investigated was the possibility that variation between injection and production well permeabilities could be correlated with some measure of heterogeneity. For this purpose, we define a dimensionless permeability difference as

$$\Delta k_D = \frac{| k_{inj} - k_{prd} |}{k_{ss}} \tag{4.1.7}$$

For each combination of V_{DP} and λ_D, we calculated the average value of this parameter as obtained from twenty simulation runs. Fig. 4.1.9 shows the behavior of the averaged value of Δk_D as a function of V_{DP} and λ_D. Notice that as the correlation length λ_D increases, the mean value of Δk_D also increases, and the increase is larger when V_{DP} is also large. This trend suggests that some suitable combination of V_{DP} and λ_D might prove to be a single correlating parameter. One possible grouping is $\sigma^2_{ln(k)}\lambda_D$, since V_{DP} and $\sigma^2_{ln(k)}$ are related through Eq. 4.1.3. This parameter group, termed *heterogeneity index*, is a convenient measure of heterogeneity because it captures both variability and spatial continuity of the stochastic permeability field.

The choice of $\sigma^2_{ln(k)}\lambda_D$ as a correlating parameter was based on two lines of reasoning. Studies on tracer dispersion in stochastic velocity fields have shown that dispersivity due to convective effects is related to this parameter group (Gelhar 1986). Since our objective is to compare pressure and tracer responses, it is useful to establish the way in which permeability variation (as obtained from pressure test analysis) can be linked to this group. The second argument, which is more heuristic in nature, is as follows. The dimensionless parameter Δk_D, which is a measure of the difference in mean effective permeability at the two wells, quantifies the significance of the trend in the permeability distribution over the scale of the problem. When trends are significant, i.e. when λ_D is of the order of unity, the probability of clustering of like-permeability blocks is high. Thus, if the average permeability around the injection well is higher than the median, the average permeability around the injection well would be lower than the median. The difference between these two values would then be

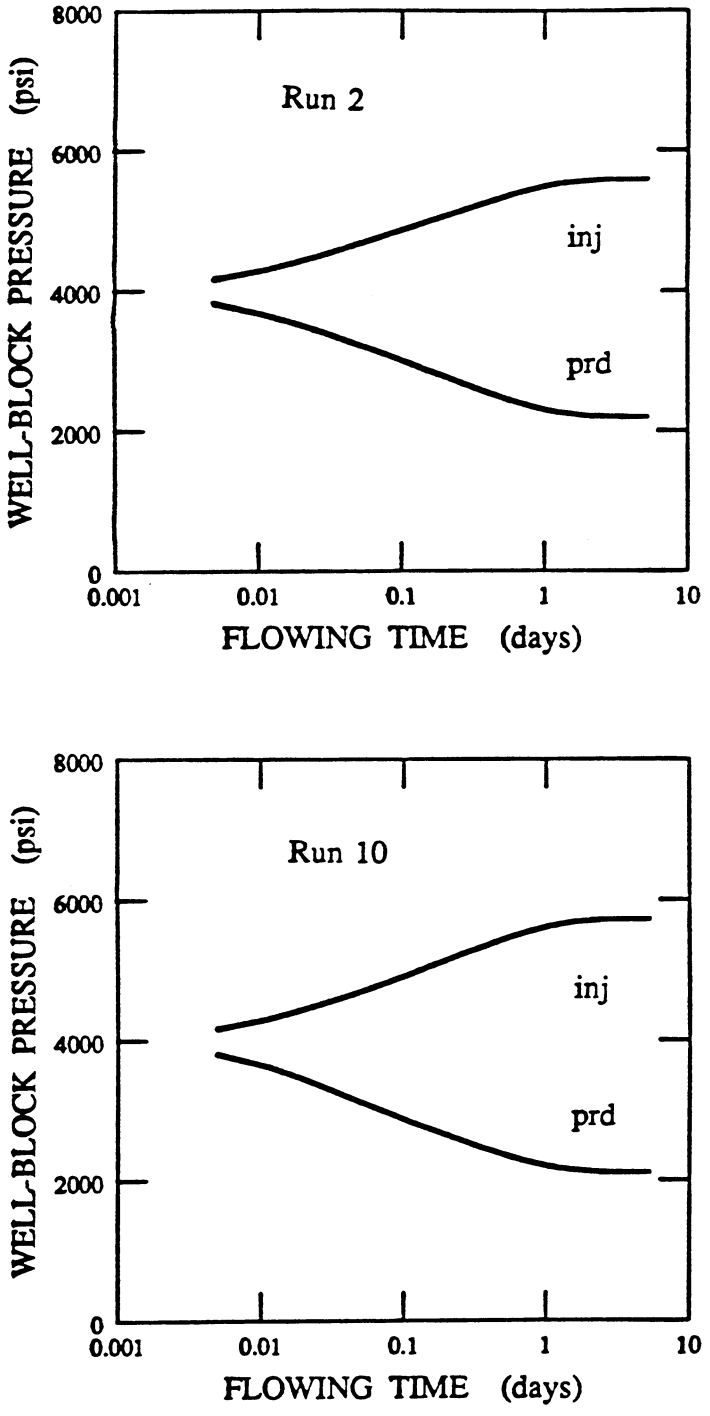

Fig. 4.1.5. Simulated pressure response, $V_{DP} = 0.35$, $\lambda_D = 1/15$.

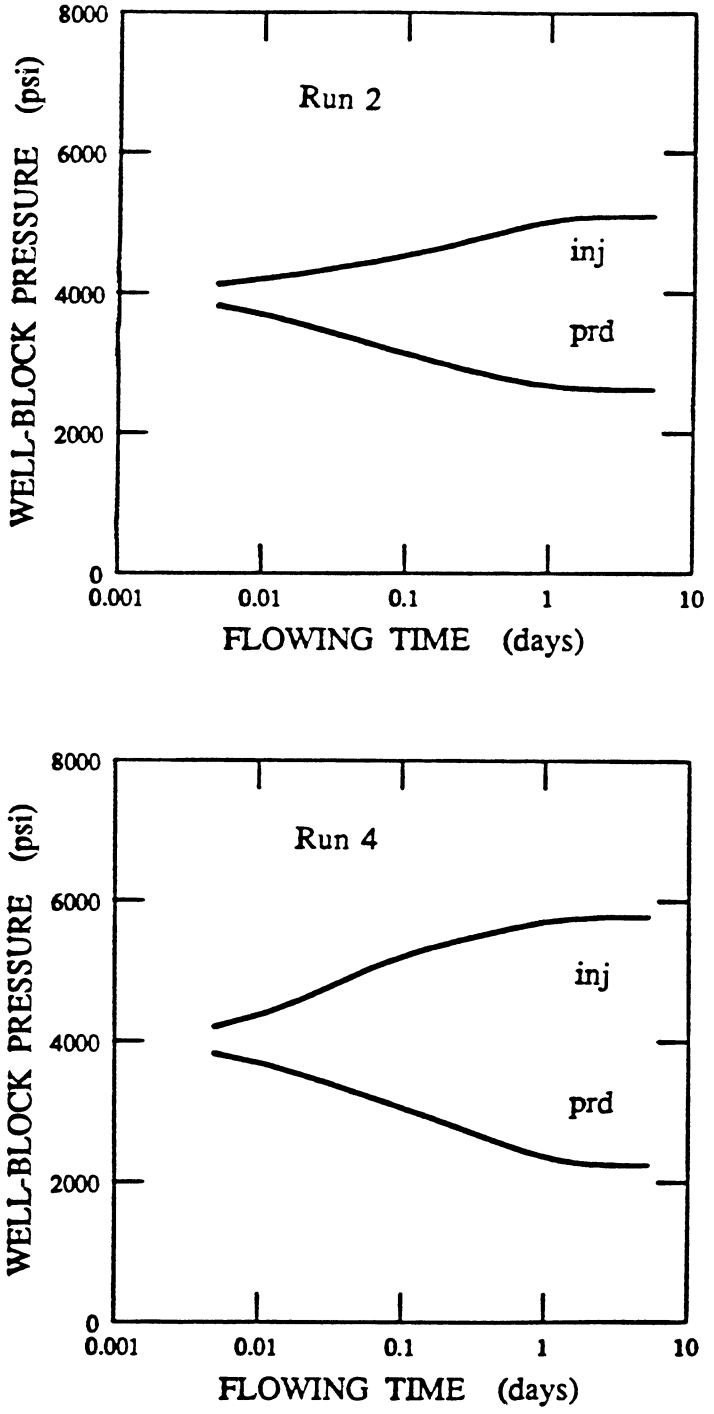

Fig. 4.1.6. Simulated pressure response, $V_{DP} = 0.50$, $\lambda_D = 6/15$.

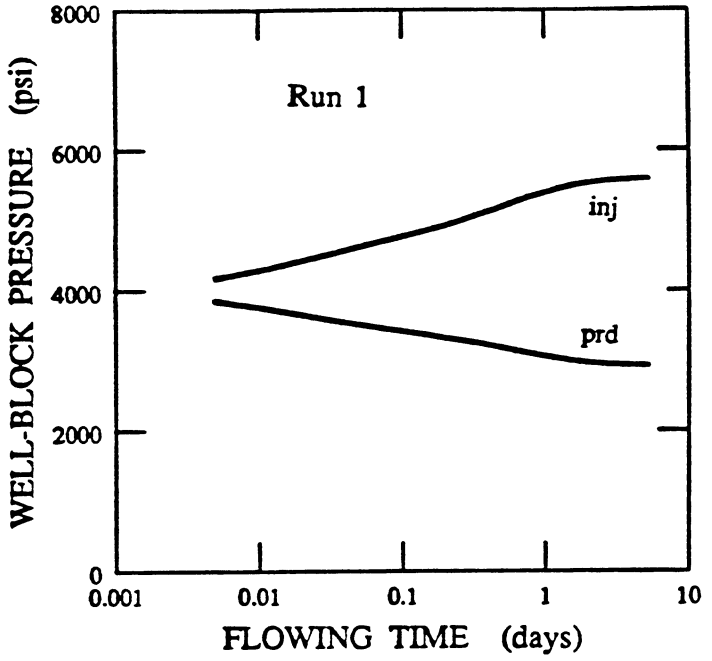

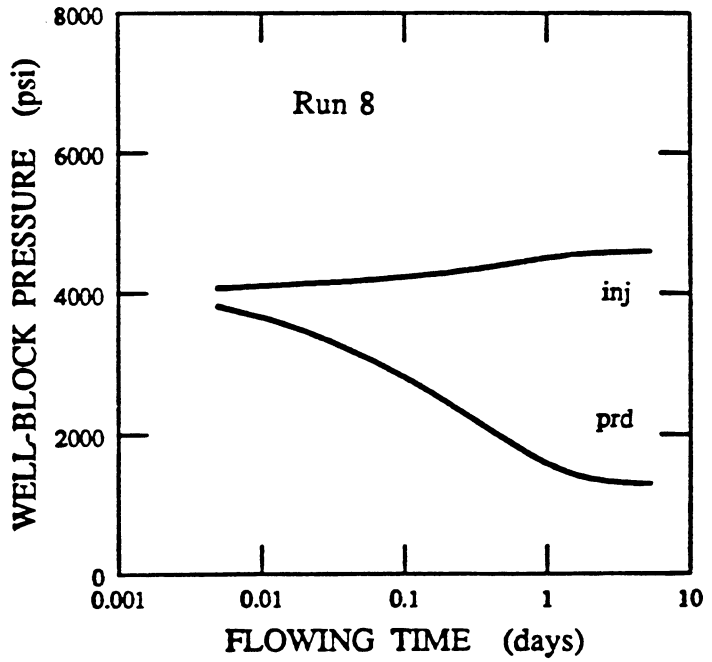

Fig. 4.1.7. Simulated pressure response, $V_{DP} = 0.65$, $\lambda_D = 16/15$.

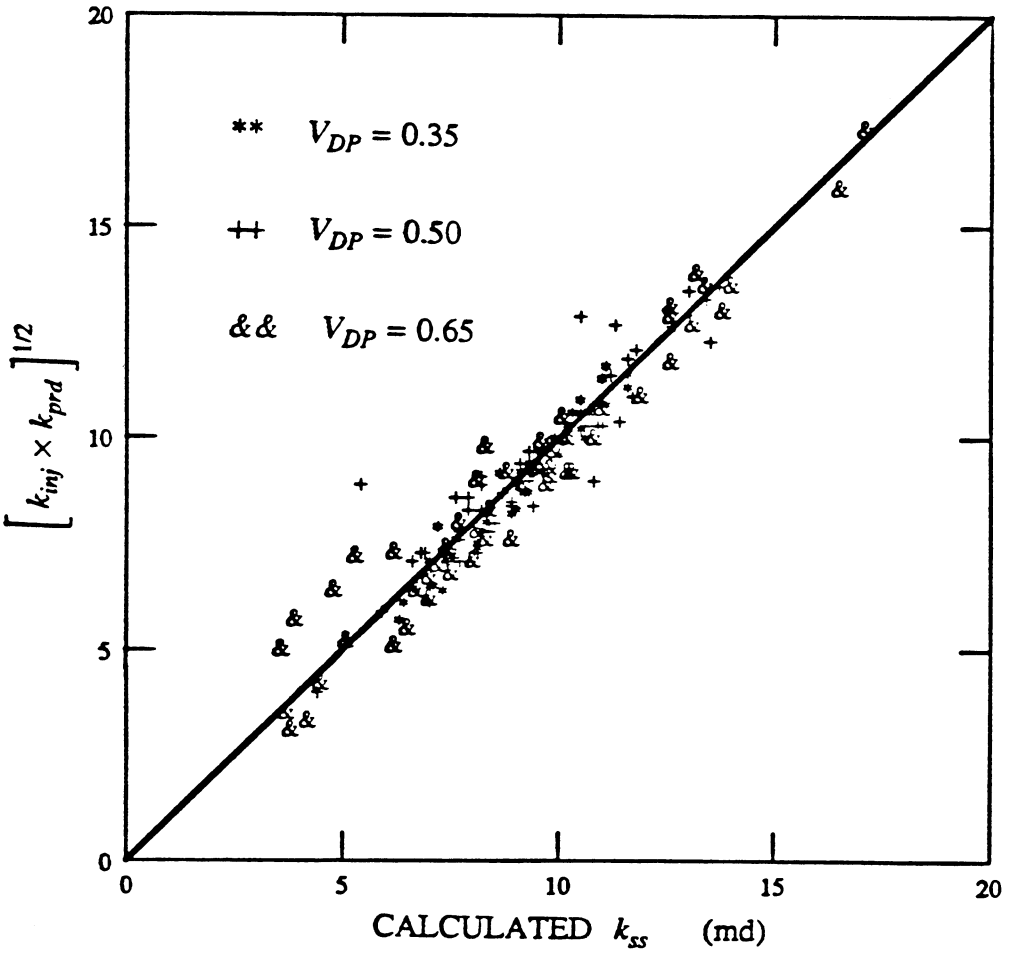

Fig. 4.1.8. Comparison between calculated and predicted k_{ss} values.

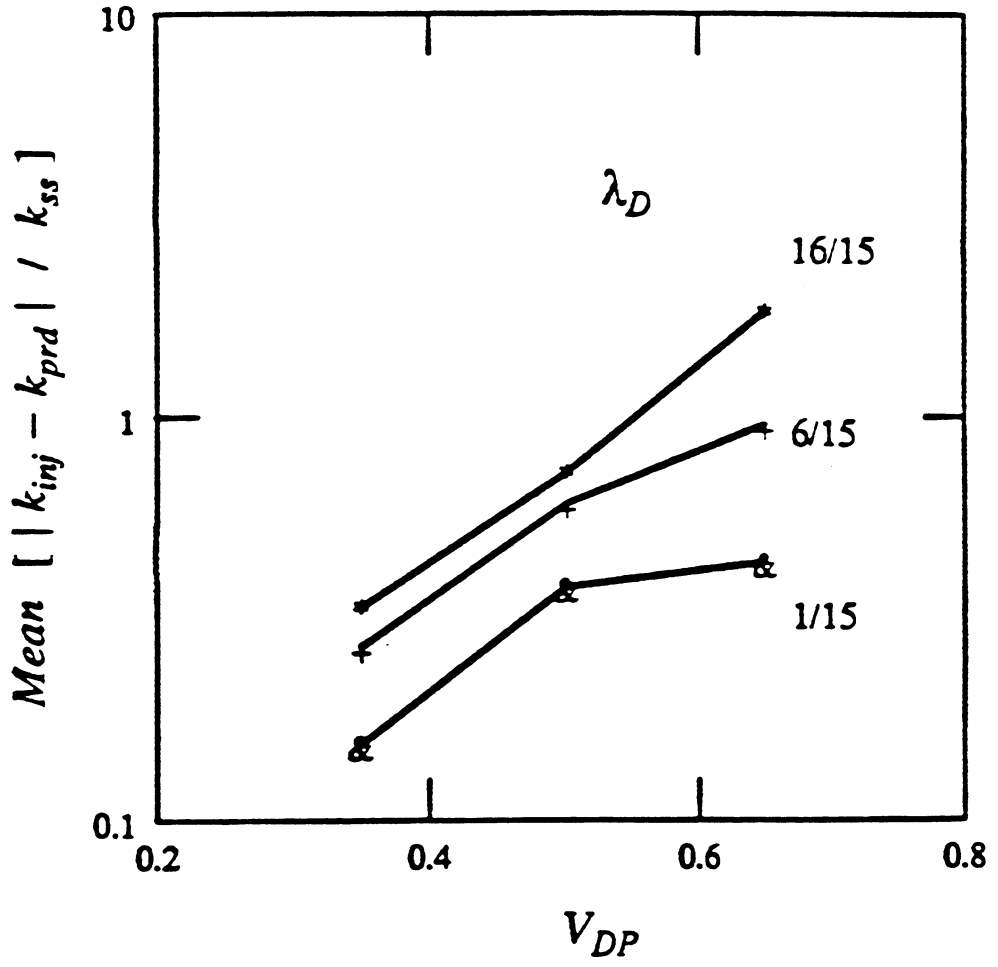

Fig. 4.1.9. Dimensionless permeability difference Δk_D as a function of V_{DP} and λ_D.

proportional to σ_k. Since the steady-state interwell permeability is related to $\bar{k}$, this implies that $\Delta k_D \approx \sigma_k / \bar{k} \approx \sigma_{ln(k)}$. It follows that the group $\sigma^2_{ln(k)}\lambda_D$ is a suitable correlating parameter, at least over some range of Δk_D. Fig. 4.1.10 is a graph of the expected value of Δk_D against $\sigma^2_{ln(k)}\lambda_D$ in log-log coordinates. Also shown are the 95% confidence intervals around the data points. A least-squares fit of this data set yields the following power law relationship

$$\Delta k_D = 1.3 \left[\sigma^2_{ln(k)}\lambda_D \right]^{1/2} \tag{4.1.8}$$

This simple relation can be used to quantify in situ permeability variation from pressure transient data alone.

4.1.3 Tracer Test Response

The convection-dispersion equation (Eq. 4.1.1), which is commonly used to model tracer flow in porous media, represents tracer transport as the result of two physical processes, convection and dispersion (Bear 1972). Convection refers to bulk fluid flow, and dispersion to spreading of the tracer slug due to a combination of molecular diffusion and local velocity fluctuations. Diffusional effects are important only at the pore scale, and/or at low displacement velocities (Perkins and Johnston 1963). Consequently, it is customary to lump all dispersive factors into one transport parameter, the dispersion coefficient, D. Based on laboratory measurements, D is generally expressed as the product of displacement velocity, v, and a constant , α, known as dispersivity, a characteristic of the medium (Bear 1972). Such a representation is sometimes referred to as the Fickian model, by analogy with molecular diffusion processes.

Application of the Eq. 4.1.1 to field scale problems has yielded inconsistent results, particularly with respect to dispersivity. Field dispersivities have been found to be orders of magnitude higher than those measured in the laboratory, even for similar media. Moreover, dispersivity has also been observed to be dependent on the time and scale of displacement. Such anomalies have been ascribed to large-scale formational heterogeneities which are successively encountered as tracer transport progresses in space. See Ref. 21 for a review of pertinent field evidence.

A tracer test is essentially a displacement experiment at the interwell scale, and hence convective effects (caused by local permeability/velocity variations) are likely to be the dominant mechanism of tracer transport. Therefore it is necessary to examine the appropriateness of the convection-dispersion equation for modelling tracer flow at this scale. Of particular interest is whether the solutions of Abbaszadeh-Dehghani and Brigham (1982), derived for homogeneous systems, can be used to analyze tracer breakthrough curves for heterogeneous media and yield effective dispersivities. Associated objectives are to examine the conditions under which Eq. 4.1.1 is valid, and to relate dispersivity to measures of permeability variation.

Simulation of Tracer Flow

The numerical tool used in modelling tracer flow under steady-state unit mobility ratio miscible displacement conditions was the USGS 2-D Solute Transport simulator (Konikow and Bredehoeft 1978), which is based on a method of characteristics scheme first proposed for solving miscible displacement problems (Garder et al. 1964). This simulator solves a finite-difference approximation to the flow equation (Eq. 4.1.2) to calculate the steady-state velocity distribution. A particle tracking procedure is then used to represent convective flow, and a two-step explicit procedure to solve a finite-difference equation that describes the effects of hydrodynamic dispersion and fluid sources and sinks. Details of the model and the computer code is given by Konikow and Bredehoeft (1978).

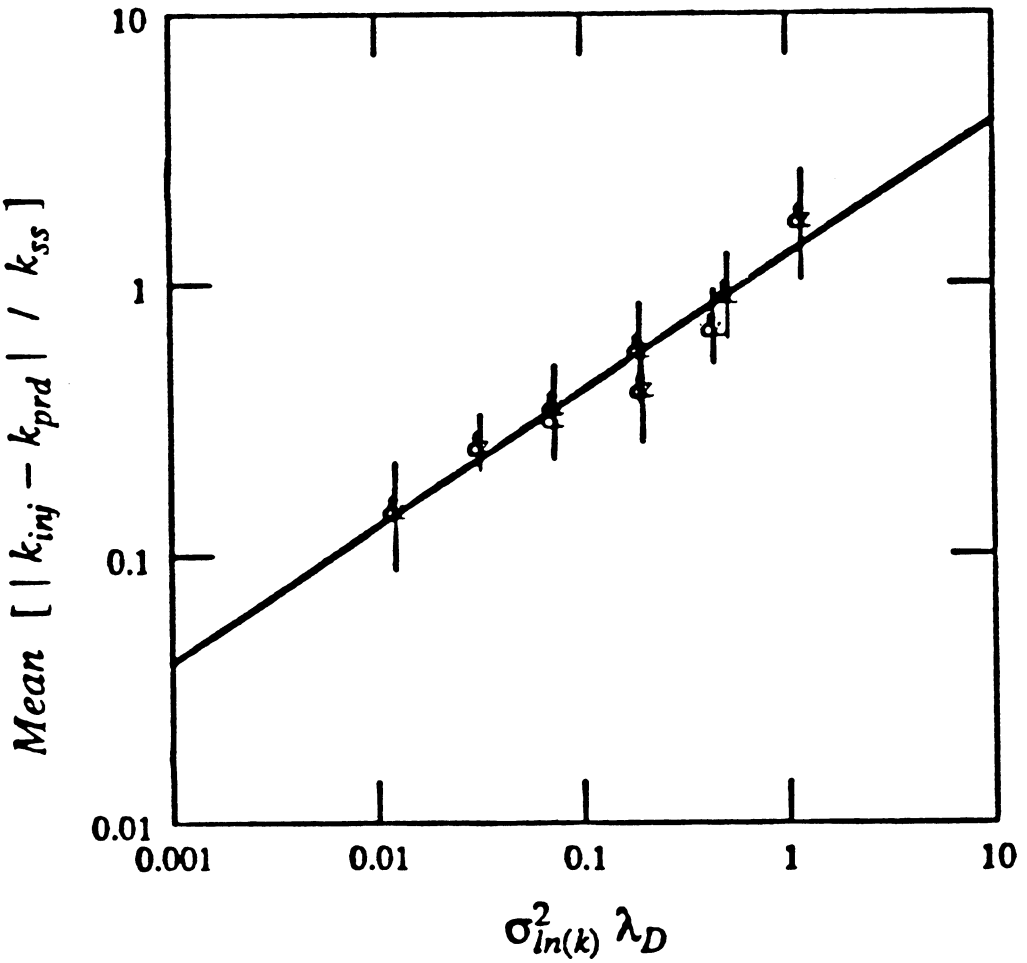

Fig. 4.1.10. Relationship between Δk_D and heterogeneity index $\sigma^2_{ln(k)}\lambda_D$.

The computer program was verified by matching simulated tracer breakthrough curves for homogeneous systems with the analytical solutions of Abbaszadeh-Dehghani and Brigham (1982). Comparison of the analytical and numerical model results, shown in Fig. 4.1.11, indicates that use of the method of characteristics effectively eliminates the problem of numerical dispersion, a drawback of conventional finite-difference or finite-element modeling of the convection-dispersion equation.

The basis for interpreting simulated tracer test data is an analytical solution of the Eq. 4.1.1, derived for unit-mobility ratio flow in a repeated 5-spot (Abbaszadeh-Dehghani and Brigham 1982). The expression for pattern tracer breakthrough curve is developed by first combining the mixing that occurs within each streamline with its time of travel, and then integrating this result over all the streamlines. Details of the derivation are given by Abbaszadeh-Dehghani and Brigham (1982). Here we present only the final solution

$$C = 0.57726\, C_i\, F_r \sqrt{\frac{a}{\alpha}} \int_0^{\frac{\pi}{4}} \frac{\exp\left[\dfrac{0.645776}{Y(\psi)}\,\dfrac{a}{\alpha}\left[V_{pDBT}(\psi) - V_{pD}\right]^2\right] d\psi}{Y(\psi)} \qquad (4.1.9)$$

where C is the concentration of tracer in the produced fluid, C_i the injected concentration, a the distance between wells in a five spot (2L), $V_{pDBT}(\psi)$ is the pore volumes injected at breakthrough of streamline ψ, V_{pD} is the total pore volumes injected and F_r is the injected tracer slug size expressed in pore volumes. The $Y(\psi)$ function is a hyperelliptic integral relating velocity in a streamline and dispersivity to total spreading in the streamline. Note that when the system size and injection parameters are known, observed tracer concentration is a function of only one parameter, dispersivity, α.

Analysis of Tracer Test Data

Tracer responses were generated for several cases, only a few of which are presented here. Figs. 4.1.12-4.1.14 show tracer breakthrough curves for the same physical systems for which pressure responses were graphed in Figs. 4.1.5-4.1.7. As expected, tracer concentration-time data show greater sensitivity to permeability variation than transient pressure data. Similar behavior has been observed for the case noncommunicating layered reservoirs in a repeated 5-spot (Mishra and Ramey 1985).

Breakthrough in all simulated tracer tests occurred much earlier than a time corresponding to an injected volume of approximately 56,000 bbl (0.72 pore volumes), which is the theoretical value for breakthrough in a homogeneous 5-spot. Early breakthrough indicates the presence of preferential flow paths or substantial fluid mixing. Since the simulation model considers no dispersion and numerical dispersion effects have been minimized through the use of the method of characteristics, the breakthrough behavior must have been caused by velocity fluctuations in a spatially varying permeability field.

The overall shapes of the tracer breakthrough curve also indicate the nature of the flow system. In general, two types of flow behavior can be distinguished qualitatively. The first kind (e.g. Fig. 4.1.12), which we term diffusive, or Fickian, produces a tracer response resembling that of a homogeneous system where the slug has been dissipated by mixing. In this case, the tracer response can be matched with the appropriate solution of the convection-dispersion equation (Abbaszadeh-Dehghani and Brigham 1982) to determine an effective dispersivity. Since slug dilution is attributable only to velocity/permeability variations in a heterogeneous flow field, the computed effective dispersivity is essentially a measure of permeability variation.

The second kind of flow behavior (e.g. Figs. 4.1.13 and 4.1.14), termed convective, or non-Fickian, is characterized by multiple peaks in the tracer breakthrough curve, indicating the presence of more than one channel for fluid flow. Such a geometry, consisting of multiple discrete flow channels within a single layer, is effectively equivalent to a layered system with several noncommunicating strata. Because the mobility ratio is unity, tracer response in this

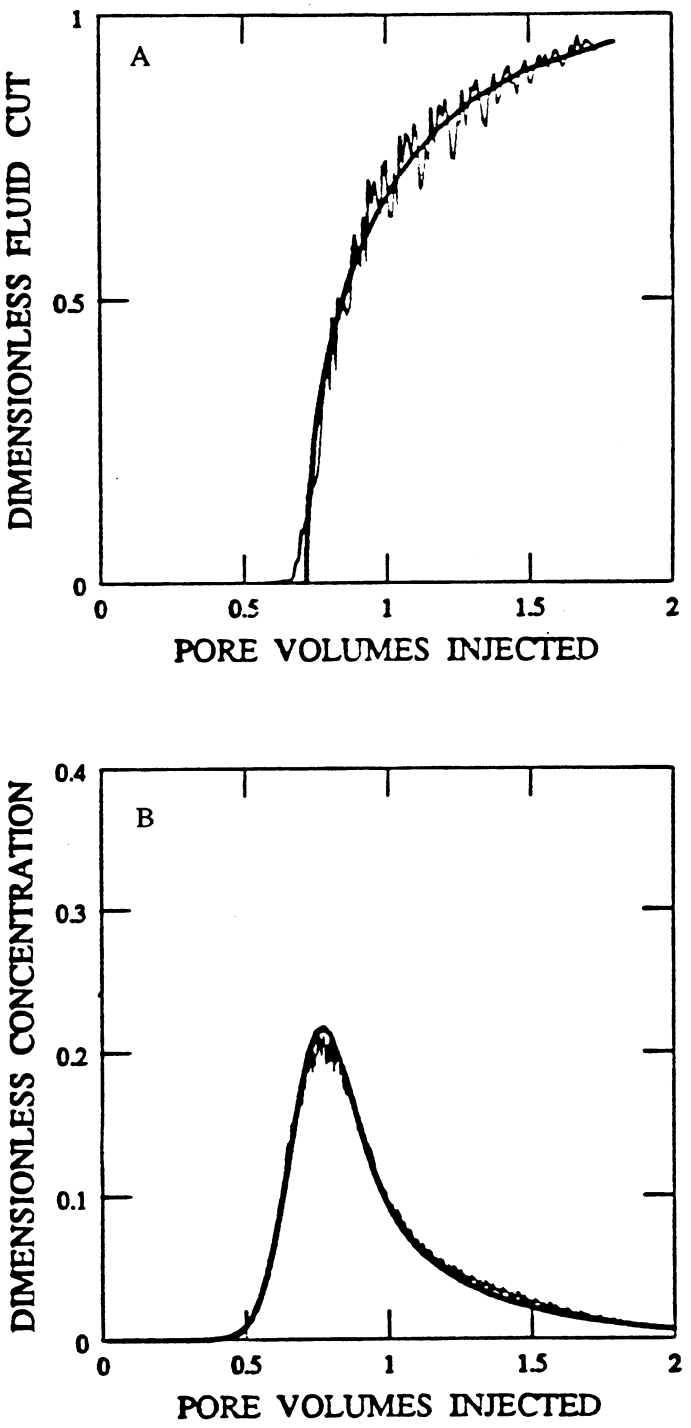

Fig. 4.1.11. Tracer flow simulator validation; A: continuous injection, no dispersion; B: slug injection, $\alpha = 10\ ft.$

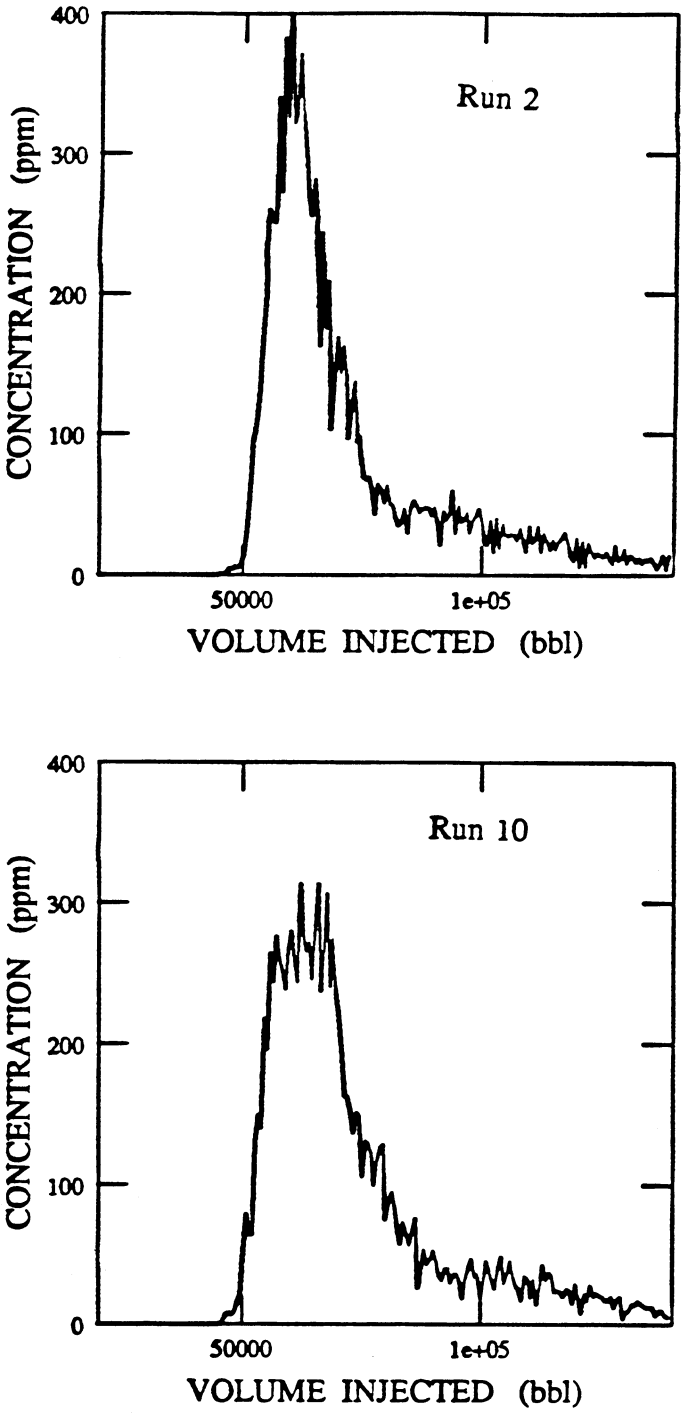

Fig. 4.1.12. Tracer breakthrough curve, $V_{DP} = 0.35$, $\lambda_D = 1/15$.

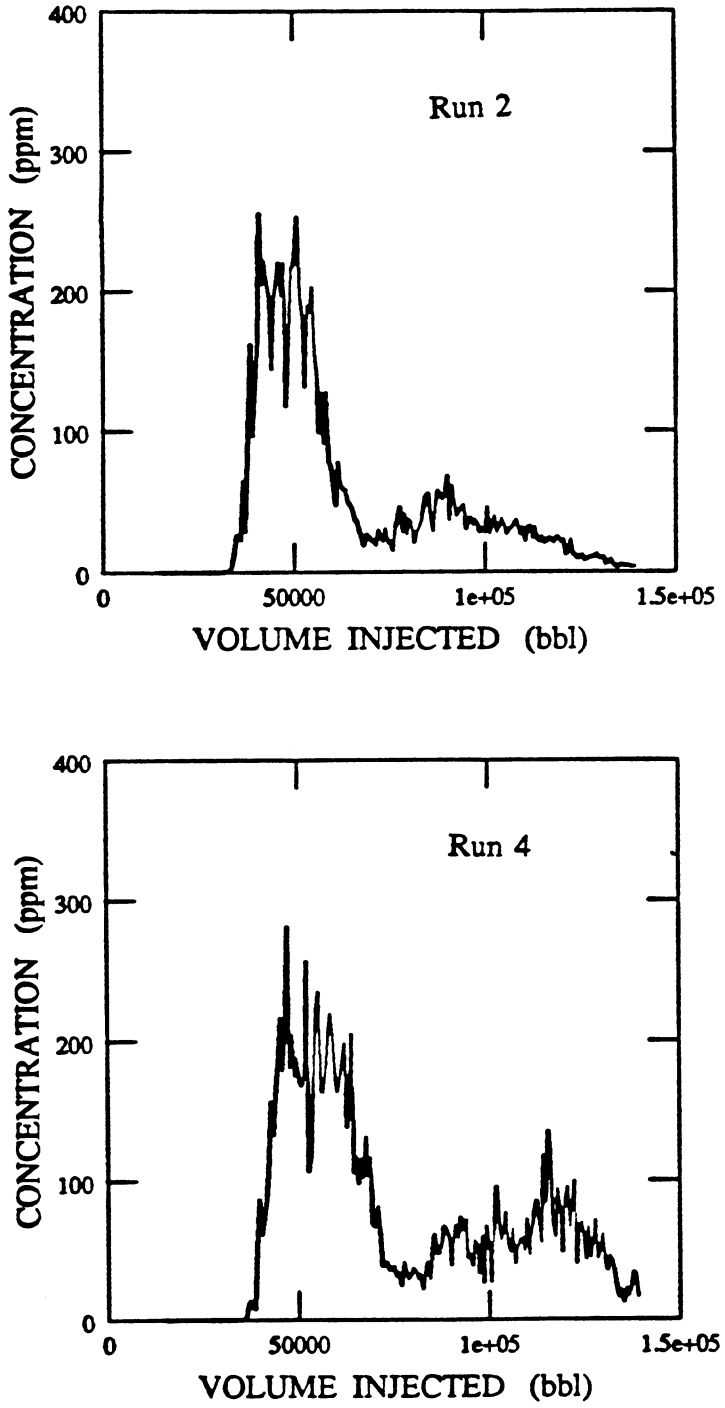

Fig. 4.1.13. Tracer breakthrough curve, $V_{DP} = 0.50$, $\lambda_D = 6/15$.

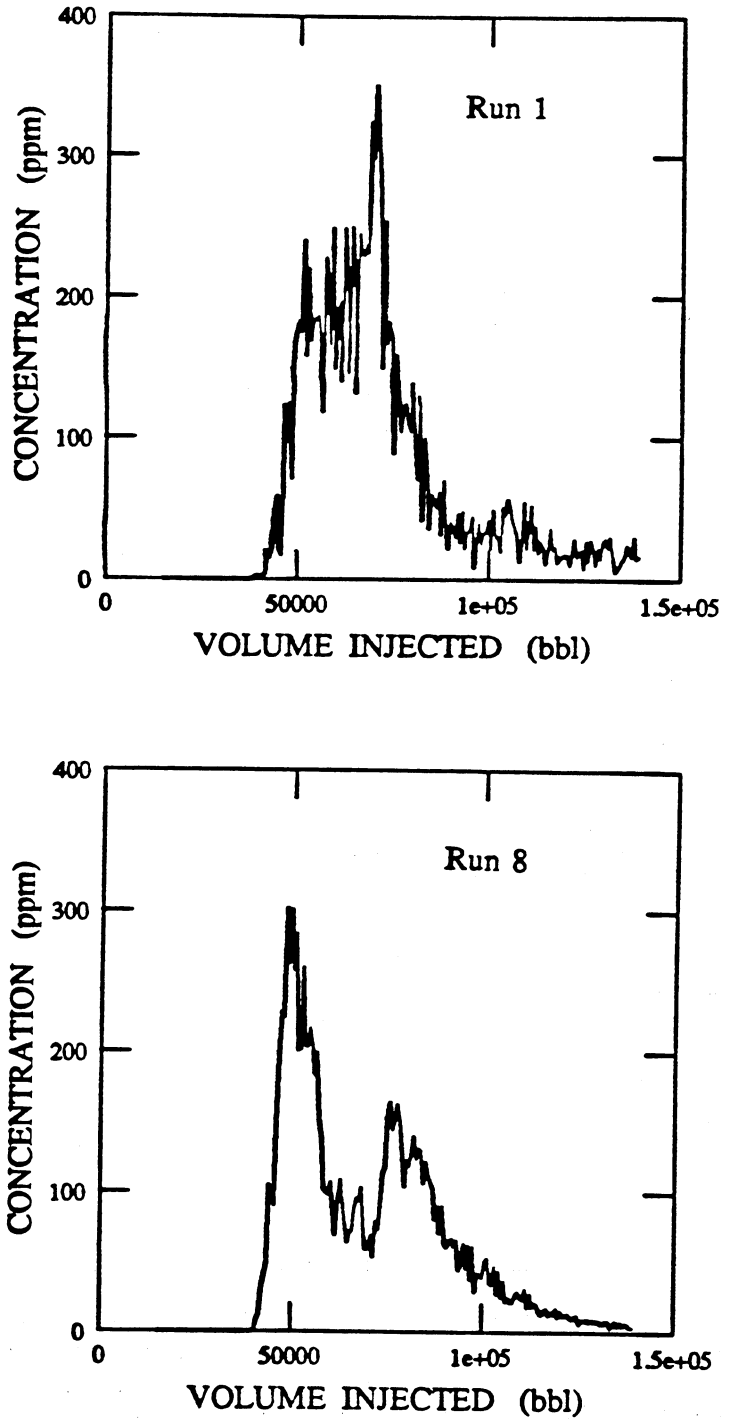

Fig. 4.1.14. Tracer breakthrough curve, $V_{DP} = 0.65$, $\lambda_D = 16/15$.

system can be modelled by superposition of individual layer solutions, and a nonlinear optimization scheme can be used to deconvolve the integrated tracer breakthrough curve for estimating effective-layer properties (Abbaszadeh-Dehghani and Brigham 1982).

Validity of the Convection-Dispersion Equation

It has been pointed out that the Fickian model of field-scale dispersion is appropriate only for large time and length scales (Gelhar 1986). Thus, when the dimensions of the flow field are fixed, as in this study, Fickian behavior can be expected only if permeability variation and correlation lengths are small enough to permit sufficient averaging of spatial velocities during tracer transport. In the simulations described here, Fickian behavior was observed for small V_{DP} and λ_D. For larger values of V_{DP} and λ_D preferential flow paths were generated and caused a non-Fickian (multi-modal) tracer response, and the convection-dispersion equation with a single-value of dispersivity could no longer be used to match effluent tracer concentration data.

These observations can be quantified using the heterogeneity index ($\sigma^2_{ln(k)}\lambda_D$) defined previously. This group contains information on the degree of permeability variation, as well as the spatial scale over which such variations persist. In Fig. 4.1.15, we plot the percentage of Monte Carlo runs showing non-Fickian behavior as a function of $\sigma^2_{ln(k)}\lambda_D$. As expected, the relationship is monotonically increasing, and asymptotically approaches Fickian and non-Fickian limits at the two extremes. Note that the dashed portions represent extrapolation beyond the range of available data. Fig. 4.1.15 establishes the uncertainty associated with Monte Carlo simulation results of convective flow processes, even when the statistics of the medium are known. However, it is possible to deduce approximately conditions under which Fickian or non-Fickian behavior will be dominant. Fig. 4.1.15 suggests that Fickian behavior is restricted to values of $\sigma^2_{ln(k)}\lambda_D$ less than about 4×10^{-2}, and non-Fickian behavior is expected for values of $\sigma^2_{ln(k)}\lambda_D$ greater than about 4×10^{-1}.

Smith and Brown (1984) computed effective dispersivities in a two-dimensional heterogeneous medium by fitting space-averaged concentration-time data to a Fickian model. The maximum value of $\sigma^2_{ln(k)}\lambda_D$ considered was about 8×10^{-2} (see their Fig. 4.1.6a), which is slightly higher than our limiting criterion for diffusive behavior. This also explains the general success of the Fickian model in matching their simulated data.

Arya *et al.* (1985) followed a similar procedure for matching concentration-time data in two-dimensional randomly heterogeneous media, and found that the Fickian model may not be appropriate when permeability variation and correlation length scale are large. Their results suggest that diffusive behavior is limited to cases when λ_e is less than $0.1–0.2\ L$, where λ_e is the integral range of an exponential semi-variogram of log-permeability values, and is approximately equal to $0.32\ \lambda$. They used a V_{DP} value of 0.6 (Arya, A., personal communication), for which case their criterion becomes equivalent to $\sigma^2_{ln(k)}\lambda_D < 3–6 \times 10^{-2}$, which is consistent with our results.

Significance of Effective Parameters

At this stage, we ask if the effective parameters calculated from tracer test data (i.e. dispersivities and effective-layer properties) can be correlated with some measure of permeability variation such as the heterogeneity index. Based on the criteria derived from Fig. 4.1.15, we inferred that Fickian behavior was probable for (a) $V_{DP} = 0.35$, $\lambda_D = 1/15$, and (b) $V_{DP} = 0.50$, $\lambda_D = 1/15$. For these two cases, effective dispersivities were computed from all simulation runs exhibiting qualitative Fickian behavior (unimodal tracer breakthrough response). The average value of dispersivity, α, for each of these two data sets, normalized by the characteristic flow length, L, is plotted in Fig. 4.1.16 as a function of $\sigma^2_{ln(k)}\lambda_D$. The

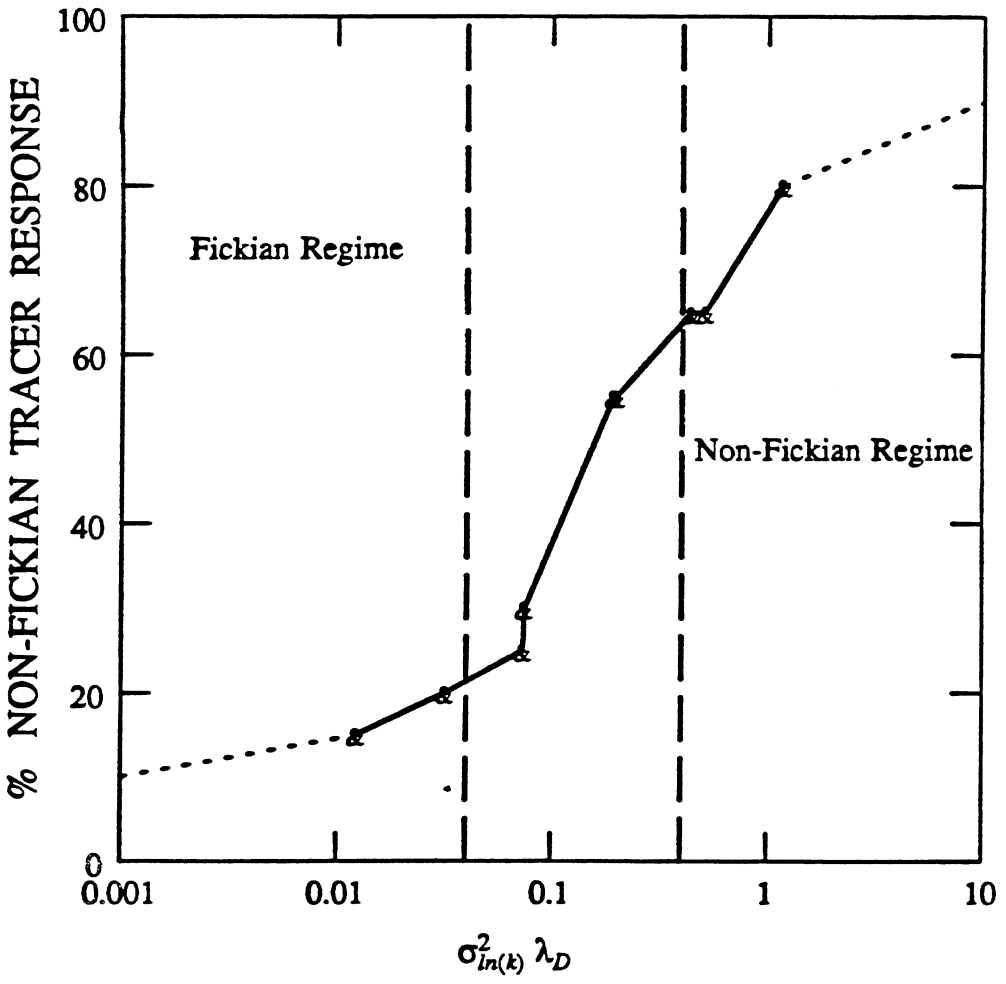

Fig. 4.1.15. Influence of $\sigma^2_{ln(k)}\lambda_D$ on nature of tracer response.

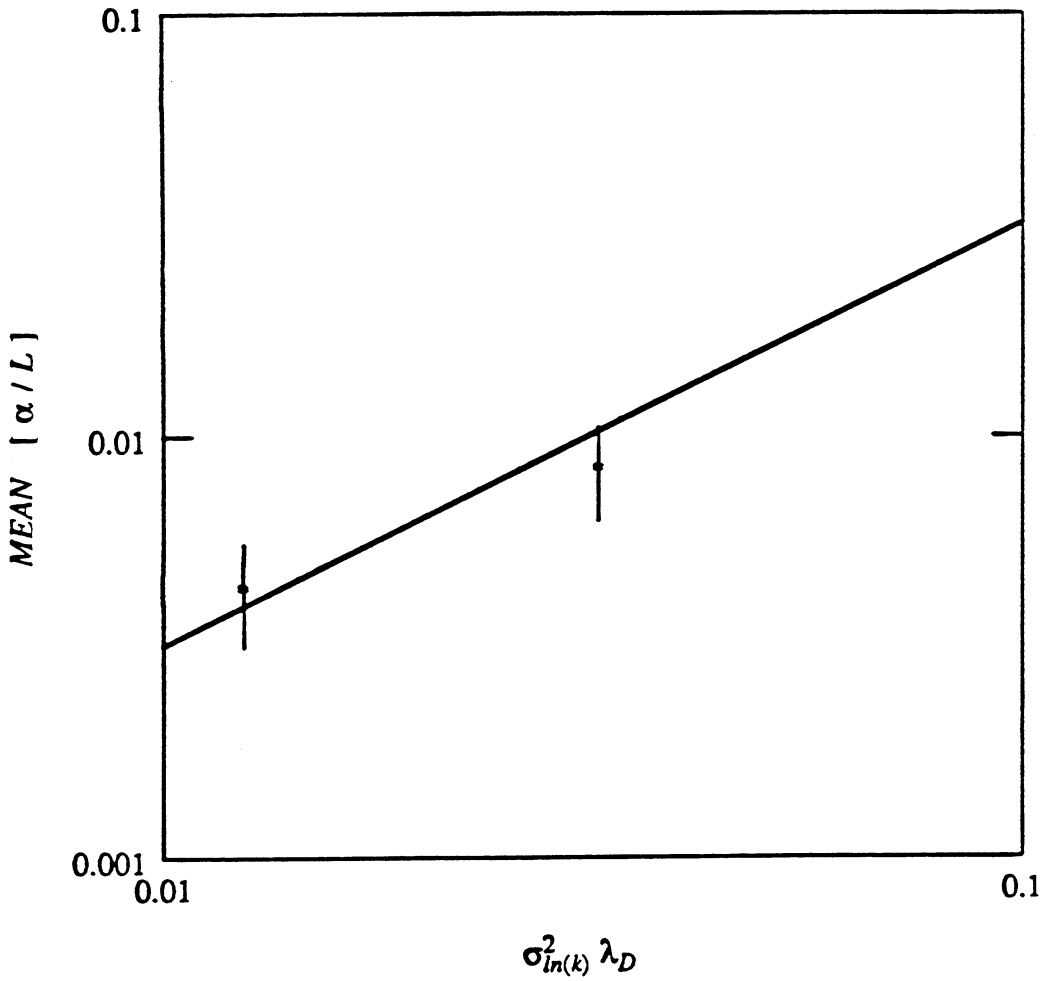

Fig. 4.1.16. Comparison of computed Fickian dispersivities with analytical results.

straight line shown is the analytical result of Gelhar and Axness (1983) for two-dimensional isotropic media derived from stochastic theory

$$\frac{\alpha}{L} = 0.32\ \sigma^2_{ln(k)}\lambda_D \qquad (4.1.10)$$

where α is the dispersivity.

Also shown are 95% confidence intervals around the data points. The agreement between simulation results and predictions of stochastic theory is reasonable in view of the limited number of Monte Carlo runs used for averaging.

For the non-Fickian examples, it was possible to match most tracer breakthrough curves with a 2-layered model. In each case, the dispersivity, α, was fixed at an arbitrary value of 1 ft. so as to make the problem convection dominated. A non-linear regression program (Abbaszadeh-Dehghani and Brigham 1982) was then used to fit the simulated breakthrough data to the appropriate analytical solution. Each match yielded four parameters, two for each pseudolayer, the fractional ϕh and kh products. No trend was observed in either of these parameters as a function of V_{DP}, λ_D or a combination of the two. Thus, an effectively layered interpretation model can be used to reproduce tracer response, though it is clear that the parameters obtained apply only at that scale. Such parameters can also be used in conjunction with simple models for computing displacement performance (Pande et al 1987). It is obvious that when the scale of heterogeneities is comparable to system dimensions, the tracer flow response is strongly dependent on the exact arrangement of permeability in the flow field. Thus, even when average measures (variance, correlation length scale) of permeability variation are the same, tracer flow behavior (as well as the recovery behavior from an EOR process) might be completely different. An example is Fig. 4.1.14, where two distinctly differing breakthrough curves are shown for the same statistical parameters. Their effective-layer properties are also quite different, as given in Table 4.1.2. An additional statistical parameter, which measures the *connectivity* effect of permeability, would improve correlation of non-Fickian tracer responses, though it is not obvious what that parameter should be.

4.1.4 Discussion

Using a Monte Carlo approach, we have demonstrated how pressure and tracer test data show different degrees of sensitivity to the presence of a heterogeneous permeability field. A parametric connection between the two test responses has been established empirically using the concept of heterogeneity index. This parameter also forms the basis of a proposed reservoir description procedure:

1. From transient pressure data, compute k_{inj} and k_{prd}. Calculate k_{ss} from steady-state data, or use the geometric mean of k_{inj} and k_{prd} as a working approximation.
2. Compute dimensionless permeability difference Δk_D from Eq. 4.1.7, and estimate heterogeneity index $\sigma^2_{ln(k)}\lambda_D$ from Eq. 4.1.8.
3. Predict the qualitative nature of the tracer test response (Fickian or non-Fickian) using Fig. 4.1.15.
4. If Fickian behavior is expected, calculate effective dispersivity from Eq. 4.1.10.
5. When tracer test data is available, verify the results of step (3), or compute effective-layer properties.

Simulation results reported here are based on a V_{DP} range of 0.35-0.65, and a λ_D range of 1/15-16/15 ($60 < \lambda < 1000$ ft). We believe the V_{DP} values to be representative of actual field conditions, even though these are less than typical core V_{DP} bounds, because a reduction in variance occurs when core measurements are scaled up to grid-block values (Journal and Huijbregts 1978). However, the same degree of confidence cannot be assigned to

Table 4.1.2. Pseudolayer Parameters from Simulated Tracer Test Data

$V_{DP} = 0.65$, $\lambda_D = 16/15$

Run	Layer 1		Layer 2	
	$kh/\Sigma kh$	$\phi h/\Sigma\phi h$	$kh/\Sigma kh$	$\phi h/\Sigma\phi h$
1	0.43	0.39	0.56	0.60
8	0.56	0.48	0.38	0.45

the λ values used. The uncertainty arises from the lack of information regarding permeability correlation length scales in actual reservoirs. Data from groundwater aquifers suggest that λ may be of the order of tens of kilometers, (Hoeksema and Kitanidis 1985) and may also be scale dependent (Gelhar 1986).

Da Costa e Silva (1985) presented data on permeability variation and continuity from a North Sea oil reservoir. He fitted a spherical semi-variogram model (the three-dimensional analog of the circular model used in this study) to permeability measurements, and estimated $\sigma^2_{ln(k)} = 0.85$, and $\lambda = 3.4$ miles. We have used these parameters to calculate heterogeneity index as a function of well spacing. The results of this computation, shown in Fig. 4.1.17, suggest that under typical field scale displacement conditions, non-Fickian behavior can be expected to be the norm based on the criterion derived from Fig. 4.1.15.

The computations reported here indicate that routine use of the convection-dispersion equation for modelling tracer (and miscible fluid) displacement in heterogeneous media is open to question. In the groundwater literature, the current philosophy is to obtain some knowledge of the spatial variation and continuity of the permeability field and then use stochastic theory to calculate the components of an apparent dispersion tensor (Gelhar 1986). Such an approach may be useful in the context of contaminant transport, but its applicability in petroleum reservoir engineering seems limited because of the small number of wells available for sampling the permeability distribution. An alternative is to ignore the dispersion formulation, and view spreading of the tracer slug as the result of convective effects in a heterogeneous flow field. This modelling approach also requires a detailed knowledge of the permeability field. However, by using information from cores, logs and pressure tests, permeability values can be obtained at some pilot points (wells). Conditional simulation (Journel and Huijbregts 1978) can then be used to construct the entire permeability field with some interpolation in the interwell region that honors known information at the wells.

The need for well-designed field tests for detection of reservoir heterogeneities is paramount. A single-well pressure test would reveal only an average permeability in its drainage area, but the combination of several such tests has the potential to reveal structures in permeability variation, albeit in some averaged sense. Even though there are limits to detection with well tests, procedures such as those developed in this study can yield simple measures of in situ permeability variation. That, in itself, is an important first step.

4.1.5 Conclusions

The major conclusions from this numerical study of pressure and tracer responses in single-layer areally heterogeneous permeable media are:

(1) For a single 5-spot in a repeated pattern, the steady-state interwell permeability is approximated by the geometric mean of injection and production well permeabilities.

(2) A dimensionless permeability difference, defined in terms of these quantities, is related to a measure of permeability variation $\sigma^2_{ln(k)}\lambda_D$, termed the heterogeneity index.

(3) When the heterogeneity index is small, tracer test data can be matched with solutions of the convection-dispersion equation to calculate dispersivities, which are proportional to the heterogeneity index.

(4) For larger values of heterogeneity index the convection-dispersion equation alone is inappropriate for modelling tracer flow, since preferential flow channels are created and cause tracer breakthrough curves to behave as if resulting from a layered flow system.

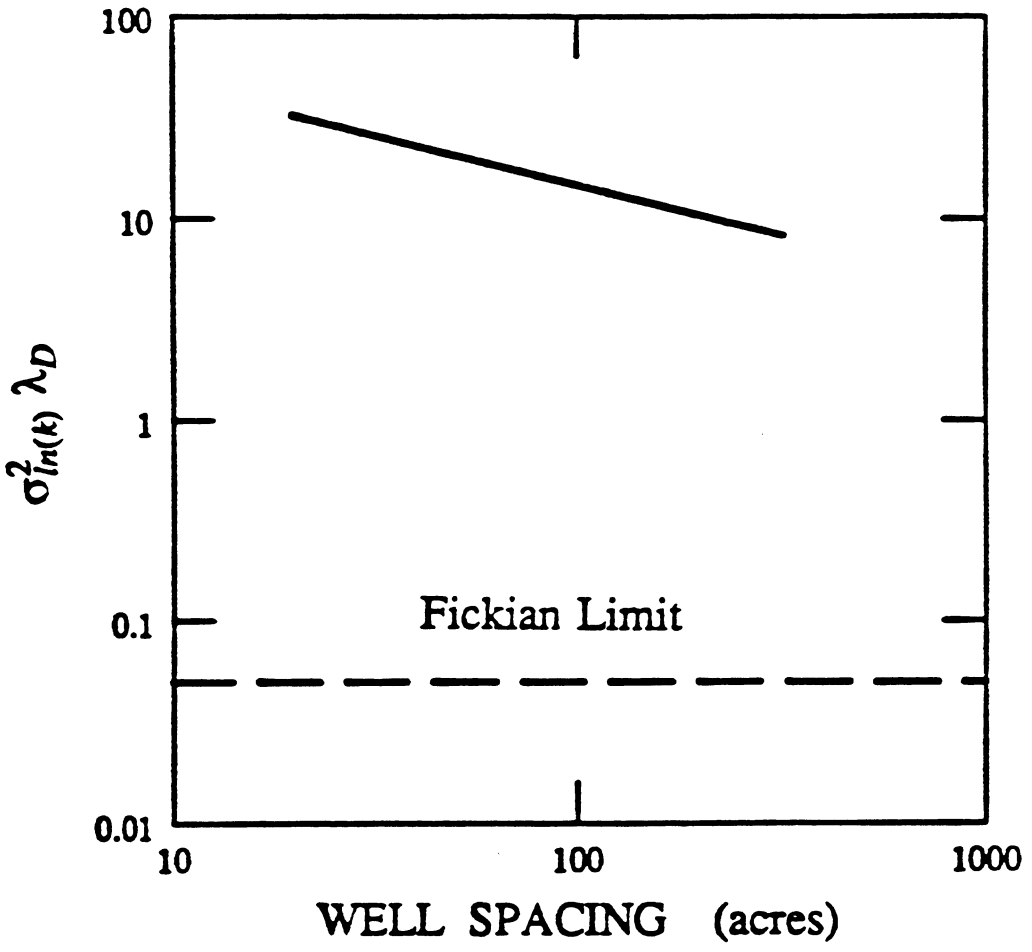

Fig. 4.1.17. Heterogeneity index as a function of well spacing, North Sea reservoir data.

(5) A reservoir description scheme, based on the analysis of pressure and tracer test data and the concept of heterogeneity index, is proposed. This procedure can be used to obtain an estimate of the likelihood of significant permeability correlation at interwell distances.

4.2 The Effects of Size Shape and Orientation of an Impermeable Region on Transient Pressure Testing

Paulo Britto

A practical consideration of the effects of the shape, size, and orientation of an impermeable reservoir region on transient pressure testing is presented. The constant rate production well is external to the impermeable region. Impermeable regions may be in the form of sealing fractures of finite length, that have little volume associated with them and are only a local restriction to fluid flow. These regions may also be shale lenses or reduced permeability regions that in addition to being a restriction to flow occupy a significant reservoir volume. This paper considers a single impermeable region with various sizes, shapes, and orientations with respect to the active source well.

The transient pressure response of the constant rate well is generated by replacing the impermeable boundaries by a set of line sources, and then applying the method of superposition. This method can be extended to include pressure responses of interference wells. The method is validated by matching the pressure responses of simple cases like a linear no-flow boundary and an internal circular no-flow boundary.

The key issue of this paper is the detectability of large scale impermeable reservoir regions by transient pressure analysis. The presence of an impermeable region causes the pressure response to deviate from the homogeneous line source response. This pressure deviation is the indication that the reservoir is heterogeneous. Four major parameters affect the pressure response of the active source well in the presence of an impermeable region: 1. the shortest distance between the well and the impermeable region, 2. the size of the region, 3. the shape of the region, and 4. the orientation of the region. This paper presents combinations of these four parameters that significantly affect the transient pressure response as well as some criteria for deciding what impermeable regions may be uniquely detected.

Many transient pressure analysis methods are aimed at attainment of the homogeneous reservoir properties such as the transmissivity and storativity, or wellbore properties such as storage and skin. While early and intermediate time data provide estimations of the local flow characteristics around the well, late time data are usually used to obtain information about reservoir boundaries, or large scale heterogeneities. Flow systems that are composed of two or more regions with different flow properties are known as composite reservoirs.

Essentially constant pressure subregions may occur in reservoirs as original gas caps, or they can be generated by steam flooding, in-situ combustion, immiscible gas drive, aquifer gas storage, or as secondary gas caps when the reservoir pressure declines below the bubble-point pressure. Large scale impermeable reservoir regions may occur as shale lenses, or during the injection of low mobility and compressibility fluids into a reservoir whose fluids are more mobile and compressible, as it occurs in some enhanced oil recovery methods like polymer flooding.

Can large scale reservoir heterogeneities be detected by transient pressure analysis? The key parameters in detecting the presence of impermeable subregions are the shortest distance between the observation well and the boundary, the relative size of this boundary, and its shape and orientation with respect to the active well. In some cases, the combined effects of these four parameters make it impossible to detect the presence of heterogeneous subregions, and the pressure response at the active well is similar to the line source response.

Most of the transient pressure problems that are posed in petroleum engineering have their counterpart in the heat transfer field. The differential equations, or system of equations,

and the boundary conditions are of the same kind, and, therefore, the techniques used to solve problems in one field are used to solve the corresponding problems in the other. Carslaw and Jaeger (1960) presented the solution for the heat conduction problem corresponding to the constant flow rate line source well in a homogeneous infinite slab porous medium. Van Everdingen and Hurst (1949) extented the solution for a finite wellbore radius. Their results demonstrated that at intermediate times, after the effects of wellbore storage and skin have ended, finite size reservoirs show an "infinite-acting" flow behavior, described by Theis (1935).

By using line source imaging, Stallman (1952) generated the response of a well producing at constant flow rate near an infinite linear boundary. He presented log-log curves for both constant pressure and impermeable linear boundaries. The pressure responses of other semi-infinite reservoirs bounded by linear boundaries have been described in the literature. Tiab and Kumar (1980) studied the transient pressure behavior of a constant rate well arbitrarily located between two parallel sealing faults. Tiab and Crichlow (1979) presented type curves for the case of multiple sealing faults and bounded reservoirs. Prasad (1975) considered the case of a well located near two intersecting boundaries in an otherwise infinite system. He developed an analytical solution that is valid for all angles of intersection and well locations using the concept of fluid flow in a wedge. Yaxley (1985) described the effects of a partially communicating fault on transient pressure behavior. In his approach he treated the well as a constant rate line source, and the partially communicating fault as an infinitely long vertical semipermeable barrier. Van Everdingen and Hurst (1949) studied circular reservoirs with different internal and external boundary conditions. Earlougher and Ramey (1973) described interference testing in closed rectangular reservoirs.

The effects of internal reservoir discontinuities have not been considered extensively in the literature. Carslaw and Jaeger (1960) derived the Green's function for a point source external to a non-conductive circular boundary in an infinite slab medium. However, this solution is not readily integrated in space and time to yield the continuous line source. Cinco et al. (1976) studied the transient flow behavior of a well near an infinite conductivity natural fracture of finite length. Sageev and Horne (1983) considered single well transient pressure analysis near a circular constant pressure or impermeable subregion. Their method allows the detection of the minimum distance between the active well and the circular boundary. Sageev and Horne (1983) and Sageev (1986) presented an interpretation method for analyzing single well tests and interference tests in the presence of a steam cap or a local compressible two-phase region. Sageev and Horne (1985) described the detection of impermeable and constant pressure circular regions using interference pressure data.

In this study, we consider composite reservoirs with two different regions, one that is continuous and homogeneous in its properties, and another that acts as an impermeable internal boundary to the first. The effects of size, shape, and orientation of the impermeable reservoir subregion on the pressure response observed in an active well are presented. By analyzing transient pressure data from an active well, it may be possible to infer the presence of an impermeable subregion.

4.2.1 Theory

In the following derivation we assume that the reservoir is horizontal, with isotropic properties, and infinite in the lateral extent. We consider a line source well, without wellbore storage and skin, producing at a constant rate near a single large scale impermeable subregion. The impermeable subregion may have volume associated with it or may be a linear feature like a fracture. The pressure response of any point in the reservoir is described by the diffusivity equation and by the internal boundary condition associated with the shape and the location of the impermeable subregion.

The transient dimensionless pressure response of a well producing with constant flow rate near an impermeable subregion is calculated by replacing that region by a set of line source wells producing with variable flow rates, and then applying the method of superposition. The

dimensionless pressure is calculated at the production (active) well, but can also be calculated at any other observation well external to the impermeable subregion.

Fig. 4.2.1A shows schematically an impermeable line boundary of finite length and arbitrary shape. The impermeable boundary is approximated using a set of image wells located a few wellbore radii away from the location of the boundary, as described in Fig. 4.2.1B. These image wells are all line source wells, that have a variable flow rate. However, during a time step, we assume that the image wells flow rates are constant. Fig. 4.2.1B shows points on the actual impermeable boundary where the normal velocity to the boundary is computed and required to be zero. The number of zero velocity points is equal to the number of image wells. The dimensionless pressure and the normal derivative at a point on the boundary are calculated by adding the contributions of the active well and all the image wells for each time step, using the method of superposition. For each time step we have a system of linear equations, and the unknowns are the flow rates at all the image boundary wells for the time step.

The dimensionless pressure and time are defined in the standard manner

$$p_D = \frac{2\,\pi\,k\,h\,(p_i - p)}{q_0\,B\,\mu} \tag{4.2.1}$$

$$t_D = \frac{k\,t}{\phi\,\mu\,c_t\,r_w^2} \tag{4.2.2}$$

where:

p_D = dimensionless pressure
k = permeability
h = formation thickness
p = pressure
p_i = initial pressure
q_0 = active well flow rate
B = formation volume factor
μ = viscosity
t = time
t_D = dimensionless time
ϕ = porosity
c_t = total compressibility
r_w = wellbore radius

Let r be the number of line source wells used to replace the boundary, and j any point on the boundary. The dimensionless pressure $p_{Dj}\,(t_{Dn})$ at point j at time t_{Dn} is given by

$$\begin{aligned} p_{Dj}\,(t_{Dn}) = p_{Dj,0}\,(t_{Dn}) + \frac{1}{q_0}\Bigg\{ & \\ & \Big[q_{1,1}\,p_{Dj,1}\,(t_{Dn}) + \cdots + (q_{1,n} - q_{1,n-1})\,p_{Dj,1}\,(t_{Dn} - t_{Dn-1})\Big] + \\ & \Big[q_{2,1}\,p_{Dj,2}\,(t_{Dn}) + \cdots + (q_{2,n} - q_{2,n-1})\,p_{Dj,2}\,(t_{Dn} - t_{Dn-1})\Big] \\ & + \cdots + \cdots + \\ & \Big[q_{r,1}\,p_{Dj,r}\,(t_{Dn}) + \cdots + (q_{r,n} - q_{r,n-1})\,p_{Dj,r}\,(t_{Dn} - t_{Dn-1})\Big]\Bigg\} \end{aligned} \tag{4.2.3}$$

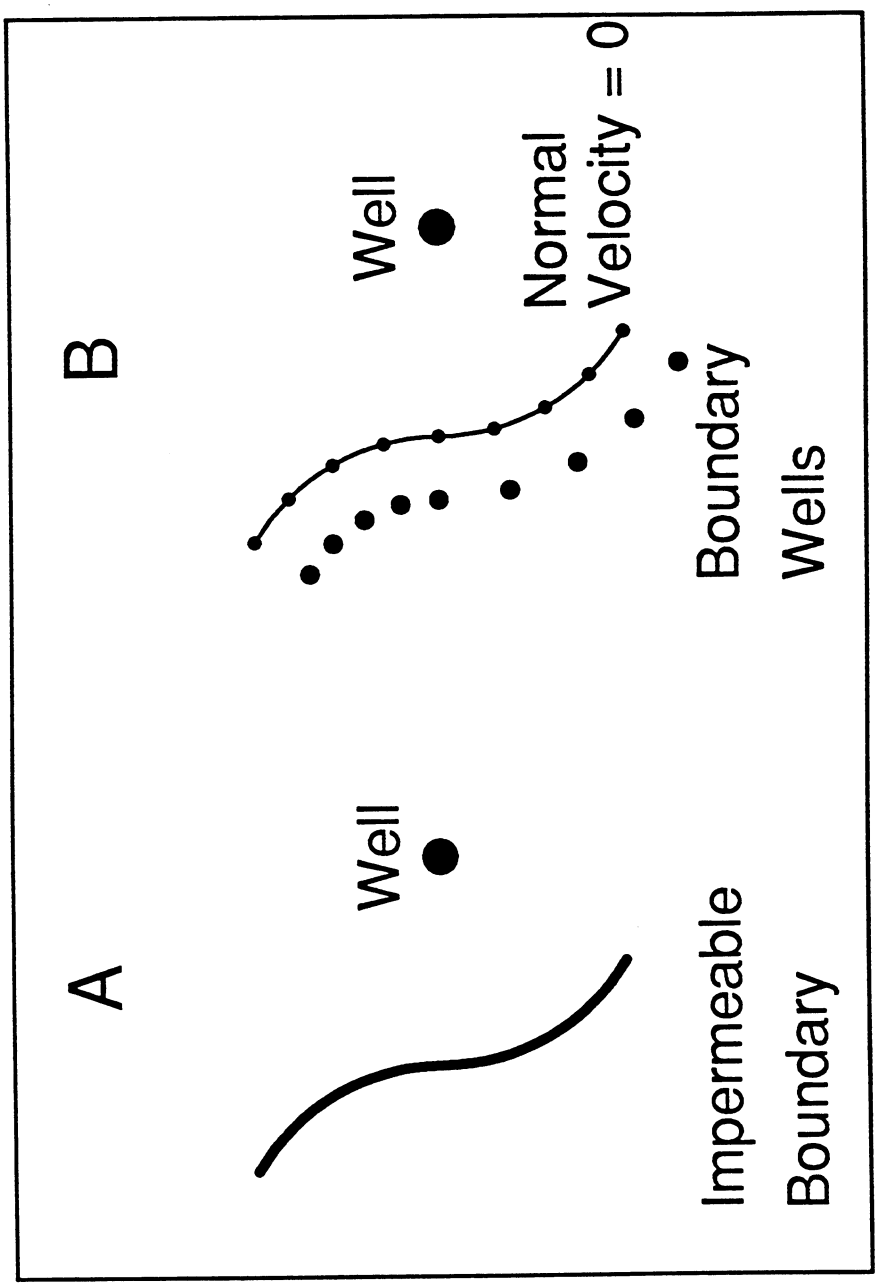

Fig. 4.2.1. Schematic diagram for a well near an impermeable boundary ; A: actual ; B: model.

where:

p_{Dn} = dimensionless pressure at time step n
t_{Dn} = dimensionless time at time step n
$q_{r,n}$ = flow rate of line source well r at time step n

The first term in the right hand side of Eq. (4.2.3) represents the dimensionless pressure caused by the active well. The next group of terms represents the dimensionless pressure caused by the line source well 1 at time steps 1, 2, $\cdots$, n ; the next next group represents the dimensionless pressure caused by line source well 2, and so on, up to the line source well r. We define the following term

$$\Delta q_i^k = \frac{q_{i,k} - q_{i,k-1}}{q_0} \tag{4.2.4}$$

Substituting Eq. (4.2.4) into Eq. (4.2.3) yields

$$\begin{aligned} P_{Dj}(t_{Dn}) &= p_{Dj,0}(t_{Dn}) + \\ &\left\{ \left[\Delta q_1^1 p_{Dj,1}(t_{Dn}) + \cdots + \Delta q_1^n p_{Dj,1}(t_{Dn} - t_{Dn-1}) \right] + \right. \\ &\left[\Delta q_2^1 p_{Dj,2}(t_{Dn}) + \cdots + \Delta q_2^n p_{Dj,2}(t_{Dn} - t_{Dn-1}) \right] \\ &+ \cdots + \cdots + \\ &\left. \left[\Delta q_r^1 p_{Dj,r}(t_{Dn}) + \cdots + \Delta q_r^n p_{Dj,r}(t_{Dn} - t_{Dn-1}) \right] \right\} \end{aligned} \tag{4.2.5}$$

In Eq. (4.2.5) the p_D's are given by

$$p_{Dj,0}(t_{Dn}) = -\frac{1}{2} E_i \left[-\frac{r_{j,0}^2}{4 t_{Dn}} \right] \tag{4.2.6}$$

and

$$p_{Dj,m}(t_{Dn} - t_{Dk}) = -\frac{1}{2} E_i \left[-\frac{r_{j,m}^2}{4 (t_{Dn} - t_{Dk-1})} \right] \tag{4.2.7}$$

where E_i is the Exponential Integral, $r_{j,0}$ is the distance between point j and the active well, and $r_{j,m}$ is the distance between point j and line source boundary well m.

Equation (4.2.5) is valid for any impermeable boundary geometry. However, the next step in the algorithm is to impose the no-flow condition at point j at time step n. In doing so, we need to calculate the normal spatial derivative of p_{Dj} (t_{Dn}), that depends on the geometry of the system. Therefore, each different geometry gives rise to a different equation. The mathematical algorithm derived here is for the impermeable linear boundary cases: linear, circular, and elliptical.

Linear Boundary

Fig. 4.2.2A presents a schematic diagram of a well near an impermeable linear boundary. This linear boundary is replaced by a set of line source wells, as shown schematically in Fig. 4.2.2B. The zero velocity points are not presented in Fig. 4.2.2B, but are located on the impermeable boundary opposite the line source image wells. The line of image wells and the impermeable boundary are separated by a dimensionless distance d.

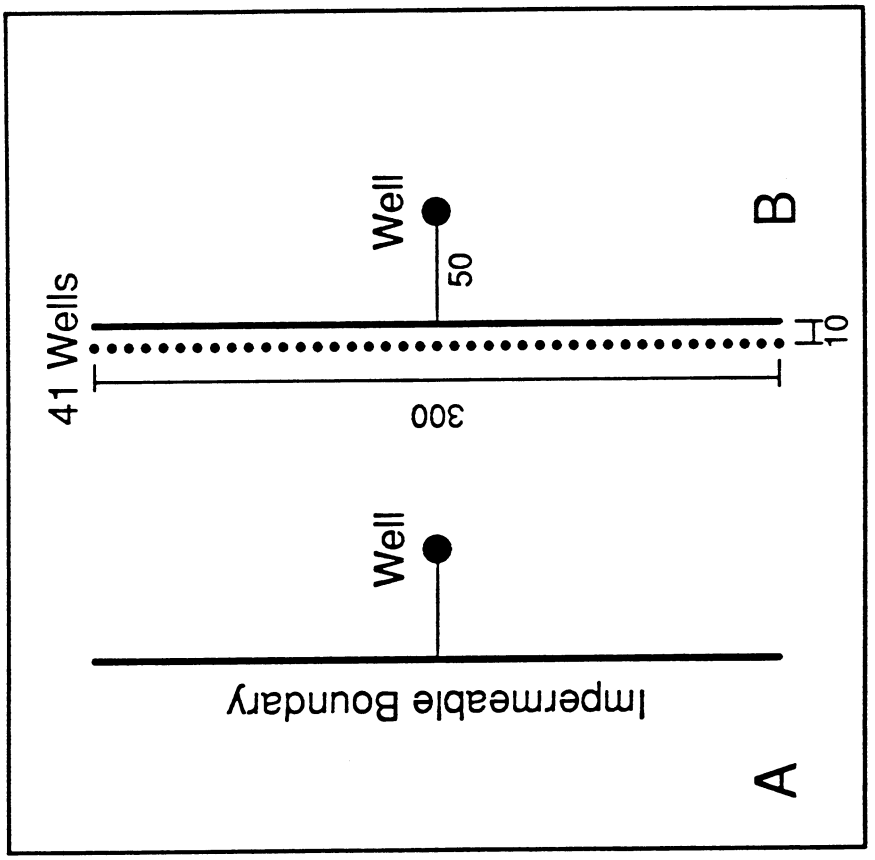

Fig. 4.2.2. Schematic diagram for a well near an infinite impermeable linear boundary ; A: actual ; B: model.

In the case of a finite length linear boundary presented in Fig. 4.2.2, all the image wells are positioned on the side of the boundary not containing the active production well. Also, all the image boundary wells are producers. The local pressure depressions around these wells prevent fluid from flowing through the impermeable boundary toward the production well. The results of the derivation are presented and discussed in the Validation section.

The dimensionless distances $r_{j,0}$ and $r_{j,m}$ are written in terms of an $(x-y)$ coordinate system centered at the active production well. Hence,

$$r_{j,0}^2 = x_j^2 + y_j^2 \tag{4.2.8}$$

and

$$r_{j,m}^2 = (x_j - \bar{x}_m)^2 + (y_j - \bar{y}_m)^2 \tag{4.2.9}$$

where:

x_j = x coordinate of point j
$\bar{x}_m$ = x coordinate of line source well m
y_j = y coordinate of point j
$\bar{y}_m$ = y coordinate of line source well m

Notice that (x,y) refers to a point on the no-flow linear boundary, while $(\bar{x}, \bar{y})$ are the coordinates of a line source boundary well. Also, we note that for the linear boundary case considered here:

$$x_j = \bar{x}_j - d \tag{4.2.10}$$

and

$$y_j = \bar{y}_j \tag{4.2.11}$$

where:

d = dimensionless distance between point j and the corresponding line source boundary well

Substitution of Eqs. (4.2.6), and (4.2.7) into Eq. (4.2.5) yields

$$\begin{aligned} p_{Dj}(t_{Dn}) = & -\frac{1}{2} E_i\left[-\frac{r_{j0}^2}{4\, t_{Dn}} \right] \\ & -\frac{1}{2}\left\{ \Delta q_1^1 E_i\left[-\frac{r_{j,1}^2}{4\, t_{Dn}} \right] + \cdots + \Delta q_1^n E_i\left[-\frac{r_{j,1}^2}{4\,(t_{Dn} - t_{Dn-1})} \right] \right\} \\ & -\frac{1}{2}\left\{ \Delta q_2^1 E_i\left[-\frac{r_{j,2}^2}{4\, t_{Dn}} \right] + \cdots + \Delta q_2^n E_i\left[-\frac{r_{j,2}^2}{4\,(t_{Dn} - t_{Dn-1})} \right] \right\} \\ & - \cdots - \cdots - \\ & -\frac{1}{2}\left\{ \Delta q_r^1 E_i\left[-\frac{r_{j,r}^2}{4\, t_{Dn}} \right] + \cdots + \Delta q_r^n E_i\left[-\frac{r_{j,r}^2}{4\,(t_{Dn} - t_{Dn-1})} \right] \right\} \end{aligned} \tag{4.2.12}$$

We now impose the no-flow condition at point j on the linear boundary. Mathematically,

$$\frac{\partial}{\partial x_j} p_{Dj}(t_{Dn}) = 0 \tag{4.2.13}$$

The derivative of the Exponential Integral is given by

$$\frac{\partial}{\partial w} Ei\,(-G) = -\frac{Exp\,(-G)}{G}\,\frac{\partial G}{\partial w} \tag{4.2.14}$$

where G = generic argument of the Exponential Integral function.

Combining Eqs. (4.2.8), (4.2.9), (4.2.12), (4.2.13), and (4.2.14) and rearranging yields

$$\begin{aligned}
0 &= \frac{x_j}{r_{j,0}^2}\,Exp\left[-\frac{r_{j,0}^2}{4\,t_{Dn}}\right] \\
&+ \frac{(x_j-\overline{x}_1)}{r_{j,1}^2}\left\{\Delta q_1^1\,Exp\left[-\frac{r_{j,1}^2}{4\,t_{Dn}}\right]\right. \\
&\left. + \cdots + \Delta q_1^n\,Exp\left[-\frac{r_{j,1}^2}{4\,(t_{Dn}-t_{Dn-1})}\right]\right\} \\
&+ \frac{(x_j-\overline{x}_2)}{r_{j,2}^2}\left\{\Delta q_2^1\,Exp\left[-\frac{r_{j,2}^2}{4\,t_{Dn}}\right]\right. \\
&\left. + \cdots + \Delta q_2^n\,Exp\left[-\frac{r_{j,2}^2}{4\,(t_{Dn}-t_{Dn-1})}\right]\right\} \\
&+ \cdots + \cdots + \\
&+ \frac{(x_j-\overline{x}_r)}{r_{j,r}^2}\left\{\Delta q_r^1\,Exp\left[-\frac{r_{j,r}^2}{4\,t_{Dn}}\right]\right. \\
&\left. + \cdots + \Delta q_r^n\,Exp\left[-\frac{r_{j,r}^2}{4\,(t_{Dn}-t_{Dn-1})}\right]\right\}
\end{aligned} \tag{4.2.15}$$

The unknowns in Eq. (4.2.15) are $\Delta q_1^n, \Delta q_2^n, \cdots, \Delta q_r^n$. The other Δq's were already determined in the previous time steps. Equation (4.2.15) is written in a more concise form as follows:

$$\begin{aligned}
&\left\{\frac{(x_j-\overline{x}_1)}{r_{j,1}^2}\,Exp\left[-\frac{r_{j,1}^2}{4\,(t_{Dn}-t_{Dn-1})}\right]\right\}\Delta q_1^n + \\
&\left\{\frac{(x_j-\overline{x}_2)}{r_{j,2}^2}\,Exp\left[-\frac{r_{j,2}^2}{4\,(t_{Dn}-t_{Dn-1})}\right]\right\}\Delta q_2^n + \\
&+ \cdots + \left\{\frac{(x_j-\overline{x}_r)}{r_{j,r}^2}\,Exp\left[-\frac{r_{j,r}^2}{4\,(t_{Dn}-t_{Dn-1})}\right]\right\}\Delta q_r^n \\
&= -\frac{x_j}{r_{j,0}^2}\,Exp\left[-\frac{r_{j,0}^2}{4\,t_{Dn}}\right] \\
&- \sum_{p=1}^{r}\sum_{k=2}^{n}\left\{\frac{(x_j-\overline{x}_p)}{r_{j,p}^2}\,Exp\left[-\frac{r_{j,p}^2}{4\,(t_{Dn}-t_{Dk-2})}\right]\right\}\Delta q_p^{k-1}
\end{aligned} \tag{4.2.16}$$

Equation (4.2.16) holds for j=1,2,....r, and, therefore, represents a linear system of equations that must be solved at each time step. In this system, $AX=B$, matrix A is symmetric.

The pressure effects of the boundary line source wells on the active well are computed only after $t_{Dn} / r^2_{min} \geq 0.1$, where r_{min} is the minimum distance between the active well and the impermeable boundary. Hence, defining z as the number of time steps that boundary well effects are computed, Eq. (4.2.16) becomes

$$\left\{ \frac{(x_j - \bar{x}_1)}{r^2_{j,1}} Exp\left[- \frac{r^2_{j,1}}{4 (t_{Dn} - t_{Dn-1})} \right] \right\} \Delta q^n_1 +$$
$$\left\{ \frac{(x_j - \bar{x}_2)}{r^2_{j,2}} Exp\left[- \frac{r^2_{j,2}}{4 (t_{Dn} - t_{Dn-1})} \right] \right\} \Delta q^n_2 +$$
$$+ \cdots + \left\{ \frac{(x_j - \bar{x}_r)}{r^2_{j,r}} Exp\left[- \frac{r^2_{j,r}}{4 (t_{Dn} - t_{Dn-1})} \right] \right\} \Delta q^n_r$$
$$= - \frac{x_j}{r^2_{j,0}} Exp\left[- \frac{r^2_{j,0}}{4 t_{Dn}} \right]$$
$$- \sum_{p=1}^{r} \sum_{k=2}^{z+1} \left\{ \frac{(x_j - \bar{x}_p)}{r^2_{j,p}} Exp\left[- \frac{r^2_{j,p}}{4 (t_{Dn} - t_{Dn-k})} \right] \right\} \Delta q^{n-k+1}_p \qquad (4.2.17)$$

The linear system of equations is solved using the IMSL subroutine LEQ2S that is suitable for symmetric matrices. Once the flow rates at time step n are determinated, the dimensionless pressure at the active well is computed by

$$p_{D0} (t_{Dn}) = - \frac{1}{2} E_i \left[- \frac{1}{4 t_{Dn}} \right]$$

$$- \frac{1}{2} \sum_{m=1}^{r} \sum_{k=1}^{z} \Delta q^{n-k+1}_m E_i \left[- \frac{\bar{r}^2_{m,0}}{4 (t_{Dn} - t_{Dn-k})} \right] \qquad (4.2.18)$$

where $\bar{r}_{m,0}$ is the distance between boundary well m and the active production well

$$\bar{r}^2_{m,0} = \bar{x}^2_m + \bar{y}^2_m \qquad (4.2.19)$$

The first term in the right hand side of Eq. (4.2.18) is the contribution of the active well, while the double summation terms represent the superposition effects of the line source boundary wells from previous and current time steps.

Circular Boundary

To derive the algorithm for the no-flow circular boundary we start with Eq. (4.2.12) of the theory section. The no-flow condition at point j on the boundary is expressed as

$$\frac{\partial}{\partial s} p_{Dj} (t_{Dn}) = 0 \qquad (4.2.20)$$

where s is the direction normal to the boundary at point j. The normal derivative of a general function f is given by

$$\frac{\partial f}{\partial s} = \vec{s} . \nabla f \qquad (4.2.21)$$

where $\vec{s}$ is the unitary vector normal to the boundary, and ∇f is the gradient of the function f. The unitary normal vector $\vec{s}$ at point j is given by

$$\vec{s} = \frac{(x_j - x_o) \vec{i} + (y_j - y_o) \vec{j}}{\left[(x_j - x_o)^2 + (y_j - y_o)^2 \right]^{1/2}} \qquad (4.2.22)$$

where $\vec{i}$ and $\vec{j}$ are the unitary vectors in the directions x and y respectively, and (x_o,y_o) are the coordinates of the center of the circular boundary. Let the function f be any one of the Exponential Integral terms that appear in Eq. (4.2.12). Thus,

$$f = -Ei\left[-\frac{(x_j-\bar{x}_b)^2+(y_j-\bar{y}_b)^2}{4\,(t_{Dn}-t_{Dp})}\right] \tag{4.2.23}$$

By definition

$$\nabla f = \frac{\partial f}{\partial x_j}\vec{i} + \frac{\partial f}{\partial y_j}\vec{j} \tag{4.2.24}$$

The derivative of the Exponential Integral is

$$\frac{\partial}{\partial w} Ei(-G) = -\frac{Exp(-G)}{G}\frac{\partial G}{\partial w} \tag{4.2.25}$$

Supstitution of Eq. (4.2.23) into Eq. (4.2.24), and using Eq. (4.2.25) yields

$$\nabla f = \left\{-\frac{2(x_j-\bar{x}_b)}{r_{j,b}^2}\,Exp\left[-\frac{r_{j,b}^2}{4\,(t_{Dn}-t_{Dp})}\right]\right\}\vec{i} + \left\{-\frac{2(y_j-\bar{y}_b)}{r_{j,b}^2}\,Exp\left[-\frac{r_{j,b}^2}{4\,(t_{Dn}-t_{Dp})}\right]\right\}\vec{j} \tag{4.2.26}$$

where

$$r_{j,b}^2 = (x_j-\bar{x}_b)^2 + (y_j-\bar{y}_b)^2 \tag{4.2.27}$$

Substituting Eqs. (4.2.22), (4.2.26), and (4.2.27) into Eq. (4.2.21) we obtain

$$\frac{\partial f}{\partial s} = -\frac{2(x_j-x_o)(x_j-\bar{x}_b)}{\left[(x_j-x_o)^2+(y_j-y_o)^2\right]^{1/2} r_{j,b}^2}\,Exp\left[-\frac{r_{j,b}^2}{4\,(t_{Dn}-t_{Dp})}\right] - \frac{2(y_j-y_o)(y_j-\bar{y}_b)}{\left[(x_j-x_o)^2+(y_j-y_o)^2\right]^{1/2} r_{j,b}^2}\,Exp\left[-\frac{r_{j,b}^2}{4\,(t_{Dn}-t_{Dp})}\right] \tag{4.2.28}$$

For each well in the system there is a term given by Eq. (4.2.28). Therefore, when the no-flow condition is imposed at point j on the boundary, and after the cancellation of common terms, we obtain the following equation:

$$0 = \left[\frac{x_j(x_j-x_o)+y_j(y_j-y_o)}{r_{j,0}^2}\right]Exp\left[-\frac{r_{j,0}^2}{4\,t_{Dn}}\right] + \left[\frac{(x_j-\bar{x}_1)(x_j-x_o)+(y_j-\bar{y}_1)(y_j-y_o)}{r_{j,1}^2}\right]\left\{\Delta q_1^1\,Exp\left[-\frac{r_{j,1}^2}{4\,t_{Dn}}\right] + \cdots + \Delta q_1^n\,Exp\left[-\frac{r_{j,1}^2}{4\,(t_{Dn}-t_{Dn-1})}\right]\right\} +$$

$$\left[\frac{(x_j-\bar{x}_2)\,(x_j-x_o)+(y_j-\bar{y}_2)\,(y_j-y_o)}{r_{j,2}^2}\right]\left\{\Delta q_2^1\,Exp\left[-\frac{r_{j,2}^2}{4\,t_{Dn}}\right]\right.$$

$$\left.+\cdots+\Delta q_2^n\,Exp\left[-\frac{r_{j,2}^2}{4\,(t_{Dn}-t_{Dn-1})}\right]\right\}$$

$$+\cdots+\cdots+$$

$$\left[\frac{(x_j-\bar{x}_r)\,(x_j-x_o)+(y_j-\bar{y}_r)\,(y_j-y_o)}{r_{j,r}^2}\right]\left\{\Delta q_r^1\,Exp\left[-\frac{r_{j,r}^2}{4\,t_{Dn}}\right]\right.$$

$$\left.+\cdots+\Delta q_r^n\,Exp\left[-\frac{r_{j,r}^2}{4\,(t_{Dn}-t_{Dn-1})}\right]\right\} \tag{4.2.29}$$

The unknowns in Eq. (4.2.29) are Δq_1^n, Δq_2^n, $\cdots$ Δq_r^n, since the remaining $\Delta q's$ were already computed in the previous time steps. Equation (4.2.29) is rearranged and written in a concise form that also accounts for interference only after $t_{Dn}/r_{\min}^2 \geq 0.1$, in the same way that was done for the linear boundary case. Hence

$$\left\{\frac{(x_j-\bar{x}_1)(x_j-x_o)+(y_j-\bar{y}_1)(y_j-y_o)}{r_{j,1}^2}\,Exp\left[-\frac{r_{j,1}^2}{4(t_{Dn}-t_{Dn-1})}\right]\right\}\Delta q_1^n+$$

$$\left\{\frac{(x_j-\bar{x}_2)(x_j-x_o)+(y_j-\bar{y}_2)(y_j-y_o)}{r_{j,2}^2}\,Exp\left[-\frac{r_{j,2}^2}{4(t_{Dn}-t_{Dn-1})}\right]\right\}\Delta q_2^n$$

$$+\cdots+\cdots+$$

$$\left\{\frac{(x_j-\bar{x}_r)(x_j-x_o)+(y_j-\bar{y}_r)(y_j-y_o)}{r_{j,r}^2}\,Exp\left[-\frac{r_{j,r}^2}{4(t_{Dn}-t_{Dn-1})}\right]\right\}\Delta q_r^n$$

$$=-\left[\frac{x_j\,(x_j-x_o)+y_j\,(y_j-y_o)}{r_{j,0}^2}\right]Exp\left[-\frac{r_{j,0}^2}{4\,t_{Dn}}\right]-\sum_{p=1}^{r}\sum_{k=2}^{z+1}$$

$$\left\{\left[\frac{(x_j-\bar{x}_p)(x_j-x_o)+(y_j-\bar{y}_p)(y_j-y_o)}{r_{j,p}^2}\right]Exp\left[-\frac{r_{jp}^2}{4(t_{Dn}-t_{Dn-k})}\right]\right\}\Delta q_p^{n-k+1} \tag{4.2.30}$$

Finally, the pressure drop at the production well is computed by Eq. (4.2.18).

Elliptical Boundary

The starting point is Eq. (4.2.12) of the theory section. The no-flow condition at point j on the boundary is expressed as

$$\frac{\partial}{\partial s} p_{Dj}\,(\,t_{Dn}\,) \;=\; 0 \tag{4.2.31}$$

where s is the direction normal to the boundary at point j. The normal derivative of a general function f is given by

$$\frac{\partial f}{\partial s} \;=\; \vec{s}\,.\,\nabla f \tag{4.2.32}$$

where $\vec{s}$ is the unitary vector normal to the boundary, and ∇f is the gradient of the function f. For a elliptical boundary centered at (x_o,y_o), whose major axis is parallel to the Y axis, $\vec{s}$ is given by

$$\vec{s} = \frac{(\,x_j - x_o\,)\;\vec{i}}{b^2\left[\dfrac{(\,x_j - x_o\,)^2}{b^4} + \dfrac{(\,y_j - y_o\,)^2}{a^4}\right]^{1/2}} + \frac{(\,y_j - y_o\,)\;\vec{j}}{a^2\left[\dfrac{(\,x_j - x_o\,)^2}{b^4} + \dfrac{(\,y_j - y_o\,)^2}{a^4}\right]^{1/2}} \tag{4.2.33}$$

Now, let the function f be any one of the exponential integral terms that appear in Eq. (4.2.12). Thus,

$$f \;=\; -\,Ei\left[-\frac{(\,x_j - \bar{x}_b\,)^2 + (\,y_j - \bar{y}_b\,)^2}{4\,(\,t_{Dn} - t_{Dp}\,)}\right] \tag{4.2.34}$$

The gradient of f is given by

$$\nabla f = \left\{-\frac{2(\,x_j - \bar{x}_b\,)}{r_{j,b}^2}\,Exp\left[-\frac{r_{j,b}^2}{4\,(\,t_{Dn} - t_{Dp}\,)}\right]\right\}\vec{i} + \left\{-\frac{2(\,y_j - \bar{y}_b\,)}{r_{j,b}^2}\,Exp\left[-\frac{r_{j,b}^2}{4\,(\,t_{Dn} - t_{Dp}\,)}\right]\right\}\vec{j} \tag{4.2.35}$$

For each well in the system there is a term given by Eq. (4.2.35). Thus, imposing the no-flow condition at point j on the boundary, and cancelling the common terms, we get

$$0 = \left[\frac{x_j\,(x_j - x_o)}{b^2\,r_{j,0}^2} + \frac{y_j\,(y_j - y_o)}{a^2\,r_{j,0}^2}\right]Exp\left[-\frac{r_{j,0}^2}{4\,t_{Dn}}\right] +$$

$$\left[\frac{(x_j - \bar{x}_1)\,(x_j - x_o)}{b^2\,r_{j,1}^2} + \frac{(y_j - \bar{y}_1)\,(y_j - y_o)}{a^2\,r_{j,1}^2}\right]\left\{\Delta q_1^1\,Exp\left[-\frac{r_{j,1}^2}{4\,t_{Dn}}\right]\right.$$

$$\left. + \cdots + \Delta q_1^n\,Exp\left[-\frac{r_{j,1}^2}{4\,(t_{Dn} - t_{Dn-1})}\right]\right\} +$$

$$\left[\frac{(x_j - \bar{x}_2)\,(x_j - x_o)}{b^2\,r_{j,2}^2} + \frac{(y_j - \bar{y}_2)\,(y_j - y_o)}{a^2\,r_{j,2}^2}\right]\left\{\Delta q_2^1\,Exp\left[-\frac{r_{j,2}^2}{4\,t_{Dn}}\right]\right.$$

$$+ \cdots + \Delta q_2^n \, Exp\left[- \frac{r_{j,2}^2}{4\,(t_{Dn} - t_{Dn-1})} \right] \Bigg\}$$

$$+ \cdots + \cdots +$$

$$\left[\frac{(x_j - \bar{x}_r)\,(x_j - x_o)}{b^2\, r_{j,r}^2} + \frac{(y_j - \bar{y}_r)\,(y_j - y_o)}{a^2\, r_{j,r}^2} \right] \left\{ \Delta q_r^1 \, Exp\left[- \frac{r_{j,r}^2}{4\, t_{Dn}} \right] \right.$$

$$+ \cdots + \Delta q_r^n \, Exp\left[- \frac{r_{j,r}^2}{4\,(t_{Dn} - t_{Dn-1})} \right] \Bigg\} \qquad (4.2.36)$$

The unknowns in Eq. (4.2.36) are Δq_1^n, Δq_2^n, $\cdots$ Δq_r^n, since the remaining $\Delta q's$ were already computed in the previous time steps. Equation (4.2.36) is rearranged and written in a concise form that also accounts for interference only after $t_{Dn}/r_{\min}^2 \geq 0.1$, in the same way that was done for the linear boundary case. Hence

$$\left\{ \frac{(x_j - \bar{x}_1)(x_j - x_o)}{b^2\, r_{j,1}^2} + \frac{(y_j - \bar{y}_1)(y_j - y_o)}{a^2\, r_{j,1}^2} \, Exp\left[- \frac{r_{j,1}^2}{4(t_{Dn} - t_{Dn-1})} \right] \right\} \Delta q_1^n +$$

$$\left\{ \frac{(x_j - \bar{x}_2)(x_j - x_o)}{b^2\, r_{j,2}^2} + \frac{(y_j - \bar{y}_2)(y_j - y_o)}{a^2\, r_{j,2}^2} \, Exp\left[- \frac{r_{j,2}^2}{4(t_{Dn} - t_{Dn-1})} \right] \right\} \Delta q_2^n$$

$$+ \cdots + \cdots +$$

$$\left\{ \frac{(x_j - \bar{x}_r)(x_j - x_o)}{b^2\, r_{j,r}^2} + \frac{(y_j - \bar{y}_r)(y_j - y_o)}{a^2\, r_{j,r}^2} \, Exp\left[- \frac{r_{j,r}^2}{4(t_{Dn} - t_{Dn-1})} \right] \right\} \Delta q_r^n$$

$$= - \left\{ \frac{x_j (x_j - x_o)}{b^2\, r_{j,0}^2} + \frac{y_j (y_j - y_o)}{a^2\, r_{j,0}^2} \, Exp\left[- \frac{r_{j,0}^2}{4\, t_{Dn}} \right] - \sum_{p=1}^{r} \sum_{k=2}^{z+1} \right.$$

$$\left\{ \frac{(x_j - \bar{x}_p)(x_j - x_o)}{b^2\, r_{j,p}^2} + \frac{(y_j - \bar{y}_p)(y_j - y_o)}{a^2\, r_{j,p}^2} \, Exp\left[- \frac{r_{j,p}^2}{4(t_{Dn} - t_{Dn-k})} \right] \right\} \Delta q_p^{n-k+1} \qquad (4.2.37)$$

For the case in which the major axis of the elliptical boundary is parallel to X axis an equation similar to Eq. (4.2.37) is obtained, with a and b interchanged. Finally, the pressure drop at the production well is computed by Eq. (4.2.18).

4.2.2 Validation

In this section we present two applications of the new model for generating the effects of impermeable boundaries for cases that have analytical solutions. These two cases are an impermeable linear boundary and an impermeable internal circular subregion near an active

constant rate production well. These two reservoir configurations characterize two classes of impermeable boundaries. The impermeable linear boundary is infinitely long, and the internal circular region is of finite size having reservoir volume associated with it.

Figs. 4.2.2A and 4.2.2B present the geometrical configuration of the actual and approximated reservoir configurations respectively for a well near an impermeable linear boundary. The dimensions in Fig. 4.2.2 are all in dimensionless units based on the active well radius. The infinite linear boundary is approximated by 41 line source image boundary wells with about seven well radii between every two wells. The line of boundary wells is ten wellbore radii away from the actual location of the impermeable linear boundary. Also, the infinite linear boundary is approximated by a boundary with a dimensionless length of 300, located at a dimensionless distance of 50 away from the active well.

The comparison of the new model and the analytical solution for a well near an impermeable linear boundary is presented in Fig. 4.2.3. The lower curve in Fig. 4.2.3 is the line source solution, or the Theis (1935) solution for a constant rate well in an infinite homogeneous reservoir. The upper solid curve represents the analytical pressure response of a well near an impermeable linear boundary, generated by the method of superposition presented by Stallman (1952). The dotted data represent the results of the new model developed in this paper. The pressure response in the presence of an impermeable linear boundary deviates from the line source solution, doubling the semi-log slope. The data from the new model match the analytical model for two log cycles beyond the beginning of boundary effects. As shown by Sageev et al (1985) this match is sufficient for determining the distance between the well and the linear boundary. The late time data from the new model deviate below the analytical solution since we used a finite number of boundary wells. The pressure response computed with the new model represents a finite length linear boundary, and the late time semi-log slope, not shown in Fig. 4.2.3, is identical to the line source semi-log slope. The effects of the number of boundary wells and their distance from the actual impermeable boundary on the performance of the new model are considered in the Discussion section.

Next, we examine the application of the new model to a finite volumetric impermeable circular subregion. Fig. 4.2.4 presents the geometrical configuration of this case. The distances presented in Fig. 4.2.4 are dimensionless, based upon the active well radius. The image boundary wells are located inside the impermeable subregion, ten wellbore radii away from the actual boundary. During the test, the image boundary wells located along the portion of the boundary facing the active well are producers. The other image boundary well facing away from the active well are injectors. This injection-production distribution allows the image wells to prevent fluid from flowing out of the impermeable region toward the active well. Also, this distribution prevents fluid from flowing through the impermeable region, and forces the fluid to flow around the boundary.

Fig. 4.2.5 presents a comparison of the new model to the analytical solution for a constant rate well near a circular impermeable boundary. The analytical solution was presented by Sageev and Horne (1983) and is the heavy solid curve. The line source solution and the impermeable linear boundary solution are presented in Fig. 4.2.5 as a reference. The dotted data, representing the pressure response generated by the new model, match well the analytical solution. Since the impermeable region is finite in size, the late time pressure response is parallel to the line source solution response. The constant pressure separation between the late time line source curve, and the curve for the boundary case is considered as a late time skin, and was discussed by Sageev and Horne (1983)

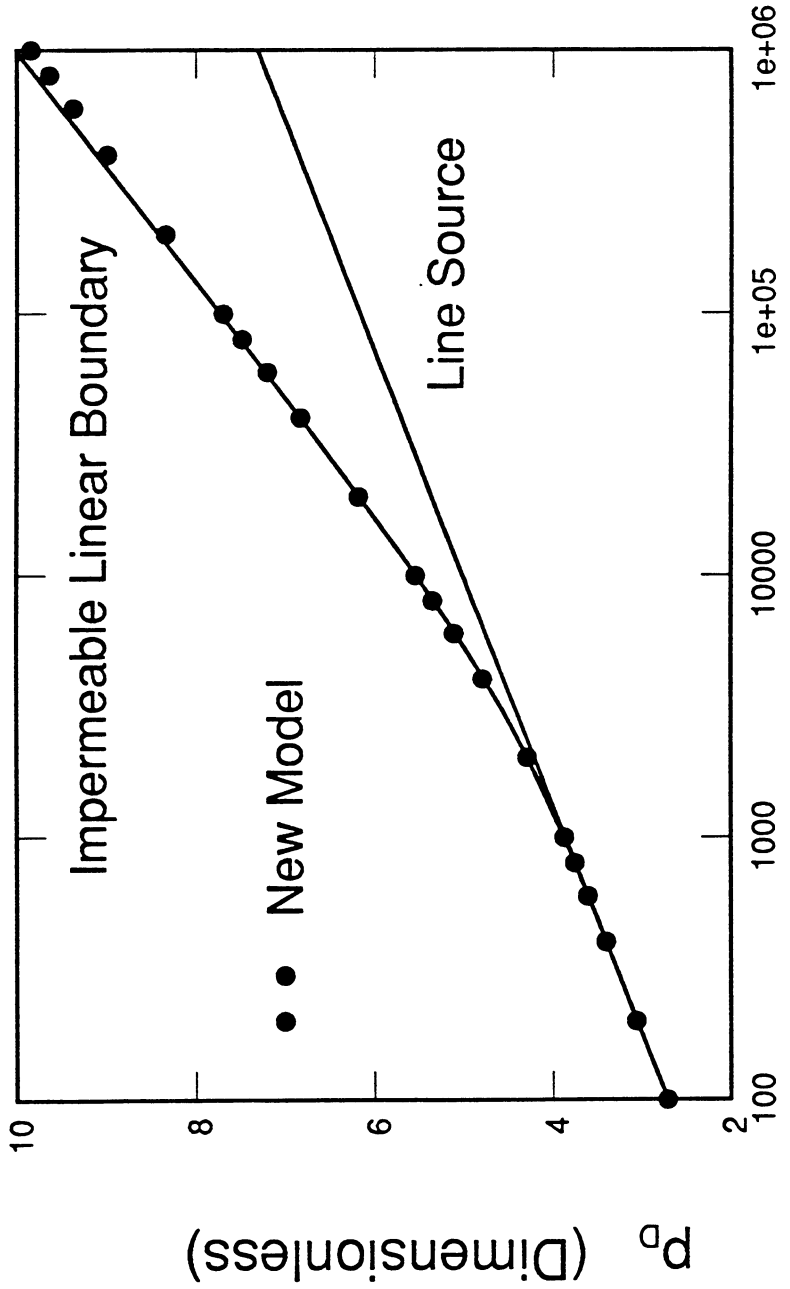

Fig. 4.2.3. Semi-log pressure response for a well near an impermeable linear boundary.

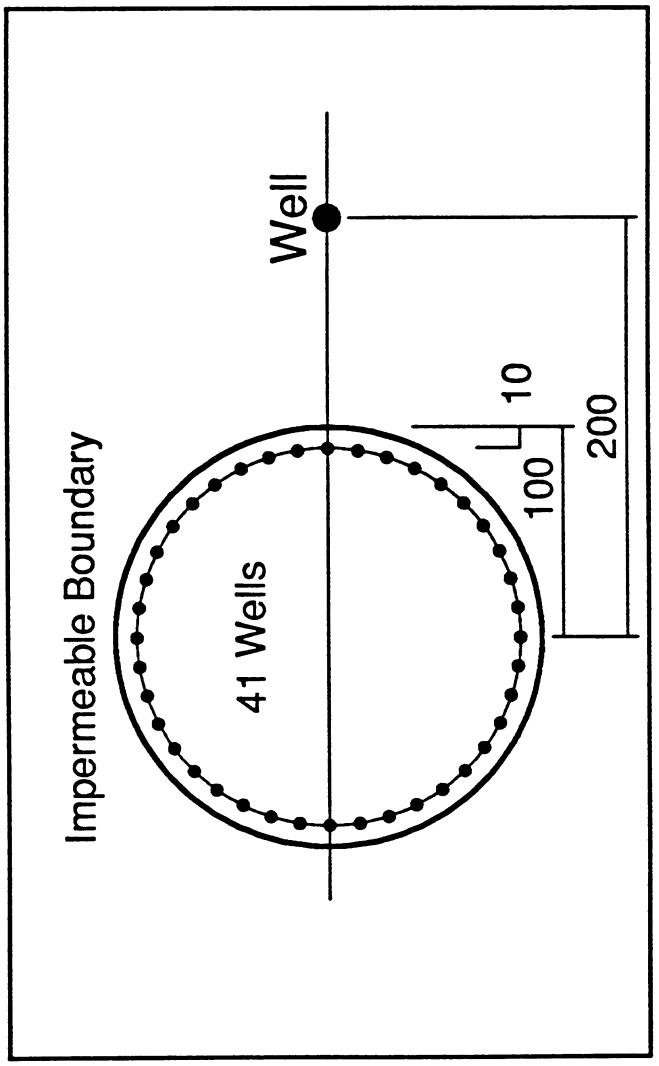

Fig. 4.2.4. Schematic diagram for a well near an impermeable circular boundary.

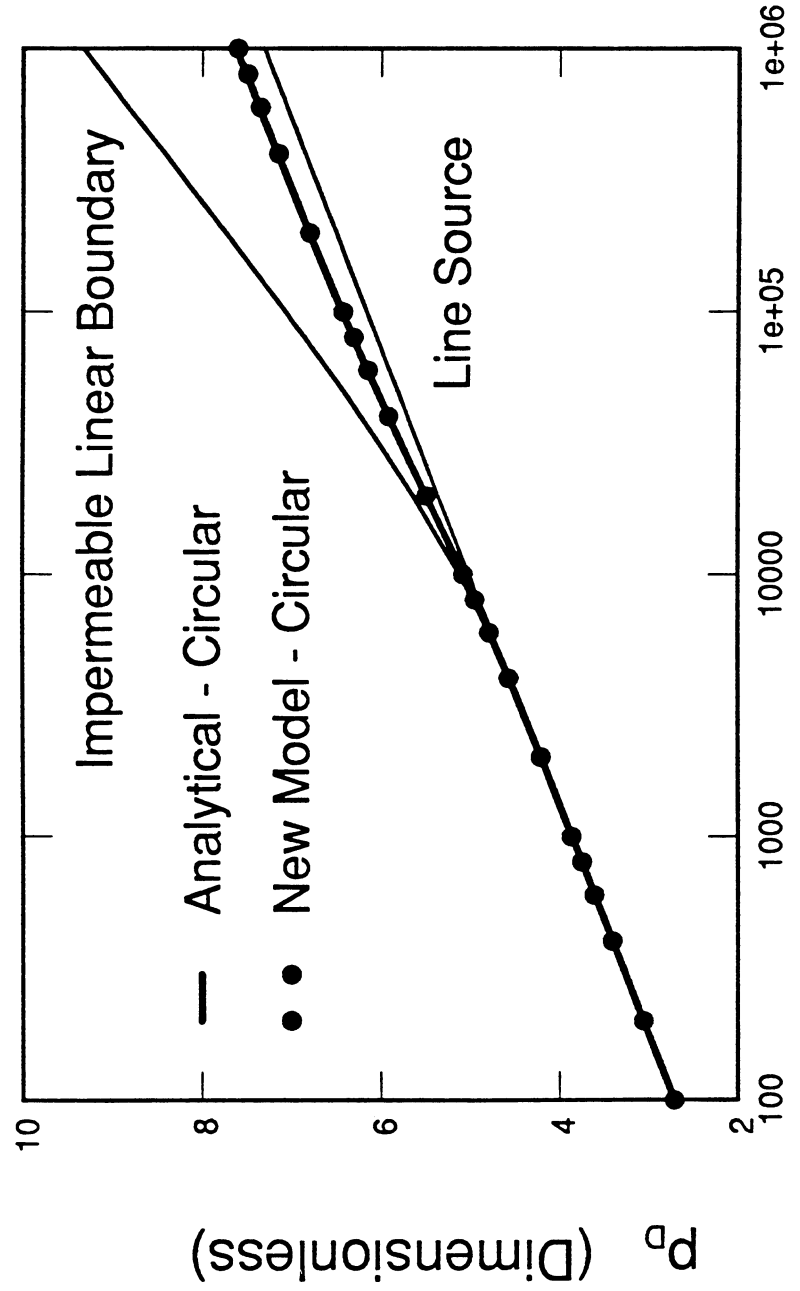

Fig. 4.2.5. Semi-log pressure response for a well near an impermeable circular boundary.

4.2.3 Results

The Effect of Size

In this section we examine the effect of the size of impermeable regions on the pressure responses of a constant rate well. Two shapes of boundaries are considered: circular and elliptical. One of the important parameters affecting the pressure response is the shortest distance between the active well and the impermeable boundary. For a given set of different sizes of impermeable boundaries with the same shape and orientation, the shortest distance between the well and the boundaries is maintained constant.

Fig. 4.2.6 presents a suite of circular boundaries external to a well in an infinite reservoir. The relative size of the circular boundary is defined as:

$$F = R/T \tag{4.2.38}$$

where R is the radius of the circular boundary, and T is the distance between the active well and the center of the boundary. Hence, F varies between zero for relatively small boundaries, and unity for relatively large boundaries. The shortest distance between the well and the boundaries is 100 wellbore radii, and the relative size of the boundaries varies between 0.4 and 0.9.

The pressure responses of a well near these impermeable circular boundaries are presented in Fig. 4.2.7. As the relative size of the boundary increases, the magnitude of the pressure deviation from the line source solution increases. The impermeable subregion has to be relatively large in order to be detected by the first deviation from the line source solution. The detection of the finiteness of the impermeable region depends on the resumption of the line source semi-log slope. The transition from the linear boundary slope to the line source slope occurs later for relatively large impermeable regions. However, since all the circular boundaries shown in Fig. 4.2.6 have the same shortest distance to the production well, all the corresponding pressure responses shown in Fig. 4.2.7 deviate from the line source response at the same time. Hence, the shortest distance is determined from the first deviation from the line source response, and the size of the impermeable circular region is determined by the deviation of the pressure response from the linear boundary response.

We now consider the effects of the size of impermeable regions with elongated shapes on pressure responses of the active production well. Fig. 4.2.8 presents three elliptical impermeable boundaries. Again, the shortest distance between the well and the boundaries is 100 wellbore radii. The elliptical boundaries have the same shape, with an axis ratio $b/a = 0.25$. Here, a is the length of the long axis of the ellipse, and b is the length of the short axis of the ellipse. The ellipses denoted by A, B, and C have dimensionless a values of 400, 200, and 100 respectively.

Fig. 4.2.9 presents the pressure responses of the three elliptical boundaries of Fig. 4.2.8. The three responses are all between the line source curve and the impermeable linear boundary curve, and exhibit the early and late time line source slope. The magnitude of the deviation from the line source curve depends on the size of the elliptical boundary. The relatively small impermeable ellipse denoted by C can hardly be detected from the pressure response. However, the relatively large impermeable ellipse denoted by A exhibits a significant deviation from the line source pressure response, and the presence of the impermeable boundary can be detected. Also, the pressure response of the relatively large impermeable ellipse follows the linear boundary curve for about one log cycle of time after the first deviation from the line source curve.

From the deviation time, and the early transition flow period, the shortest distance between the well and the boundary can be determined. We also note, that in order to detect the fact that the impermeable region is finite in size, the test must be continued for at least one log cycle of time beyond the first deviation from the line source response. However, the pressure response curves for elliptical shapes are similar to the curves for circular shapes, hence, preventing the independent determination of the shape of the impermeable boundary from a transient pressure test.

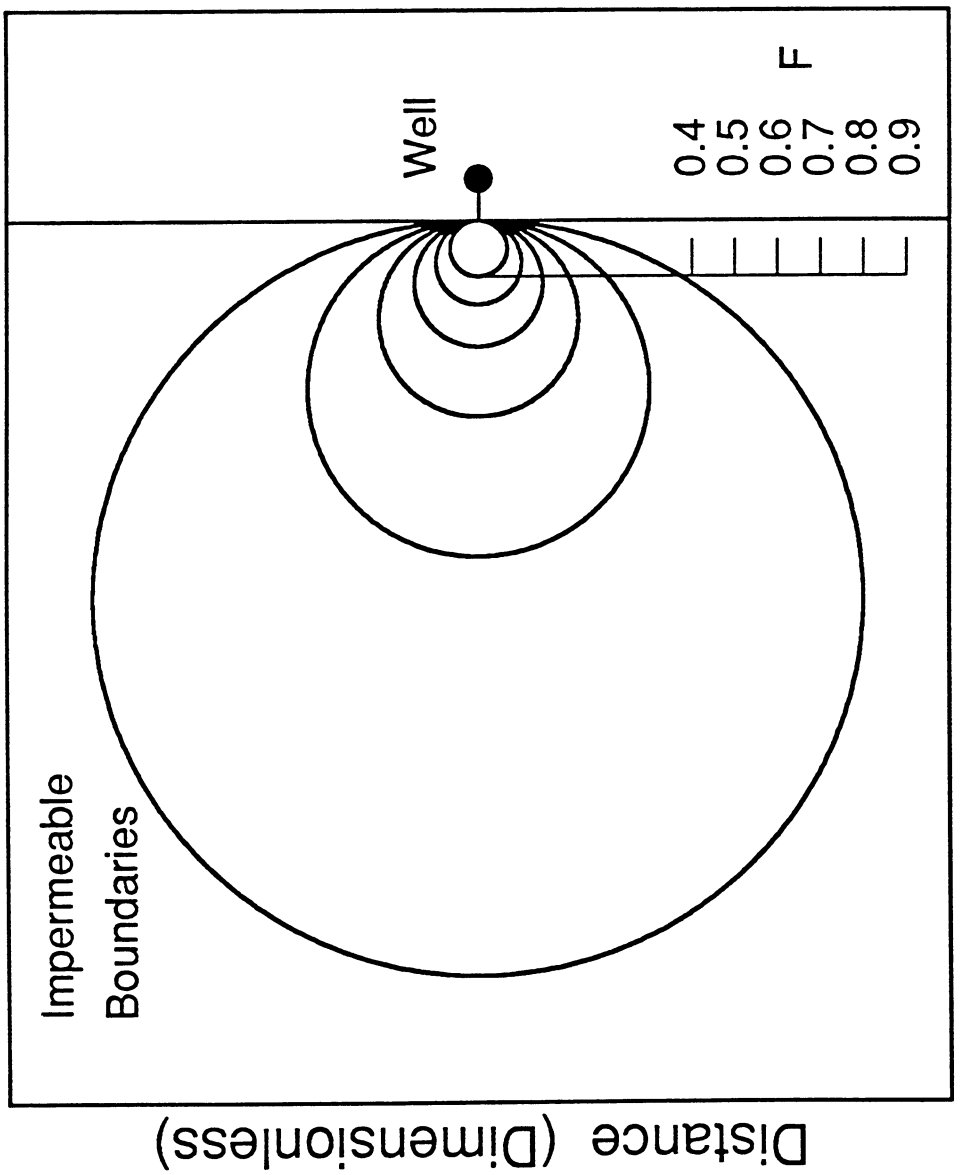

Fig. 4.2.6. Schematic diagram for a well near impermeable circular regions of different sizes.

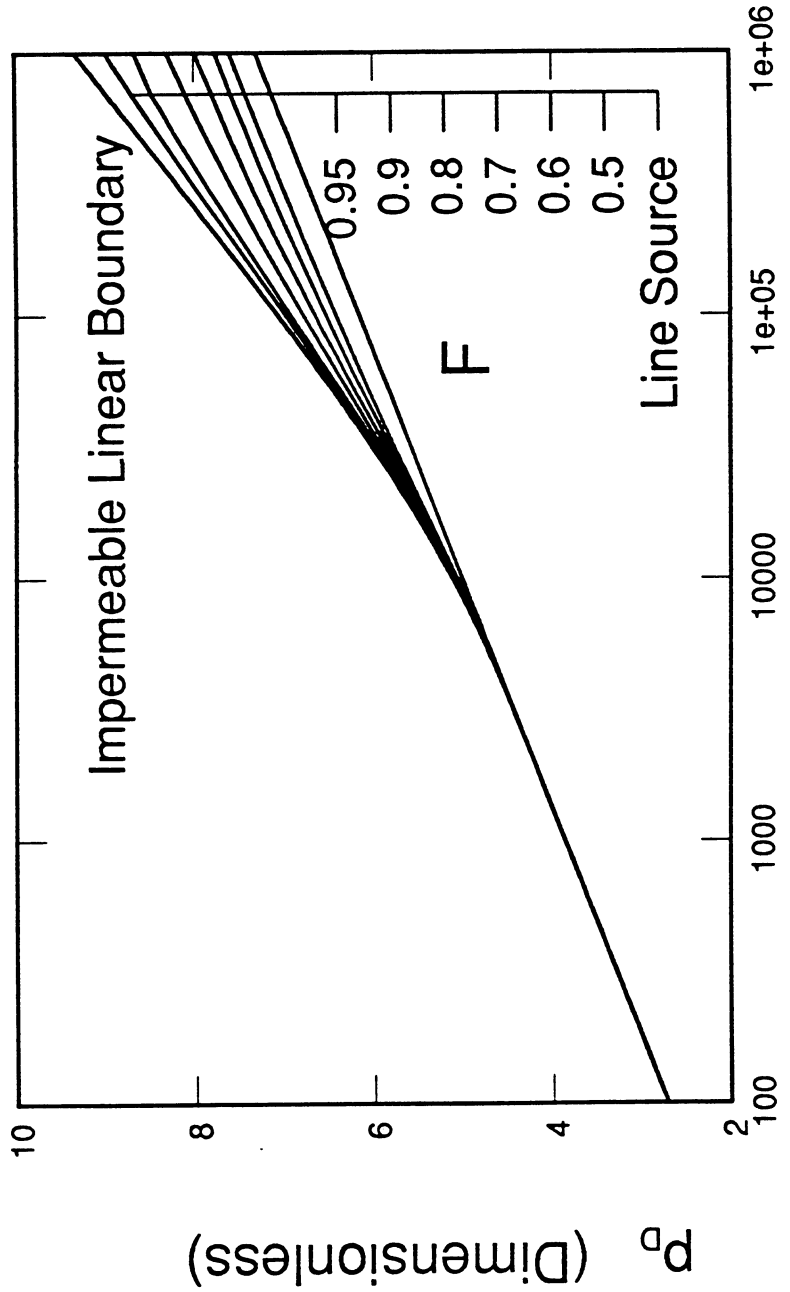

Fig. 4.2.7. Semi-log pressure responses for a well near impermeable circular regions of different sizes.

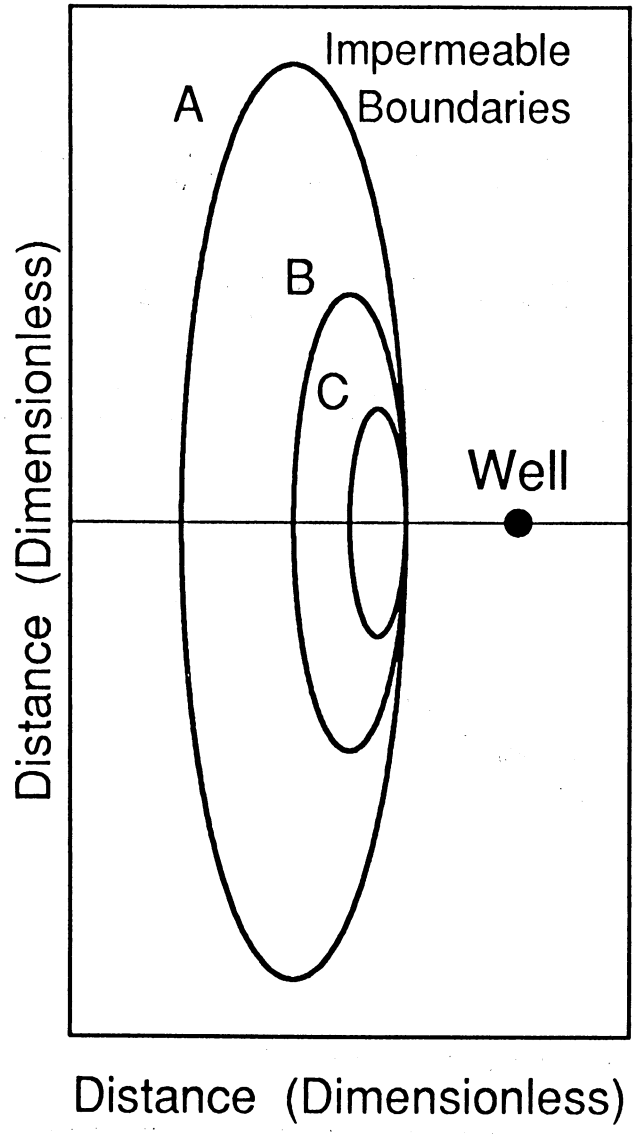

Fig. 4.2.8. Schematic diagram for a well near impermeable elliptical regions of different sizes and the same b/a ratio ; $r_{min} = 100$; A: $a = 400$, $b = 100$; B: $a = 200$, $b = 50$; C: $a = 100$, $b = 25$.

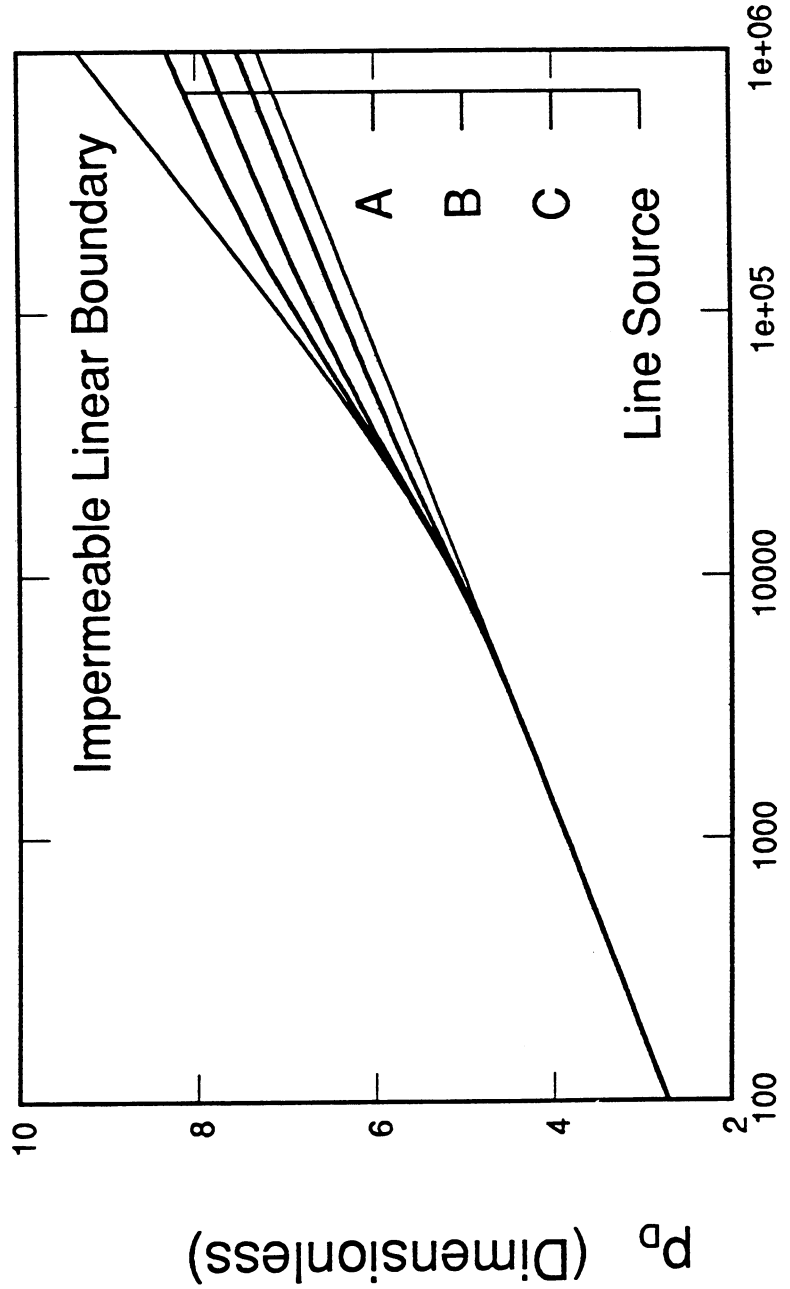

Fig. 4.2.9. Semi-log pressure responses for a well near impermeable elliptical regions of different sizes and the same b/a ratio ; $r_{min} = 100$; A: $a = 400$, $b = 100$; B: $a = 200$, $b = 50$; C: $a = 100$, $b = 25$.

The Effects of Shape

In this section we examine the effect of the shape of impermeable regions on the pressure responses of a constant rate well. Three shapes of boundaries are considered: linear, circular and elliptical. Fig. 4.2.10 shows circular and elliptical boundaries having the same area, and the same shortest distance between them and the active well of 100 wellbore radii. The circular boundary has a radius of 100 wellbore radii, and the ellipse axis ratio is 0.25, with the long axis equal to 200 wellbore radii. The pressure responses in the presence of the boundaries shown in Fig. 4.2.10 are presented in Fig. 4.2.11.

The effect of the shape of the impermeable boundary is significant. The long axis of the elliptical boundary is parallel to an impermeable linear boundary, and disrupts the homogeneous stream lines more than the circular boundary. Hence, the elliptical boundary causes a larger deviation of the pressure response from the line source homogeneous response than the circular case. A linear boundary can be considered as an elliptical boundary with an infinitely long axis and a zero short axis. Hence, the uppermost curve in Fig. 4.2.11, represents the largest pressure deviation we may observe caused by an impermeable boundary having the same area as the circle and the ellipse shown in Fig. 4.2.10, and located the same distance from the production well. However, the effects of the shape depends upon the orientation of elongated impermeable boundaries, with respect to the production well. These effects are considered in the next section.

The Effect of Orientation

In this section we consider the effects of the orientation of elongated impermeable boundaries. Fig. 4.2.12 shows four elliptical boundaries, denoted by *A*, *B*, *C*, and *D*. The ellipses are identical in size and shape, but have different locations and orientations with respect to the active production well. The ellipses denoted by *B*, *C*, and *D* are simply rotated around a pivot point located at one end of the ellipse.

The pressure responses for the cases described in Fig. 4.2.12 are shown in Fig. 4.2.13. The effects of orientation are linked to the disturbing of the homogeneous radial stream lines. Hence, the ellipse denoted by *A* causes the largest deviation from the line source solution curve. The ellipse denoted by *D*, where the long axis of the ellipse is in the direction of the production well, cannot be detected from the pressure response. The curves for ellipses *B*, *C*, and *D* are close to each other in the cases presented here. Yet, if the axis ratio were smaller (the ellipses were relatively longer), and if the production well were closer to the impermeable region, these three pressure responses would be greatly different.

We note that the pressure responses of ellipses *C* and *D* are practically identical. This observation is explained by the fact that the orientation of the long axis of these ellipses is almost parallel to the homogeneous radial stream lines, hence, minimizing the deviation from the line source response. The pressure responses shown in Fig. 4.2.13 imply that even relatively large impermeable regions near an active well may not be detected by transient pressure tests if the orientation of these regions are in the direction of the radial stream lines.

The Effect of A Fracture

In this section we consider the effects of line impermeable boundaries on the pressure responses of a constant rate well. We examine the combination of the effects of shape and orientation of an impermeable boundary that has no reservoir volume associated with it. Fig. 4.2.14 shows three impermeable fracture boundaries, denoted by *A*, *B*, and *C*. The ellipse denoted by *A* is half of ellipse *A* shown in Fig. 4.2.12. The semi-circle denoted by *B*, is half of a circular boundary presented in Fig. 4.2.6, with a relative size, *F*, of 0.5. The second ellipse in Fig. 4.2.14 denoted by *C* is half of ellipse *D* shown in Fig. 4.2.12. The shortest distance between the well and the boundaries is 100 wellbore radii.

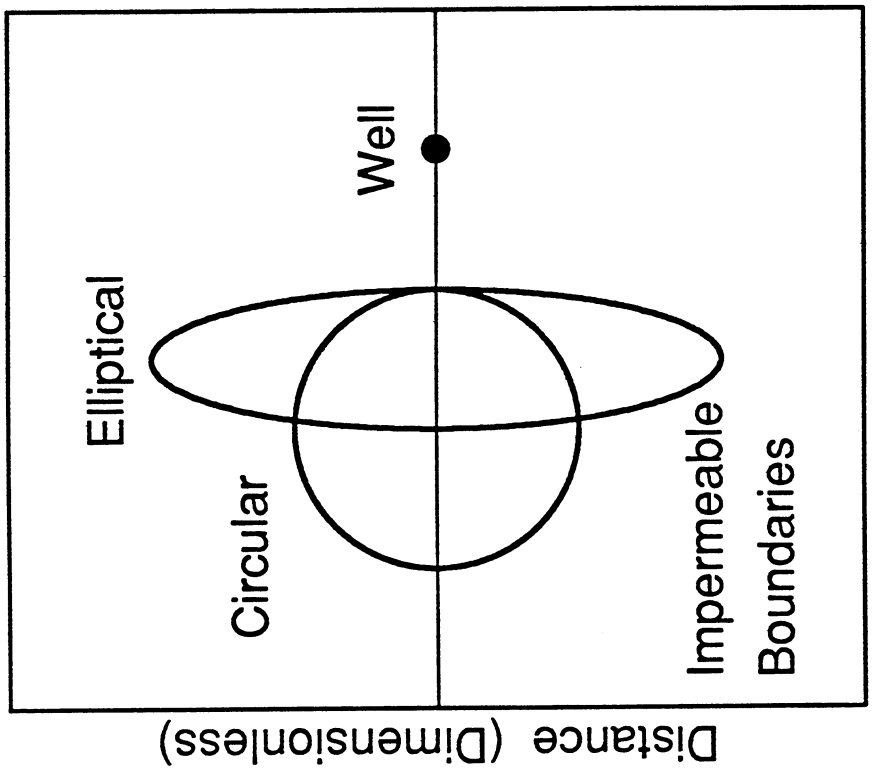

Fig. 4.2.10. Schematic diagram for a well near impermeable regions of different shapes and the same area ; r_{min} = 100 ; Circle: R = 100 ; Ellipse: a = 200 , b = 50.

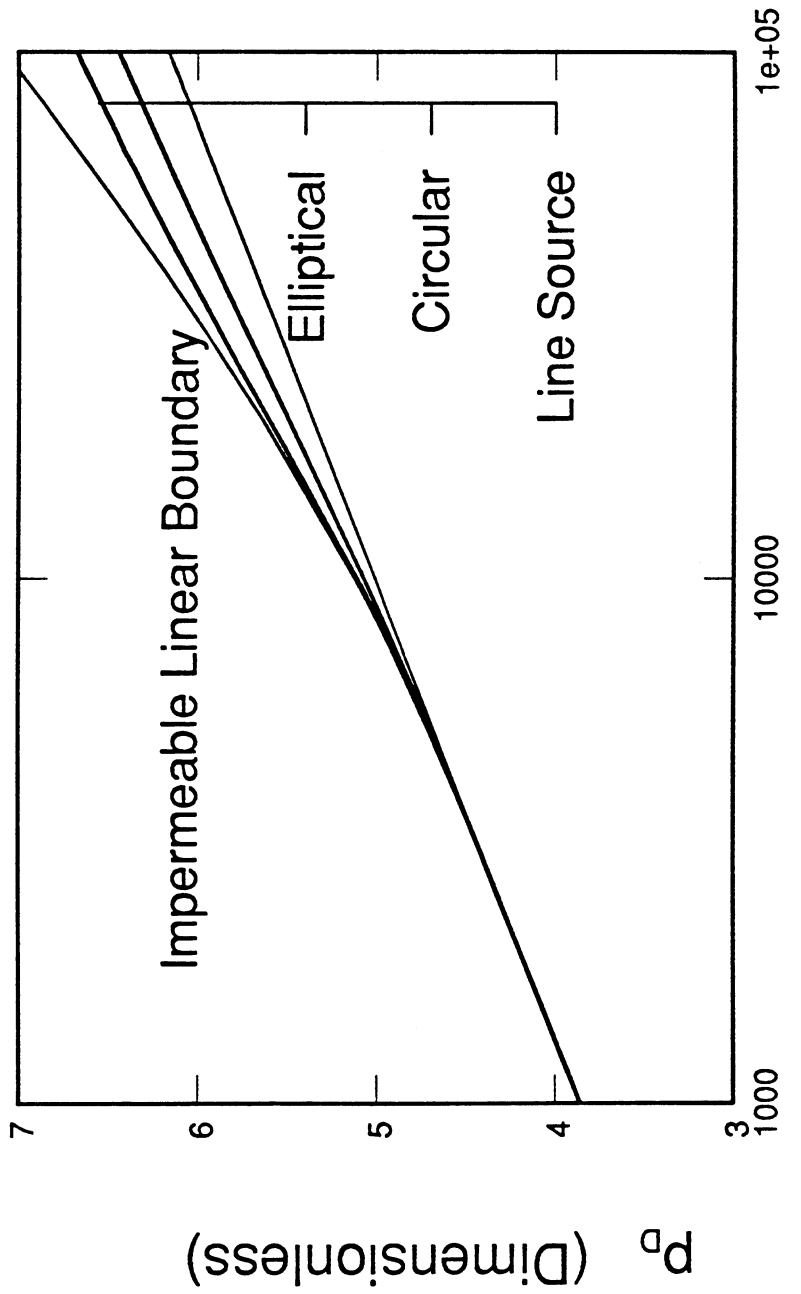

Fig. 4.2.11. Semi-log pressure responses for a well near impermeable regions of different shapes and the same area ; $r_{min} = 100$; Circle: $R = 100$; Ellipse: $a = 200$, $b = 50$.

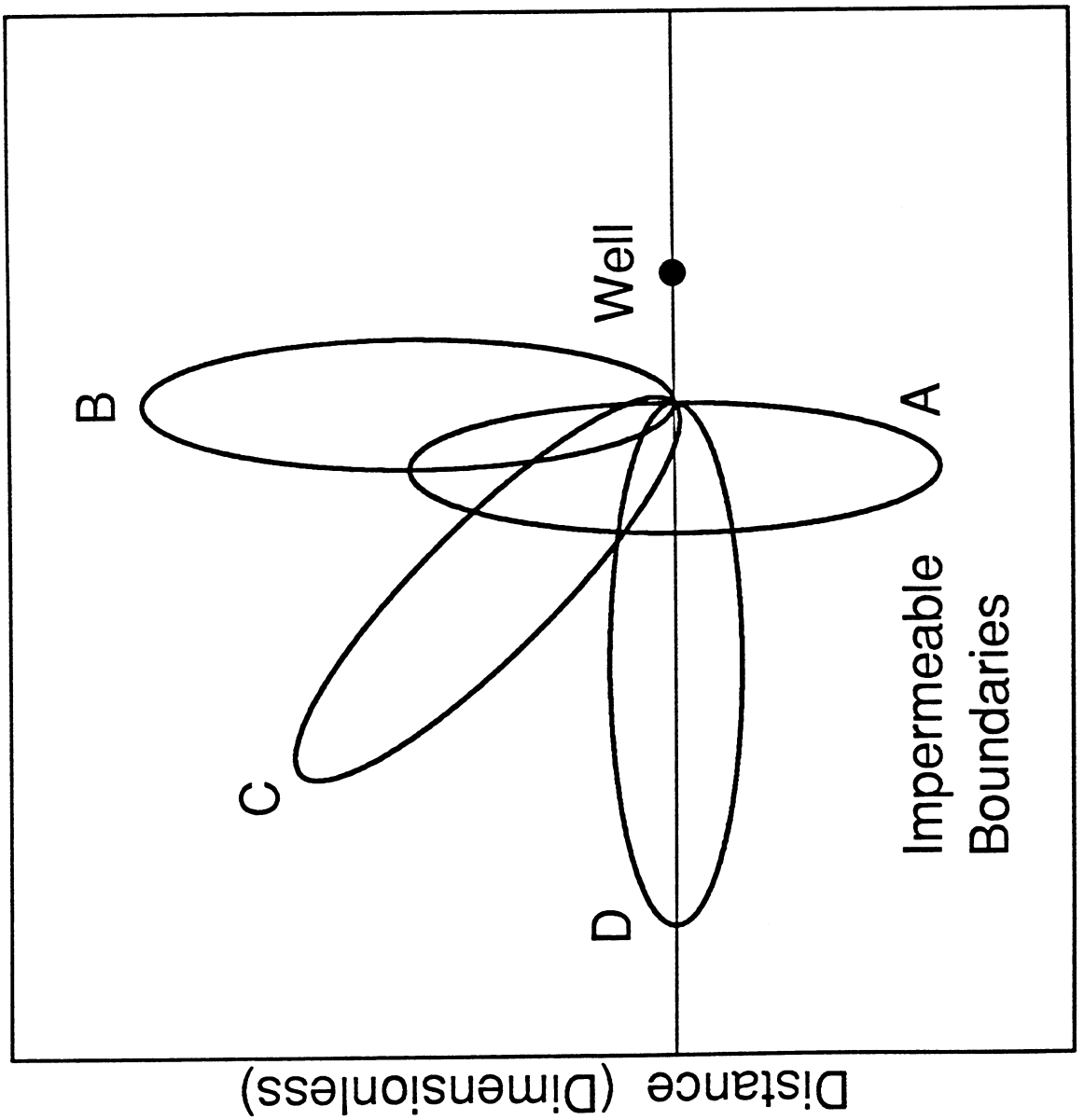

Fig. 4.2.12. Schematic diagram for a well near impermeable regions of different orientations and the same shape and area ; Ellipses: $a = 200$, $b = 50$.

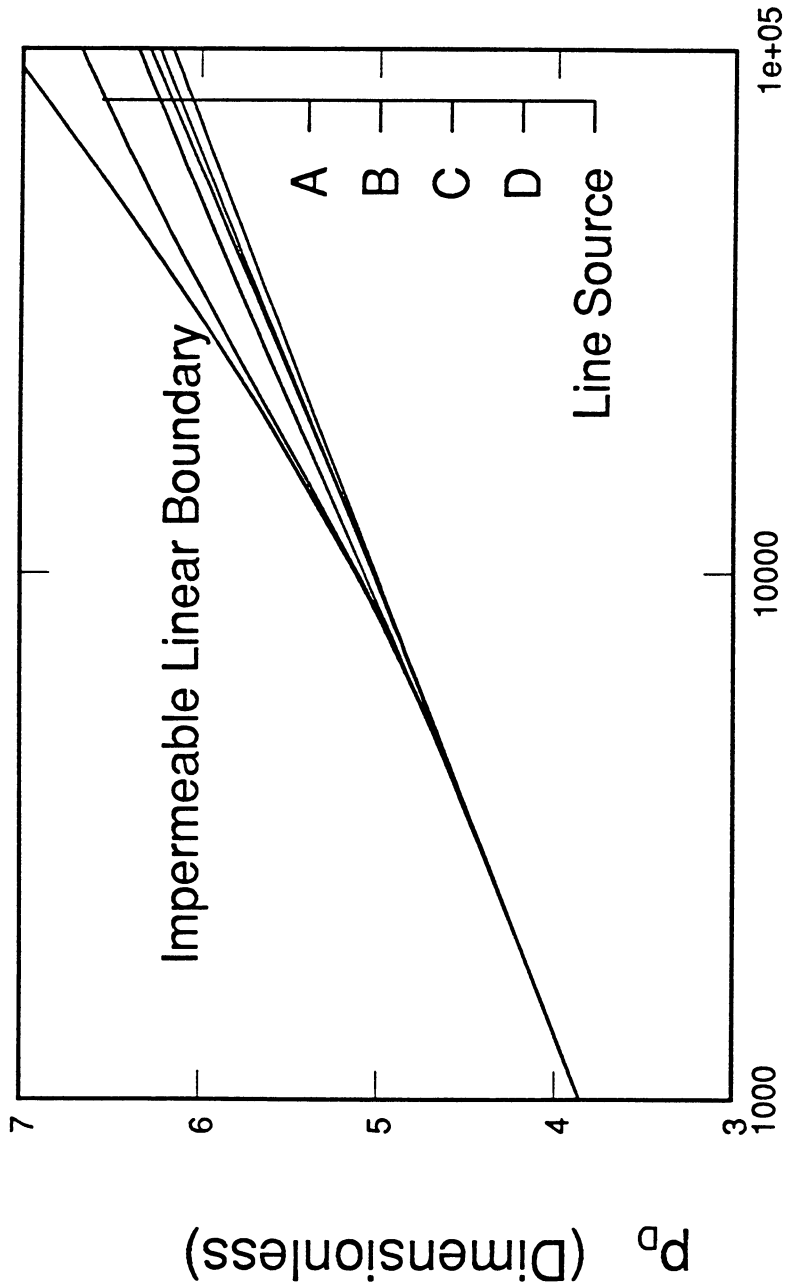

Fig. 4.2.13. Semi-log pressure response for a well near impermeable regions of different orientations and the same shape and area.

Fig. 4.2.15 presents the pressure responses corresponding to the reservoir configurations shown in Fig. 4.2.14. Again, the more we disturb the radial stream lines, the larger the deviation from the line source response. Also, the early time deviation from the line source curve is determined by the portion of the impermeable boundary facing the production well. Only the late time response, could possibly indicate the difference between an impermeable boundary with volume and an impermeable boundary without volume. The pressure responses during the first log cycle of time after the deviation from the line source response for the complete elliptical and circular boundaries are practically identical to the pressure responses of the semi-elliptical and semi-circular boundaries. For example, curve *A* in Fig. 4.2.15 is practically identical to curve *A* in Fig. 4.2.13. Hence, in order to detect the volume of an impermeable boundary in addition to the shortest distance to it, we need long tests, fine pressure resolution and a relatively large impermeable boundary.

4.2.4 Discussion

The main issue considered in this paper is the detection of large scale impermeable reservoir regions from transient pressure tests. The approach that we have taken is similar to a finite difference or a finite element approach in the observation that the analytical solution to the true problem is not readily attainable. In a finite difference approach, for example, the diffusivity equation and the boundary conditions are kept and discretized in space and in time yielding a set of algebraic equations that must be solved for each time step. In the method presented in this paper, we represent the boundary condition by a finite set of boundary wells, and impose the boundary condition at discrete points. In addition, we discretize the time domain and assuming a constant rate per time step at the boundary wells we solve the new problem analytically using the method of superposition.

Another way to look at our approach is that the true system that is infinite in the lateral extent and contains a single well and a single impermeable boundary is replaced by a system with wells without an impermeable boundary. By controlling the rates of production and injection at the boundary wells, we create the effects of an impermeable boundary. This method is directly applicable for finite volumetric impermeable boundaries. The boundary wells that are distributed inside the impermeable region along its boundary allow us to achieve three objectives: 1. prevent the early time migration of fluid from within the impermeable region toward the production well; 2. prevent the late time flow of reservoir fluid into the impermeable region and movement through it to the production well; and 3. produce the impermeable region so that its pressure declines with time as in the actual case. Hence, there is a net production out of the boundary wells that accounts for the decompression of the boundary volume that in our model is part of the reservoir.

The above observations are valid for finite volumetric boundaries, and not valid for infinite volumetric boundaries. We have applied the new model for a case of a single well in the center of a closed outer boundary reservoir. In this case, most of the reservoir volume is not connected to the production well. The boundary wells produce at an ever increasing rate, and the new method fails at late time. However, the early time portion of the pseudo steady state flow period was generated by the new model.

There is a fundamental error in applying this new model to finite length impermeable line boundaries such as fractures. Since the line boundary has no volume associated with it, the boundary wells have no volume to deplete, hence, the excess production of the boundary wells does not relate to the real reservoir configuration. For infinitely long fractures, like an impermeable linear boundary, the application of the new model is reasonable, but like the closed outer boundary case, fails at late time. For finite length fractures, such as presented in the Fracture section, the new model is applicable only for the early time boundary effects, where the reservoir area on the side of the boundary not containing the well is not allowed to expand toward the production well. The late time pressure response is affected by the net over production at the boundary wells, and is not correct. However, the early time pressure

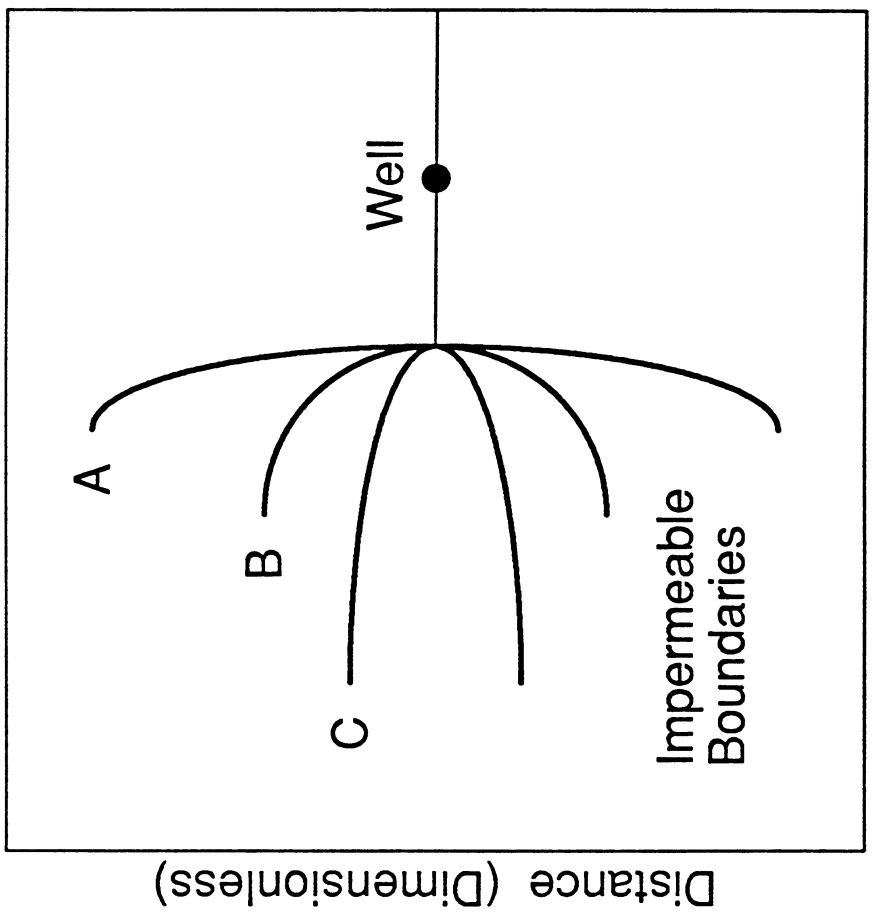

Fig. 4.2.14. Schematic diagram for a well near impermeable fractures ; r_{min} = 100 ; Ellipses with a = 200, and b = 50 ; Circle with R = 100.

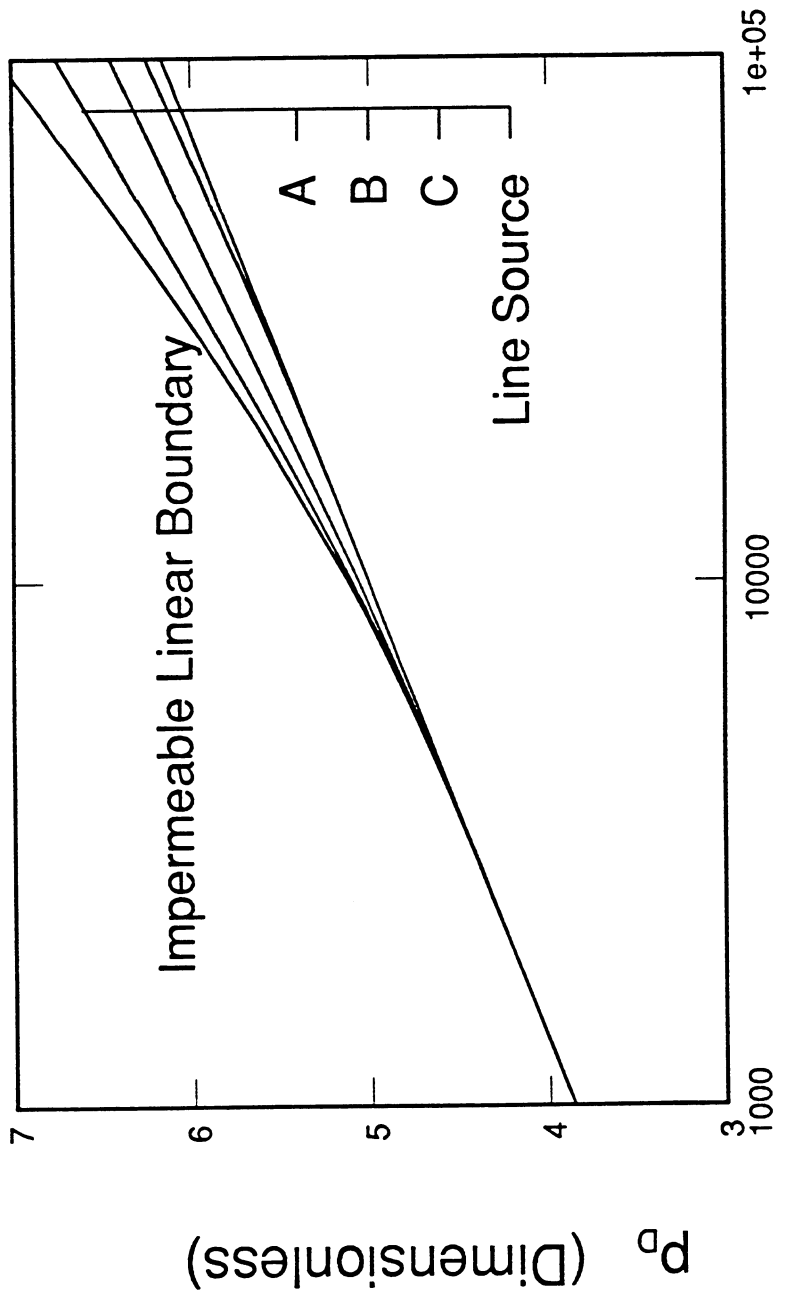

Fig. 4.2.15. Semi-log pressure response for a well near impermeable fractures ; r_{min} = 100 ; Ellipses with a = 200, and b = 50 ; Circle with R = 100.

deviation from the line source curve allows us to determine the minimum distance between the well and the impermeable fracture.

The effectiveness of the new model is sensitive to the density of the boundary wells, and their distance from the actual location of the impermeable boundary. We have found, by matching the results from the new model to analytical solutions, that an average dimensionless distance between adjacent boundary wells of 10 yielded good pressure responses. The dimensionless distance between the line of boundary wells and the actual location of the impermeable boundary varied between 1 and 10, with an average value of 5 yielding good pressure responses. In general, boundary sections with large curvature required a high density of boundary wells. Also, the portions of the boundary facing the production well required a high density of boundary wells.

The new model presented in this paper can be extended to interference testing in the presence of large scale impermeable boundaries. However, interference wells must not be close to the impermeable boundary, where the local discretization of the boundary affects interference responses in an unrealistic manner. The new model can also be applied to reservoir-well configurations that contain two or more large scale impermeable subregions, and to study isopressure finite fractures. Also, the new model can be used to study the effects of constant pressure regions on the response of a production well.

4.2.5 Conclusions

An algorithm is presented to study the effects of internal impermeable boundaries on the transient pressure response of a well producing with constant flow rate. The effects of the impermeable boundary are generated by replacing the boundary by a set of line source wells producing with variable flow rates, and then applying the method of superposition.

Keeping the other factors constant, the greater the size of the impermeable region the more the pressure response deviates from the line source homogeneous response. Also, impermeable regions must be relatively large with respect to their distance from the production well in order to be detected.

An impermeable region whose shape causes a disturbance to the radial steam lines yields a significant deviation of the pressure response from the line source solution. The more the boundary resembles a linear impermeable barrier, the greater the deviation.

From a practical point of view, there is essentially no difference in the early time transient responses of impermeable regions with volume, and impermeable fractures without volume. It would be necessary to extend a drawdown test for several log-cycles of time in order to distinguish between a volumetric and a nonvolumetric impermeable region.

The orientation of an impermeable region with respect to the production well has a great influence on the transient pressure response. Together with the shortest distance between the production well and the boundary, orientation is the most significant characteristic parameter that affects the transient pressure response.

In practice, the combined effects of size, shape, and orientation, and the distance to the production well are so intermingled that it is difficult to evaluate the effect of each parameter independently. However, those configurations that significantly disturb the radial stream lines, produce the largest deviations from the homogeneous line source solution.

The model can also be used to study the effect of different external geometries, the effects of multiple heterogeneous regions, iso-pressure finite fractures, and constant pressure regions on transient pressure responses of a production well. Its main drawback is its sensitivity to the number and distribution of line source wells used to simulated the heterogeneous region under study.

4.3 Effects of a Partially Communicating Fault in a Composite Reservoir on Transient Pressure Testing

Anil K. Ambastha

Many reservoirs are faulted and the hydraulic characterization of these faults is essential for the design of field scale developments. In addition to the effects that a fault has on fluid flow in the reservoir, it may be separating two different reservoir regions with distinctly different properties. The detection of the properties on both sides of the fault, in addition to the detection of the distance to the fault are important in the reservoir characterization process.

In this study, a linear fault is modeled as an infinitesimal thickness skin boundary. Analytical solutions for pressure transient behavior for a line-source constant-rate well in a composite reservoir are obtained using one space Fourier transformation and time-space Laplace transformations. The solutions are presented for strip and infinite reservoirs.

This study examines drawdown pressure and pressure derivative behavior, and extends and generalizes many studies presented in the past. Correlating parameters for pressure transient responses are presented. The possibilities of boundary detections are considered, and interference pressure responses in a composite, strip reservoir are briefly discussed.

4.3.1 Introduction

Many reservoirs are faulted and the hydraulic characterization of these faults is essential for the design of field scale developments. Traditionally, the faults have been treated as sealing boundaries. The method of images has been used to study drawdown, buildup or interference pressure transient behavior for a well in a homogeneous reservoir, containing single or multiple linear, sealing boundaries. The "doubling of slope" is used to indicate the presence of a linear, sealing boundary. The intersection time of the two semi-log straight lines is used to calculate the distance to a barrier (Horner 1951, Davis and Hawkins 1963, and Gray 1965). Also, the deviation time at which the pressure response departs from the line-source solution can be used to calculate the distance to a barrier. Log-log (Stallman 1952) and semi-log (Horner 1951) type-curve matching methods have been developed to calculate the distance to a barrier. The pressure transient behavior of a well in a long narrow reservoir has been studied (Tiab and Kumar 1980, Ehlig-Economides and Economides 1982, Nutakki and Mattar 1982, and Ehlig-Economides and Economides 1985). Streltsova and McKinley (1984) discuss the pressure transient behavior for a well in a reservoir, limited by one or more linear boundaries. They consider both closed and constant-pressure boundaries, and discontinuities in reservoir properties. Prasad, (1975) and Wong et al. (1986) used a Green's function approach to generate multiple sealing boundaries.

Figure 4.3.1 presents a number of homogeneous reservoir configurations with single or multiple linear, sealing boundaries considered in the literature. Recently, the effects of a partially communicating fault in an infinite, homogeneous reservoir have been considered numerically (Stewart et al 1984) and analytically (Yaxley 1985). Pressure derivative techniques have been used to analyze pressure transient data for fault detection (Clark 1985). The pressure transient behavior of an infinitely large composite reservoir with a linear discontinuity in reservoir properties has been considered by Bixel et al., (1963) and Streltsova and McKinley (1984). The effects of a partially communicating fault (or a linear leaky discontinuity) in a composite reservoir (Fig. 4.3.2a) on transient pressure testing have not been considered. The upper part of Fig. 4.3.2a shows a side view of two reservoir regions separated by a fault. Also, the fault may be partially communicating, depending on its characteristics. The reservoir configuration of the upper part of Fig. 4.3.2a is simplified by removing the vertical discontinuity caused by the fault, making the two reservoir parts horizontal, and by making the fault discontinuity vertical as described in the lower part of Fig. 4.3.2a. Figures 4.3.2b and 4.3.2c are top views of

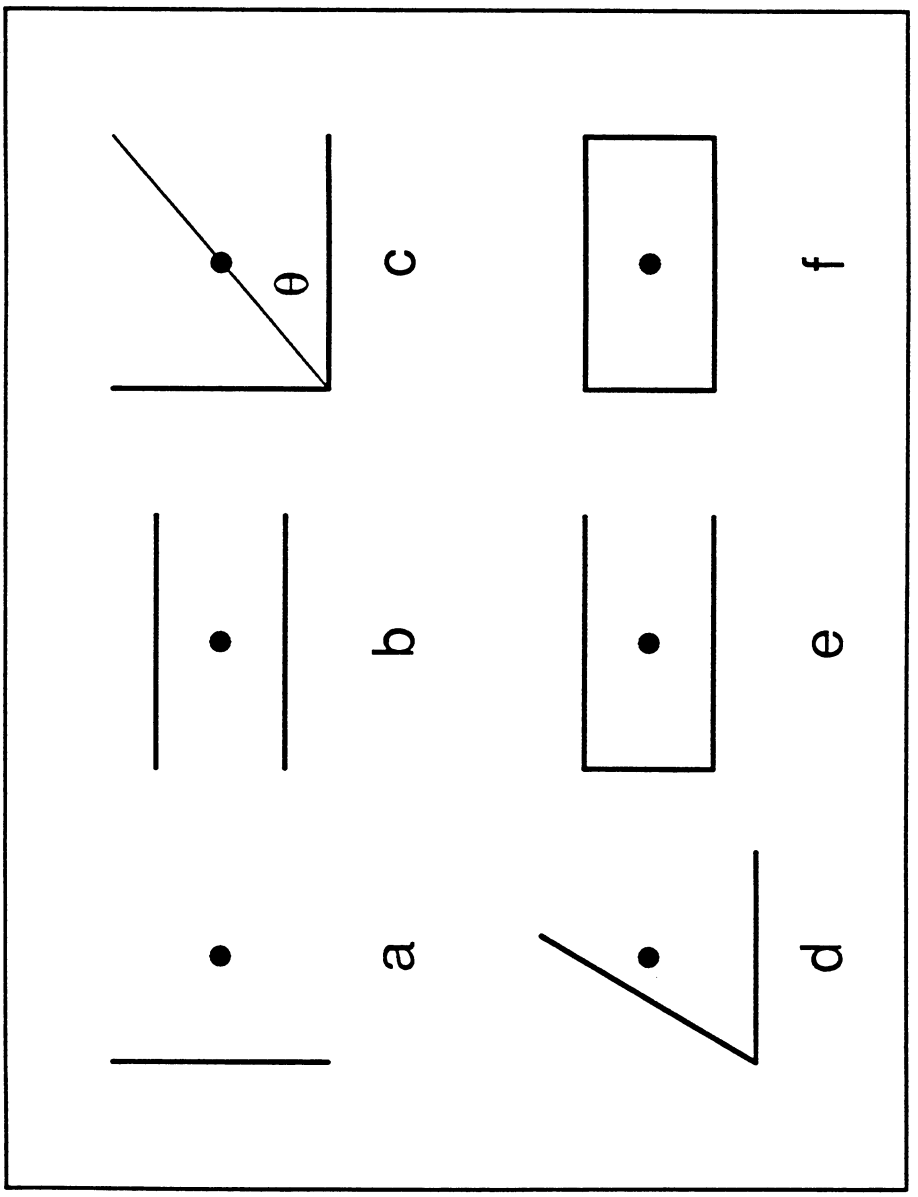

Fig. 4.3.1. Homogeneous reservoir configurations studied in the literature.

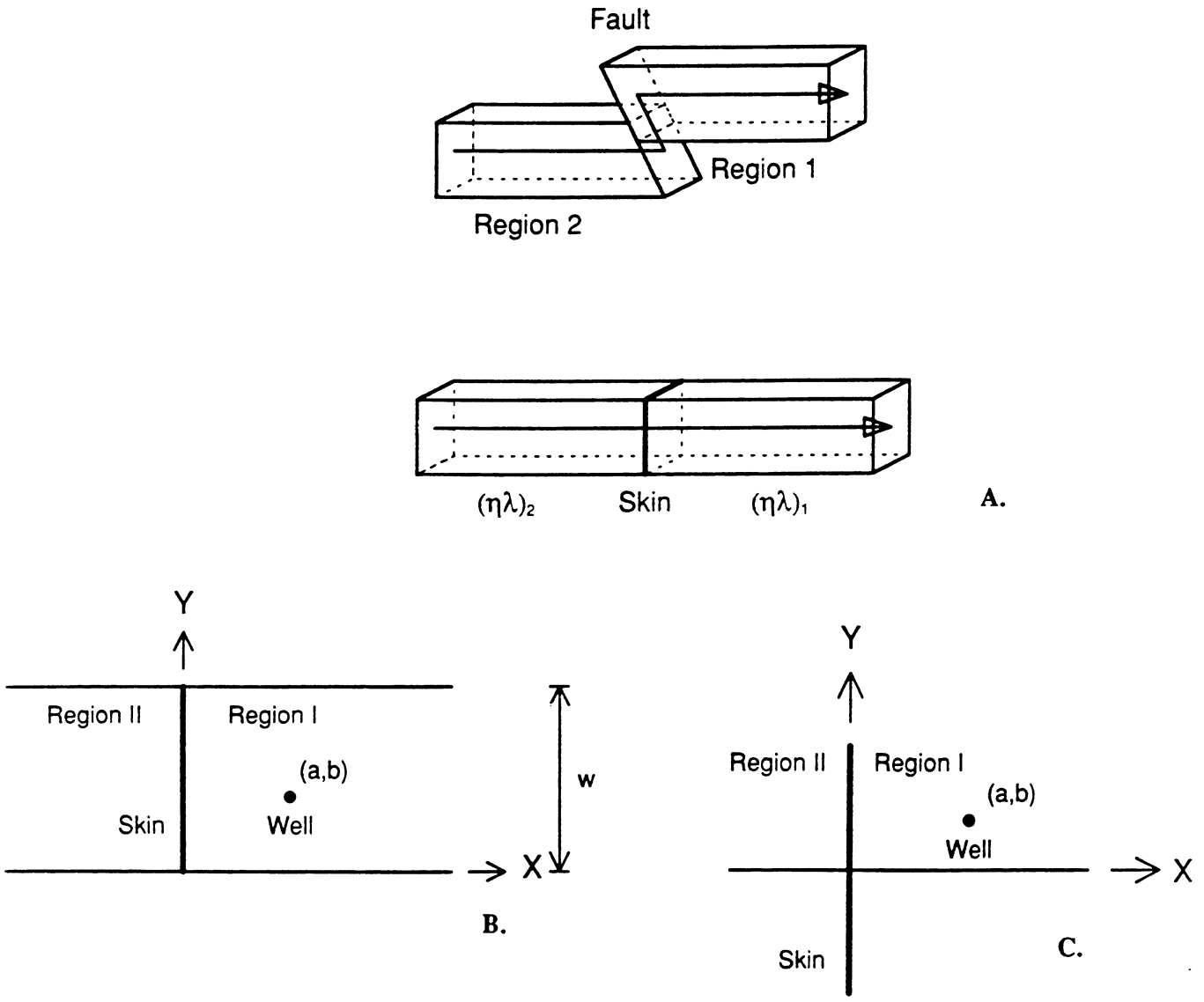

Fig. 4.3.2 Schematic diagram of a composite reservoir with a partially communicating fault; A: modeling fault as a skin boundary; B: idealized composite strip reservoir, top view, and C: idealized composite infinite reservoir, top view.

the simplified reservoir configurations that we considered in this paper. Figure 4.3.2b represents a strip reservoir with two parallel no-flow boundaries and Fig. 4.3.2c represents an infinite reservoir with a linear discontinuity. The two reservoir regions on both sides of the fault (discontinuity) may have different diffusivities and transmissivities, and the resistance to flow at the fault is modeled as a thin skin, using the concepts of van Everdingen (1953) and Hurst (1953). The active well is located in region I and is considered as a constant rate line source. The problem is solved along the approach taken by Bixel et al. (1963), and Yaxley (1985), using one Fourier space transformation and two Laplace time-space transformations. The solutions for the pressure responses for the active and observation wells, and drawdown pressure and pressure derivative behaviors are presented. Interference pressure behavior is also briefly discussed.

4.3.2 Theory

The mathematical model and a solution technique for the strip reservoir configuration of Fig. 4.3.2b are detailed in Ambastha et al. (1987). In developing the mathematical model, we make the assumptions that we have a single-phase slightly compressible fluid of constant compressibility, a homogeneous and isotropic reservoir on each side of the partially communicating fault, a constant formation thickness, and a line-source well. The diffusivity equations for both regions along with the appropriate outer and skin boundary conditions are posed. The Laplace transformation with respect to the time variable and the Fourier transformation with respect to the y variable reduce the two partial differential equations to two ordinary differential equations. The ordinary differential equation for region II is readily solved. However, the ordinary differential equation for region I (the region containing the well) is solved by taking the Laplace transformation with respect to the x variable, and inverting the resulting solution analytically with respect to the x variable. Thus, the dimensionless pressure drops in the Laplace-Fourier space at any location in regions I and II at any time are given by Eqs. (4.3.1) and (4.3.2) respectively:

$$\hat{\bar{p}}_{D1} = -\frac{\alpha_3}{2\sqrt{\alpha_1}}\left[e^{-|x_D - a_D|\sqrt{\alpha_1}} + \frac{\sqrt{\alpha_1} + S\lambda\sqrt{\alpha_1\alpha_2} - \lambda\sqrt{\alpha_2}}{\sqrt{\alpha_1} + S\lambda\sqrt{\alpha_1\alpha_2} + \lambda\sqrt{\alpha_2}}\; e^{-(x_D + a_D)\sqrt{\alpha_1}}\right] \quad \text{for } x_D \geq 0 \qquad (4.3.1)$$

$$\hat{\bar{p}}_{D2} = -\frac{\alpha_3\, e^{x_D\sqrt{\alpha_2} - a_D\sqrt{\alpha_1}}}{\sqrt{\alpha_1} + S\lambda\sqrt{\alpha_1\alpha_2} + \lambda\sqrt{\alpha_2}} \quad \text{for } x_D \leq 0 \qquad (4.3.2)$$

where:

$\hat{\bar{p}}_{D1}$ = Laplace-Fourier dimensionless pressure drop in region I
$\hat{\bar{p}}_{D2}$ = Laplace-Fourier dimensionless pressure drop in region II
λ = Mobility ratio, $(k/\mu)_2 / (k/\mu)_1$
S = Skin effect at the discontinuity
x_D = Dimensionless distance, x/r_w
a_D = Distance between the well and the fault
α_1 = $\nu^2 m^2 + 1$
α_2 = $\nu^2 m^2 + \frac{1}{\eta}$
α_3 = $\frac{-2\pi\nu \cos(m\bar{b}_D)}{1}$
b = y co-ordinate of well location
ν = Constant = π/w_D
m = Fourier variable
l = Laplace variable with respect to time

Equations (4.3.1) and (4.3.2) are of an exponential form in the x variable, and the Laplace time variable and the Fourier y variable are in the α terms. The variable S denotes the van Everdingen (1953) and Hurst (1953) skin assigned to the fault and the variable λ represents the mobility ratio between region II and region I. All the variables are defined in Ambastha et al. (1987). The numerical inversion technique of the Laplace-Fourier solutions is described in Ambastha et al. (1987). Equations (4.3.1) and (4.3.2) also represent the dimensionless pressure drops in the Laplace-Fourier space at any location in regions I and II respectively for an infinitely large composite reservoir shown in Fig. 4.3.2c with the modified definitions of α_1, α_2 and α_3 as presented in Ambastha et al. (1987). The solution to the infinite reservoir case follows the solution for the strip reservoir case, except for the y direction Fourier transformation. In the strip case, we use a finite cosine Fourier transformation and in the infinite case, we use a complex infinite Fourier transformation. The numerical inversion technique of the solutions for an infinitely large composite reservoir and some computational experiences are discussed in Ambastha et al. (1987).

4.3.3 Validation

There are several special cases in the literature against which the model developed in this study can be validated. Fig. 4.3.3 presents a number of pressure responses in semi-log coordinates for infinite reservoirs generated using the solution presented in this study. The wellbore pressure is computed at $x_D = a_D - 1$. In Fig. 4.3.3, the dimensionless distance between the well and the boundary, a_D, and the diffusivity ratio, η, are 400 and 1, respectively. The values of mobility ratio, λ, and skin at the boundary, S, used to generate the different curves are shown on Fig. 4.3.3. Computing the dimensionless wellbore pressure drop in real space involves successive numerical inversions of the Fourier and Laplace transformations. The linearity of the Fourier and Laplace transformations is shown by curve E, where the solution represented by the solid line is obtained by a numerical inversion of the Fourier transformation first. The circles represent the solution obtained by a numerical inversion of the Laplace transformation first. The different curves in Fig. 4.3.3 represent the following reservoir configurations:

- Curves A and B: A well near a sealing fault (Horner 1951, Stallman 1952, Tiab and Kumar 1980, Yaxley 1985, and Bixel et al 1963, Fig. 4.3.1a).
- Curve C: A well near a partially communicating fault in a homogeneous reservoir (Yaxley 1985).
- Curve D: A line-source well in an infinite, homogeneous reservoir (Theis 1935).
- Curve E: A well in an infinite, composite reservoir (Streltsova and McKinley 1984, Bixel et al 1963).
- Curve F: A well near a constant-pressure boundary (Tiab and Kumar 1980, Yaxley 1985, and Bixel et al 1963).

A small mobility ratio or a large skin (curves A and B) results in the pressure drawdown behavior that follows the line-source solution, until the boundary effects become significant. Then, the pressure response exhibits the doubling of slope, indicating the presence of a linear sealing boundary. However, if the boundary is leaky, as in curve C, the pressure transient behavior follows the double slope line after departing from the line-source solution for some time, and then depending on the magnitude of boundary skin, the pressure response becomes parallel to the line-source solution at late time. The pressure drawdown response for a well in an infinitely large homogeneous reservoir ($\lambda = 1$, $\eta = 1$, $S = 0$) is the same as the line-source solution (curve D). However, if there is a property contrast, such as shown in curve E, the pressure transient behavior departs from the line-source solution, and tries to follow the constant-pressure boundary solution (curve F) for $\lambda > 1$. But the pressure response remains bounded between the line-source solution (curve D) and the constant-pressure boundary solution (curve F), depending upon the mobility ratio.

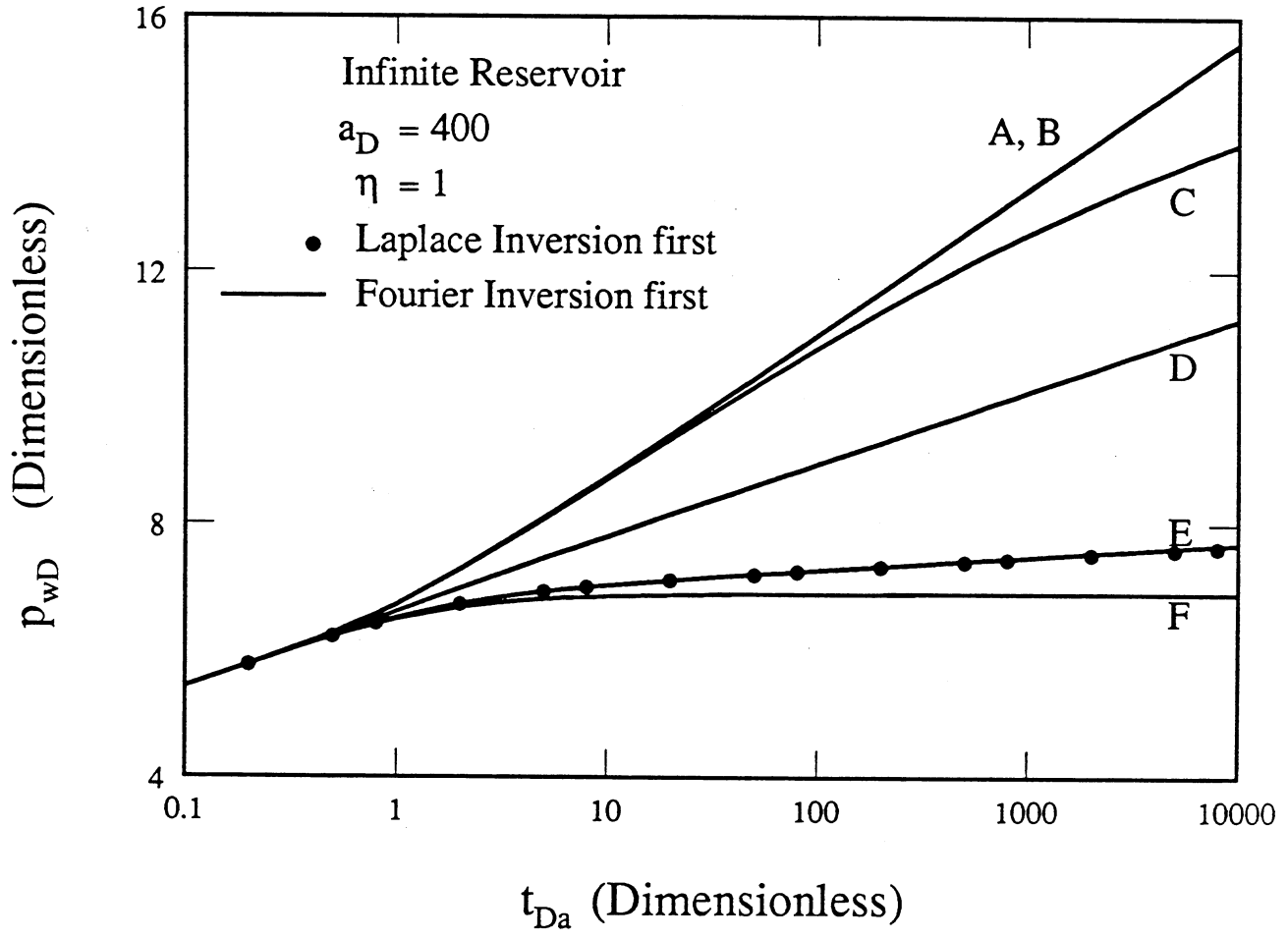

Fig. 4.3.3. Drawdown pressure responses for a well in an infinite reservoir; A: $\lambda = 1$, $S = 10^6$; B: $\lambda = 10^{-4}$, $S = 0$; C: $\lambda = 1$, $S = 100$; D: $\lambda = 1$, $S = 0$ (Line-source solution); E: $\lambda = 10$, $S = 0$; and F: $\lambda = 10^4$, $S = 0$.

Figure 4.3.4 presents the dimensionless wellbore pressure responses for several strip reservoir cases generated using the solution developed in this study. The different curves represent the following configurations:

- Curve A: A well in the center of a strip reservoir (Ramey and Cobb 1973, Tiab and Kumar 1980, Ehlig-Economides and Economides 1982, Nutakki and Mattar 1982, Ehlig-Economides and Economides 1985 Streltsova and McKinley 1984, Fig. 4.3.1b)
- Curve B: A well located arbitrarily between parallel sealing faults (Tiab and Kumar 1980, Streltsova and McKinley 1984, Fig. 4.3.1b)
- Curve C: A well between two perpendicular intersecting faults (Tiab and Crichlow 1979 and Van Poolen 1965, Fig. 4.3.1c)
- Curve D: A well in a three fault system (Tiab and Crichlow 1979, Fig. 4.3.1e)

The pressure transient response of a line-source well is also shown in Fig. 4.3.4. The wellbore pressure is computed at $x_D = a_D - 1$. Figure 4.3.5 shows the semi-log pressure derivatives corresponding to the cases shown in Fig. 4.3.4. The semi-log pressure derivative is computed as:

$$p'_D = \frac{dp_{wD}}{d \ln t_D} = t_D \frac{dp_{wD}}{dt_D} \tag{4.3.3}$$

where p_{wD} = dimensionless wellbore pressure, t_D = dimensionless time and $dp_{wD}/dt_D = L^{-1}[l\, \bar{p}_{wD}]$. Figures 4.3.4 and 4.3.5 are for $\lambda = 1$, $\eta = 1$, and $a_D = 5$. Curves A and B are for $w_D = 100$ and $S = 0$ with $b_D = 50$ and 10, respectively. Curves C and D are for $S = 10^6$ to generate the effects of a sealing skin boundary. Curve C is for $b_D = 0.88$ and $w_D = 200$, while curve D is for $b_D = 5$ and $w_D = 10$. The distance $b_D = 0.88$ for curve C corresponds to $\theta = 10°$ (Fig. 4.3.1c) for a well between two perpendicular intersecting faults. The distance $b_D = 0.88$ is intentionally selected to observe the behavior of the reservoir configuration presented in Fig. 4.3.1c for the most part of the pressure on Fig. 4.3.4. For curves A and B, the value of a_D is irrelevant, as we are considering a homogeneous reservoir with $S = 0$. Curve A follows the line-source solution before the effects of two parallel boundaries are felt concurrently. After the departure of the pressure response of curve A from the line-source solution, the late time linear flow behavior is illustrated by half slope lines on the log-log graphs of the pressure (Fig. 4.3.4) and the pressure derivative (Fig. 4.3.5) responses. However, for curve B, the effect of one boundary at a distance of $b_D = 10$ is felt first, and then at late time, the transient response on curve B approaches the linear flow behavior, as in curve A. For curve B, the doubling of the semi-log slope is also evident in Fig. 4.3.5 for a short duration. For curve C, the effect of the boundary at a distance of $b_D = 0.88$ has been felt even before $t_D = 1$, and therefore, the dimensionless wellbore pressure drop is always above the line source solution. However, before curve C may double the slope, the effects of the skin boundary (that is a sealing fault because of large skin value) are felt, and the semi-log pressure derivative rises to 2 at $t_D \approx 100$, and lasts up to $t_D \approx 9000$. The quadrupling of the semi-log slope to 2 is the same as the pressure transient behavior for a well between two perpendicular intersecting faults. At late time, the effects of the third boundary at a distance of $w_D - b_D = (200 - 0.88)$ from the wellbore is felt, and the linear flow in a semi-infinite strip reservoir is observed as half slope lines on Figs. 4.3.4 and 4.3.5 for the curve C. For curve D, the effects of three boundaries at distances of $a_D = 5$, $b_D = 5$, and $w_D - b_D = 5$ are felt simultaneously at $t_D \approx 10$. At late time, half slope lines on the log-log graphs of Figs. 4.3.4 and 4.3.5 depict the linear flow in a semi-infinite strip system. A more detailed analysis of the linear flow in a semi-infinite system appears in Ambastha and Sageev (1987). The departure of the pressure response from the line-source solution, the doubling or quadrupling of semi-log slopes, and the late time linear flow is discussed in detail later.

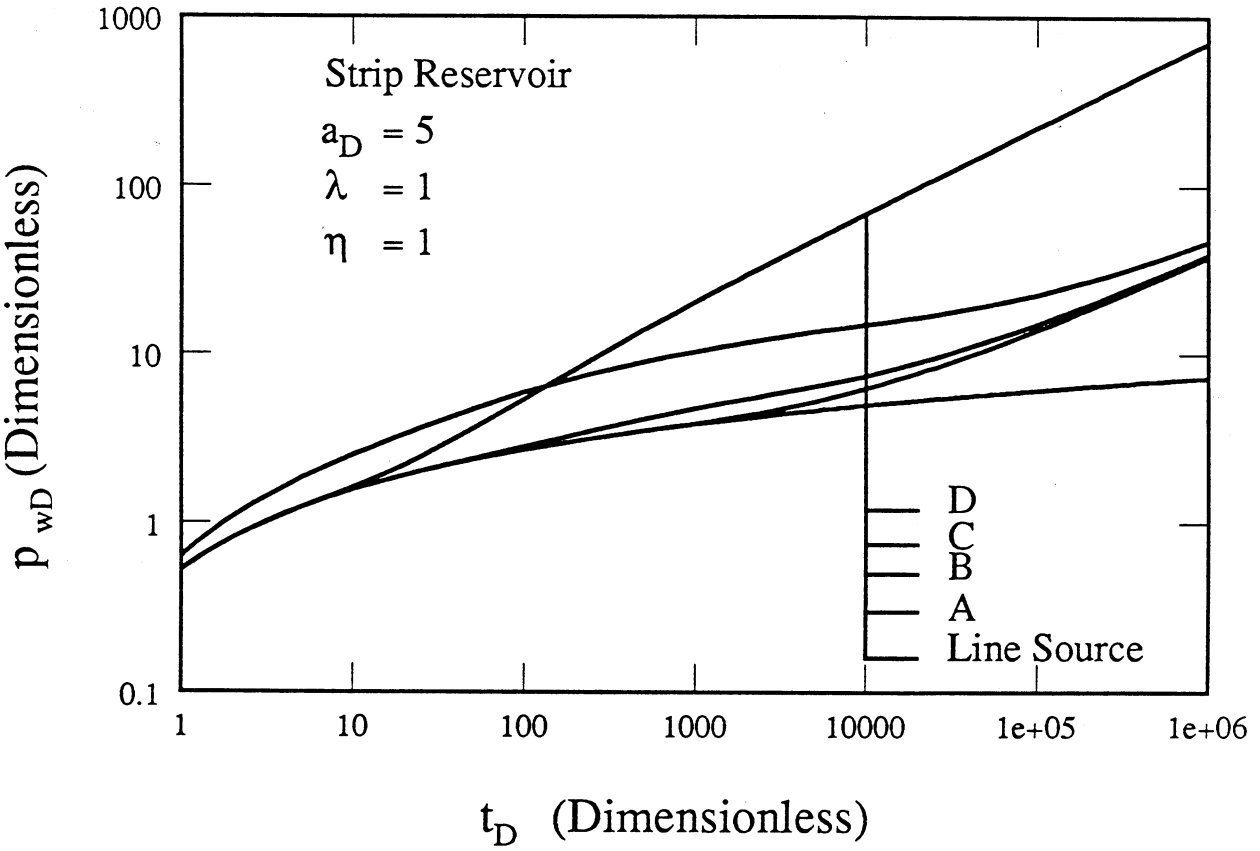

Fig. 4.3.4. Drawdown pressure responses for a well in a strip reservoir; A: $b_D = 50$, $w_D = 100$, $S = 0$; B: $b_D = 10$, $w_D = 100$, $S = 0$; C: $b_D = 0.88$, $w_D = 200$, $S = 10^6$; and D: $b_D = 5$, $w_D = 10$, $S = 10^6$.

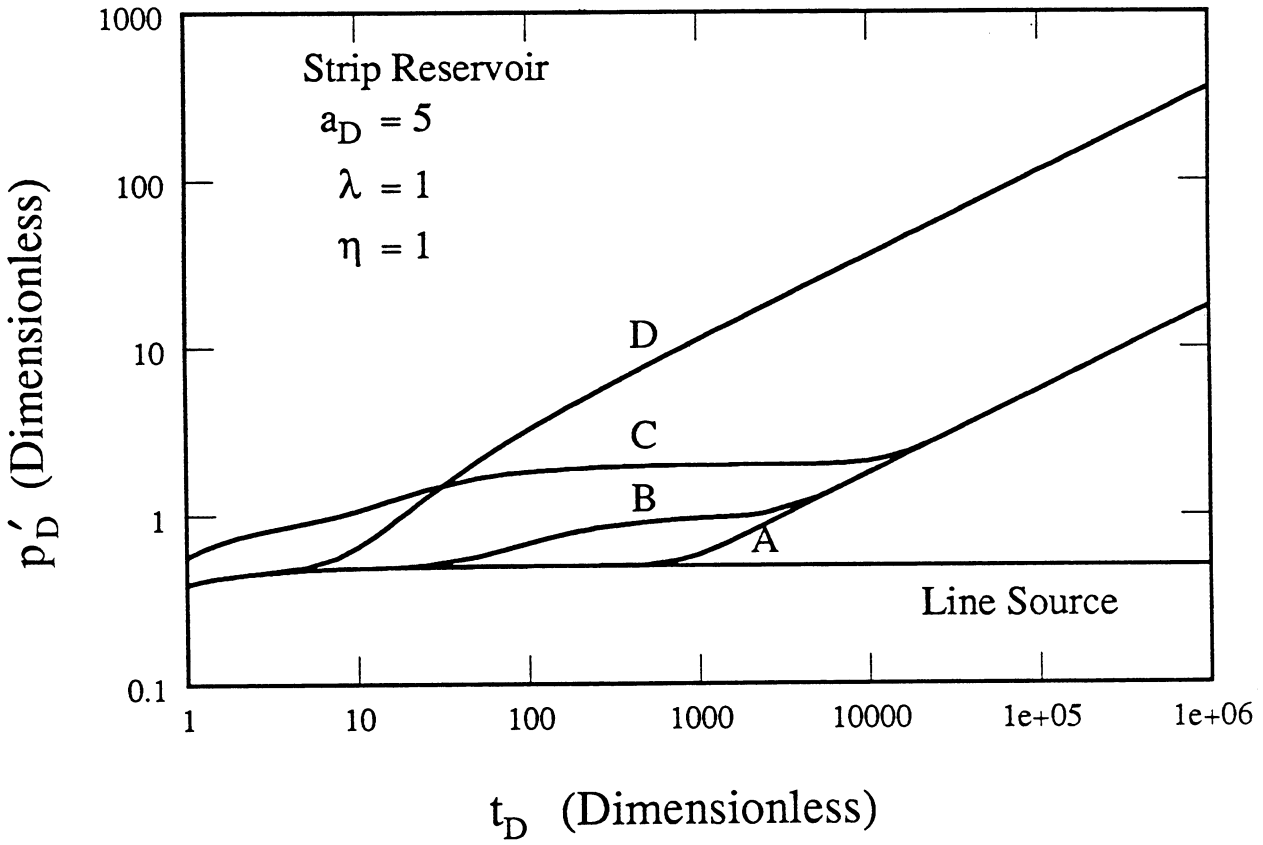

Fig. 4.3.5. Drawdown pressure derivative responses for a well in a strip reservoir; A: $b_D = 50$, $w_D = 100$, $S = 0$; B: $b_D = 10$, $w_D = 100$, $S = 0$; C: $b_D = 0.88$, $w_D = 200$, $S = 10^6$; and D: $b_D = 5$, $w_D = 10$, $S = 10^6$.

4.3.4 Drawdown Behavior of Infinite Reservoirs

Bixel et al. (1963) presented the pressure transient behavior for a well in an infinitely large composite reservoir. The two reservoir regions are separated by a linear discontinuity. Bixel et al. (1963) stated that such a configuration may represent a well in a relatively thin reservoir near a fluid-fluid contact, or a well in a reservoir exhibiting a sudden change in rock and fluid characteristics because of clay fill, facies changes, buried shore lines, and channel deposits. Bixel et al. (1963) presented semi-log graphs of the dimensionless wellbore pressure vs. dimensionless time based on the distance to the discontinuity, a, with the mobility and storativity ratios as the parameters. They defined the storativity ratio, F, as $(\phi c_t)_{II} / (\phi c_t)_I = \lambda/\eta$. They presented the results only for $a_D = 400$. They observed that if $t_D > 25$ (i.e., if the log approximation of exponential-integral solution is valid), the effect of a change in a or x is the addition or subtraction of a constant to the dimensionless wellbore pressure drops for any given a_D (in their case, $a_D = 400$). This additive constant is $\ln (400 / a_D)$, if the dimensionless wellbore pressure drops for any a_D are correlated with the pressure response for $a_D = 400$. A similar pressure scale shift has been used by Sageev et al. (1985) to develop a semi-log type-curve for a well near a linear boundary. Yaxley (1985) considered the effects of a partially communicating fault on the transient pressure behavior of a well in an infinite, homogeneous reservoir. He treated a partially communicating fault as an infinitely long, vertical semipermeable barrier. He presented the drawdown pressure and pressure derivative behavior vs. t_{Da} as semi-log graphs with the specific transmissivity ratio, α_A, as a parameter. α_A is defined as:

$$\alpha_A = \frac{k_S / \Delta X}{k / a} \tag{4.3.4}$$

for uniform viscosity and thickness in the reservoir and the fault regions. k_S and ΔX are the permeability and horizontal thickness of the fault zone, respectively. k is the reservoir permeability, and a is the distance between the fault and the active well. Since we model a partially communicating fault as an infinitesimally thin skin, a relationship between α_A and S can be derived using Darcy's law for steady-state flow across the fault zone. This relationship is:

$$S = \frac{2\pi a}{\alpha_A} \tag{4.3.5}$$

per unit of reservoir width. In Eq. (4.3.5), a is in centimeters. The consideration of an example with $a = 10$ cm., and $\alpha_A = 0.001$ shows that $S = 10000\ \pi$. A relationship among the variables S, k_S / k, and ΔX is:

$$S = \frac{2\pi}{k_S / k}\ \Delta X \tag{4.3.6}$$

Equation (4.3.6) yields $S = 200\ \pi$ for $k_S / k = 0.1$ and $\Delta X = 10$ cm. Thus, large skin values may generate the effects of a sealing fault.

The parameters for the pressure drawdown behavior of a well in an infinite composite reservoir with a partially communicating fault are λ, η, and S, when the pressure and the pressure derivative responses are graphed as a function of the dimensionless time based on the distance between the fault and the well, t_{Da}, given by:

$$t_{Da} = \left[\frac{k}{\phi\mu c_t}\right]_I \frac{t}{a^2} \tag{4.3.7}$$

where:

t = Time, hour
t_{Da} = Dimensionless time, normalized by the distance a.
k = Permeability, md
μ = Viscosity, cp
ϕ = Porosity, fraction
c_t = Total system compressibility, psi $^{-1}$

Figure 4.3.6 presents the effects of mobility ratio on the pressure drawdown behavior for $a_D = 400$, $\eta = 1$, and $S = 0$. The circles for $\lambda = 0.1$ are the results for $a_D = 100$. This shows that graphing $p_{wD} + \ln(400/a_D)$ vs. t_{Da} correlates the pressure transient responses for all a_D to an arbitrarily selected a_D of 400. The curve representing $\lambda \leq 0.01$ shows the transient pressure response for a well near a sealing fault in an infinite, homogeneous reservoir. The transient pressure responses for the cases where $\lambda \leq 0.01$ are similar to the pressure responses of a well near a constant-pressure boundary in an infinite, homogeneous reservoir. Also, the presence of a discontinuity causes the pressure response to depart from the homogeneous line-source response ($\lambda = 1$, $\eta = 1$, $S = 0$) at $t_{Da} \simeq 0.4$. Bixel et al. (1985) also report the departure to occur at $t_{Da} \simeq 0.4$.

Figure 4.3.7 shows the effects of the diffusivity ratio on the pressure drawdown behavior for $\lambda = 1$, $S = 0$, and $a_D = 400$. Since $\lambda = 1$, $\eta = 1/F$ (see Bixel et al. 1985). Thus, Fig. 4.3.7 shows the effects of the storativity ratio, F. The curve for $\eta = 1$ represents the line-source solution. The pressure response departs from the line-source solution at $t_{Da} \simeq 0.4$ for all η. For small η (or large F), the pressure response resembles that of a well near a constant-pressure boundary in an infinite, homogeneous reservoir. This is because region II has a large amount of fluid stored in comparison to the amount of fluid stored in region I. Also, since the fluid in the region II has the same mobility as that of the fluid in the region I, region II can supply the fluid across the boundary as fast as the well can produce. However, for large η (or small F), the pressure response departs from the line-source solution and doubles the slope resembling a sealing boundary effect, but then becomes parallel to the line-source solution (solution for $\lambda = 1$) at late time. This is because for large values of η (or small F), most of the fluid is stored in the region I containing the well, and only a small fraction in region II. Therefore, the boundary is felt as a sealing boundary first. However, later on, since the fluids in the two regions have the same mobilities, the well produces mostly from region I, and only a small fraction from region II. Thus, the pressure response becomes parallel to the line-source solution (solution for $\lambda = 1$). A low storativity in region II appears as a constant pressure difference on a semi-log graph, which can be interpreted as a late time skin. The pressure responses shown in Figs. 4.3.6 and 4.3.7 compare with those obtained by Bixel et al. (1985) for the corresponding cases.

Figure 4.3.8 shows the effects of storativity ratio for mobility ratios of 0.1 and 10. Again, for a given mobility ratio, the effects of a low storativity in region II (i.e., a small F) appear as a constant pressure difference on a semi-log graph of the pressure behavior for that particular mobility ratio, but with $F = 1$. For large mobility and storativity ratios (see the case for $\lambda = 10$, $F = 10^6$), the pressure response resembles that for a well near a constant-pressure boundary. This is caused by less resistance for the flow of fluid stored in region II into region I, as $\lambda > 1$. A large amount of fluid flow from region II may equal the well production rate, causing the pressure transient behavior to resemble that for a well near a constant-pressure boundary. However, if the mobility ratio is less than unity, there is greater resistance to the flow of fluid from region II across the boundary. This causes the wellbore pressure behavior to resemble that of a well near a sealing boundary. But, if $F > 1$, there is a possibility of enough fluid flow from region II across the boundary, despite the greater resistance to flow as $\lambda < 1$, and the wellbore pressure behavior may resemble that for a well near a constant-pressure boundary. The relative magnitudes of λ and F determine the resulting pressure drawdown behavior. For $\lambda = 0.1$ and $F = 10^6$, Fig. 4.3.8 shows that the wellbore pressure drop follows the behavior for a well near a constant-pressure boundary to $t_{Da} \simeq 200$. Thus, for a given mobility

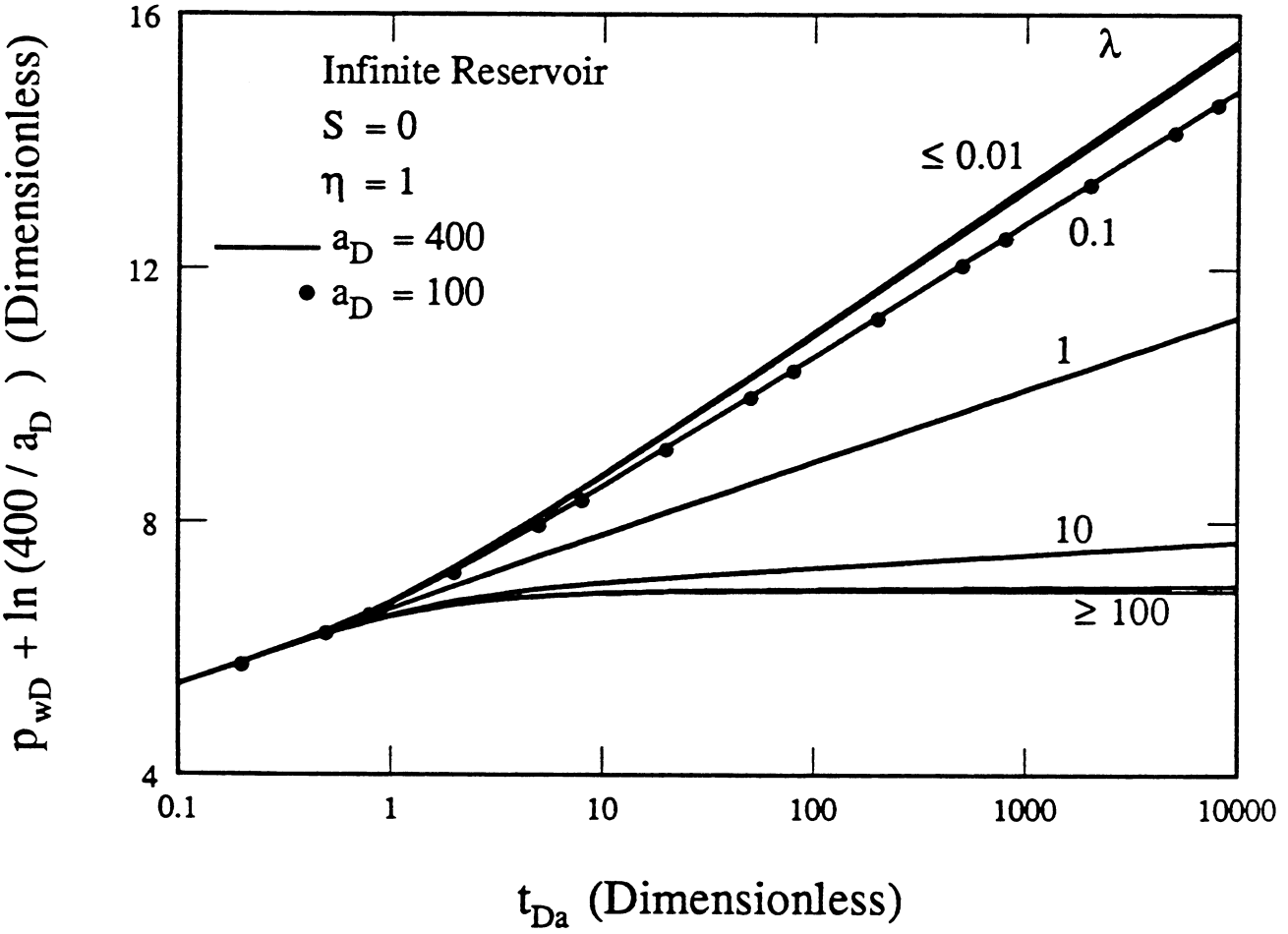

Fig. 4.3.6. Effect of mobility ratio on pressure drawdown responses for a well in an infinite reservoir.

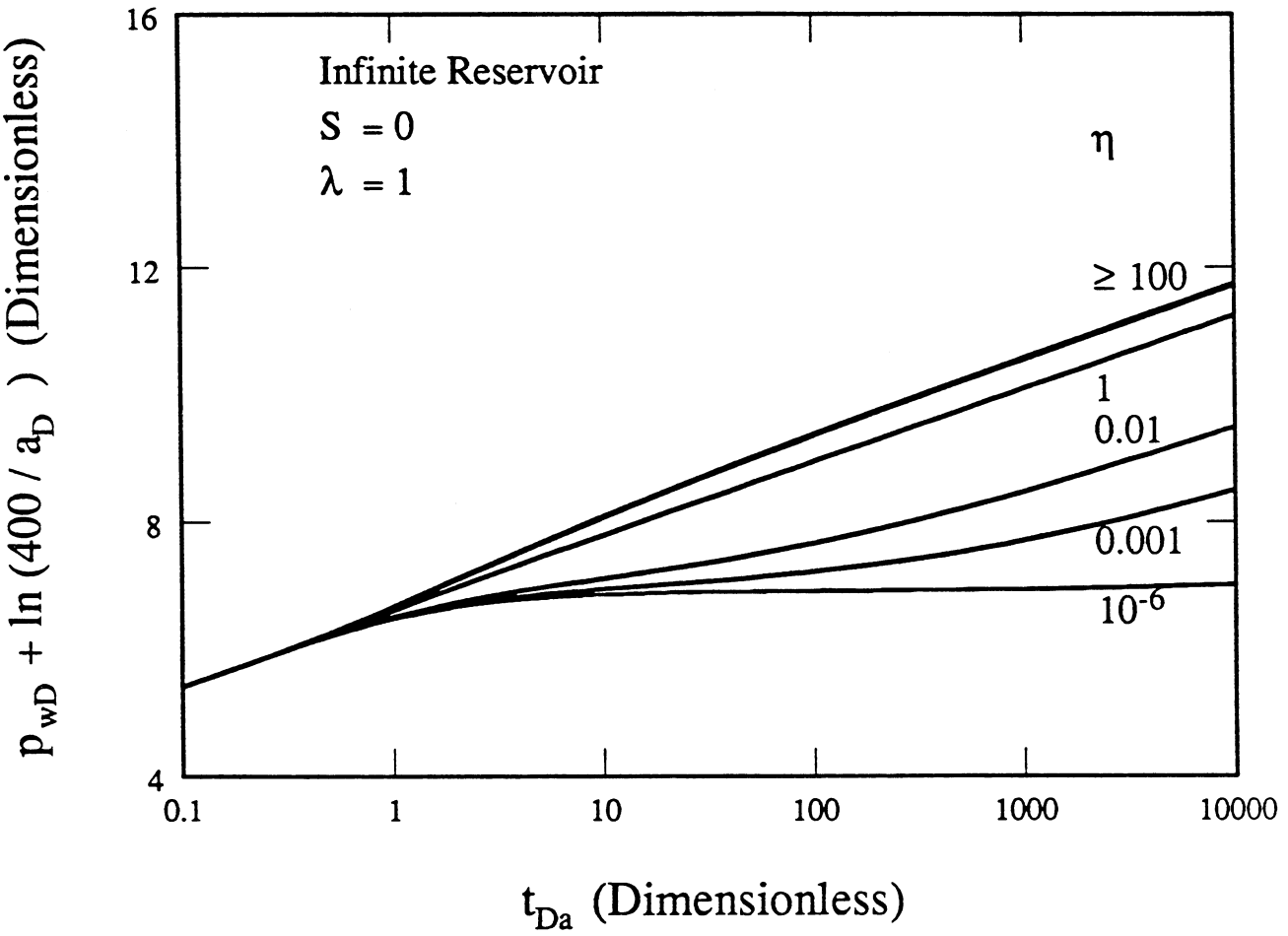

Fig. 4.3.7. Effect of diffusivity ratio on pressure drawdown responses for a well in an infinite reservoir.

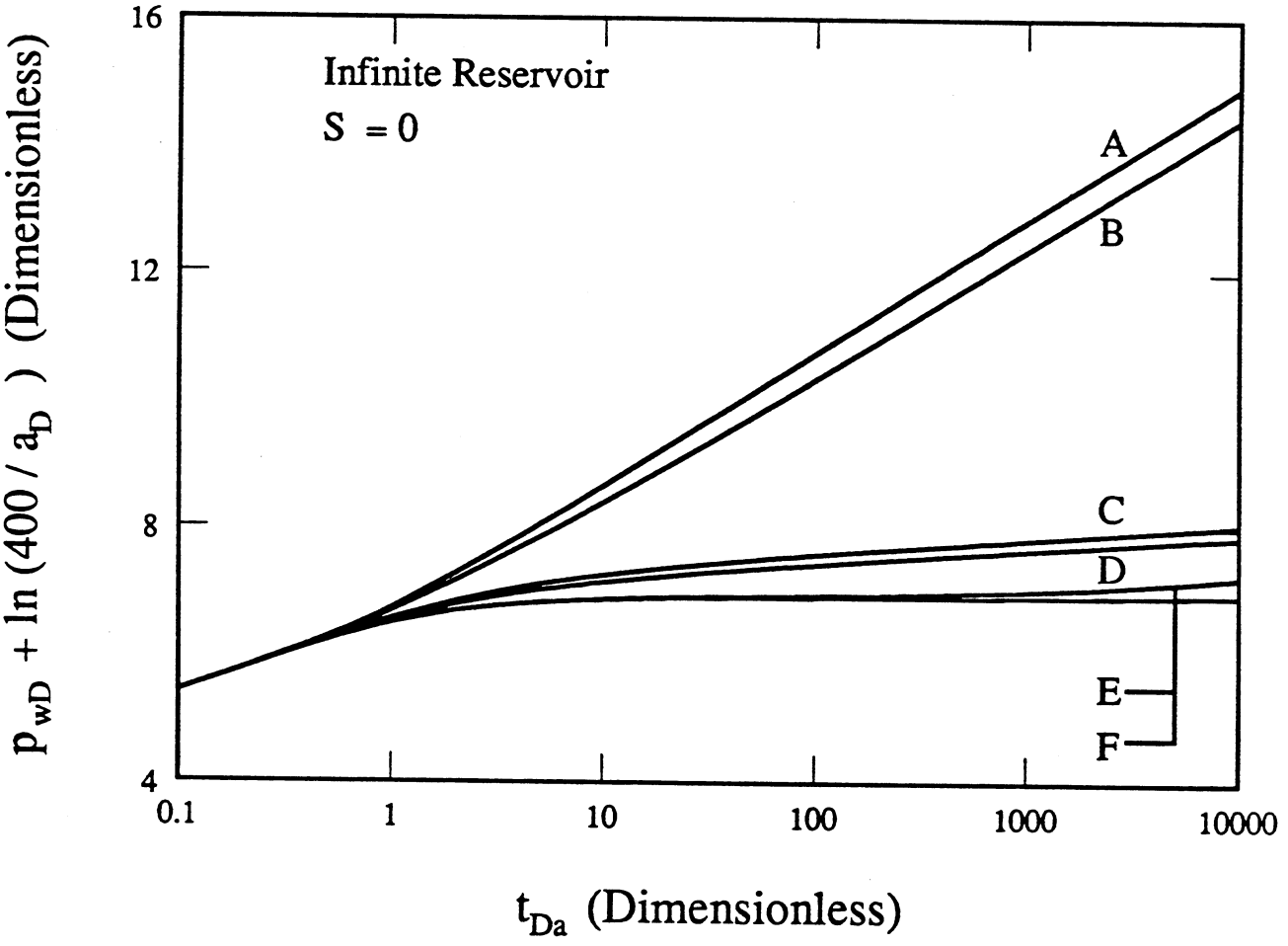

Fig. 4.3.8. Effect of storativity ratio on pressure drawdown responses for a well in an infinite reservoir; A: $\lambda = 0.1$, $F = 10^{-6}$; B: $\lambda = 0.1$, $F = 1$; C: $\lambda = 10$, $F = 10^{-6}$; D: $\lambda = 10$, $F = 1$; E: $\lambda = 0.1$, $F = 10^{6}$; and F: $\lambda = 10$, $F = 10^{6}$.

ratio and $S = 0$, the pressure drawdown behavior resembles that for a well near a constant-pressure boundary for a large storativity ratio. But the effect of a small storativity ratio is exhibited as an additive late time skin to the pressure response for the specified λ with $F = 1$.

Figure 4.3.9 shows the semi-log pressure drawdown behavior for a well in an infinite, homogeneous reservoir for several values of skin at the discontinuity. Again, the pressure response departs from the homogeneous reservoir behavior at $t_{Da} \approx 0.4$. For large values of skin ($S \geq 10^4$), the pressure drawdown response resembles that for a well near a sealing fault. But for moderate values of skin, the pressure response departs from the line-source solution, and then follows the double slope behavior for some time. Later, the pressure response reverts back to a semi-log line parallel to the line-source solution, as flow occurs across the partially communicating fault.

4.3.5 Drawdown Behavior of Strip Reservoirs

The pressure transient behavior of a well in a homogeneous strip reservoir (or a reservoir with parallel sealing boundaries) has been considered in the literature. A strip reservoir is shown in Fig. 4.3.1b. Such a reservoir approaches linear flow behavior at late time. But due to the convergence of the flow lines near the wellbore, there is an additional pressure drop. This additional pressure drop is termed "pseudo-skin", σ, and the late time dimensionless wellbore pressure drop is given by:

$$p_{wD} = \frac{2\sqrt{\pi t_D}}{w_D} + \sigma \tag{4.3.8}$$

where w_D = dimensionless reservoir width.

Figure 4.3.10 presents σ vs. w_D for several well locations in a strip reservoir shown in Fig. 4.3.1b. This extends the study presented by Nutakki and Mattar (1982). The various curves in Fig. 4.3.10 are approximately semi-log straight lines. Ehlig-Economides and Economides (1985) presented type-curves for a well in the center of a strip reservoir shown in Fig. 4.3.1b with the dimensionless reservoir width, w_D, as a parameter. Streltsova and McKinley, (1984) and Tiab and Kumar (1980) studied the pressure transient behavior for an arbitrarily located well in a strip reservoir. They presented the pressure responses in terms of dimensionless well location, b/w. Tiab and Kumar (1980) also presented the pressure derivative behavior for an arbitrarily located well in a strip reservoir.

Since the model presented in Section 4.3.8 considers a skin boundary (Fig. 4.3.2b) in a strip reservoir, the model can be used to study the cases such as shown in Figs. 4.3.1c and 4.3.1e. The drawdown behavior for a well located between two intersecting faults (which includes the case of Fig. 4.3.1c) in a homogeneous reservoir was studied by van Poollen (1965) and Prasad (1975). Drawdown behaviors for a well in multiple-sealing fault systems (including the cases of Figs. 4.3.1c and 4.3.1e) were studied by Tiab and Crichlow (1979). However, the effects of a partially communicating skin boundary (or fault) in a homogeneous, strip reservoir have not been treated. The pressure drawdown response of an arbitrarily located well in a homogeneous, strip reservoir with a partially communicating fault is described by three parameters: a/w, b/w, and S. However, as Fig. 4.3.11 shows, the responses do not correlate exactly at intermediate times. Figures 4.3.11 through 4.3.13 present the effects of a/w, b/w, and S, respectively, on the pressure transient behavior for a well in a homogeneous, strip reservoir with a partially communicating fault. Figures 4.3.11 through 4.3.13 are presented in terms of the semi-log pressure derivatives computed as per Eq. (4.3.3). The line-source or exponential-integral solution exhibits a semi-log slope of 0.5 for $t_D \geq 25$. Also, if the effects of one sealing boundary are felt, the semi-log pressure derivative should double its value to 1. If the effects of two perpendicular intersecting sealing boundaries are simultaneously felt, the semi-log slope should quadruple to 2. The quadrupling of the semi-log derivative should also

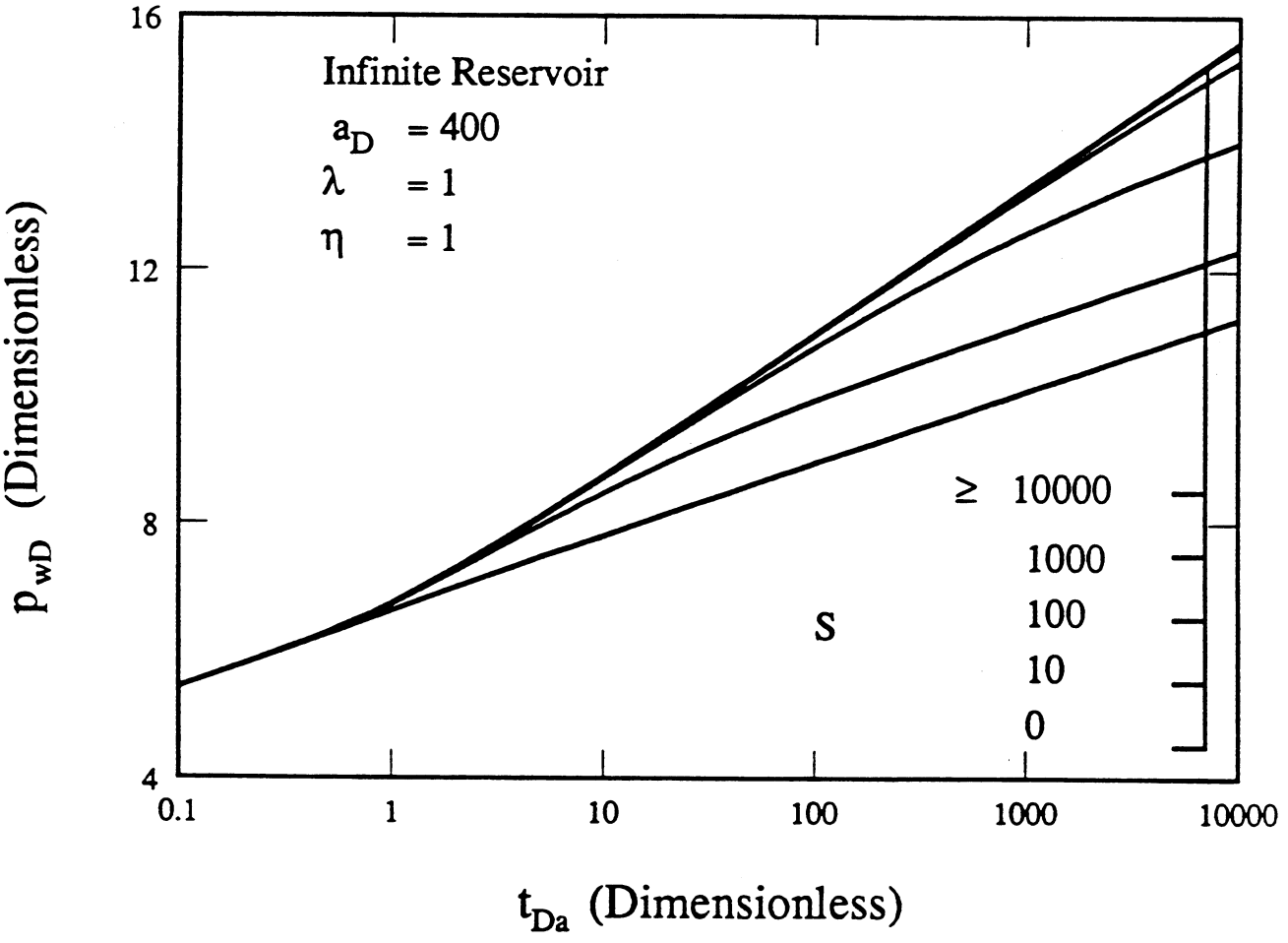

Fig. 4.3.9. Effect of skin on pressure drawdown responses for a well in a homogeneous infinite reservoir.

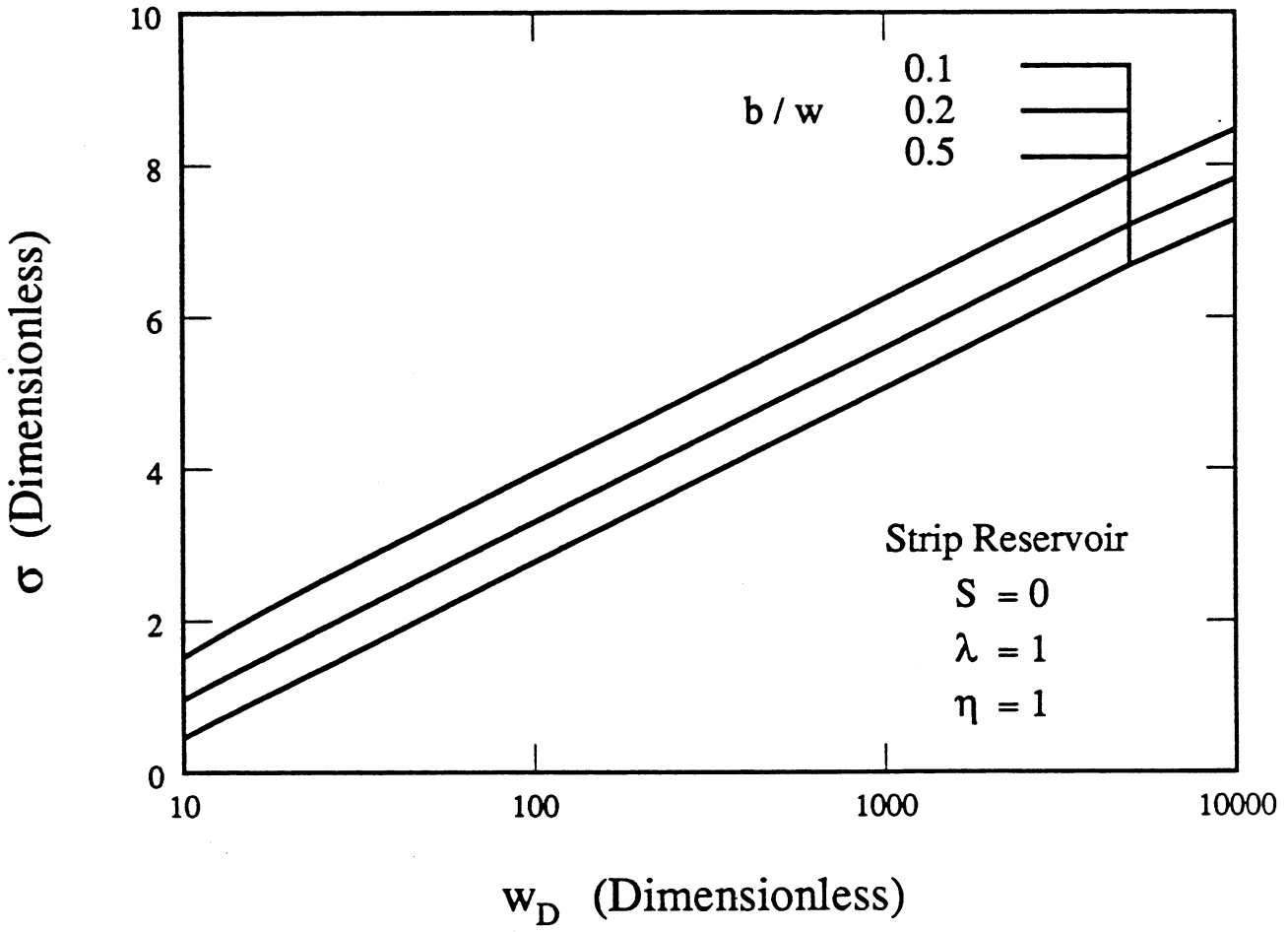

Fig. 4.3.10. Late time pseudoskin for several well locations in a homogeneous strip reservoir.

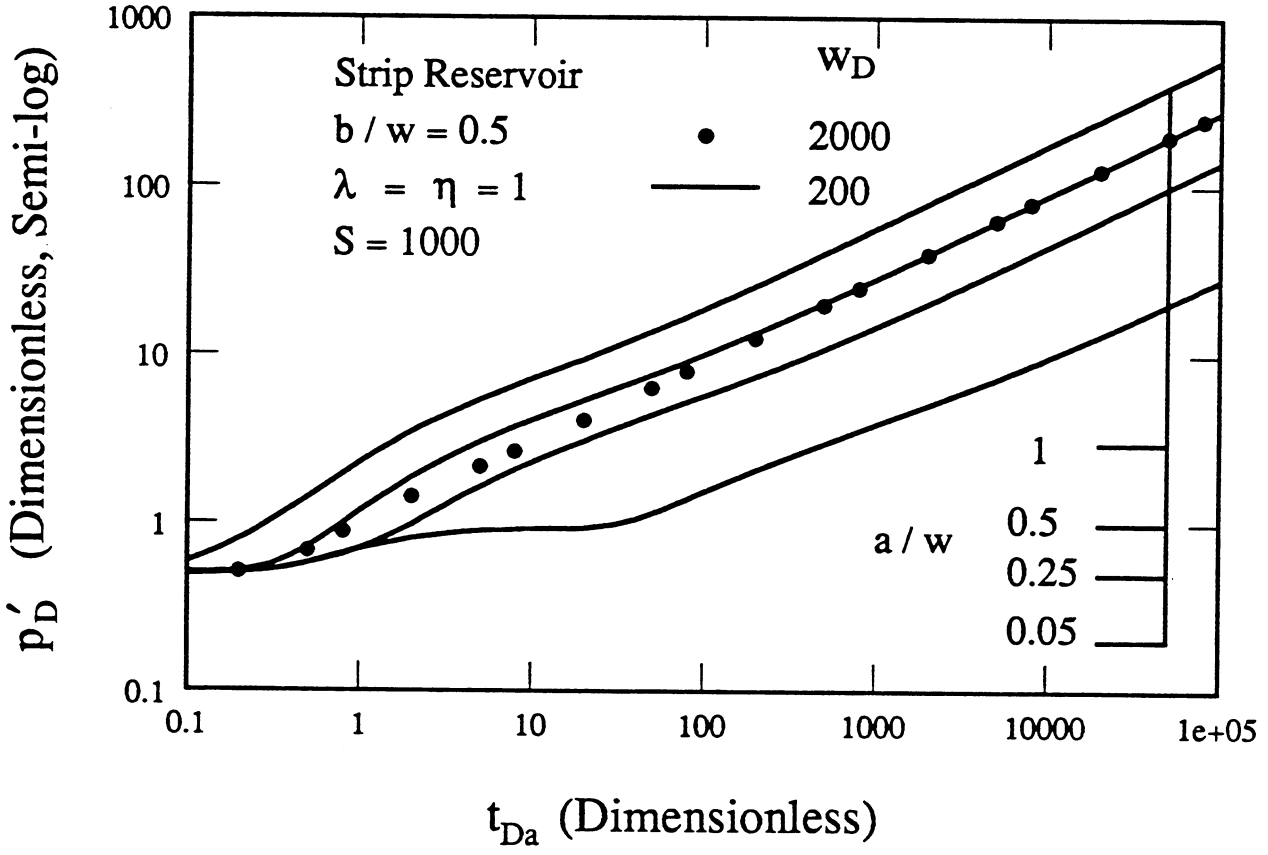

Fig. 4.3.11. Effect of *a/w* on drawdown pressure derivatives for a well in a homogeneous strip reservoir.

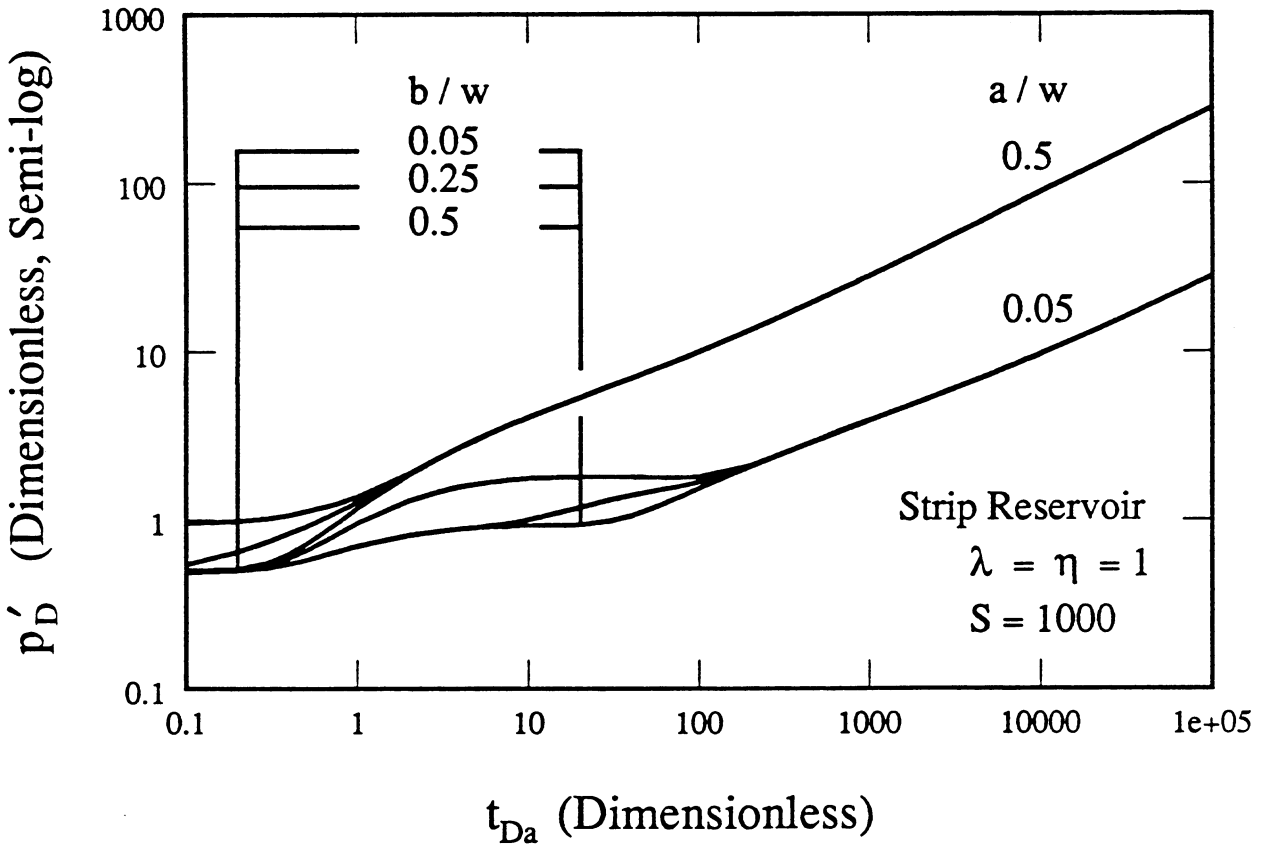

Fig. 4.3.12. Effect of *b/w* on drawdown pressure derivatives for a well in a homogeneous strip reservoir.

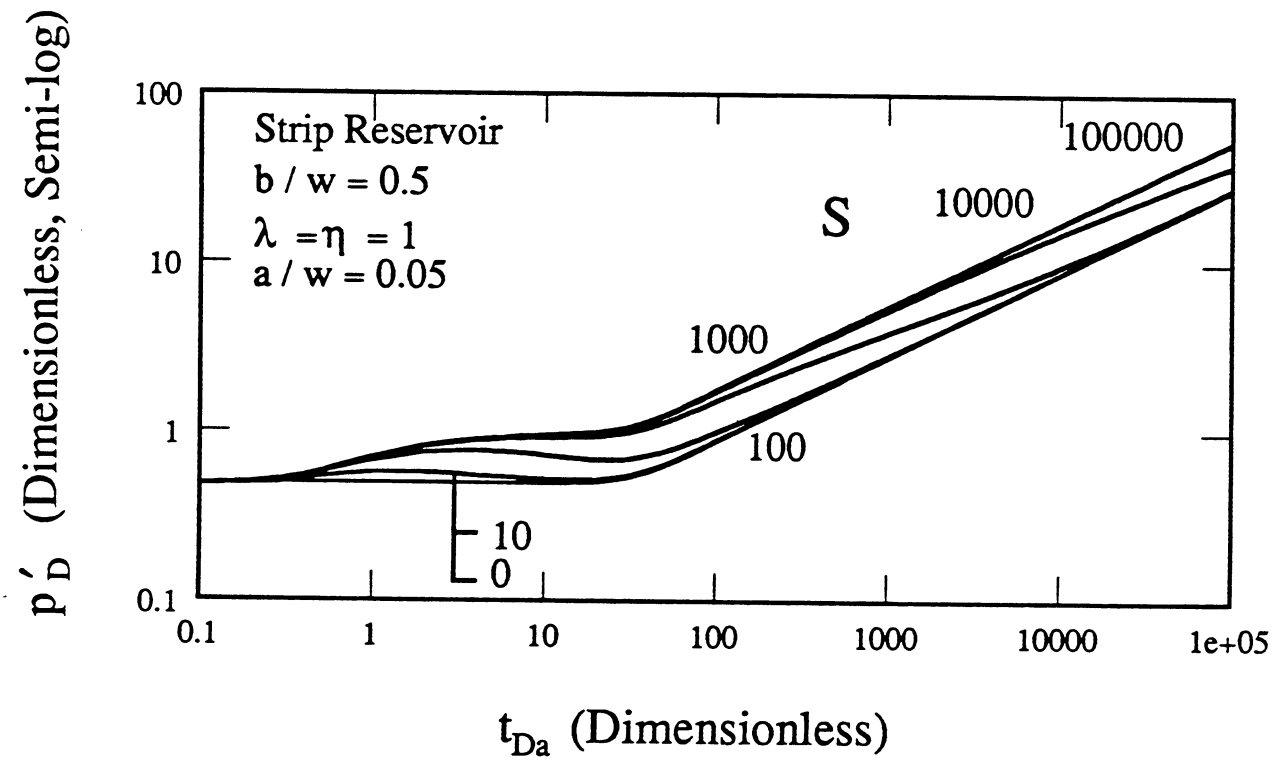

Fig. 4.3.13. Effect of *S* on drawdown pressure derivatives for a well in a homogeneous strip reservoir (well close to skin boundary).

be observed, if the effects of two perpendicular sealing boundaries are felt in succession. However, the parallel sealing boundaries of a strip reservoir cause the late time flow configuration to resemble Fig. 4.3.1b or 1e for homogeneous reservoirs, depending on the magnitude of boundary skin. The late time dimensionless wellbore pressure drop is given by Eq. (4.3.8) for the configuration of Fig. 4.3.1b, and the semi-log pressure derivative is:

$$\frac{dp_{wD}}{d \ln t_D} = \frac{\sqrt{\pi\, t_D}}{w_D} \tag{4.3.9}$$

From Eq. (4.3.9), a log-log graph of the semi-log pressure derivative vs. t_D yields a half slope line at late time. Similarly, the dimensionless wellbore pressure drop and the semi-log pressure derivative at late time for the configuration of Fig. 4.3.1e are:

$$p_{wD} = \frac{4\sqrt{\pi\, t_D}}{w_D} + \sigma_s \tag{4.3.10}$$

$$\frac{dp_{wD}}{d \ln t_D} = \frac{2\sqrt{\pi\, t_D}}{w_D} \tag{4.3.11}$$

where σ_s is the late time pseudoskin for a semi-infinite reservoir configuration of Fig. 4.3.1e, and is different from σ of Eq. (4.3.8). Equation (4.3.11) shows that a log-log graph of the semi-log pressure derivative vs. t_D yields a half slope line. Thus, the late time linear flow for the reservoir configurations of both Figs. 4.3.1c and 4.3.1e are characterized by half slope lines on a log-log graph of the semi-log derivative.

All the three boundaries (two parallel boundaries, and one skin boundary) are felt concurrently at $t_{Da} \approx 0.4$ for the case of $a/w = 0.5$ as shown in Fig. 4.3.11. However, for $a/w = 0.25$, the skin boundary is felt first at $t_{Da} \approx 0.4$, and the two parallel boundaries later at $t_{Da} \approx 1.6$ (which is $t_{Db} \approx 0.4$). The time, $t_{Da} \approx 1.6$, is the time at which the response for $a/w = 0.25$ departs from the response for $a/w = 0.05$. For the case of $a/w = 1$, the effects of the two parallel boundaries are felt first at $t_{Db} \approx 0.4$ or $t_{Da} \approx 0.1$. Then, the effects of the skin boundary cause an inflection point in the case of $a/w = 1$. The inflections in the responses for $a/w = 0.5$ and 0.25 are also due to the effects of skin. In the case of $a/w = 0.05$, the skin boundary is felt at $t_{Da} \approx 0.4$, and the semi-log derivative doubles to 1. Then, at $t_{Da} \approx 40$ or $t_{Db} \approx 0.4$, the effects of the two parallel sealing boundaries are felt. All the curves approach a linear flow behavior at late time. The doubling of the slope is observed only for $a/w = 0.05$, suggesting that a well should be relatively close to one sealing boundary compared to the other boundaries of the reservoir for the semi-log derivative to stabilize at 1. This observation is consistent with the work presented by Tiab and Crichlow (1979).

Fig. 4.3.12 shows the effects of different well locations in the y direction on the pressure derivative response for two different a/w values of 0.05 and 0.5. Again, the departures of the pressure transient responses, whenever one or more boundaries are felt, occur at $t_{DL} \approx 0.4$, where L is the distance between the well and the boundary first felt. For example, for the case of a/w and b/w both equal to 0.5, all the three boundaries are felt concurrently at $t_{Da} \approx 0.4$. For the case of a/w and b/w both equal to 0.05, the two perpendicular intersecting boundaries are felt at $t_{Da} \approx 0.4$, and thus, the semi-log derivative quadruples to 2. At $t_{DL} \approx 0.4$ (where t_{DL} is based on the distance $w - b$) or $t_{Da} \approx 145$, the effects of the upper parallel boundary of the strip reservoir (Fig. 4.3.2b) are felt, and the derivative behavior changes from a constant slope of two to the late time linear flow behavior. The doubling of the semi-log derivative to 1 for the cases of $b/w = 0.05$ and $a/w = 0.5$, and for $a/w = 0.05$ and $b/w = 0.5$ is observed. This again suggests that the doubling or quadrupling of slope is observed, if the well is relatively close to one

sealing boundary or two equidistant perpendicular intersecting sealing boundaries compared to other reservoir boundaries.

Fig. 4.3.13 shows the effects of the magnitude of boundary skin on the semi-log pressure derivatives for a homogeneous strip reservoir with $a/w = 0.05$ and $b/w = 0.5$. The skin boundary is felt first at $t_{Da} \approx 0.4$, and causes the doubling of the semi-log derivative to 1 for large skin values ($S \geq 1000$). For low values of skin ($S \leq 10$), the semi-log derivative reverts back to 0.5 producing a local maximum of the derivative. Again, the effects of the two parallel boundaries of the strip reservoir are felt at $t_{Db} \approx 0.4$ or $t_{Da} \approx 40$. Figure 4.3.13 shows that the effects of the parallel boundaries are felt at $t_{Da} \approx 40$ for small skin values as the departure from a semi-log slope of 0.5, and for large skin values as the departure from the semi-log derivative of one. However, for moderate skin values (in this case, $10 < S < 1000$), the characteristic departure of the derivative response from a slope of 0.5 or 1 is not evident. The semi-log derivative behavior merges to the behavior described by Eq. (4.3.9) for linear flow in a strip reservoir at late time, depending on the value of skin. The larger the skin, the longer is the transition time before the onset of the response described by Eq. (4.3.9). The duration of the transition for a large skin shows the behavior described by Eq. (4.3.11) for linear flow in a semi-infinite strip reservoir, before finally exhibiting the linear flow behavior of an infinite strip reservoir.

Fig. 4.3.14 shows the effects of the magnitude of boundary skin on the semi-log pressure derivative for a homogeneous strip reservoir with $a/w = 1$ and $b/w = 0.5$. In this case, the effects of the two parallel boundaries are felt at $t_{Db} \approx 0.4$ or $t_{Da} \approx 0.1$, and the semi-log derivative behavior tries to exhibit linear flow behavior in an infinite strip reservoir as per Eq. (4.3.9). But depending on the value of skin, the derivative behavior departs from that of $S = 0$ at $t_{Da} \approx 0.4$. However, as the distance between the well and the skin boundary is twice the distance between the well and the parallel boundaries, the departure at $t_{Da} \approx 0.4$ cannot be detected unless the skin is large ($S \geq 100$). In Fig. 4.3.13, the effects of the skin boundary could be felt for $S \geq 10$, as the distance between the well and the skin boundary was 1/10th the distance between the well and the parallel boundaries. Thus, the farther the well is from the skin boundary, the larger the skin must be to have a significant effect on the pressure derivative. Again, the larger the skin, the longer is the duration of the transition, before the derivative behavior is described by Eq. (4.3.9). Also, for large skin values, the duration of the transition exhibits the behavior described by Eq. (4.3.11) for some time.

The pressure drawdown response of an arbitrarily located well in a composite strip reservoir with a partially communicating fault is described by five parameters: a/w, b/w, S, λ, and η. The responses for a well in the center ($b/w = 0.5$) of a strip reservoir with $a/w = 1$ and $S = 0$ are presented in Figs. 4.3.15 through 4.3.18. Figures 4.3.15 and 4.3.17 show the effects of mobility and diffusivity ratios, respectively, on the wellbore pressure behavior. Figures 4.3.16 and 4.3.18 show the effects of mobility and diffusivity ratios, respectively, on the semi-log pressure derivative behavior. Figures 4.3.15 and 4.3.16 are for $\eta = 1$, and Figures 4.3.17 and 4.3.18 are for $\lambda = 1$. The effects of a constant-pressure or closed boundary perpendicular to the two parallel boundaries of a strip reservoir (Fig. 4.3.19) on the wellbore pressure behavior are also shown in Figs. 4.3.15 through 4.3.18.

The pressure and the pressure derivative responses for the cases in Fig. 4.3.19 were generated using the method of images. The wellbore pressure response is the sum of the pressure contributions of the two lines of image wells and the real well. The case of Fig. 4.3.19b has been analyzed by Tiab and Crichlow (1970). In the case of a constant-pressure boundary intersecting parallel strip boundaries (Fig. 4.3.19a), one line of image wells consists of injectors, and the other line consists of producers. The pressure drawdown response of a line-source well is also shown on Figs. 4.3.15 and 4.3.17. For the cases of Figs. 4.3.19a and 4.3.19b, the effects of parallel strip boundaries are felt simultaneously at $t_{Db} \approx 0.4$ or $t_{Da} \approx 0.1$, as the departure of the pressure transient response from the line-source solution. However, at $t_{Da} \approx 0.4$, the effects of a closed (Fig. 4.3.19b) or a constant-pressure (Fig. 4.3.19a) boundary perpendicular to parallel strip boundaries are felt. For the case of Fig. 4.3.19b, the pressure transient response shows linear flow behavior in a semi-infinite system (Fig. 4.3.1e) as per Eq. (4.3.10).

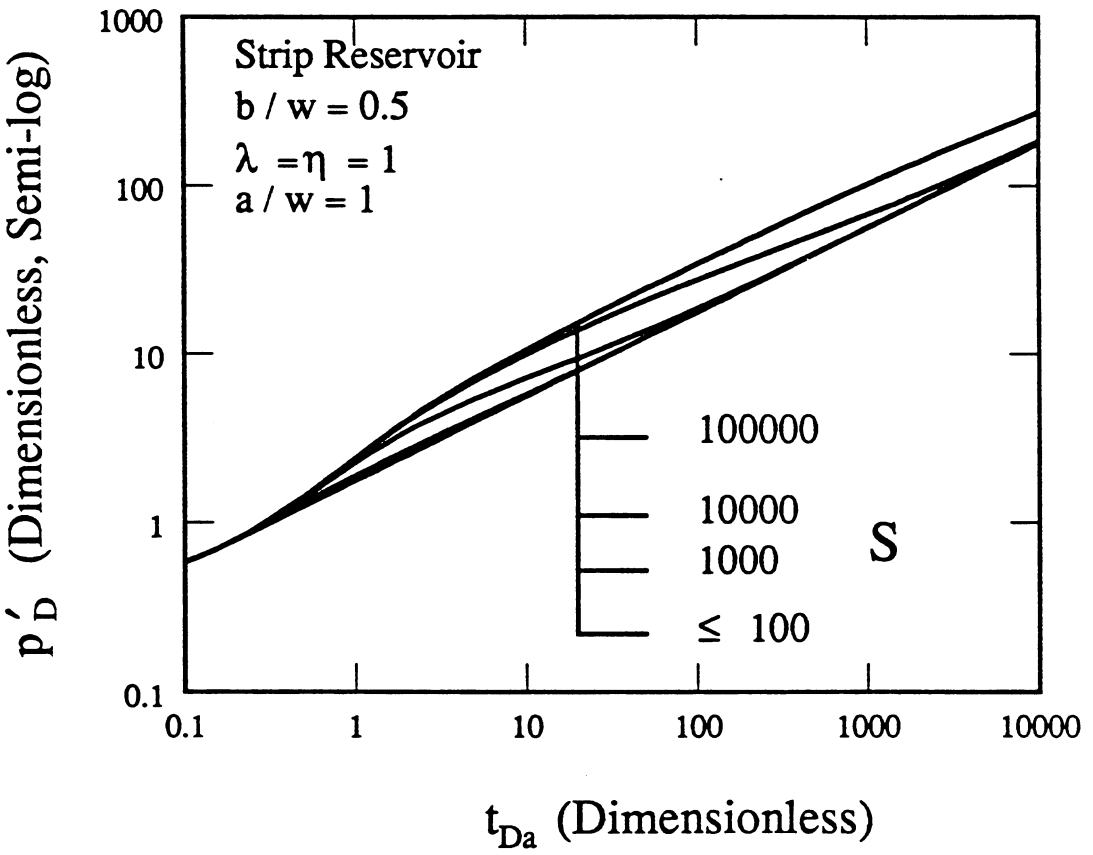

Fig. 4.3.14. Effect of *S* on drawdown pressure derivatives for a well in a homogeneous strip reservoir (well close to parallel strip boundaries).

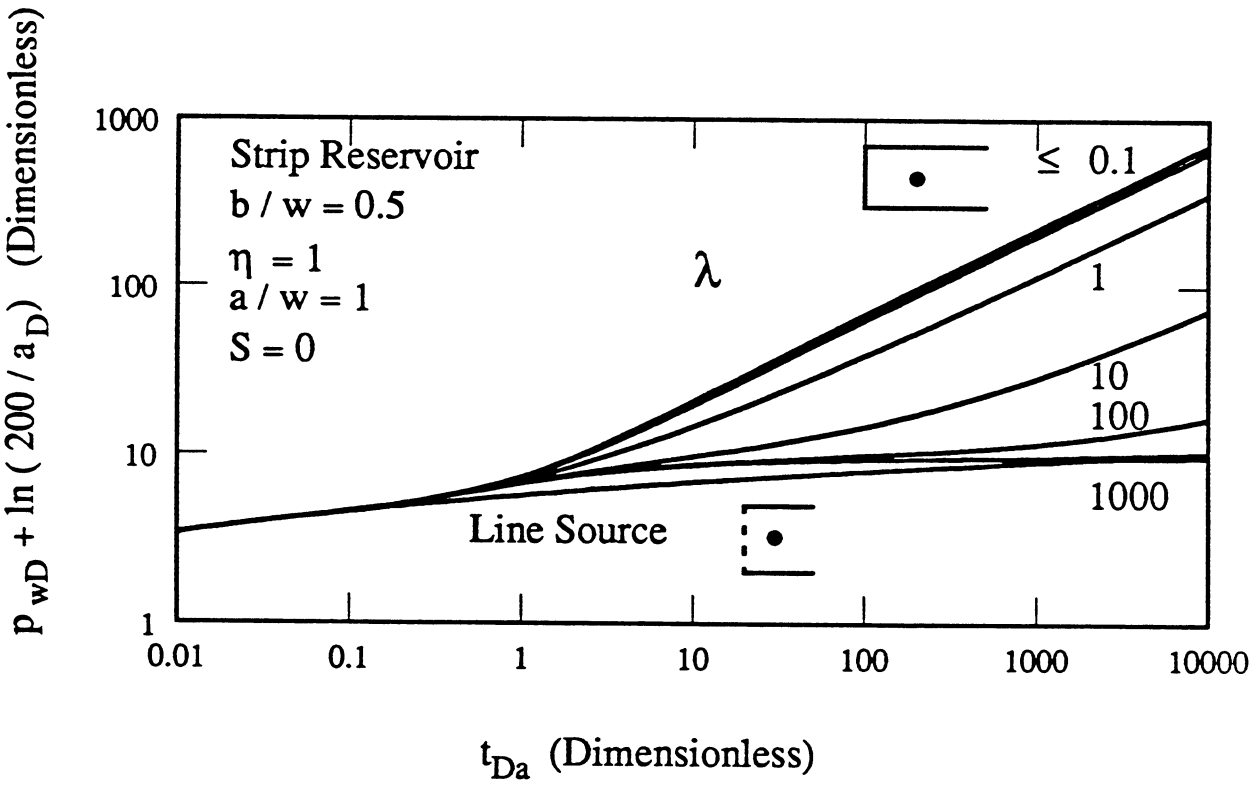

Fig. 4.3.15. Effect of mobility ratio on pressure drawdown responses for a well in a composite strip reservoir.

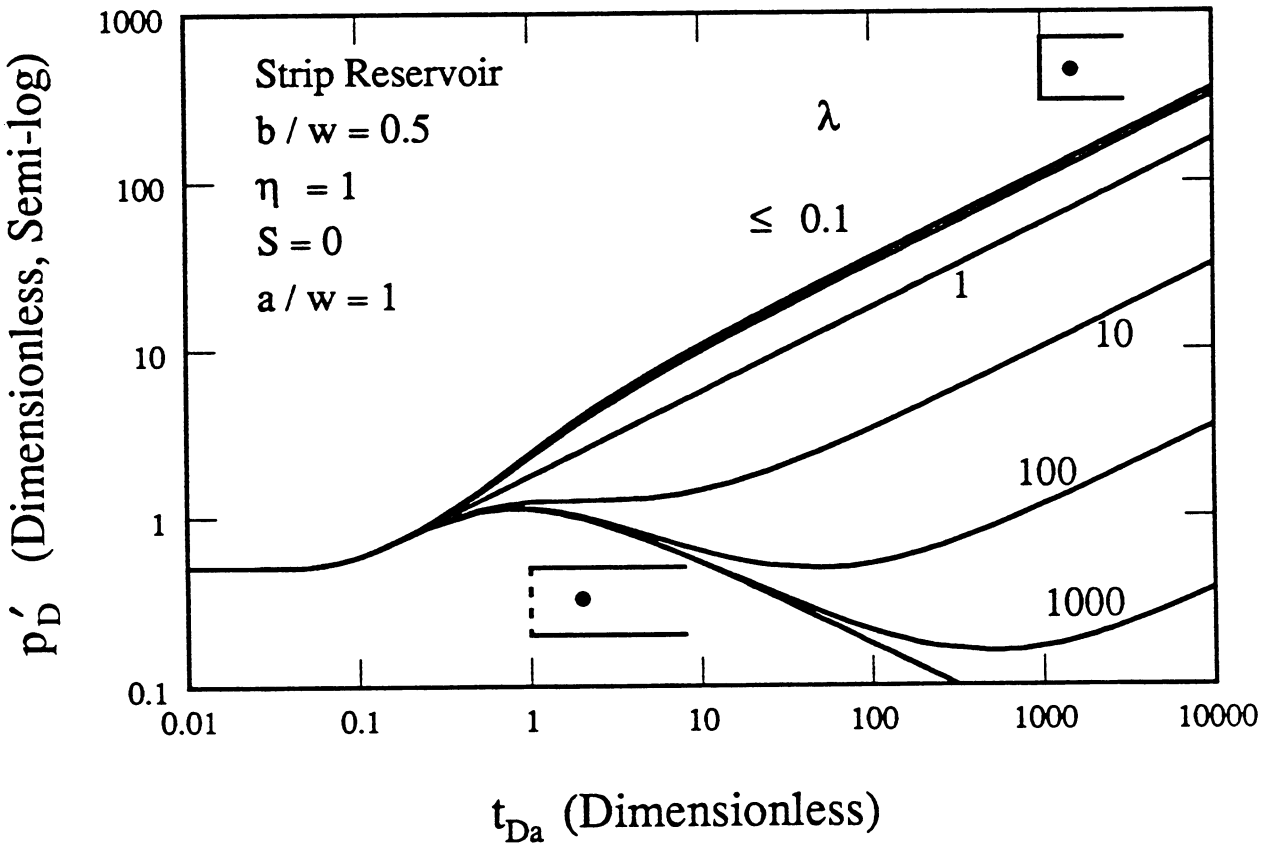

Fig. 4.3.16. Effect of mobility ratio on drawdown pressure derivatives for a well in a composite strip reservoir.

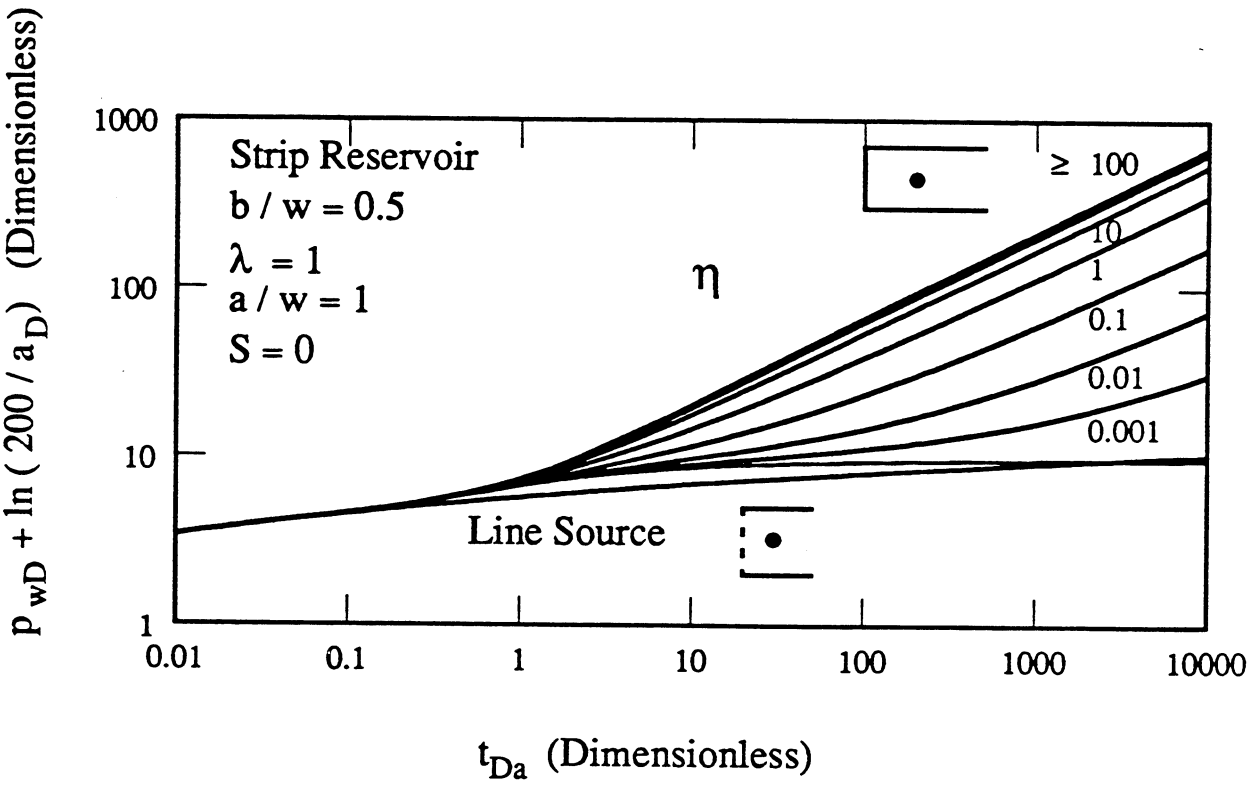

Fig. 4.3.17. Effect of diffusivity ratio on pressure drawdown responses for a well in a composite strip reservoir.

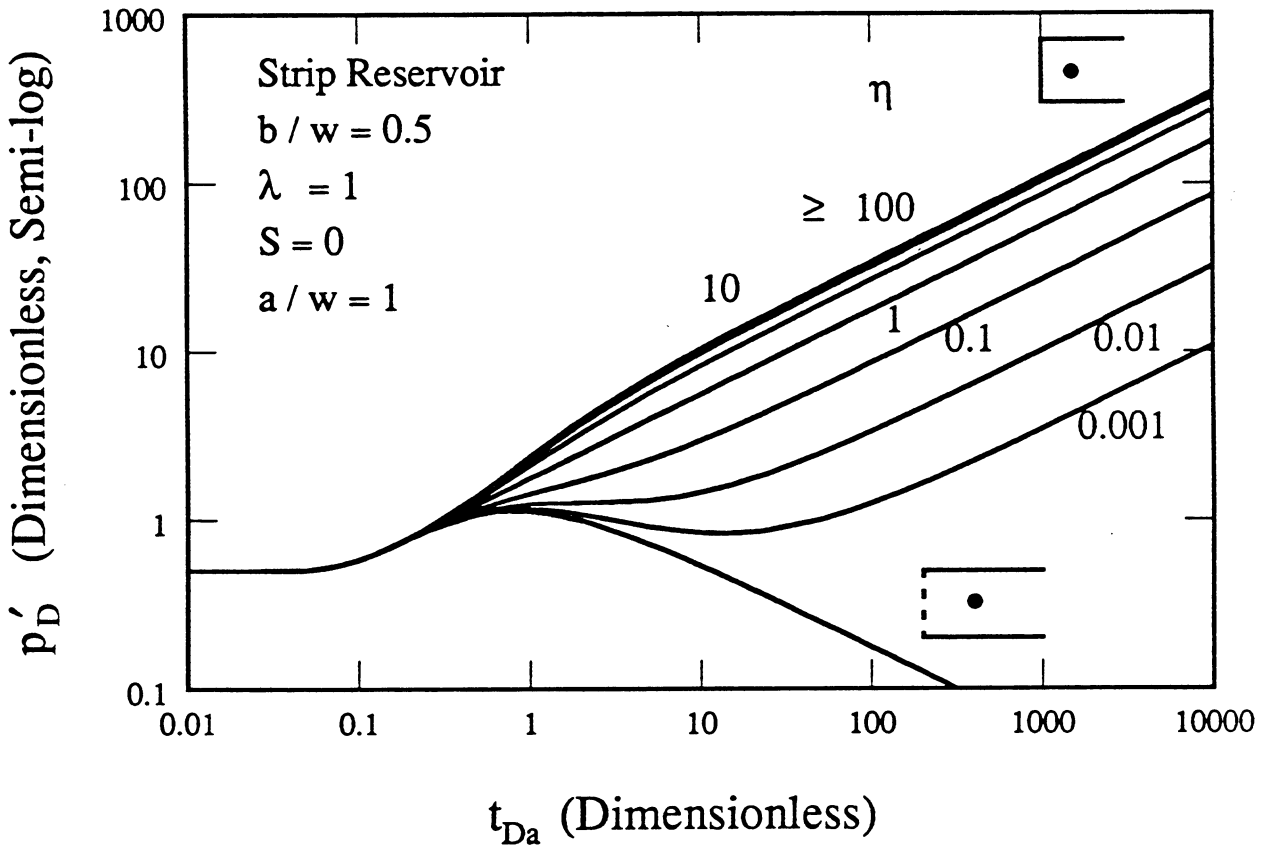

Fig. 4.3.18. Effect of diffusivity ratio on drawdown pressure derivatives for a well in a composite strip reservoir.

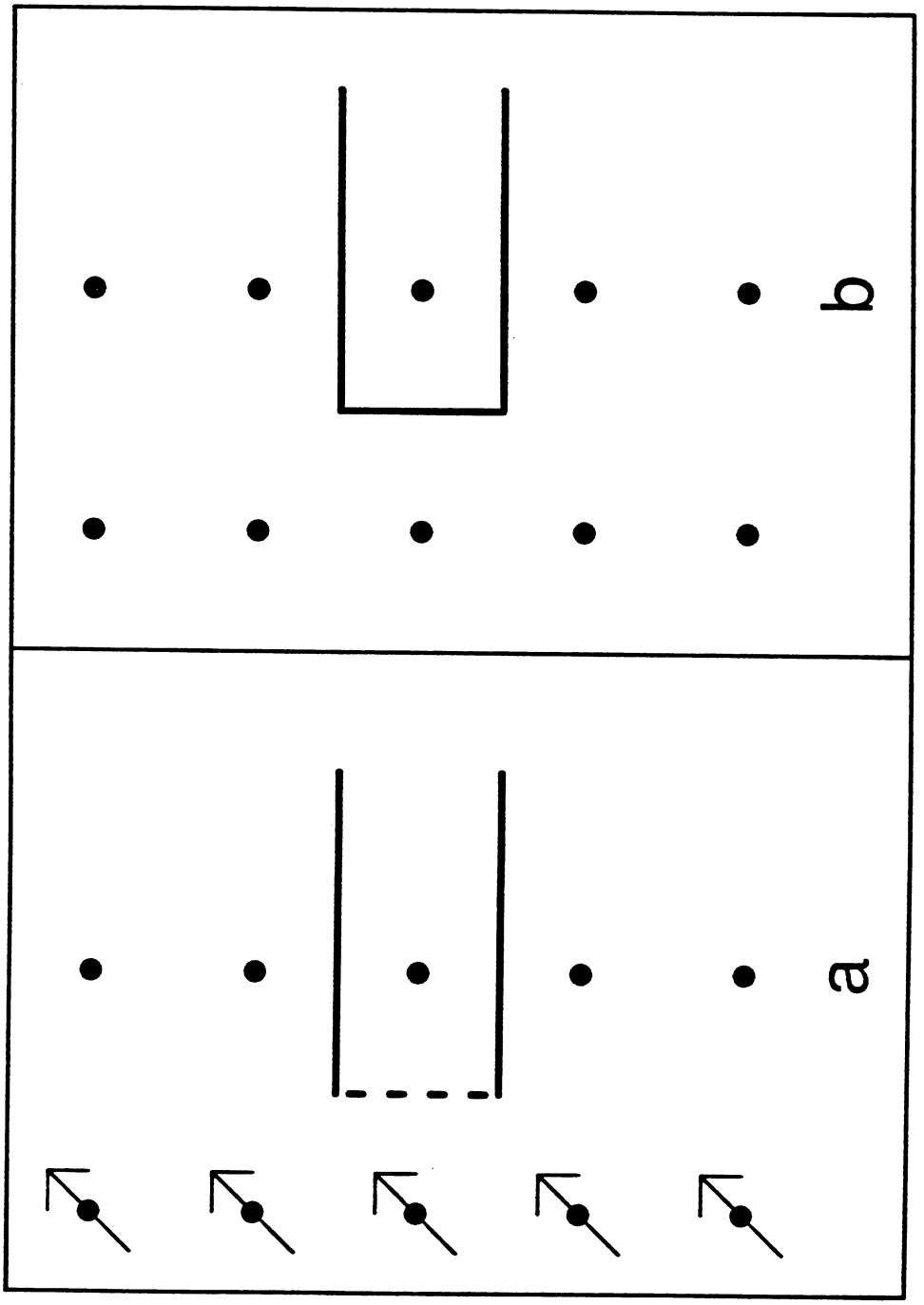

Fig. 4.3.19. Method of images for a well in a homogeneous strip reservoir with a perpendicular intersecting boundary; A: constant-pressure intersecting boundary; and B: closed intersecting boundary.

For the case of Fig. 4.3.19a, the pressure response tends to stabilize and the pressure derivative falls due to the supply of fluid across the constant-pressure boundary. The local maximum of the pressure derivative (Figs. 4.3.16 and 4.3.18) for the case of Fig. 4.3.19a occurs since the effects of the strip boundaries are felt before the effects of the constant-pressure boundary. The effects of the parallel strip boundaries are felt at $t_{Db} \simeq 0.4$ or $t_{Da} \simeq 0.1$ as the departure of the pressure transient responses for different cases from the line-source solution. At $t_{Da} \simeq 0.4$, the effects of the boundary, representing a discontinuity in rock and/or fluid properties on both sides of the boundary, are felt. For small mobility ratios (Figs. 4.3.15 and 4.3.16) or large diffusivity ratios (Figs. 4.3.17 and 4.3.18), the pressure transient behavior resembles that for the case of Fig. 4.3.19b. For large mobility ratios or small diffusivity ratios, the pressure transient behavior resembles that for the case of Fig. 4.3.19a. For intermediate values of mobility and diffusivity ratios, the responses lie between the two limiting cases. However, at late time, the behavior approaches a linear flow condition illustrated by the half slope lines on the log-log graphs of the semi-log derivatives in Figs. 4.3.16 and 4.3.18.

Figure 4.3.20 shows the effects of the boundary skin on the dimensionless wellbore pressure derivative response for $b/w = 0.5$, $a/w = 1$, $\lambda = 10$ and $\eta = 1$. The effects of the parallel strip boundaries are felt at $t_{Db} \simeq 0.4$ or $t_{Da} \simeq 0.1$ as the departure of the semi-log derivative from the value of 0.5. Then, the effects of the boundary representing the discontinuity in fluid and/or rock properties are felt at $t_{Da} \simeq 0.4$. If there is a small skin at the boundary (in this case, $S \leq 10$), then fluid flows easily from region II across the boundary and the pressure derivative flattens. For large values of skin, the fluid from region II can not flow easily across the boundary, despite of $\lambda = 10$, and therefore, the pressure derivative continues to rise. As the flow from region II occurs in larger amounts, the pressure derivative shows a tendency to stabilize. At late time, the semi-log pressure derivative shows the linear flow behavior in a composite strip reservoir, irrespective of the magnitude of the skin. This is characterized by half slope line on a log-log graph of the semi-log pressure derivative in Fig. 4.3.20. Though the pressure derivative responses for $S = 10^4$ and 10^5 have not merged with the response for $S = 0$ on Fig. 4.3.20, these responses also show the late time linear flow at times beyond $t_{Da} = 10000$.

Figure 4.3.21 considers a correlating parameter $\lambda / \sqrt{\eta}$ for drawdown pressure derivative behavior for a well in a strip reservoir. The solid line shows the pressure derivative behavior for $\lambda = 10$ and $\eta = 1$. The circles are for $\lambda = 1$ and $\eta = 0.01$. For both cases, $\lambda / \sqrt{\eta} = 10$. Both responses are generated for $b/w = 0.5$, $a/w = 1$ and $S = 0$. Identical responses for the two cases establish $\lambda / \sqrt{\eta}$ as a correlating parameter. Ambastha and Sageev (1987) have established $\lambda / \sqrt{\eta}$ as a correlating parameter for the pressure responses in a linear semi-infinite system while considering linear water influx through a partially communicating fault.

4.3.6 Interference Behavior of Strip Reservoirs

The effects of a partially communicating fault in an infinite homogeneous reservoir on interference testing have been considered by Stewart et al. (1984) and Yaxley (1985). Interference testing in an infinite or strip composite reservoir with a partially communicating fault has not been considered. The solutions presented in this paper make such studies possible. A complete study on interference testing in composite reservoirs is in progress. However, an example presents the difficulties involved in interpreting interference responses.

Figure 4.3.22 shows a strip composite reservoir with several wells located in regions I and II. The dimensionless reservoir width, w_D, is 4000. The producing well is marked P on Fig. 4.3.22, and A through G represent various observation wells. The observation wells A, B, and C are in region I containing the active production well, and D through G are in region II. The distances represented on Fig. 4.3.22 are the dimensionless distances with respect to the well radius. Such a reservoir situation may represent a well close to a sealing boundary and a fluid-fluid contact.

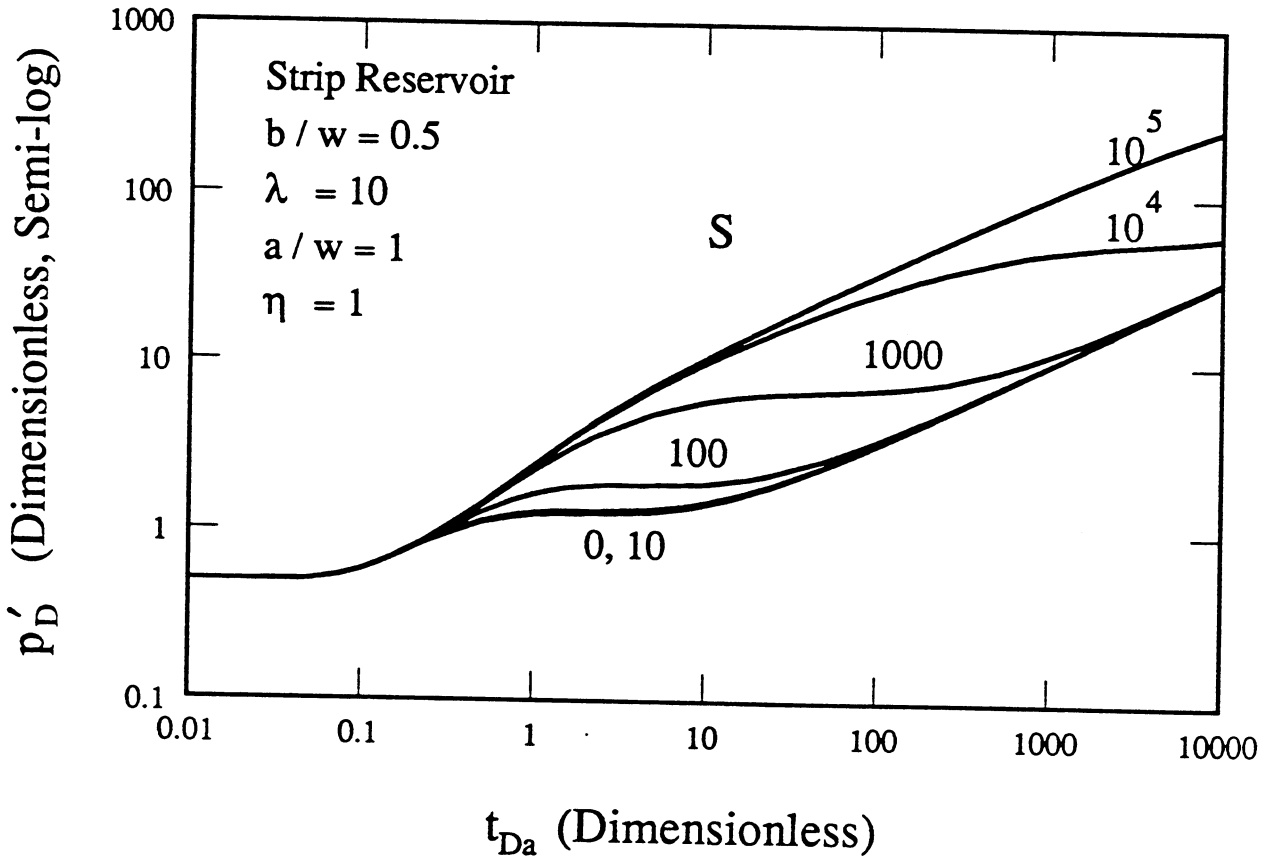

Fig. 4.3.20. Effect of skin on drawdown pressure derivatives for a well in a composite strip reservoir.

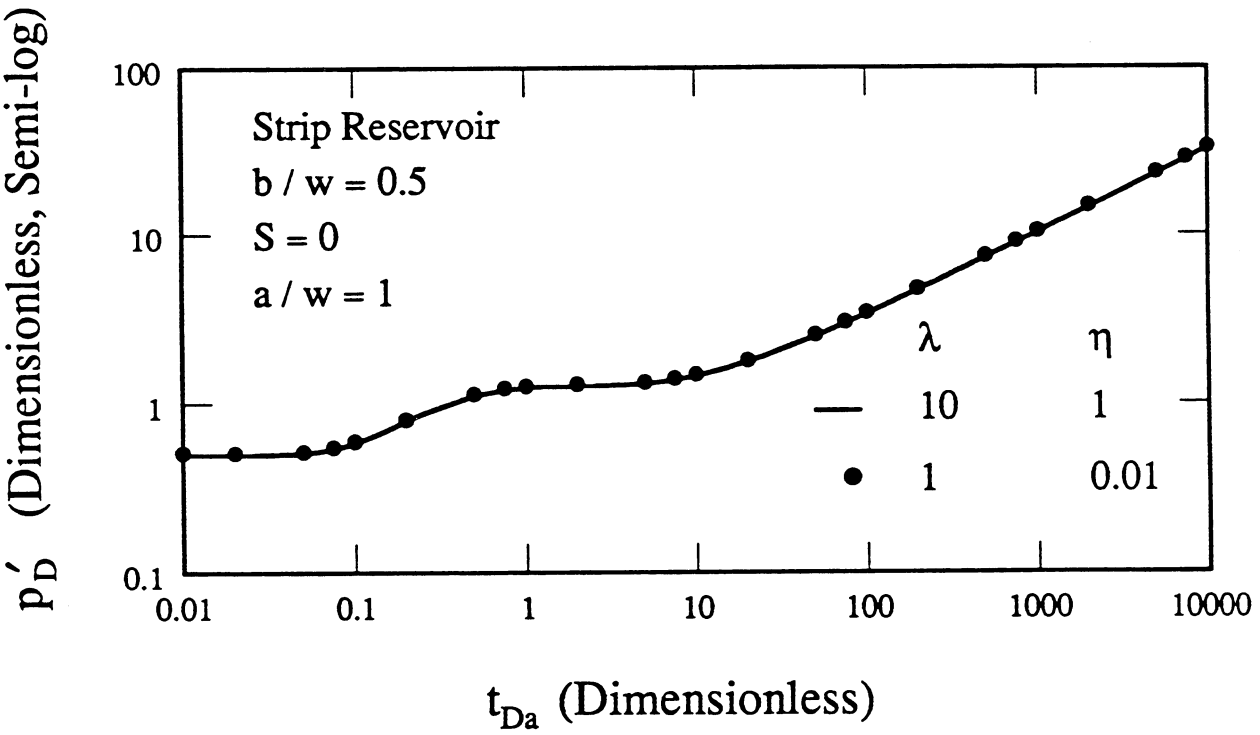

Fig. 4.3.21. Establishing $\lambda / \sqrt{\eta}$ as a correlating parameter for transient pressure responses for a well in a composite strip reservoir.

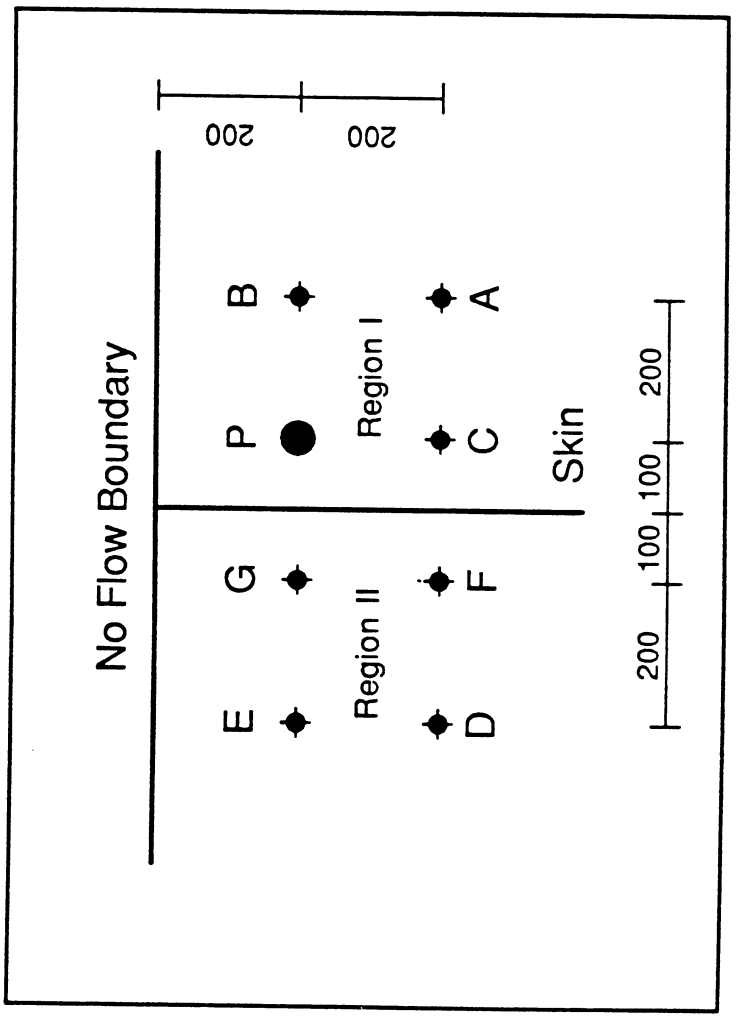

Fig. 4.3.22. Well locations for interference example.

Figure 4.3.23 shows the interference pressure responses at the locations A through G. The pressure drawdown response at the active well P, and the line-source solution are also graphed on Fig. 4.3.23. We use $\lambda = 0.1$, $\eta = 0.1$ and $S = 0$ to generate pressure transient responses. Since $\lambda = \eta$, $F = 1$. Thus, the storativities of the two regions are the same, and the mobility of region I is 10 times larger than the mobility of region II. Figure 4.3.23 presents p_D vs. t_{DL}, where t_{DL} is the dimensionless time with respect to the distances, L, between the active well and the observation wells. The interference pressure responses of the observation wells in region I follow the line-source solution to $t_{DL} \simeq 0.3 - 0.4$, exhibiting a homogeneous reservoir behavior. The interference response then departs from the line-source solution representing the effects of the upper sealing boundary. The larger pressure drops for the observation wells in the region I compared to those in region II represent the larger mobility of region I with respect to region II and hence, the larger contribution of region I to the production from the wellbore. The half slope lines at late time for the observation well responses characterize the late time linear flow in a strip reservoir.

The early and the late time spreading of the interference pressure responses for the observation wells in region II, and the late time spreading of the interference pressure responses for the observation wells in region I show that the resultant response depends on the properties of the two regions and the location of an observation well with respect to the active well. This complicates interference test analysis in a composite reservoir. For example, the interference response of the observation well D is matched to the line-source solution by shifting the time scale to the left by a factor of 9 and by shifting the pressure scale upward by a factor of 1.9. The shifted response is shown by the solid circles on Fig. 4.3.23. The upward shift causes an overestimation of the mobility of region II by a factor of 1.9. The horizontal shift to the left causes an underestimation of the diffusivity of region II by a factor of 9. The combined effect is to produce a storativity, $(\phi c_t)_{II}$, which is $9 \times 1.9 = 17.1$ times the correct storativity of region II. Similar difficulties in the interpretation of interference tests near a steam cap are reported by Sageev (1985).

4.3.7 Conclusions

1. A new analytical solution is presented for the pressure transient behavior of a line-source well producing at a constant rate in a strip or infinitely large reservoir with skin at the linear discontinuity and property contrasts on both sides of the discontinuity. The solution for the dimensionless pressure drop is in Laplace-Fourier space, and some computational experiences in the numerical inversions of the solutions are discussed.
2. The pressure drawdown behavior in an infinitely large homogeneous reservoir shows the behavior of a well near a sealing fault for large values of skin. However, for moderate values of skin, the pressure response departs from the line-source solution, follows the double slope behavior for some time, and then reverts back to a semi-log linear pressure response parallel to the line-source solution at late time.
3. The pressure drawdown behavior in an infinitely large composite reservoir shows the behavior of a well near a constant-pressure boundary for large mobility ratio or small diffusivity ratio (large storativity ratio). However, the effects of a small storativity in region II for a given mobility ratio appear as a constant-pressure difference on a semi-log pressure graph compared to the pressure behavior for the same mobility ratio, but with $F = 1$. This pressure behavior is not explained analytically.
4. A correlation for pseudoskin vs. reservoir width is presented for various well locations in a homogeneous strip reservoir. This extends the study by Nutakki and Mattar (1982).
5. The effects of the boundaries are felt at $t_{DL} \simeq 0.4$, where L is the distance between the well and the boundary felt. If several boundaries are at the same distance from the well, their effects are still felt at $t_{DL} \simeq 0.4$. However, the detection of the boundary effects is not possible in all cases.

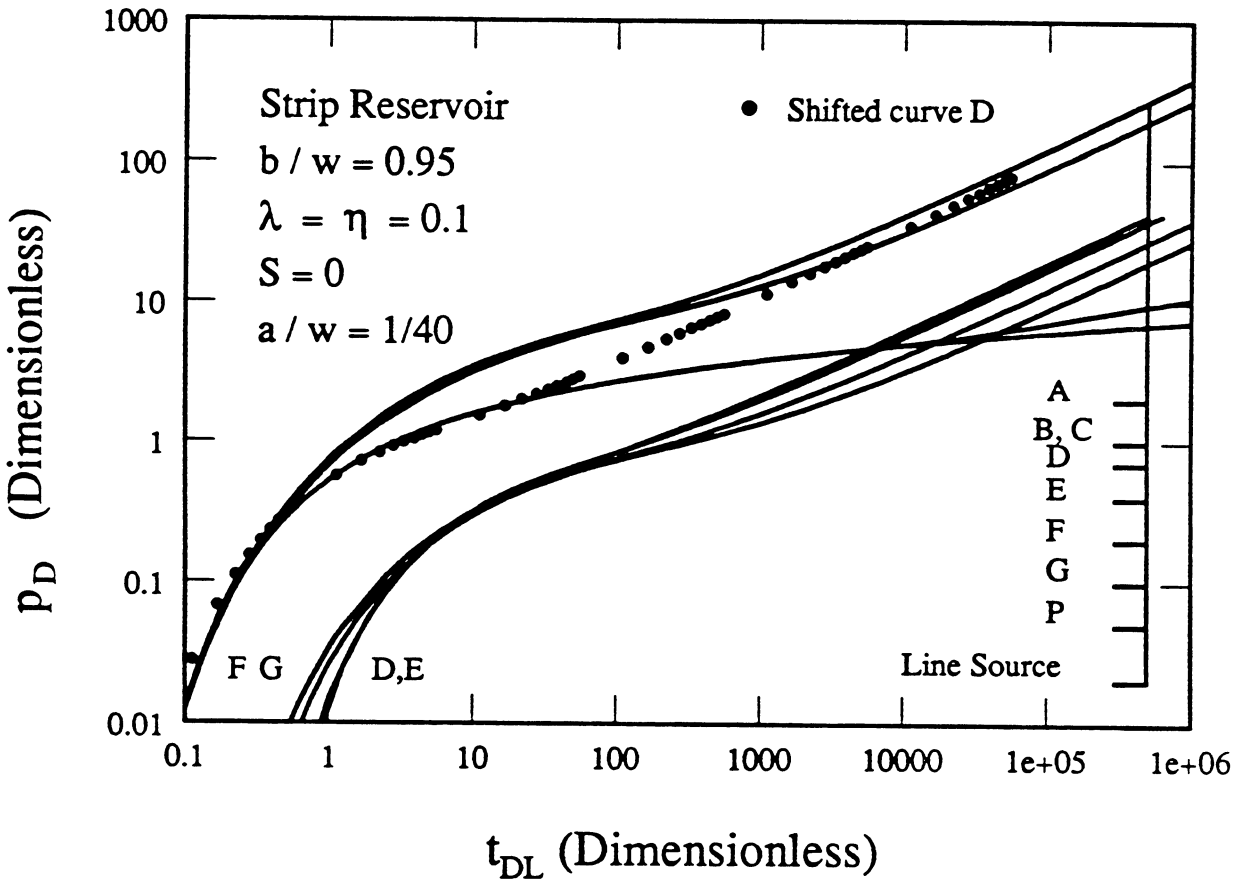

Fig. 4.3.23. Interference pressure responses.

6. The doubling or quadrupling of semi-log derivative is observed, if the well is relatively close to one sealing boundary or two equidistant perpendicular intersecting sealing boundaries, compared to the other reservoir boundaries in a homogeneous reservoir.
7. The pressure drawdown behavior in a composite strip reservoir is bounded by the behavior for the cases in Figures 4.3.19a and 19b. The late time linear flow characteristic of strip reservoirs is observed, irrespective of mobility ratio, diffusivity ratio or skin.
8. Analysis of interference tests in a composite reservoir is not straightforward as the response depends on the property contrasts and the location of the observation well. A simple match of the observed interference response to the line-source solution may yield inaccurate results.

4.4 Immiscible Displacements through Heterogeneous Porous Media: Capillarity, Convection and Scale Dependence

Chris White

The efficiency of immiscible displacements is controlled by rock-fluid properties, boundary conditions, gross system dimensions and the correlation and variability of rock properties. The length and time scales of laboratory and field displacements are very different: laboratory measurements must be systematically averaged or scaled if they are to be used to model field-scale displacements. The scaling problem is complicated by the variability of reservoir properties; porous medium transport properties vary over distances as fine as centimeters (Giordano *et al.*, 1985) and as long as kilometers (Hoeksema and Kitanidis, 1985). Methods to compute large-scale properties must account for spatially correlated properties *and* for differences in the effects of rock-fluid properties at the laboratory and interwell scales.

In this study, the effects of hetrogeneity and scale upon displacement behavior was investigated by (1) examining the governing partial differential equations to define scaling groups and (2) performing a suite of numerical simulations to determine the values of the various scaling groups for which capillary or viscous forces are dominant. The different flow regimes which the dimensionless numbers and simulations delineate should scale differently: a convection dominated system may require that viscous fingering be considered, a capillary-dominated system might be modeled by a transversely uniform front, and intermediate cases could be treated in yet another way. Simulation results can also be used to compute average (or pseudo-) relative permeabilities; examples are presented later in this section.

4.4.1 Partial Differential Equations and Dimensionless Groups

The conservation equation for the water phase in a water-oil system is

$$\frac{\partial}{\partial x}\left[\frac{k_w^x}{\mu_w}\left[\frac{\partial p_o}{\partial x}-\frac{\partial P_c}{\partial x}\right]\right]+\frac{\partial}{\partial y}\left[\frac{k_w^y}{\mu_w}\left[\frac{\partial p_o}{\partial y}-\frac{\partial P_c}{\partial y}\right]\right]=\phi\frac{\partial S_w}{\partial t}\,. \tag{4.4.1}$$

where k, μ and ϕ are permeability, viscosity and porosity, P is pressure, P_c is capillary pressure and S is saturation. Subscripts o and w refer to oil and water and superscripts refer to coordinate directions.

In Eq. 4.4.1 the fluids and rock are assumed to be incompressible. Oil pressure and water saturation are taken as the primary unknowns. Rewriting Eq. 4.4.1 in dimensionless form gives

$$\frac{\partial}{\partial x_D}\left[\lambda_{wD}^x\frac{\partial p_D}{\partial x_D}\right]-N_{CL}\frac{\partial}{\partial x_D}\left[\lambda_{wD}^x\frac{\partial P_{cD}}{\partial x_D}\right]+R_L^2\frac{\partial}{\partial y_D}\left[\lambda_{wD}^y\frac{\partial p_D}{\partial y_D}\right]-N_{CT}\frac{\partial}{\partial y_D}\left[\lambda_{wD}^y\frac{\partial P_{cD}}{\partial y_D}\right]=\frac{\partial S_w}{\partial t_D} \tag{4.4.2}$$

The dimensionless variables in Eq. 4.4.2 are defined as follows:

$$x_D = \frac{x}{L} \; ; \; L = \text{system length} \tag{4.4.3a}$$

$$y_D = \frac{y}{H} \; ; \; H = \text{system thickness} \tag{4.4.3b}$$

$$\lambda^x_{wD} = \frac{k^x k^x_{rw} \mu_{w,ref}}{k^x_{ref} \, \mu_w} \tag{4.4.3c}$$

$$\lambda^y_{wD} = \frac{k^y k^y_{rw} \mu_{w,ref}}{k^y_{ref} \, \mu_w} \tag{4.4.3d}$$

$$t_D = \frac{u_T t}{L\phi} \; ; \; u_T = u_o + u_w = \text{superficial total fluid velocity} \tag{4.4.3e}$$

The dimensionless dependent variables are

$$p_D = \frac{k^x_{ref}}{u_T \, \mu_{w,ref} \, L} \left[p_o(x,t) - p_L \right]$$

$$p_o(x,t) = \text{oil phase pressure}$$

$$p_L = p_o(L,0)$$

$$P_{cD} = \frac{P_c}{P^*_c} \tag{4.4.4b}$$

In these definitions, the subscript *ref* indicates a reference or average value to be used in scaling the equation. P^*_c is a reference capillary pressure or capillary pressure difference; here, $P^*_c = P_c(S_{wc})$.

The dimensionless longitudinal capillary number increases as capillary pressure exerts a greater smoothing influence in the direction parallel to the mean flow

$$N_{CL} = \frac{k^x_{ref}}{u_T \, \mu_{w,ref} \, L} \, P_c^* \tag{4.4.5a}$$

Physically, N_{CL} is the ratio of capillary pressure difference to viscous pressure difference. N_{CL} varies inversely with system length, even when the rock-fluid properties and flow velocity are constant. For systems with identical properties and aspect ratio, capillary pressure will tend to be more important in short systems (small L).

The transverse capillary number is a measure of the capillary-induced flux in the direction transverse to the mean flow,

$$N_{CT} = N_{CL} \left[\frac{L}{H}\right]^2 \frac{k^y_{ref}}{k^x_{ref}} = N_{CL}\, R_L{}^2 \,. \tag{4.4.5b}$$

$$R_L = \frac{L}{H} \sqrt{\frac{k^y_{ref}}{k^x_{ref}}} \tag{4.4.5c}$$

R_L can be thought of as a hydraulic aspect ratio, where the geometric aspect ratio $\frac{L}{H}$ has been corrected by the permeability anisotropy ratio. As the aspect ratio increases (at constant L), N_{CT} increases since the distance over which the transverse flow must occur is decreased; as L increases at constant $\frac{L}{H}$, N_{CT} decreases and the larger value of H impedes transverse capillary equilibrium. The dimensionless groups defined above are similar to those formulated by Yokoyama and Lake (1981), except for their use of the Leverett (1941) j-function rather than P_c^*, which was used here.

4.4.2 Behavior of Layered Systems

Many petroleum reservoirs are composed of several horizontal layers with distinct transport properties. The forces that drive crossflow and stabilize displacements through layered media can be studied analytically for some particular cases: no crossflow (Dykstra and Parsons, 1950; Pande *et al.*, 1987), viscous dominated (Zapata and Lake, 1981), and capillary dominated (Yokoyama and Lake, 1981). The current study requires that viscous, capillary, and gravity crossflow be investigated simultaneously; thus, a numerical simulation procedure was used. The understanding gained from the dimensionless groups defined above can be used to analyze and categorize displacements through layered systems.

Simulation of Layered Systems

Numerical simulations of diplacements were performed using the parameters summarized in Table 4.4.1. The simulations included uniform systems, systems with no crossflow, with viscous crossflow only, and systems with viscous and capillary crossflow. The capillary number, aspect ratio and some results are given in Table 4.4.2.

As comparison of runs 0 and 1 in Table 4.4.2 shows, a 10-to-1 permeability contrast in layer permeabilities resulted in a reduction of up to 0.26 moveable hydrocarbon pore volumes in cumulative recovery at 1.67 movable pore volumes injected. Water breakthrough, reported as τ_{BT} in Table 4.4.2, occurred up to 0.42 pore volumes earlier. Clearly, layering may affect production behavior significantly. However, if capillary pressure or other crossflow-inducing forces are large, the effect of layering may be small. Therefore, some knowledge of individual layer thicknesses and permeabilities is needed in order to predict production accurately. Techniques to obtain layer properties include tracer tests (Abbaszadeh-Dehghani and Brigham, 1982) or pressure transient tests.

For the parameters considered here, capillary pressure stabilizes the immiscible displacement to a much greater degree than viscous forces do. Fig. 4.4.1 shows recovery curves for a uniform system, a layered system with no crossflow, a layered system with viscous crossflow, and a layered system with viscous and capillary crossflow. The recovery for the capillary crossflow case (Run 8, $N_{CT} = 11.52$) is nearly the same as the uniform case recovery (Run 1), while the viscous crossflow recovery (Run 5) is only a little higher than the no crossflow recovery (Run 2).

As the longitudinal capillary number increases, recovery falls slightly due to imbibition near the front — that is, the saturation behind the front is decreased, and breakthrough occurs earlier. Yokoyama and Lake (1981) estimate that longitudinal capillary dispersion is significant for $N_{CL} \geq 0.01$. The results obtained in this study (see Table 4.4.2) confirm their result.

Table 4.4.1. Simulation Description

Two-dimensional, 50-by-20, N_x-by-N_z.

Symmetric, parabolic, isotropic k_{rw} and k_{ro}.

Exponentially decaying P_c, $P_c^* = 0.0 - 4.0$

Incompressible flow, constant viscosity.

Uniform pressure at $x = 0$ and $x = L$, $0 \leq z \leq L$.

Constant rate, $u_T = 1\frac{\text{ft}}{\text{day}}$.

Isotropic intrinsic permeability.

Two equal-thickness layers.

Ten-to-one contrast in layer permeabilities.

Block centered, fully implicit simulation.

Table 4.4.2. Summary of Simulation Results

Run	m	$\frac{L}{H}\sqrt{\frac{k^z}{k^x}}$	N_{CL}	N_{CT}	N_{GT}[1]	τ_{BT}, MHCPV[2]	Q_o τ = 1.67, MHCPV[2]
1	1.0					0.77	0.91
0	10.0					0.35	0.65
2	1.0	0.0				0.45	0.66
3	10.0	0.0				0.19	0.44
5	1.0	28.76				0.47	0.70
6	1.0	5.75				0.46	0.70
7	10.0	28.76				0.19	0.45
8	1.0	28.76	0.014	11.52		0.71	0.89
9	1.0	5.75	0.014	0.46		0.51	0.80
10	10.0	28.76	0.0014	1.152		0.25	0.63
11	10.0	28.76	0.00028	0.230		0.22	0.59
12	10.0	5.75	0.00028	0.009		0.19	0.47
13	1.0	28.76	0.0028	2.30		0.62	0.86
14	1.0	5.75	0.0028	0.09		0.49	0.74
15	1.0	28.76	0.00056	0.46		0.53	0.80
16	1.0	28.76	0.070	2.30		0.58	0.85
17	1.0	5.75	0.014	0.46	0.205	0.65	0.999
18	1.0	28.76	0.014	11.52	1.026	0.84	0.98
19	1.0	5.75	0.014	0.46	-0.205	0.42	0.89
20	1.0	28.76	0.014	11.52	-1.026	0.56	0.78

1. Negative sign indicates gravity flow into high k layer
2. MHCPV--Mobile Hydrocarbon Pore Volume = $\phi AL(S_{oi}-S_{or})$

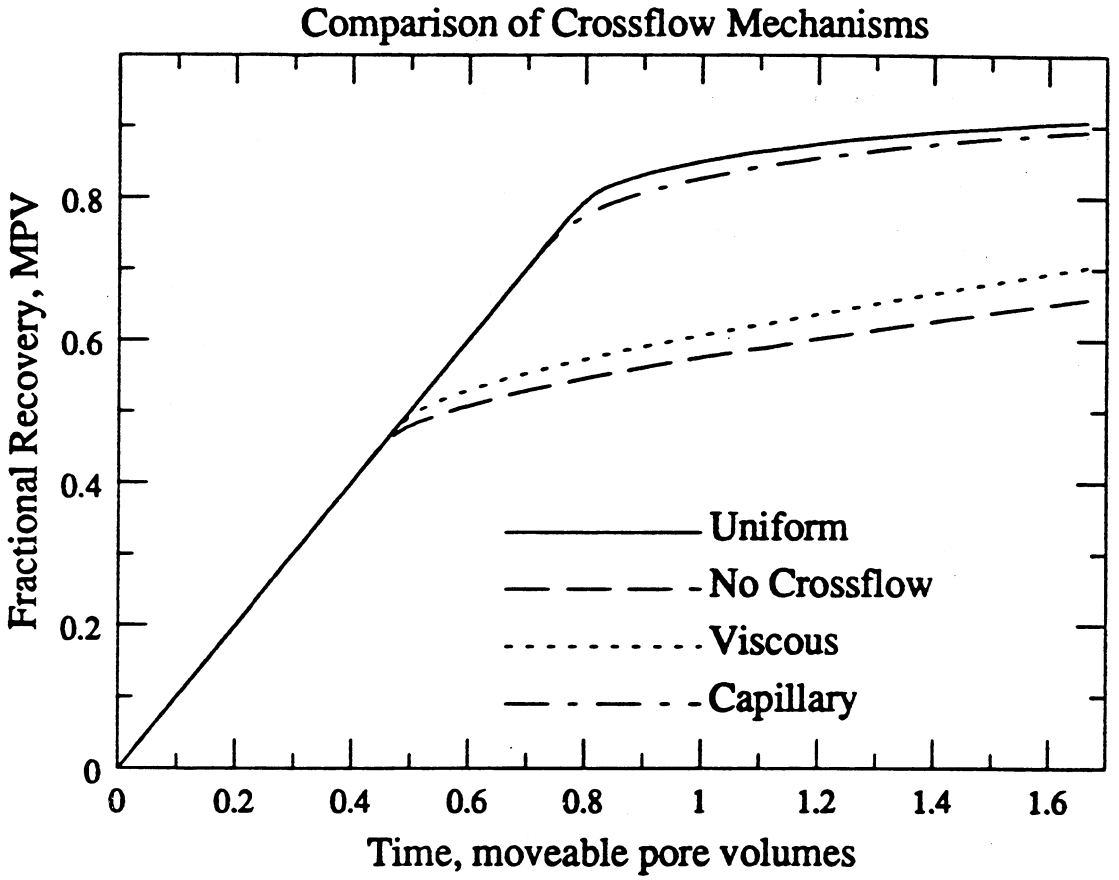

Fig. 4.4.1. Recovery versus time for displacements through layered systems.

Increasing the transverse capillary number increases recovery. Higher N_{CT} indicates that more water flows from the high- to the low-permeability region due to capillary pressure. The crossflow equalizes the front velocity in the two layers, retarding breakthrough and increasing sweep efficiency. For $N_{CT} > 1$, the displacement can be reasonably approximated as uniform. For $N_{CT} < 0.10$, the production behavior is much nearer the segregated flow than the uniform flow case. Yokoyama and Lake state that the displacement should be capillary dominated for $N_{CT} > 0.10$; this study confirms that their result is apparently of the correct order of magnitude, though $N_{CT} > 0.25 - 0.50$ might be more appropriate (see discussion of pseudofunctions, below). Thus, the capillary numbers are good predictors of process efficiency for layered systems.

Pseudofunctions for Layered Systems

Besides delineating flow regimes, simulation results may be used to estimate pseudorelative permeabilities (Jones and Rozelle, 1978; Johnson *et al.*, 1959; Pande *et al.*, 1987; Orr and Sageev, 1986). The results for two cases, Run 8 with $N_{CT} = 11.52$ and Run 14 with $N_{CT} = 0.09$, are shown in Figs. 4.4.2 and 4.4.3, respectively. The pseudofractional flows were estimated by both the vertical equilibrium (*VE*) method (Coats *et al.*, 1971) and the inverse method of Pande *et al.* (1987).

There are several reasons for studying pseudofractional flow, $\hat{f}_w$, rather than pseudorelative permeability. First, $\hat{f}_w$, incorporates the ratio of pseudorelative permeabilities, $\frac{\hat{k}_{rw}}{\hat{k}_{ro}}$. Subtle changes in $\hat{k}_r$ are magnified in $\hat{f}_w$. Also, the shock velocity (and thereby the breakthrough time) can be read from a simple tangent construction on the $\hat{f}_w$ *vs.* S_w graph (Welge, 1952); production behavior is more explicit on the $\hat{f}_w$ curve than on the $\hat{k}_r$ curves. Finally, fractional flow, not relative permeability, is used to solve the saturation equations. (It is also necessary to know the total mobility as a function of saturation to solve the pressure equations; $\hat{\lambda}_T(S_w)$ and $\hat{f}_w(S_w)$ must both be tabulated.)

For high transverse capillary number displacements (Fig. 4.4.2), the VE and inverse method are nearly equivalent — the portion of the fractional flow curve before the tangent point has no effect on the shock velocity or saturation profile (Welge, 1952). For Run 14 (Fig. 4.4.3), the capillary number ($N_{CT} = 0.09$) is too low for vertical equilibrium to apply, and pseudofunctions based on VE yield an incorrect shock velocity. The failure of the VE method in this case suggests that the critical value of $N_{CT} = 0.10$ given by Lake and Yokoyama (1981) may be too low. The inverse pseudofunction method will, by construction, estimate the correct shock velocity and production history (Pande *et al.*, 1987).

The frontal advance formalism used to derive the inverse pseudofunctions is strictly valid only if the velocity of a given concentration is a function of local concentration only — $\frac{d\hat{f}_w}{dS_w}$ cannot be a function of x or t (Pande *et al.*, 1987). In other words, the characteristic curves, curves that give the spatial positions of given saturations as a function of time, must be straight lines in the x–t plane. Of course, the same restriction applies to both VE and inverse pseudofunctions. As shown in Fig. 4.4.4, the characteristic curves for Run 14 are not quite straight. Thus, the inverse pseudofunctions cannot be expected to reconstruct the longitudinal saturation distribution exactly. However, as shown in Fig. 4.4.5, the errors in prediction using the frontal advance formalism are small except in the capillary transition region near the front.

Some effects of gravity were also investigated. In particular, the arrangement of the layers (low-k above high-k, or *vice versa*) was found to be important. Figure 4.4.6 shows the the pseudofractional flow curve for case with high permeability above low (Run 17, favorable g) and the low over high case (Run 19, unfavorable g). The two fractional flow curves are different, even though the capillary number, system size, and average permeabilities are identical. Further, for the favorable gravity case the VE method yields a fractional flow curve which

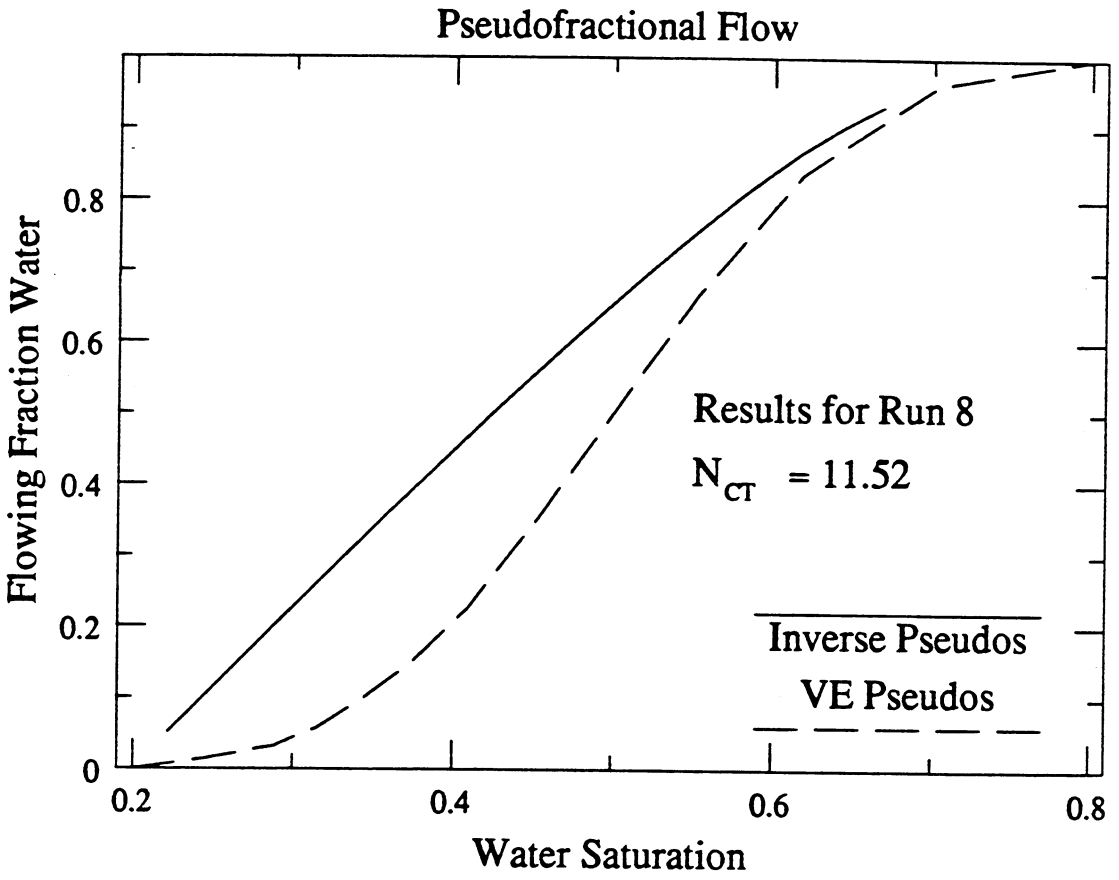

Fig. 4.4.2. Pseudofractional flow for a layered system in vertical equilibrium (Run 8).

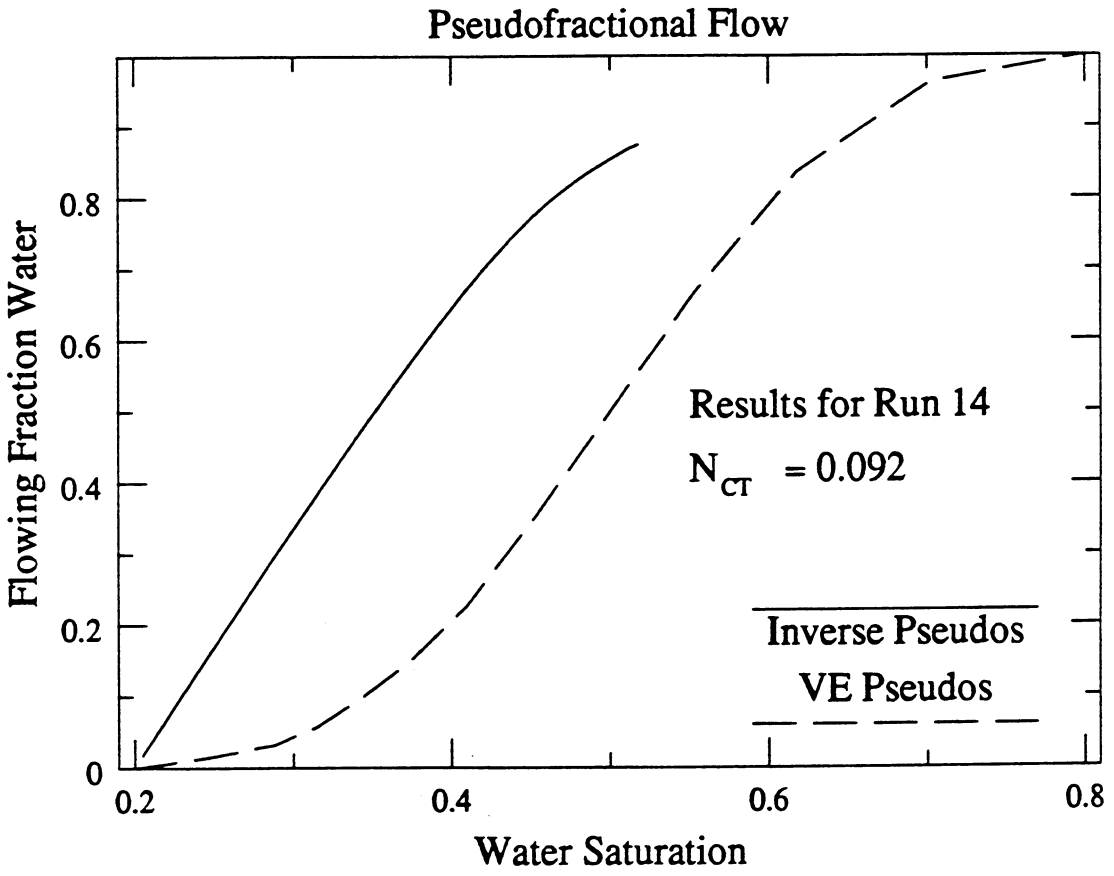

Fig. 4.4.3. Pseudofractional flow for a layered system not in vertical equilibrium (Run 14).

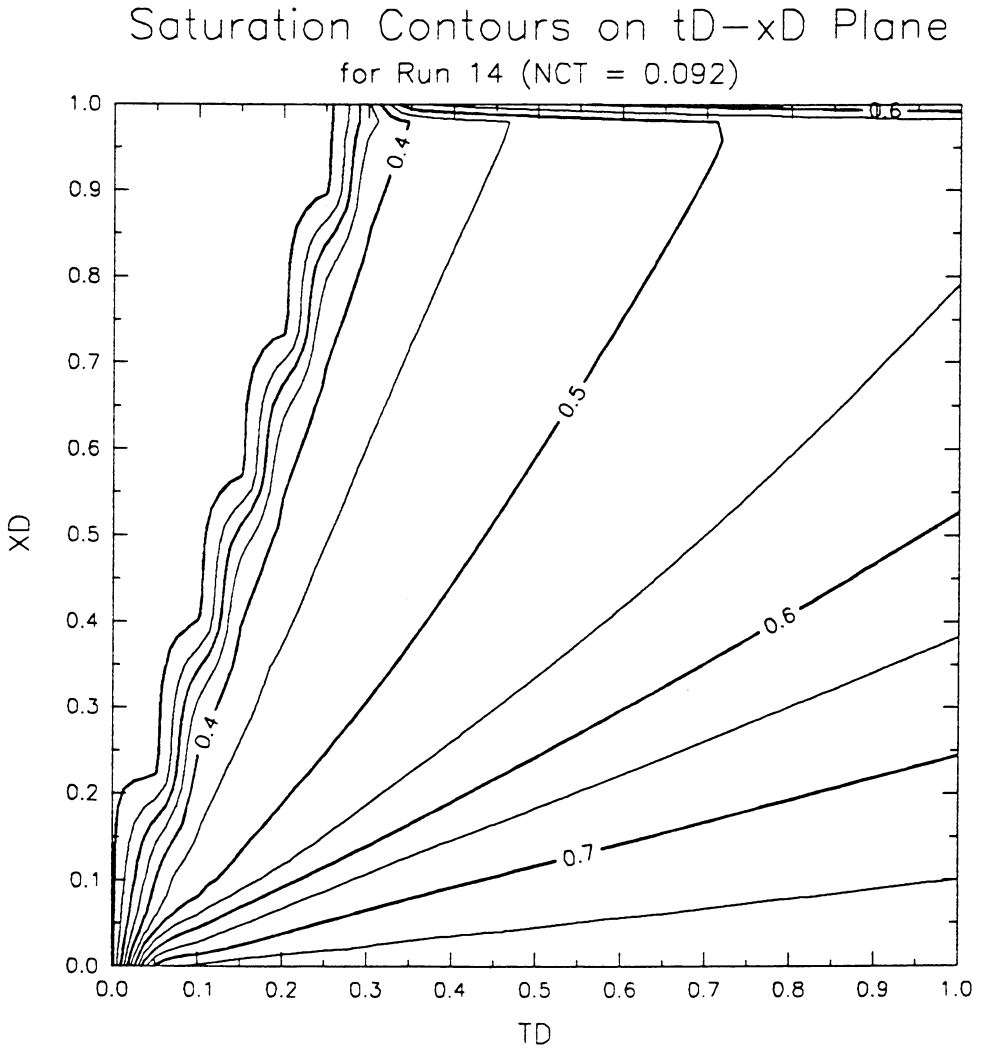

Fig. 4.4.4 Characteristics diagram for a non-VE layered system (Run 14).

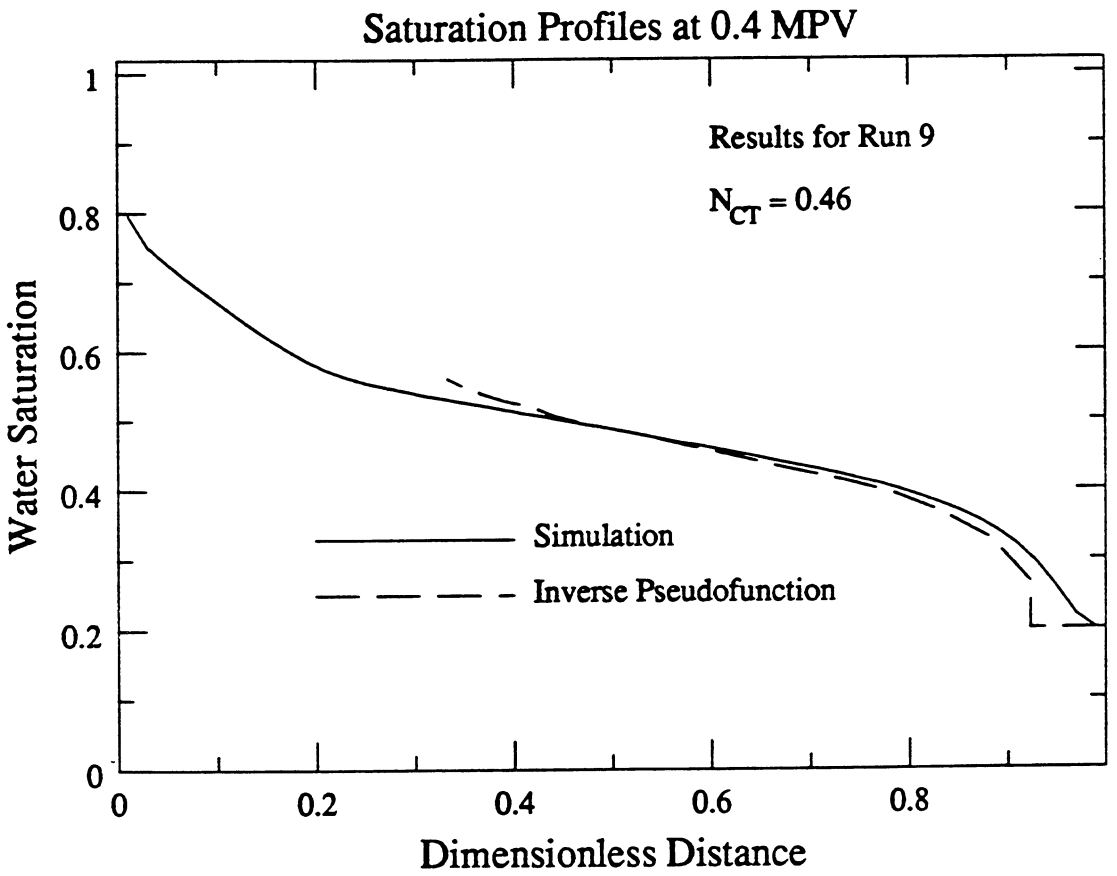

Fig. 4.4.5. Saturation profile for a non-VE layered system.

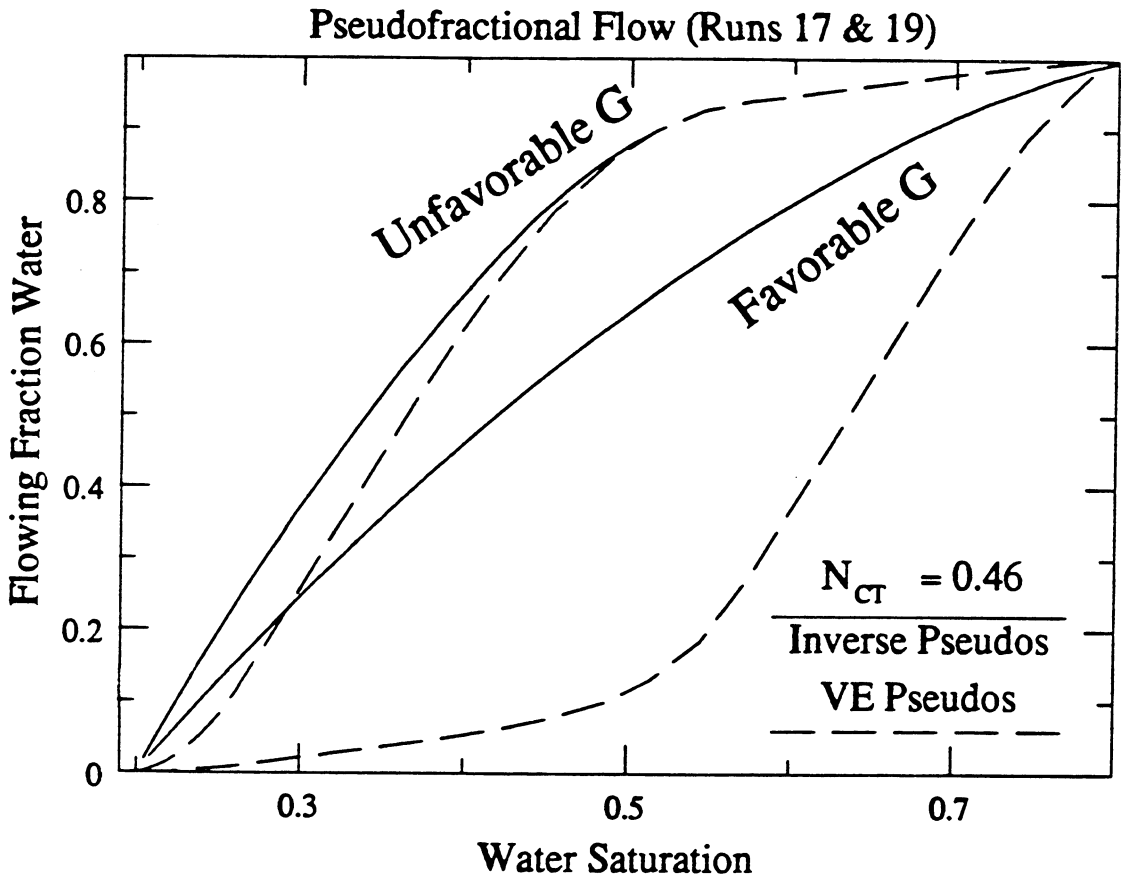

Fig. 4.4.6. Pseudofractional flow for layered systems with gravity crossflow.

predicts the wrong shock velocity (in fact, it predicts no shock at all). Thus, while both displacements ostensibly meet the capillary domination criterion of Yokoyama and Lake (1981) ($N_{CT} = 0.46 \gg 0.01$), only the unfavorable gravity case can be modeled approximately by the VE method. The favorable gravity case has the larger amount of stabilizing crossflow. Since VE implies maximum crossflow (Zapata and Lake, 1981), it does not make sense that the favorable case should be less in vertical equilibrium than the unfavorable case. It is possible that gravity-stabilized displacements should be modeled using a permanent-form solution (Marle, 1981) rather than the Buckley-Leverett shock theory (Buckley and Leverett, 1942). Clearly, further examination of these displacements is needed, so that the interplay of viscous, gravity and capillary forces can be evaluated and more broadly applicable criteria for VE can be established. Finally, these examples emphasize the importance of geometry: a histogram of permeability and/or layer thicknesses is not sufficient. The spatial arrangement of the layers of contrasting permeability must be known also.

4.4.3 Systems with Areal Permeability Variations

Permeability varies areally as well as vertically. Areal variations tend to be more gradual and of smaller magnitude; the scale of variations may be much different in the vertical and horizontal directions. Thus, the coupling of heterogeneity and fluid properties to production behavior will be different. In the following paragraphs, methods to study the permeability distribution and model production behavior are discussed.

Geostatistical Analysis of an Areal Permeability Map

Due to paucity of data, the horizontal variation of rock properties is difficult to quantify; frequently, we resort to probabilistic means. One of the simplest means of describing correlation and variation is the semivariogram function, which has been described and exploited by Journel and Huijbregts (1978), Desbarats (1987), Stalkup (1985), White (1987), Mishra (1987), and Orr and Sageev (1986), among others.

Variography and nonspatial statistical analysis have been applied to the permeability data obtained by Giordano *et al.* (1985). Giordano *et al.* measured the permeability at 1600 points on 2 two-by-two foot slabs of Berea sandstone using a minipermeameter (Eijpe and Weber, 1971).

The probability density functions (pdf's) for both slabs are approximately normal — not lognormal as is commonly assumed. The statistics are summarized in Table 4.4.3.

Contour plots of the permeability fields of the two cores are shown in Figs. 4.4.7 and 4.4.8. Smoothing the data with a moving window (radius of five grid points or 0.25 feet) makes the trends more obvious (See Figs. 4.4.7b and 4.4.8b). Visual inspection suggests that Core 1 is the most continuous in the $(+x,+y)$ direction (SW to NE); Core 2 displays the most correlation along the $(+x,-y)$ direction (NW to SE). Giordano *et al.* (1985) noted that Core 2 is microlaminated. The lower permeability of Core 2 is partly due to the laminations, which are visible in the contour plots.

Variograms were computed for both cores; the results are shown in Figs. 4.4.9 and 4.4.10. Because of boundary effects, the variograms are not reliable at separation distances greater than 20 (one-half the total field size). Several features of the variograms merit discussion:

(1) The principal directions of variability may be deduced from the variograms. For Core 1, the maximum variability is NW-SE; for Core 2, the maximum variability occurs in the NE-SW direction. The direction of maximum continuity is perpendicular to the direction of maximum variability; thus, the variograms confirm the results of the inspection of the permeability contour plots.

Table 4.4.3 Permeability Distribution Statistics

Statistic	Core 1	Core 2
mean, $\bar{k}$ (md)	430.	245.
k_{min} (md)	220.	86.0
k_{max} (md)	604.	492.
variance, σ_k^2 (md^2)	28,280.	84,810.
coefficient of variation, $\frac{\sigma_k}{\bar{k}}$	0.133	0.284
confidence for χ^2 test of normal distribution	95%	90%

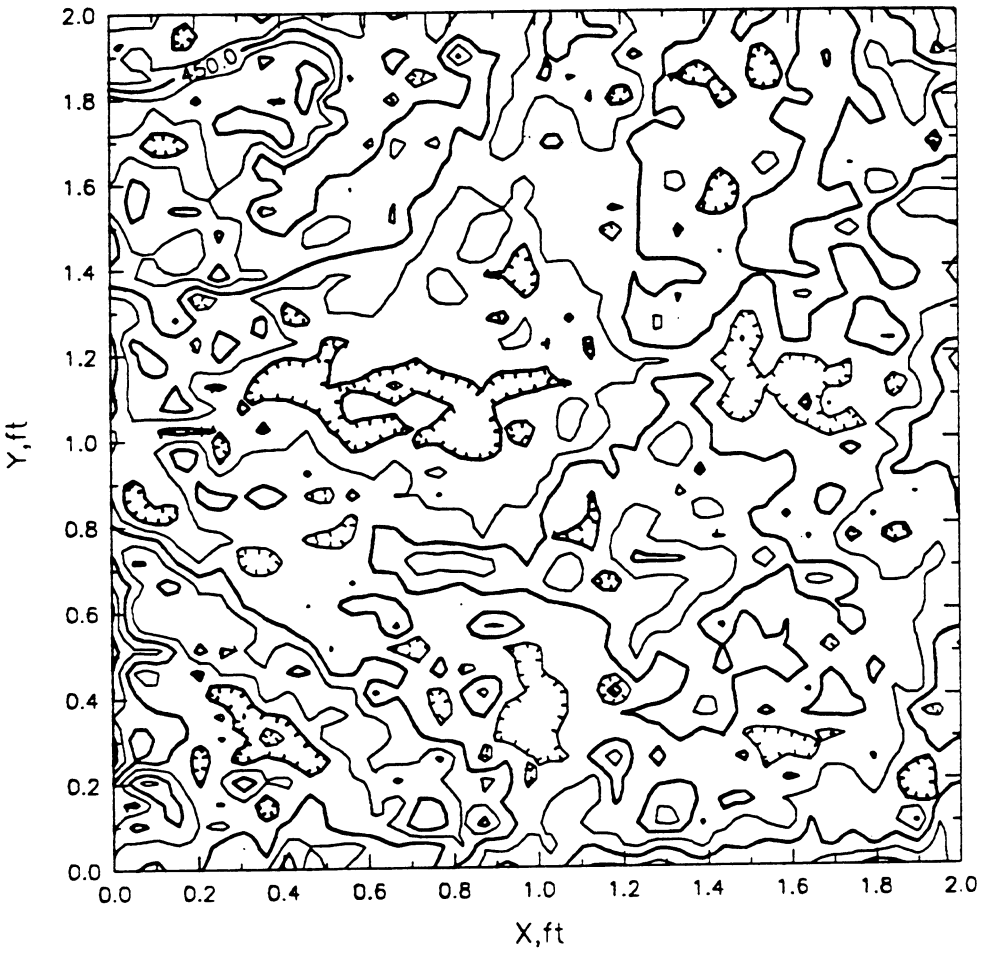

Fig. 4.4.7a. Unsmoothed contour plot for Core 1.

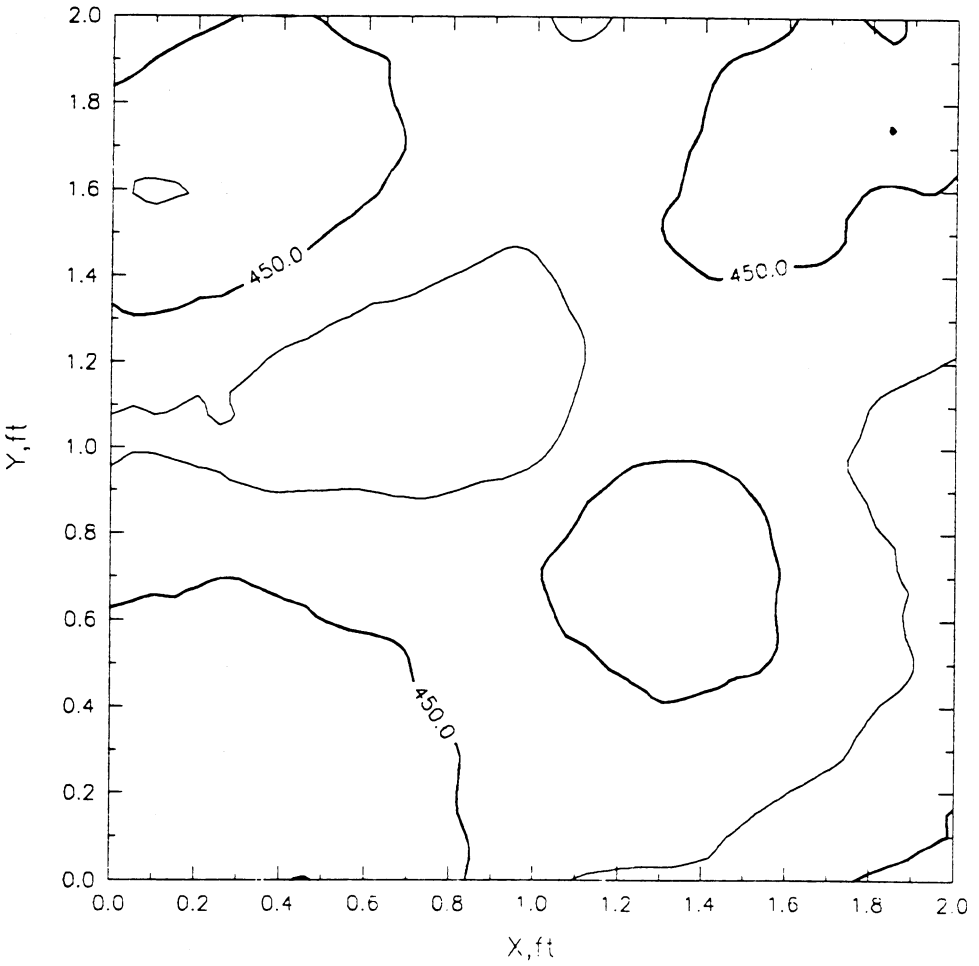

Fig. 4.4.7b. Contour plots of permeability for Core 1.

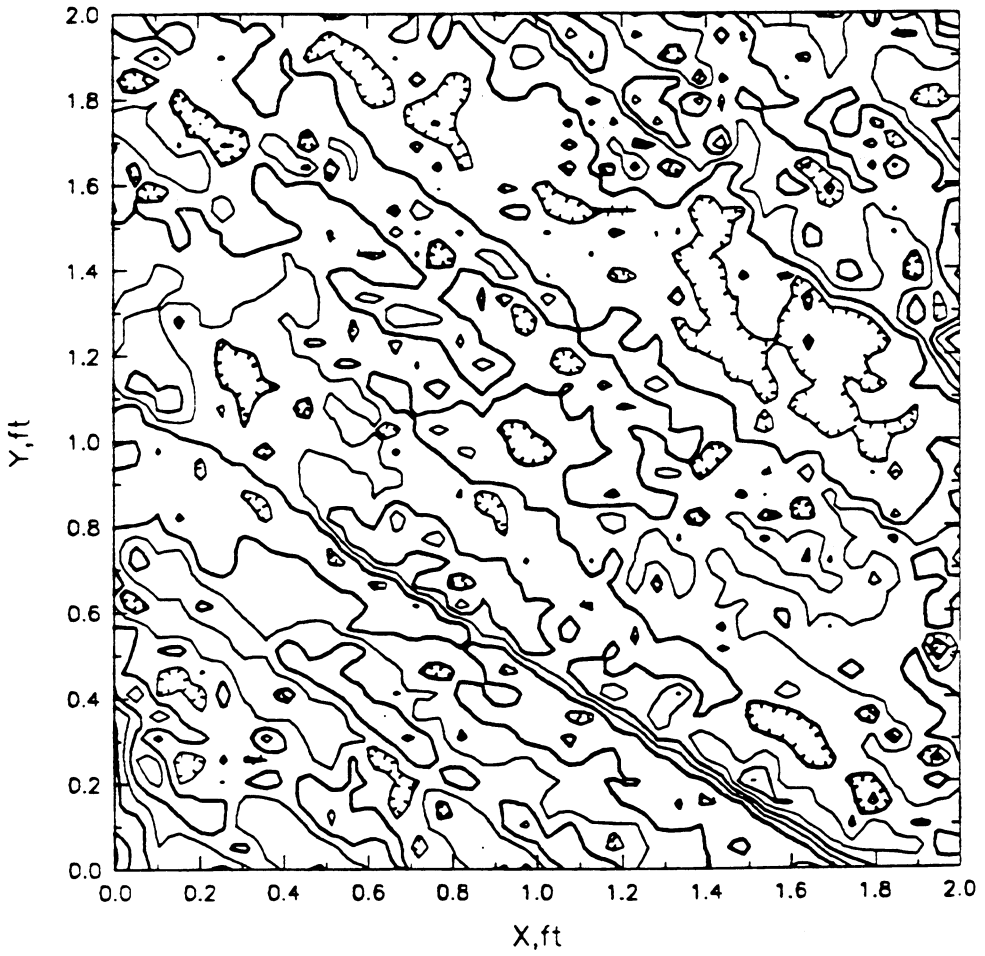

Fig. 4.4.8a. **Unsmoothed contour plot for Core 2.**

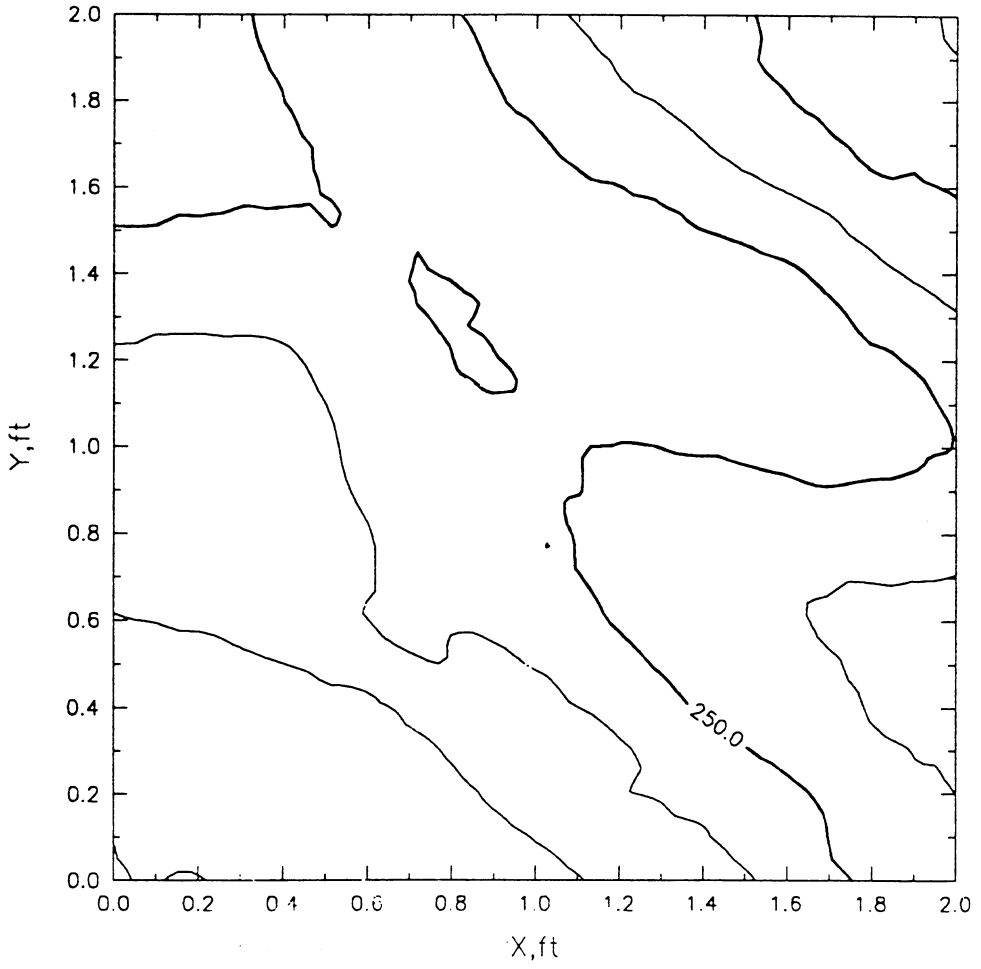

Fig. 4.4.8b. Smoothed contour plot for Core 2.

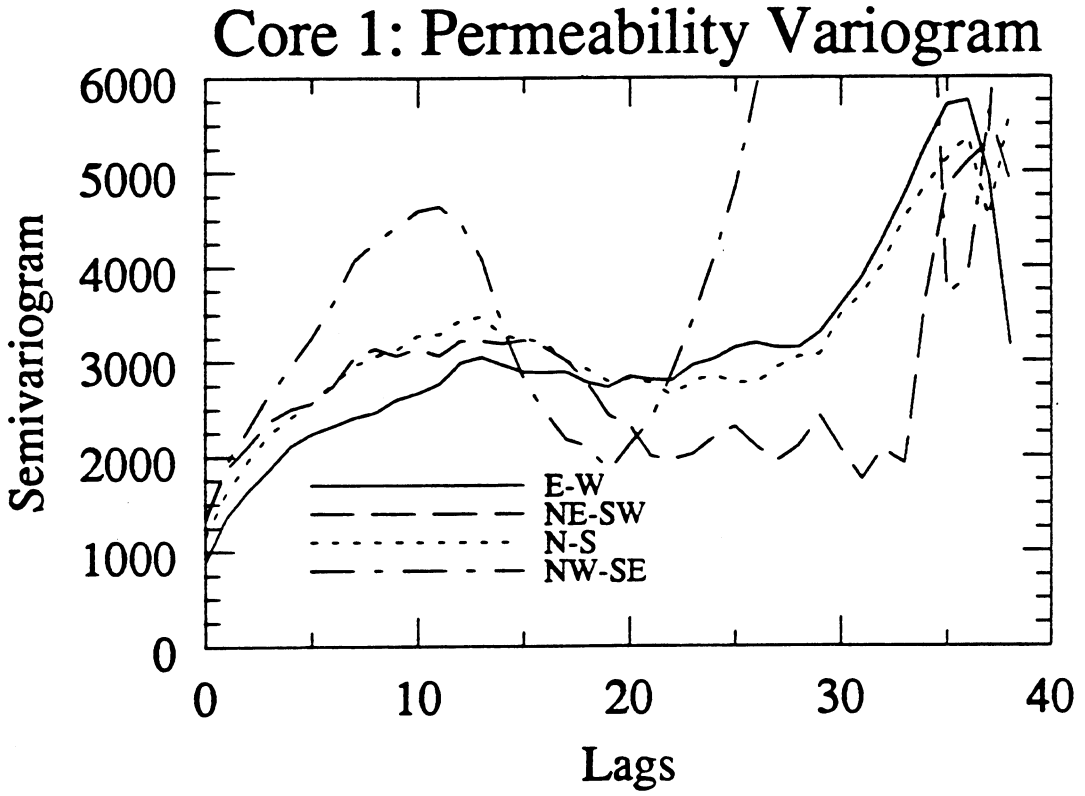

Fig. 4.4.9. Directional Variograms for Core 1.

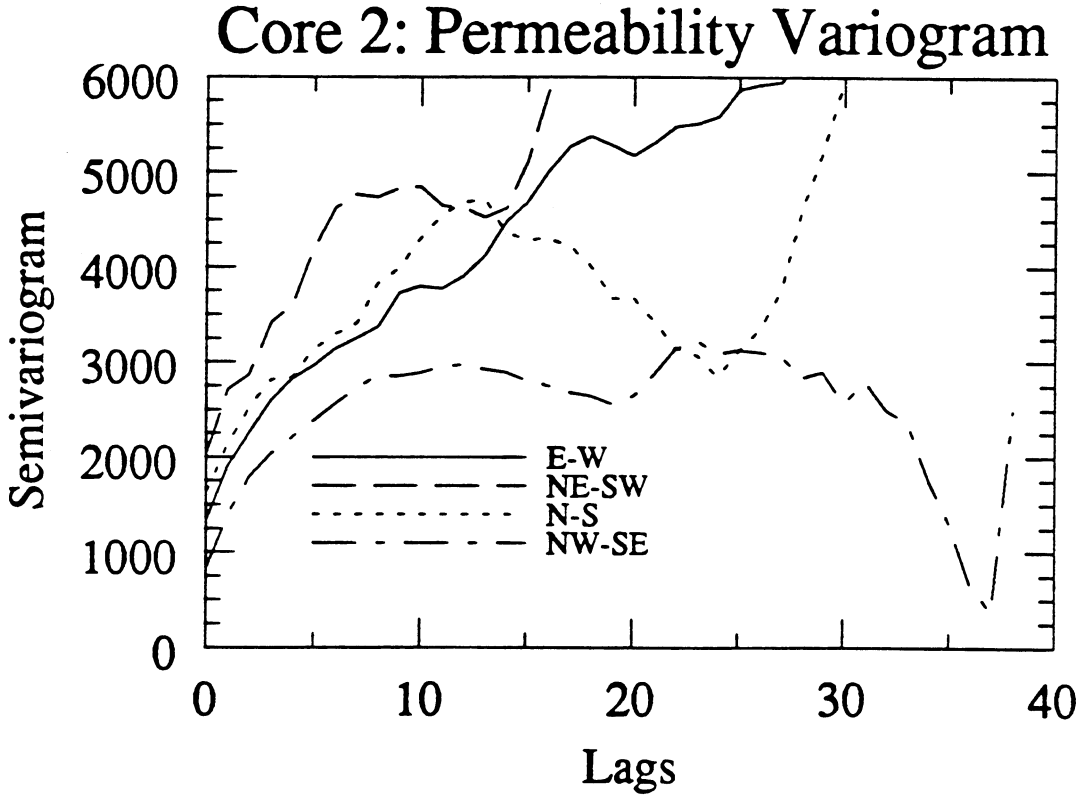

Fig. 4.4.10. Directional Variograms for Core 2.

(2) In the principal directions, the range of correlation (*i.e.*, the distance at which the semivariogram assumes its sill or maximum stable value) is about 10 lags or 0.5 feet. These data show that this areal permeability distribution is not spatially random, even at the 0.5 ft scale.

(3) Both cores exhibit zonal anisotropy. That is, the magnitude of the sill depends upon the direction. This correlation structure is more difficult to model than geometric anisotropy. In geometric anisotropy, the range may depend on direction but the height of the sill is invariant.

(4) The NW-SE variogram for Core 1 oscillates around it sill value. The oscillation is due to the laminations whose axes are roughly perpendicular to the NW-SE direction (see Figs. 4.4.7 and 4.4.9)

(5) In Core 2, the NE-SW variogram increases at separation distances $h \geq 15$ lags. The parabolic increase in the variogram is caused by a linear trend (or drift) in the permeability along this direction (see Figs. 4.4.8 and 4.4.10).

Immiscible Flow Through Small-Scale Areally Heterogeneous Systems

Numerical simulation was used to study the effects of the above-described small-scale permeability distributions upon immiscible flow. The analysis was quite simple: the simulations results (cumulative oil production, instantaneous water cut, and pressure drop) were used to estimate the pseudofractional flow by the method of Pande *et al.* (1987). The sensitivity of the pseudofunctions to flow conditions was then examined.

Fig. 4.4.11 shows several (pseudo)fractional flow curves: (1) the core (or rock) result, which was input to the simulator, (2) low flow rate with capillary pressure ($q_T = 1\frac{\text{PV}}{\text{day}}$; $N_{CT} = N_{CL} = 0.303$), (3) high flow rate with capillary pressure ($q_T = 10\frac{\text{PV}}{\text{day}}$; $N_{CT} = N_{CL} = 0.0303$) and (4) no capillary pressure ($N_{CT} \rightarrow 0$; numerical dispersion only). None of the fractional flow curves match the rock curves. The shock velocities and average saturations behind the front depend upon the capillary number. The dependence of fractional flow upon the capillary number is not an end effect, but rather reflects the effects of longitudinal (and, to a lesser extent, transverse) imbibition. The length scales in a core are small, so that capillary pressure is significant even at high rates (10 PV/day). When $P_c^* = 0$, the rate dependence vanishes — the capillary numbers are nearly zero regardless of the rate.

In order to investigate the effects of scale dependence, displacements with $N_{CT} \rightarrow 0$ ($P_c^* = 0$) were simulated using different subregions of Core 2. Fig. 4.4.12 shows the results of the pseudofunction analysis. The "half slab" runs were displacements through either the upper or lower half of Core 2 ($N_x = 40$, $N_y = 20$); the "quarter slabs" are defined analogously ($N_x = 40$, $N_y = 10$). All of the results are identical, even though the permeability fields are slightly different and the stabilizing effects of capillarity are small (numerical dispersion only). Apparently, the contrasts in permeability are not large enough to cause significant differences in the multiphase flow behavior at the scale considered. The ratio $\frac{k_{max}}{k_{min}}$ is only about 6 (versus 10 for the layered case); the limited range of correlation further mitigates the effects of the permeability contrasts. In systems with high mobility ratios or low dispersion,however, the permeability contrasts may affect the displacement more significantly (Giordano *et al.*, 1985).

4.4.4 Summary and Conclusions

By casting the differential equations for immiscible flow in dimensionless form, important aspects of the scaling behavior for these systems can be encapsulated in dimensionless groups. For example, systems with identical aspect ratios and physical properties, but different lengths,

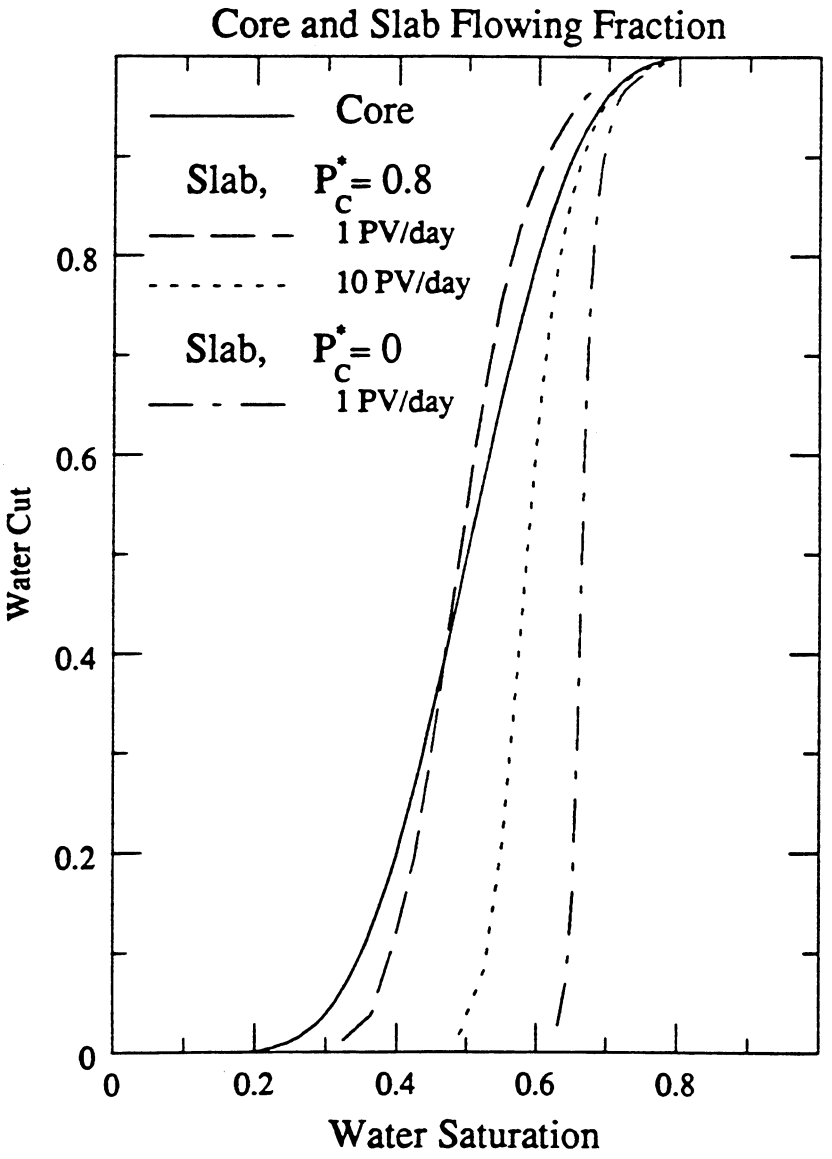

Fig. 4.4.11. Pseudofunctions showing rate effects for displacements through Core 2.

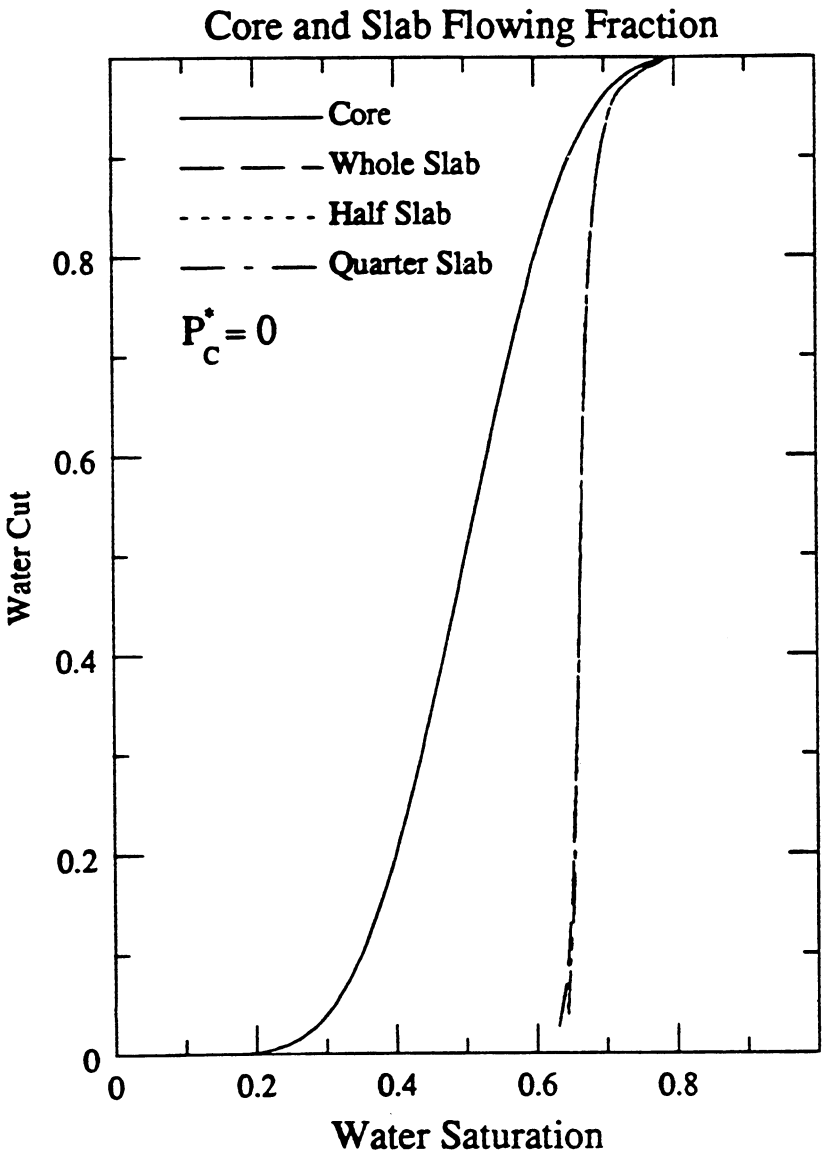

Fig. 4.4.12. Pseudofunctions for displacements through subregions of Core 2.

will have different capillary numbers and different production behavior. As a result, attempts to lump or scale the systems *via* a pseudofunction approach must respect the differences in physical behavior, as reflected in the dimensionless groups (N_{CL}, N_{CT}, R_L).

The importance of permeability contrasts in determining production behavior depends upon rock-fluid properties, system size, and the spatial correlation of the permeability. For layers, permeability contrasts are high and longitudinal correlation is nearly perfect. At low capillary numbers, the flow behavior of the composite system is very sensitive to the layering. At high capillary numbers, crossflow equalizes the saturation in the high- and low-permeability regions and the effects of layering become less pronounced. Heterogeneity and scale effects are both important for the layered systems. The core-level areal simulations showed little sensitivity to the permeability variations; the permeability contrasts were relatively low, and the length scales were short enough that capillary effects stabilized the flow very quickly. Currently, simulations of core-level displacements at higher viscosity ratios and higher coefficients of variation are being performed to determine the circumstances in which such small-amplitude, small-scale permeability variations dominate system behavior.

4.5 Summary

In this chapter, results that bear on the question of detection of reservoir heterogeneities are presented. Heterogeneities of permeability and porosity are important primarily because they determine flow performance. Tests that measure permeability directly, therefore, inevitably involve flow. Thus, we consider tracer and pressure transient tests because they depend directly on permeability. Permeability and porosity values measured are also averages over some flow domain, as are relative permeability functions. The results presented in this chapter are aimed at understanding how variations in those parameters affect flow performance at field scale and therefore, how significant heterogeneities can be detected.

Computations of the performance of well-to-well tracer tests showed that early breakthrough of injected fluid is likely if the permeability field has a significant variance and a correlation length that is also large. On average, if either the variance or the correlation length is small, then the performance of the test can be described by a single dispersion coefficient. Thus, the probability that a particular realization of a permeability field can be described well by a dispersion coefficient correlates with a heterogeneity index, defined as the product of the variance $ln\ (k)$ and a dimensionless correlation length. Comparison of calculated well test performance for the same permeability fields indicated that the heterogeneity index can be estimated using a dimensionless permeability difference determined from well tests in injection and production wells in a five spot.

Detection of heterogeneities close to a producing well was also considered. Calculations of transient pressure response for flow in the neighborhood of an impermeable region indicated that impermeable regions of large size produced greater deviations from homogeneous behavior. Thus, large regions can be detected while small ones cannot, and the size of the region must be relatively large compared to the distance from the production well. While the presence of the low permeability zone can be detected, independent determination of parameters such as size, shape and distance from the well is difficult.

Detection of the presence of a fault separating zones with different flow properties was also considered. Again, effects of the heterogeneity can be detected, but the response depends on the property contrasts and the location of the observation well, and hence, determination of the composite reservoir parameters from the well test response is not straightforward.

A key question in the discussion of the most important scales of heterogeneity is the relative importance of viscous and capillary crossflow. Permeability variations cause nonuniformity in the flood fronts, but if crossflow is strong enough it may reduce substantially the effects of mild permeability variations. Computations of displacement performance for variable permeability field at core scale indicated that for the permeability variations considered, capillary effects quickly stabilized the flow. Scaling of those results to larger flow systems is based on the dimensionless form of the flow equations. The resulting dimensionless groups, the transverse and longitudinal capillary numbers and an aspect ratio, indicate how the interplay of convective, and capillary and viscous crossflow contributions change as displacement scale changes. Future work will add the effects of phase behavior to the list of interacting mechanisms considered.

5. Summary and Conclusions

This report summarizes progress in a research effort to quantify the effects of nonuniform flow on displacement performance in CO_2 floods. Results are reported in three areas:

(1) Effect of phase behavior in one-dimensional flow.

(2) Interaction of viscous instability and flow in heterogeneous porous media.

(3) Detection and representation of reservoir heterogeneity.

In the first area, the development of a new apparatus for simultaneous measurement of the phase compositions, viscosities and densities of CO_2-hydrocarbon mixtures is described. That apparatus will be used to acquire fluid property data needed to improve correlations of mixture properties. Better description of the variation in fluid properties with composition is clearly needed if interactions of phase behavior and nonuniform flow of CO_2 and oil at reservoir conditions is to be calculated more accurately.

Also reported in the first area are the results of a calculation of the effects of the presence of methane dissolved in an oil on the development of miscibility. That calculation resolves a long-standing inconsistency between theoretical descriptions of the development of miscibility, based on analysis of ternary diagrams, and experimental observations that addition of methane to the oil has little effect on the minimum miscibility pressure unless the bubble point of the recombined oil exceeds the MMP of the dead oil. The calculated results show that the MMP is insensitive to the amount of methane present in the oil because the methane partitions so strongly into the vapor phase that all the methane has been displaced before the CO_2 arrives. Thus the CO_2 displaces dead oil, and if the pressure exceeds the dead oil MMP, that displacement is efficient. The entire displacement does, however, take place in the two-phase region. Hence, the absence of two-phase flow is not required for efficient displacement, contrary to the standard assumption made in descriptions of multiple contact miscibility. Analysis of the resulting compositions paths also indicates that as long as the flow is one-dimensional, a displacement of a live oil at a pressure below its bubble point pressure can also yield very high recovery.

The method of characteristics was used to perform the calculations of the effects of methane on development of miscibility. That technique can also be applied to the analysis of two additional problems: (1) the flow of CO_2-steam-heavy oil mixtures; and (2) flow of ternary mixtures in two layers with crossflow. In the first problem variation in temperature replaces variation in concentration of one of the components, but otherwise the analysis is similar. That analysis is complicated by the presence of three phases at some temperatures and by changes in the enthalpy balances due to the heat capacity of the rock matrix. Composition paths at fixed temperature have been completed, and analysis of temperature variations is underway now. The second problem is a prototype for studying the effects of crossflow on composition paths in multiple contact miscible displacements. Crossflow, whether viscous or capillary, causes mixing between fluids in zones of fast and slow flow. That mixing must modify composition paths, which in turn alters recovery for any displacement that relies on chromatographic separation to achieve high recovery. Calculations have been completed for binary systems, and analysis of paths for ternary systems has begun.

Also reported is an analysis of the effect of dispersion on composition paths. That analysis complements those based on the method of characteristics, which do not include effects of dispersion (or any other nonlocal mixing). Direct computations did not confirm a previously reported difference in calculated results between explicit representation of dispersion

and use of numerical dispersion. The computations showed clearly that the impact of dispersion is sensitive to the size and shape of the two-phase region. Thus, control of numerical dispersion may be more important for some fluid systems than for others.

Because CO_2 flooding is a process that depends primarily on the effects of phase behavior to achieve high displacement efficiency, description of the effects of phase behavior in one-dimensional flow is the baseline against which more complex flows that are not one dimensional, either due to viscous instability or to the presence of heterogeneity, can be evaluated. Thus, the results in the first area represent a necessary part of improved understanding of flow in the more complex systems.

In the second area, two approaches are being used to study the effects of viscous instability in the presence of variations in permeability. The first is a set of partly-scaled flow visualization experiments in which the length associated with the permeability variation is controlled and the dimensions of the resulting viscous fingers are measured. The second is a set of calculations of the growth of fingers in two-dimensional flows based on a probabilistic representation of the flow. Calculations of the growth of fingers were performed by adding random perturbations of position to account for the effects of dispersion of tracer particles being carried by convection. Calculated recovery data agreed very well with experimental observations for a full range of mobility ratios. No history matching was required. Additional calculations of the growth of fingers in heterogeneous porous media indicated that in some situations, at least, the permeability distribution dominates finger scale.

The third area recognizes that even if the impact of reservoir heterogeneity on displacement performance were completely understood, the problem of detection and representation of the relevant scales of heterogeneity would still be significant. Several aspects of the detection problem are considered. The first is the use of tracers to detect the presence of areal heterogeneities. Calculated response to injection into a five-spot at unit mobility ratio indicates that when the permeability is variable, spatial correlation leads to preferential flow paths. Thus, spatial correlation over a significant fraction of the displacement length causes early breakthrough and an effluent composition history that cannot be modeled using a dispersion coefficient alone. Calculations of tracer response for permeability fields described by a variance of $(ln\ k)$ and a correlation length indicated that a heterogeneity index, defined as the product of the variance and correlation length, gives a good indication of the type of flow behavior to be expected. For low values of the index, which result from permeability fields with small variance or little correlation, flow is likely to be described by a single dispersion coefficient. For high values of the index, the specific permeability realization has an important impact on displacement performance. Analysis of pressure transient tests for the same flow systems indicated that the heterogeneity index can be estimated from well test data.

The extent to which pressure transient tests can be used to detect the presence of heterogeneities is also considered. A technique is presented with which the transient response to large-scale heterogeneities can be calculated easily. It makes use of discreet constant pressure and impermeable flow boundary conditions to represent heterogeneities of arbitrary shape. That calculation scheme was used to examine the response to variations in the length and orientation of regions of different flow properties. In addition, the pressure response of one- and two-dimensional composite reservoirs is described. That analysis is useful because it describes either a reservoir with regions of different permeability or regions containing fluids with different viscosity. The calculated responses indicate that if the contrasts between properties in the two regions are large enough, the presence of the heterogeneities can be detected.

Also as part of the third area, the use of simplified representations of the flow effects of reservoir heterogeneities is considered. In any reservoir simulation, for example, flow properties will be assigned to large grid blocks, even though the reservoir rocks will be heterogeneous at smaller scales. To examine that behavior, calculations of the effects of heterogeneity, and capillary and viscous crossflow were undertaken. They showed that for relatively mild permeability variations, crossflow can mitigate the effects of permeability variation sufficiently that representation of the flow in terms of pseudorelative permeability functions is reasonable.

The descriptions of the effects of phase behavior, viscous instability and heterogeneity given here are not, of course, a complete description of all of the interactions of those mechanisms, particularly at field scale. Instead, the individual investigations are an attempt to simplify the analysis enough that progress can be made toward the overall goal of more accurate predictions of CO_2 flood performance at field scale. Thus, subsequent work will focus on the integration of the predictions made for the individual physical mechanisms into a more comprehensive picture of the scales on which they act.

References

Abbaszadeh-Dehghani, M. and Brigham, W.E., 1982, "Analysis of Unit-Mobility Ratio Well-to-Well Tracer Flow to Determine Reservoir Heterogeneity," SUPRI-TR-36, Stanford University.

Ambastha, A.K. and Ramey, H.J.,Jr., 1986, "An Analytical Study of Transient Flow in Linear Nonhomogeneous Aquifers," Stanford Univ. Pet. Res. Inst., Tech. Report, Stanford University.

Ambastha, A.K. and Sageev, A., 1987, "Linear Water Influx of an Infinite Aquifer through a Partially Communicating Fault," *Proc.*, 12th Geothermal Reservoir Engineering Workshop, Stanford, CA, January 20-22.

Anderson, M.P., 1984, "Movement of Contaminants of Groundwater: Groundwater Transport - Advection and Dispersion in Groundwater Contamination," Product of a Technological Society, *Natl. Res. Counc. Geophys. Study*, National Academy Press, Washington, D.C.

Arya, A., Hewett, T., Larson, R.G. and Lake, L.W., 1985, "Dispersion and Reservoir Hetrogeneity," paper SPE 14364, presented at the SPE 60th Annual Technical Conference, Las Vegas, September 24-27.

Aziz, K. and Settari, A., 1979, *Petroleum Reservoir Simulation*, Applied Science Publishers, London, 206.

Bear, J., 1972, "Dynamics of Flow in Porous Media," Elsevier, New York.

Blackwell, R.J., Rayne, J.R. and Terry, W.M., 1959, "Factors Influencing the Efficiency of Miscible Displacement," *Trans. AIME 216,* 1-8.

Begg, S.H. and King, P.R., 1985, "Modelling the Effects of Shales on Reservoir Performance: Calculation of Effective Permeability," SPE 13529, presented at the SPE Reservoir Simulation Symposium held in Dallas, February 10-13.

Bixel, H.C., Larkin, B.K. and Van Poollen, H.K., 1963, "Effect of Linear Discontinuities on Pressure Buildup and Drawdown Behavior," *J. Pet. Tech.*, 885-95.

Blackwell, R.J., Rayne, J.R. and Terry, W.M., 1959, "Factors Influencing the Efficiency of Miscible Displacement," *Trans. AIME, 216*, 1-8.

Boyce, W.E. and DiPrima, R.C., 1977, *Elementary Differential Equations and Boundary Value Problems,* Third Edition, John Wiley and Sons, Inc., New York, Ch. 3, p. 94.

Brigham, W.E. and Abbaszadeh-Dehghani, M., 1987, "Tracer Testing for Reservoir Description," *J. Pet. Tech.*, 519-527, May.

Buckley, S. E. and Leverett, M. C., 1942, "Mechanism of Fluid Displacement in Sands," *Trans. AIME 146,* 107-116.

Bowman, C.H. and Crawford, P.B., 1962, "A Practical Method for Calculating the Transient Pressure Distribution in Linear Semi-infinite Water Driven Reservoirs Having Different Fluid and Rock Properties in Each Zone," SPE Paper 272.

Campbell, B.T. and Orr, F.M., Jr., 1985, "Flow Visualization for CO_2 - Crude Oil Displacements," *Soc. Pet. Eng. J. 25,* 665-677.

Carslaw, H.S. and Jaeger, J.C., 1960, *Conduction of Heat in Solids,* 2nd ed. Oxford University Press.

Christie, M.A. and Bond, D.J., 1986, "Detailed Simulation of Unstable Processes in Miscible Flooding, SPE 14896, presented at the SPE/DOE Fifth Symposium on Enhanced Oil Recovery, Tulsa, April 20-23.

Christie, M.A., 1987, "Numerical Techniques for High Resolution Simulation of Instabilities," SPE 16005, presented at Ninth Symposium Reservoir Simulation, San Antonio, February 1-4.

Churchill, R.V., 1944, *Operational Mathematics,* McGraw Hill Book Co.

Cinco, H., Samaniego, V. and Dominguez, A., 1976, "Unsteady-State Flow Behavior for a Well Near a Natural Fracture," paper SPE 6019 presented at the Annual Technical Conference, New Orleans, October.

Clark, D.G. and Van Golf-Racht, T.D., 1985, "Pressure Derivative Approach to Transient Test Analysis: A High-Permeability North Sea Reservoir Example," *J. Pet. Tech.,* 2023-29, November.

Coats, K.H., Dempsey, J.R. and Henderson, J.H., 1971, "The Use of Vertical Equilibrium in Two-dimensional Simulation of Three-dimensional Reservoir Performance," *Trans. AIME 251,* 63-71.

Craig, F.F., Jr., 1971, *The Reservoir Engineering Aspects of Waterflooding,* Monograph 3, *Soc. of Pet. Eng. of AIME,* Dallas, 62-68.

Dai, K.K. and Orr, F.M., Jr., 1984, "Prediction of CO_2 Flood Performance: Interaction of Phase Behavior with Microscopic Pore Structure Heterogeneity," SPE 13115, presented at 59th Annual Technical Conference of SPE of AIME, Houston, September 16-19.

Davis, E.G. and Hawkins, M.F., 1963, "Linear Fluid-Barrier Detection by Well Pressure Measurements," *J. Pet. Tech.,* 1077-79, October.

Deffrenne, P. et al., 1961, "The Determination of Pressures of Miscibility," paper SPE 116, presented at Fall Meeting of SPE of AIME, Dallas, October

DeGregoria, A.J., 1985, "A Predictive Monte Carlo Simulation of Two-Fluid Flow through Porous Media at Finite Mobility Ratio," *Phys. Fluids 28,* 2313-2314.

Dougherty, E.L., 1963, "Mathematical Model of an Unstable Displacement," *Trans. AIME 222,* 155-163.

Dumore, J.M., Hagoort, J. and Risseeuw, A.S., 1984, "A Analytical Model for One Dimensional Three Component and Vaporizing Gas Drives," *Soc. Pet. Eng. J. 24,* 169-179.

Dykstra, H. and Parsons, R. L., 1950, "The Prediction of Oil Recovery by Waterflooding," Secondary Recovery of Oil in the United States, 2nd ed., API , 160-174.

Earlougher, R.C., Jr., Ramey, H.J., Jr., Miller, F.G. and Mueller, T.D., 1968, "Pressure Distributions in Rectangular Reservoirs," *J. Pet. Tech.*, 199-208, February.

Earlougher, R.C., Jr. and Ramey, H.J., Jr., 1973, "Interference Analysis in Bounded Systems," *J. Can. Pet. Tech.*, 33-45, October-December.

Eclipse User's Manual, 1985, Exploration Consultants, Ltd., Henley-on-Thames, England.

Ehlig-Economides, C. and Economides, M.J., 1982, "Analysis of a Geothermal Well Test in a Predominantly Linear Flow System," *Trans.*, Intl. Conf. on Geothermal Energy, Florence, Italy, 281-92, May 11-14.

Eijpe, R. and K. J. Weber, 1971, "Minipermeameters for Rock and Unconsolidated Sand," *Amer. Soc. of Petr. Geol. Bull.*, v. 55, 307-309.

Ehlig-Economides, C. and Economides, M.J., 1985, "Pressure Transient Analysis in an Elongated Linear Flow System," *Soc. Pet. Eng. J.*, 839-47, December.

Erdelyi, A., 1954, *Tables of Integral Transforms I*, McGraw-Hill Book Co., Inc., N.Y.

Farlow, S.J., 1982, *Partial Differential Equations for Scientists and Engineers*, John Wiley and Sons, Inc., New York, Ch. 2, p. 73-74.

Fayers, F.J., 1984, "An Approximate Model with Physically Interpretable Parameters for Representing Miscible Viscous Fingering," SPE 13166, presented at 59th Annual Technical Conference of SPE of AIME, Houston, September 16-19.

Fayers, F.J. and Newley, T.M.J., 1987, "Detailed Validation of an Empirical Model for Viscous Fingering with Gravity Effects," SPE 15933, presented at ninth Symposium reservoir Simulation, San Antonio, February 1-4.

Ferris, J.G., Knowles, D.B., Brown, R.H. and Stallman, R.W., 1962, "Theory of Aquifer Tests," *Geol. Surv. Water Supply Pap., 1536 E*, 139-71.

Firoozabadi, A., Nutakki, R. Wang, T. and Aziz, K., 1986, "EOS Predictions of Compressibility and Phase Behavior in Systems Containing Water, Hydrocarbons and and CO_2, SPE 15674, presented at 61st Annual Technical Conference, New Orleans, October 5-8.

Fried, J.J., 1975, "Groundwater Pollution," Elsevier Scientific Publishing Company, Amsterdam.

Gardner, J.W., Orr, F.M., Jr. and Patel, P.D., 1981, "The Effect of Phase Behavior on CO_2-Flood Displacement Efficiency," *Soc. Pet. Eng. J.*, 21, 2067-2081.

Gardner, J.W., Ypma, J.G.J., 1984, "An Investigation of Phase Behavior - Macroscopic Bypassing Interaction in CO_2 Flooding," *Soc. Pet. Eng. J. 24*, 508-520.

Geertsma, J., Croes, G.A. and Schwarz, N., 1956, "Theory of Dimensionally Scaled Models of Petroleum Reservoirs," *Trans. AIME 207*, 118-127.

Gelhar, L.W., Gutjhar, A.L. and Naff, R.L., 1979, "Stochastic Analysis of Macrodispersion in a Stratified Aquifer," *Water Resources Res.* 15, (6), 1387-1397.

Giordano, R. M., Salter, S. J. and Mohanty, K. K., 1985, "The Effects of Permeability Variations on Flow in Porous Media," SPE 14365, presented at the 60th Annual Technical Conference of SPE of AIME, Las Vegas, September 22-25.

Gray, K.E., 1965, "Approximating Well-to-Fault Distance from Pressure Buildup Tests," *J. Pet. Tech.*, 761-67, July.

Habermann, B., 1960, "The Efficiency of Miscible Displacement As A Function of Mobility Ratio," *Trans. AIME, 219,* 264-272.

Haldorsen, H.H. and Lake, L.W., 1984, "A New Approach to Shale Management in Field Scale Simulation Models," *Soc. Pet. Eng. J. 24,* 447-457.

Hatziavramidis, D.T., 1987, "A New Computational Approach to the Miscible Displacement Problem," SPE 16004, presented at ninth Symposium Reservoir Simulation, San Antonio, February 1-4.

Hearn, C. L., 1971, "Simulation of Stratified Waterflooding by Pseudo Relative Permeability Curves," *J. Pet. Tech.*, July, 805-813.

Helfferich, Fredrich G., 1981, "General Theory of Multicomponent, Multiphase Displacement in Porous Media," *Soc. Pet. Eng. J. 21,* 51-62.

Heller, J.P., 1966, "Onset of Instability Patterns Between Miscible Fluids in Porous Media," *J. Appl. Phys. 37,* 1566-1579.

Heller, J. P., 1963, "The Interpretation of Model Experiments for the Displacement of Fluids Through Porous Media," *AIChE J.*, July, 452-459.

Hirasaki, George J., 1981, "Application of the Theory of Multicomponent, Multiphase Displacement to Three-Component, Two-Phase Surfactant Flooding," *Soc. Pet. Eng. J. 21,* 191-204.

Hoeksema, R.J. and Kitanidis, P.K., 1985, "Analysis of the Spatial Structure of Properties of Selected Aquifers," *Water Resources Res.* 21, (4) 563-572.

Holm, L. W. and Josendal, V. A. 1974, "Mechanisms of Oil Displacement by Carbon Dioxide," *J. Pet. Tech. 16,* 1427-1436.

Holm, L. W. and Josendal, V. A., 1982, "Effect of Oil Composition on Miscible-Type Displacement by Carbon Dioxide," *Soc. Pet. Eng. J. 22,* 87-98.

Homsy, G.M., 1986, "Viscous Fingering in Porous Media," *Ann. Rev. Fluid Mech. 19,* 271-311.

Horner, D.R., 1951, "Pressure Buildup in Wells," *Proc.*, Third World Pet. Congress, The Hague, Sec. II, 503-23.

Hurst, W., 1953, "Establishment of the Skin Effect and Its Impediment to Fluid Flow into a Well Bore," *Pet. Eng.*, B-6 - B-16, October.

Hurst, W., 1958, "The Simplification of the Material Balance Formulas by the Laplace Transformation," *Trans. AIME 213,* 292.

Hutchinson, C. A., Jr. and Braun, P. H., 1961, "Phase Relations of Miscible Displacement and Oil Recovery," *A.I.Ch.E. J. 7*, 64-72.

Jap, J., Khawaja, B., Taggart, and Pinczewski, W.V., 1985, "Modelling of Phase Behavior and Displacement Performance for the Miscible Gas Flooding EOR Process," Proc. Chemeca 1985, 13th Australian Chemical Engineering Conference, Perth, Aug., 89-93.

Jennings, A., 1977, *Matrix Computations for Engineers and Scientists*, John Wiley and Sons, New York, 100-166.

Johnson, E.F., Bossler, D.P. and Naumann, V.O., 1959, "Calculation of Relative Permeability from Displacement Experiments," *Trans.*, AIME, 216, 370-372.

Jones, S.C. and Roszelle, W.O., 1978, "Graphical Techniques for Determining Relative Permeability From Displacement Experiments," *J. Pet. Tech.*, 807-817, May.

Jossi, J.A., Stiel, L.I. and Thodos, G., 1962, "The Viscosity of Pure Substances in the Dense Gaseous and Liquid Phases," *A.I.Ch.E. Journal*, vol. 8, No. 1, p. 59-62.

Journel, A.G. and Huijbregts, C.J., 1978, "Mining Geostatistics," Academic Press, London.

King, M. and Scher, H., 1985, "Probabilistic Stability Analysis of Multiphase Flow in Porous Media," SPE 14366, presented at 60th Annual Technical Conference of SPE of AIME, Las Vegas, September 22-25.

King, M. and Scher, H., 1986, "A Probability Approach to Multiphase and Multi-component Fluid Flow in Porous Media," *Phys. Rev. A.* in press.

Konikow, L.F. and Bredehoeft, J.D., 1978, "Computer Model of Two-Dimensional Solute Transport and Dispersion in Ground Water," Ch. C2, Book 7, Techniques of Water-Resources Investigations of the United States Geological Survey.

Kortekaas, T.F.M., 1983, "Water/Oil Displacement Characteristics in Cross-Bedded Reservoir Zones," SPE 12112, presented at 58th Annual Technical Conference, San Francisco, October 5-8.

Koval, E.J., 1963, "A Method for Predicting the Performance of Unstable Miscible Displacement in Heterogeneous Media," *Trans. AIME, 228*, 145-154.

Kruseman, G.P. and De Ridder, N.A., 1970, *Analysis and Evaluation of Pumping Test Data*, International Institute for Land Reclamation and Improvement, Wageningen, The Netherlands, 111-25.

Lantz, R.B., 1971, "Quantitative Evaluation of Numerical Diffusion (Truncation Error)," *Soc. of Pet. Eng. J. 11*, 315-319.

Larsen, L.L., 1984, "Prediction of Phase Behavior of CO_2-Hydrocarbon Mixtures." M.Sc. thesis, New Mexico Institute of Mining and Technology, Socorro, New Mexico.

Larsen, R.G., 1979, "The Influence of Phase Behavior on Surfactant Flooding," *Soc. Pet. Eng. J. 19*, 411-422, December.

Lasseter, T.J., Waggoner, J.R. and Lake, L.W., 1986, "Reservoir Heterogeneities and Their Influence on Ultimate Recovery," Reservoir Characterization, L. W. Lake and H. B. Carroll, Jr., Eds., Academic Press, New York, 545-560.

LeBlanc, R.J., Sr., 1977a, "Distribution and Continuity of Sandstone Reservoirs -- Part I" *J. Pet. Tech. 29*, 776-792.

LeBlanc, R.J., Sr., 1977b, "Distribution and Continuity of Sandstone Reservoirs -- Part 2" *J. Pet. Tech. 29*, 793-804.

Lee, S., Li, K.M.G. and Culham, W.E., 1984, "Stability Analysis of Miscible Displacement Processes," SPE/DOE 12631, presented at fourth Symposium Enhanced Oil Recovery, Tulsa, April 15-18.

Leverett, M. C., 1941, "Capillary Behavior in Porous Solids," *Trans., AIME,* v. 142, p. 341.

Lohrenz, John, Grey, Bruce, C. and Clark, Charles R., 1964, "Calculation Viscosities of Reservoir Fluids from their Compositions," *J. Pet. Tech. 6,* 1171-1176.

Luster, G.R., 1984, "Practical Conditional Simulation of Coregionalization, I: Basic Methods and Transformations," Progress Report 3, for Exxon Minerals Company Research Grant Geostatistical Estimation and Simulation of Ore Deposits.

Martin, J.C., 1968, "Partial Integration of Equations of Multiphase Flow," *Trans. AIME, 243,* 370-380.

Martin, J.H. and Cooper, J.A., 1984, "An Integrated Approach to the Modeling of Permeability Barrier Distribution in a Sedimentologically Complex Reservoir," SPE 13051, presented at the 59th Annual Technical Conference, Houston, September 16-19.

Martinez-Romero, N. and Cinco-Ley, H., 1983, "Detection of Linear Impermeable Barrier by Transient Pressure Analysis," Paper SPE 11833 presented at the Rocky Mountain Reg. Mtg., Salt Lake City, May 23-25.

McLeroy, P.G., 1986, "Transient Pressure Analysis in Strip Reservoirs with Linear Skin Discontinuities," *M.S. Thesis,* Stanford University, Stanford, CA.

Meiburg, E. and Homsy, G.M., 1987, "Vortex Methods for Porous Media Flows," *Phys. Fluids,* in press.

Metcalfe, R. S. and Yarborough, L., 1979, "The Effect of Phase Equilibria on the CO_2 Displacement Mechanism," *Soc. Pet. Eng. J. 19,* 242-252.

Miller, F.G., 1962, "Theory of Unsteady-State Influx of Water in Linear Reservoirs," *J. Inst. of Pet., 48,* 365, November.

Miller, M.C., 1963, "Relationship Between Unsteady Well Performance and Insitu Reservoir Characteristics," Ph.D. Thesis, The University of Michigan, Ann Arbor.

Mishra, S., 1987, "On the Use of Pressure and Tracer Test Data for Reservoir Description," Ph. D. Dissertation, Stanford University.

Monroe, W.E., 1986, "The Effects of Dissolved Methane on Composition Paths in Quaternary CO_2 - Hydrocarbon Systems," M.S. report, Department of Petroleum Engineering, Stanford University.

Mueller, T.D., 1962, "Transient Response of Nonhomogeneous Aquifers," *Soc. Pet. Eng. J.*, 33-43.

Nabor, G.W. and Barham, R.H., 1964, "Linear Aquifer Behavior," *J. Pet. Tech. 16,* 561-563.

Nutakki, R. and Mattar, L., 1982, "Pressure Transient Analysis of Wells in Very Long Narrow Reservoirs," Paper SPE 11221 presented at the 57th Annual Mtg. in New Orleans, LA, September 26-29.

Nutakki, R., Wong, T., Firoozabadi, A. and Aziz, K., 1985, "Development of general purpose simulators Part 1: Vapor-Liquid Equilibrium Calculations Using Three Equations of State and Accelerated Successive Substitution." Department of Petroleum Engineering, School of Earth Sciences, Stanford University.

Offeringa, J. and Van der Poel, C., 1954, "Displacement of Oil from Porous Media by Miscible Liquids," *Trans. AIME 201,* 310-316.

Orr, F.M., Jr., 1980, "Simulation of the One-Dimensional Convection of Four-Phase, Four-Component Mixtures," US DOE Rep. No. DOE/ET/12082-8.

Orr, F.M. Jr. and Silva M.K., 1985, "Effect of Oil Composition on Minimum Miscibility Pressure-Part 2: Correlation," *SPE* 14150, presented at 60th Annual Technical Conference of SPE of AIME, Las Vegas, September 22-25.

Orr, F. M. Jr. and Taber, J. J. 1984, "Displacement of Oil by Carbon Dioxide," Final Report to the U.S. Department of Energy, Report No. DOE /BC/10331-13.

Orr, F.M., Jr., Silva, M.K. and Lien, C.L., 1983, "Equilibrium Phase Compositions of CO_2-Crude Oil Mixtures - Part 2: Comparison of Continuous Multiple Contact and Skin Tube Displacement Tests," *Soc. Pet. Eng. J.*, 23, 281-291.

Orr, F.M., Jr., Silva, M.K., Lien, C.L. and Pelletier, M.T., 1982, "Laboratory Experiments to Evaluate Field Prospects for Carbon Dioxide Flooding," *J. Pet. Tech. 34*, 888-898.

Pande, K. K. , H. J. Ramey, Jr., W. E. Brigham and F. M. Orr, Jr., 1987, "Frontal Advance Theory for Flow in Heterogeneous Porous Media," SPE 16344, presented at the California Regional Meeting, Ventura, April 2-10.

Peaceman, D.W., 1978, "Interpretation of Well-Block Pressures in Numerical Reservoir Simulation," *Soc. Pet. Eng. J.*, 183-184, June.

Peaceman, D.W. and Rachford, H.H. Jr., 1962, "Numerical Calculation of Multidimensional Miscible Displacement," *Soc. Pet .Eng. J.*, 301-317, May.

Peng, D-Y and Robinson, D.B., 1976, "A New Two-Constant Equation of State," *Ind. Eng. Chem., 15*, 59-64.

Perkins, T.K. and Johnston, O.C., 1963, "A Review of Dispersion in Porous Media," *Soc. Pet. Eng. J.*, 70.

Perrine, R.L., 1963, "A Unified Theory for Stable and Unstable Miscible Displacement," *Soc. Pet. Eng. J. 3* 205.

Peters, E.J., Broman, W.H. and Broman, J.A., 1984, "A Stability Theory for Miscible Displacement," SPE 13167, presented at 59th Annual Technical Conference of SPE of AIME, Houston, September 16-19.

Pozzi, A. and Blackwell, R., 1963, "Design of Laboratory Models for Study of Miscible Displacement," *Soc. Pet. Eng. J., 28-40, March.*

Prasad, R.K., 1975, "Pressure Transient Analysis in the Presence of Two Intersecting Boundaries," *J. Pet. Tech. 27*, 89-96.

Prickett, T.A., Naymik, T.G. and Lonnquist, C.G., 1981, "A Random-Walk Solute Transport Model for Selected Groundwater Quality Evaluations," *Illinois State Water Survey Bulletin 65.*

Pryor, W. A., 1972, "Reservoir Inhomogeneities of Some Recent Sand Bodies," *Soc. Pet. Eng. J. 12*, 229-245, June.

Ramey, H.J., Jr. and Cobb, W.M., 1971, "A General Pressure Buildup Theory for a Well in a Closed Drainage Area," *J. Pet. Tech.*, 1493-1501, December.

Ramey, H.J., Jr., Kumar, A. and Gulati, M.S., 1973, *Gas Well Test Analysis Under Water-Drive Condition,* Monograph on Project 61-51, AGA Inc., Arlington.

Rathmell, J. J., Stalkup, F. I. and Hassinger, R. C., 1971, "A Laboratory Investigation of Miscible Displacement by Carbon Dioxide," SPE 3483 presented at 46th Annual Technical Conference of SPE of AIME, New Orleans, October 4-8.

Reamer, H.H. and Sage, B.H., 1963, "Phase Equilibria in Hydrocarbon Systems. Volumetric and Phase Behavior of the n-Decane-CO_2 System," *J. Chem. Eng. Data 8*, 508-513.

Resnik, A.A., Enick, R.M. and Panvelker, S.B., 1984, "An Analytical Extension of the Dykstra-Parsons Vertical Stratification Discrete Solution to a Continuous, Real-Time Basis," *Soc. Pet. Eng. J. 24*, 643-656.

Sageev, A. 1985, "Interference Testing Near a Steam Cap," Geothermal Resources Council, *Transactions* vol. 9, Part 2, October.

Sageev, A. and Horne, R.N., 1983a, "Pressure Transient Analysis of Reservoirs with Linear or Internal Circular Boundaries," SPE 12076, presented at 58th Annual Technical Conference, San Francisco, October 5-8.

Sageev, A. and Horne, R.N., 1983b, "Drawdown Pressure Transient Analysis of a Well Near a Steam Cap," Geothermal Resources Council, *Transactions 7*, October.

Sageev, A. and Horne, R. N., 1986, "Interference Testing: Detecting an Impermeable or Compressible Region," SPE 15585 presented at Annual Technical Conference, New Orleans, October 5-8.

Sageev, A., Horne, R.N. and Ramey, H.J., Jr., 1985, "Detection of Linear Boundaries by Drawdown Tests: A Semilog Type Curve Matching Approach," *Water Resources Research*, vol. 21, No. 3, 305-10, March.

Schowalter, W.R., 1965, "Stability Criteria for Miscible Displacement of Fluids from a Porous Medium, *AIChE. J.* 11:99-105.

Schwartz, F.W., 1977, "Macroscopic Dispersion in Porous Media : The Controlling Factors," *Water Resources Res.* 13, (4) 743-752.

Silva, M. K., Larsen, L. L. and Orr, F. M., Jr. 1985, "CO_2-Hydrocarbon Phase Behavior in Model Systems, Part 1: CO_2-C_1-C_4-C_{10}," PRRC Report No. 85-31, New Mexico Petroleum Recovery Research Center.

Slobod, R.L. and Koch, H.A., Jr., 1953, High-pressure Gas Injection - Mechanism of Recovery Increase," *Drill and Prod. Prac.*, API, 82-96.

Slobod, R.L. and Thomas, R.A., 1963, "Effect of Transverse Diffusion on Fingering In Miscible-Phase Displacement," *Soc. Pet. Eng. J.*, March 9-13.

Smith, L. and Schwartz, F.W., 1980, "Mass Transport, 1. A Stochastic Analysis of Macroscopic Dispersion," *Water Resources Res.* 16, (2) 303-313.

Smith, P.J. and Brown, C.E., 1984, "The Interpretation of Tracer Test Response from Heterogeneous Reservoirs," SPE 13262, presented at SPE 59th Annual Technical Conference, Houston, September 16-19.

Spence. A.P. and Watkins, R.W., 1980, "The Effect of Microscopic Core Heterogeneity on Miscible Flood Residual Oil Saturation," SPE 9229, presented at 55th Annual Technical Conference of SPE of AIME, Dallas, September 21-24.

Stalkup, F.I. Jr., 1983, "Miscible Displacement," Monograph 8, Society of Petroleum Engineers of AIME, New York.

Stalkup, F.I., 1986, "Permeability Variations Observed at the Faces of Crossbedded Sandstone Outcrops," in *Reservoir Characterization*, L. W. Lake and H. B. Carroll, Academic Press, New York, 141-179.

Stallman, R.W., 1952, "Nonequilibrium Type Curves Modified for Two-Well Systems," U.S. Geol. Surv., Groundwater Note 3.

Stehfest, H., 1970, "Algorithm 368, Numerical Inversion of Laplace Transforms," D-5, *Comm. of ACM 13*, No.1, 49, January.

Stewart, G., Gupta, A. and Westaway, P., 1984, "The Interpretation of Interference Tests in a Reservoir with Sealing and Partially Communicating Faults," Paper SPE 12967 presented at the 1984 European Petroleum Conf. in London, England, October 25-28.

Streltsova, T.D. and McKinley, R.M., 1984, "Effect of Flow Time Duration on Buildup Pattern for Reservoirs with Heterogeneous Properties," *Soc. Pet. Eng. J.*, 294-306, June.

Tan, C.T. and Homsy,G.M., 1986, "Stability of Miscible Displacements in Porous Media," *Phys. Fluids*, in press.

Tan, C.T. and Homsy, G.M., 1987, "Simulation of Non-Linear Viscous Fingering in Miscible Displacement," *Phys. Fluids*, in press.

Theis C.V., 1935, "Relation Between the Lowering of the Piezometric Surface and the Rate and Duration of Discharge of a Well Using Ground-Water Storage," *EOS Trans. AGU 16(2)*, 519-524.

Tiab, D. and Crichlow, H.B., 1979, "Pressure Analysis of Multiple-Sealing Fault Systems and Bounded Reservoirs by Type-Curve Matching," *Soc. Pet. Eng. J.*, 379-392, December.

Tiab, D. and Kumar, A., 1980, "Detection and Location of Two Parallel Sealing Faults Around a Well," *J. Pet. Tech.*, 1701-08, October.

Todd, M.R. and Longstaff, W.J., 1972, "The Development, Testing and Application of a Numerical Simulator for Predicting Miscible Flood Performance," *Trans. AIME 253*, 874-882.

Todd, M.R., O'Dell, P.M. and Hirasaki, G.J., 1972, "Methods for Increased Accuracy in Numerical Reservoir Simulators," *Soc. Pet. Eng. J.*, 515-530, December.

Tryggvason, G. and Aref, H., 1983, "Numerical Experiments on Hele Shaw Flow with a Sharp Interface," *J. Fluid. Mech. 136*, 1-30.

Van Everdingen, A.F., 1953, "The Skin Effect and Its Influence on the Productive Capacity of a Well," *Pet. Transactions of AIME*, vol. 198, 171-76.

Van Everdingen, A.F. and Hurst, W., 1949, "The application of the Laplace Transformation to Flow Problems in Reservoirs," *Trans. AIME 186*, 305-324.

Van Poollen, H.K., 1965, "Drawdown Curves give Angle Between Intersecting Faults," *Oil and Gas Journal*, 71-75, December 20.

Warren, J.E. and Price, H.S., 1961, "Flow in Heterogeneous Porous Media," *Soc. Pet. Eng. J. 1*, 153-169.

Warren, J.E. and Skiba, F.F., 1964, "Macroscopic Dispersion," *Soc. Pet. Eng. J.*, 215-230.

Weber, J., 1982, "Influence of Common Sedimentary Structures of Fluid Flow in Reservoir Models," *J. Pet. Tech.*, 34, 665-672.

Welge, H.J., 1948, "Displacement of Oil from Porous Media by Water and Gas, Trans. AIME 179, 133-138.

Welge, H.J., 1952, "A Simplified Method for Computing Oil Recovery by Gas or Water Drive," *Trans.*, AIME, 195, 91-98.

Welge, H. J. *et al.*, 1961, "The Linear Displacement of Oil from Porous Media by Enriched Gas," *J. Pet. Tech. 3*, 787-96.

White, C. D., 1987, "Representation of Heterogeneity for Numerical Reservoir Simulation," Ph. D. Dissertation, Stanford University.

White, C. D. and R. N. Horne, 1987, "Computing Absolute Transmissibility in the Presence of Fine-Scale Heterogeneity," SPE 16011, presented at the Ninth SPE SPE Simulation Symposium, San Antonio, February 1-4.

Witherspoon, P.A., Javandel, I., Neuman, S.P. and Freeze, R.A., 1967, "Interpretation of Aquifer Gas Storage From Water Pumping Tests," Monograph on Project NS-38, American Gas Association, Inc., New York.

Wong, W.D., Mothersele, C.D., Harrington, A.G. and Cinco-Ley, H., 1986, "Pressure Transient Analysis in Finite Linear Reservoirs Using Derivative and Conventional Techniques: Field Examples," SPE 15421 presented at the 61st Annual Mtg., New Orleans, October 5-8.

Yaxley, L.M., 1985, "The Effect of a Partially Communicating Fault on Transient Pressure Behavior," SPE 14311, presented at 60th Annual Technical Conference of SPE of AIME, Las Vegas, September 22-25.

Yellig, W. F. and Metcalfe, R. S., 1980, "Determination and Prediction of CO_2 Minimum Miscibility Pressures," *J. Pet. Tech. 32,* 160-168.

Yokoyama, Y. and L. W. Lake, 1981, "The Effects of Capillary Pressure on Immiscible Displacements in Stratified Porous Media," SPE 10109, presented at the 56th Annual Technical Conference of SPE of AIME, San Antonio, October 5-7.

Ypma, J.G.J., 1985, "Compositional Effects in Gravity-Dominated Nitrogen Displacements," SPE 14416 presented at the 60th Annual Mtg. of SPE, Las Vegas, Septemer 22-25.

Zapata, V. J. and L. W. Lake, 1981, "A Theoretical Analysis of Viscous Crossflow," SPE 10111, presented ant the 56th Annual Technical Conference of SPE of AIME, San Antonio, October 5-7.

★ U.S. GPO: 1988 561-025/80011